
**The synthesis of Pd-Ag composite membranes for H₂
separation using electroless plating method**

by
Rajkumar Bhandari

A **Ph.D.** thesis
submitted to the faculty of the
Worcester Polytechnic Institute
In fulfillment of the requirements for the
Degree of Doctor of Philosophy in Chemical Engineering
by

January 2010

APPROVED:

Dr. Yi Hua Ma
Advisor

Dr. David DiBiasio
Head of Department

Dr. Ravindra Datta
Committee Member

Dr. Jianyu Liang
Committee Member

Acknowledgment

I would like to thank my advisor, Professor Yi Hua Ma, for his guidance and support over the period of this thesis work. I am deeply impressed by his depth of knowledge, his continuous devotion to reading and learning, and his sincerity as a researcher. I especially enjoyed his style of mentoring students where you get lot of freedom to think on your own and at the same time his guidance is always there when you need it. I also want to thank my committee members, Prof. Ravindra Datta and Prof. Jianyu Liang, for their suggestions and the time they devoted to read the thesis.

I would like to thank Dr. Erik Engwall and Dr. Ivan Mardilovich for their technical inputs into my thesis work. I would like to thank chemical engineering department staff especially Jack Ferraro and Doug White for the great help they provided in overcoming any hurdles related to the experimental work I faced during my research years. I also would like to thank Federico, Engin, Ceylan, Alpna, Natalie, Mike, Alex and Reyyan for their support, help in the lab work. I would also like to thank all of my friends, especially Nikhil and Rasesh, and colleagues at WPI for their kind help and all the fun I had.

I particularly would like to thank Prof. Jianyu Liang (my committee member) for letting me use the BAS electrochemical station in her lab. I sincerely appreciate the Shell team especially Dr. Andreas Matzakos for the meetings rich in discussing innovative ideas. The financial and technical support for this project was provided by Shell International Exploration and Production, Inc. and Shell Hydrogen and is sincerely acknowledged.

Finally, I dedicate this work to my family (my parents, my wife and my daughter, Diya) without whom I find no purpose in my life and who are always there with me in good as well as in the difficult times.

Abstract

One of the key elements to the success of Pd-Ag membrane based reactor for the H₂ production is the synthesis of thin and highly selective membranes using the electroless plating method. This work describes the effect of electroless plating conditions on the obtained Pd and Ag deposits properties (morphology, compactness, phase structure, compositional homogeneity and adhesion) important from synthesis of thin and H₂ selective membrane viewpoint. Both sequential and co-deposition deposition methods were investigated.

The conventional Pd and Ag plating conditions (NH₃+EDTA based bath) produced dendritic and non-uniform sequential (multi layer) deposits, not suitable for synthesizing the thin and H₂ selective Pd-Ag membranes. Ag under the conventional plating conditions deposited at high overpotential resulting in the dendritic and non-uniform sequential deposits. The modified Ag plating conditions eliminated Ag deposition at high overpotential and the sequential deposits obtained were non-dendritic and uniform. Thin (< 10 μm thick) and H₂ selective Pd-Ag membranes were successfully synthesized using the modified Ag plating conditions. The membranes were then successfully annealed at 550 °C. After the annealing step, the membranes showed activation energy for the H₂ permeation (4.3–11.5 kJ/mole) lower than that of the pure Pd membrane (12–16.4 kJ/mole) meaning that the Pd-Ag membranes were more effective for the H₂ separation at lower temperatures than the pure Pd membrane. A Pd-Ag (20 wt%) membrane showed H₂ permeance higher by a factor of 2.47 at 250 °C than the pure Pd foil. The Pd-Ag membranes also showed decline in the H₂/He selectivity on exposure to the annealing and H₂ permeation (300–500 °C) study conditions.

The Pd-Ag co-deposits obtained (using NH₃+EDTA bath) were dendritic, inhomogeneous with poor substrate adhesion, therefore not suitable for the membrane synthesis. The co-deposits were bi-metallic and required the annealing step to form the Pd-Ag alloy. There existed a large difference in the deposition potentials (600 to 650 mV) of Pd and Ag. The Ag deposition was severely controlled by its mass transfer in the solution resulting in the dendritic and inhomogeneous deposits. Among the different complexing agents investigated, KCl showed the least difference between the Pd and Ag deposition potentials. The co-deposits obtained using the KCl bath were non-dendritic, homogeneous and were Pd-Ag alloy therefore required no annealing step.

Finally, the multi step plating, annealing and polishing approach was used to avoid the decline in the selectivity of the sequentially prepared Pd-Ag membranes. The membranes prepared by the plating, annealing and polishing approach showed very high selectivity (H₂/He) and no decline in the selectivity was observed between 300–450 °C for the total exposure time > 550 h (> 200 h at 450 °C).

Executive summary

The world energy demand is increasing day by day. The main source of energy used today is based on fossil fuels which causes a number of environmental concerns. H₂ being very clean energy carrier is likely to play an important role in the future energy scheme. The Pd-Ag composite membrane based reactor has the potential to produce H₂ by the fossil fuel reforming. In the Pd-Ag based membrane reactor, H₂ produced in the reforming reaction is simultaneously separated from the reaction products, thus making the whole process more economical than conventional approach of H₂ production in the reforming reaction and then subsequent H₂ separation from the reforming reaction products. Also the by-products of reforming in the Pd-Ag based membrane reactor could be captured and handled more efficiently to deal with the environmental effects of burning fossil fuels. One of the key elements to the success of the Pd-Ag based membrane reactor is the synthesis of thin and highly selective Pd-Ag composite membranes using the electroless plating method. The Pd-Ag membranes could be prepared either by depositing both metals simultaneously (electroless co-deposition) or individually, layer by layer (electroless sequential deposition). The conventional sequential deposition uses the bi-layer approach in which an Ag layer is deposited on the top of a thick Pd layer already selective to hydrogen. The two layers are then annealed at high temperatures (generally 600 °C or higher) to form the Pd-Ag alloy. The annealing temperature is limited in the case of the porous metal substrate due to the diffusion of the substrate components into the Pd and Ag layers. The limited annealing temperature then demands very thin multi alternate layers of the two metals to be deposited to reduce the annealing time. Depending on the phase structure (alloy or

bimetallic) and particles size of the two metals (in the case of bimetallic phase), the annealing conditions could be more mild in the co-deposition case than those required for the sequential deposition.

The properties of electroless deposits such as morphology, compactness, deposits phase structure (in the case of co-deposition) and compositional homogeneity (in the case of co-deposition) play a very important role in the synthesis of thin and H₂ selective homogenous Pd-Ag alloy membranes. The deposit properties (as described above) are highly dependent on the electroless bath components and plating conditions. This study focused on (a) to fundamentally understand the effect of the electroless plating conditions on the properties (morphology and compactness) of single Pd, Ag metal deposits and sequential Pd-Ag deposits (in the case of sequential deposition) from thin and H₂ selective homogeneous Pd-Ag membrane viewpoint (b) to prepare the Pd-Ag membranes using the sequential deposition method and studying the annealing and H₂ permeation characteristics of the synthesized membranes (c) to understand the effect of the electroless plating conditions on the co-deposit properties (important from thin and H₂ selective membrane synthesis viewpoint) such as morphology, compactness, phase structure, the compositional homogeneity (d) to gain the understanding of the leak formation in Pd and Pd-Ag membranes and develop synthesis procedure to enhance the leak stability of Pd and Pd-Ag membranes.

The conventional Pd plating conditions ($[Pd]/[N_2H_4] = 16 \text{ mM}/5.6 \text{ mM}$) using NH₃+EDTA bath, produced compact deposits with good substrate pores penetration and uniform growth in both lateral and perpendicular directions to the substrate surface. The linear sweep voltammetry (LSV) showed that the large overpotential (420-470 mV) existed for the Pd deposition. The large Pd deposition overpotential and high Pd/N₂H₄

ratio (16 mM/5.6 mM) in the bath resulted in very little Pd concentration gradient in the solution and good substrate pores penetration with uniform growth. The conventional Ag plating conditions ($[Ag]/[N_2H_4] = 3 \text{ mM}/5.6 \text{ mM}$) using NH_3+EDTA bath, produced deposits with poor substrate pores penetration and non-uniform growth. The LSV study showed that Ag showed very little overpotential for the deposition in the presence of NH_3+EDTA . Within 15-25 mV overpotential, the Ag deposition was limited by its diffusion in the solution. The low Ag/ N_2H_4 ratio (3 mM/5.6 mM) ratio in the bath resulted in the Ag deposition occurring at high overpotential and limited by its diffusion in the solution. The solution diffusion limited deposition resulted in the Ag deposits with poor substrate pores penetration and non-uniform growth. The Pd surface showed an order of magnitude higher catalytic activity for the N_2H_4 oxidation than the Ag surface. The higher N_2H_4 oxidation activity of the Pd surface and low Ag to N_2H_4 ratio in the bath (3 mM/5.6 mM) resulted in the Ag deposition severely controlled by its diffusion in the solution leading to the highly non-uniform and dendritic Pd-Ag sequential deposits, not suitable for the synthesis of thin and H_2 selective membranes. The modified electroless bath conditions such as substrate stirring or high Ag to N_2H_4 ratio (20 mM/4 mM, 3 mM/1 mM) ratio favored the Ag deposition at low overpotential. The low overpotential deposition conditions produced Ag deposits with good substrate pores penetration and uniform growth. The Pd-Ag sequential deposits obtained using the modified plating conditions were very uniform and better suited for the synthesis of thin and H_2 selective membranes.

Thin ($< 10 \mu\text{m}$) and He gas tight (i.e. selective to H_2 gas only) Pd-Ag membranes were successfully synthesized using the modified Ag plating conditions. The membranes were synthesized using the multilayer sequential deposition with each Pd

and Ag layer thickness in the range of 2.0-3.0 μm or less. The Pd-Ag sequential layers were successfully annealed to form a homogeneous Pd-Ag alloy at 550 $^{\circ}\text{C}$ for 24 h in H_2 . The EDX line scan analysis showed fairly uniform distribution of Pd and Ag across the cross-sections of the membranes. After annealing, the membranes showed lower activation energies (4.3-11.5 kJ/mole) for the H_2 permeance than those reported for the pure Pd membranes in the literature (12-16.4 kJ/mole). The lower activation energies of the Pd-Ag membranes meant that on decreasing the temperature, the H_2 permeance of the Pd-Ag membranes would decrease at a lesser rate than that of pure Pd membranes, making Pd-Ag membranes more effective for the H_2 separation at lower temperatures.

The sequentially prepared Pd-Ag membranes did not show stable selectivity (H_2/He) under the annealing and H_2 permeation study conditions (300-550 $^{\circ}\text{C}$, for 280 h) and significant decline in the selectivity (H_2/He) of the membranes was noticed particularly at 500 and 550 $^{\circ}\text{C}$.

The deposition characteristics of Pd and Ag from the conventional NH_3 +EDTA based co-deposition bath were very similar to their deposition characteristics from the individual baths. The Pd deposition occurred at the electrode potential 600 to 650 mV more cathodic than that for the Ag deposition. The deposition characteristics for the metals did not change with the nature of the surface and were very similar on both Pd and Ag surface. Under the co-deposition conditions, the Ag deposition was severely controlled by its diffusion in the solution resulting in non-uniform, dendritic deposits with poor substrate adhesion, not suitable for the membrane synthesis. The co-deposits obtained using the NH_3 +EDTA bath did not produce He gas tight membrane even after depositing a large thick layer (33.5 μm) of the co-deposits on a porous stainless tube (0.1 μm media grade) as the substrate. The variations in plating bath parameters (total

metal concentration, pH, temperature, N_2H_4 and NH_3 concentration) had minor effect on the deposits properties. The obtained co-deposits were bimetallic and non-homogeneous in composition under all the plating conditions investigated.

Different complexing agents (NH_3 , EDTA, glycine, KCl) were investigated to reduce the deposition potential difference between Pd and Ag. Pd and Ag showed large differences in their deposition potentials (~ 550-590 mV) in the presence of NH_3 , EDTA and glycine, very similar to that observed for the mixed NH_3 +EDTA bath. The Pd and Ag deposition potential difference (~250 mV) in the presence of KCl was relatively much lower than that for the other complexing agents. KCl was found to be the most suitable complexing agent for the co-deposition.

The Pd-Ag co-deposits obtained from NH_3 , EDTA and glycine bath were bimetallic and non-homogeneous in composition. In comparison to the NH_3 and EDTA baths, the co-deposits obtained from the glycine bath showed relatively uniform growth, therefore were better suited for the membrane synthesis. The annealing study of the glycine based co-deposits indicated that the deposits could be annealed in the 300-400 °C temperature range. The membrane (7-8 μm) prepared using the glycine bath showed large drop in the membrane selectivity on heating (250-300 °C, 300 h). The decline in the selectivity was believed to be due to the non-uniform growth of the as plated deposits. The polishing steps during the membrane plating resulted in improved selectivity.

The KCl bath showed homogeneous precipitation of Pd and Ag in the presence of N_2H_4 as the reducing agent in the basic conditions. The use of HCHO as the reducing agent in the acidic conditions (pH = 2) eliminated the homogeneous precipitation of Pd and Ag. The Pd and Ag deposits obtained using the acidic conditions were very uniform in the composition. The Pd-Ag deposits obtained from KCl bath were in the alloy phase,

therefore eliminated the annealing step required for the membrane synthesis.

Finally, multi step plating, annealing and polishing approach was studied for the mitigation of the decline in the selectivity (H_2/He) of the Pd-Ag sequentially synthesized membrane. The decline in the selectivity in membranes was believed to be due to the porosity present in the Pd and Ag deposits. The voids present in the deposits agglomerated on heating causing the through-through pinholes formation in the membrane and decline in the selectivity. The plating annealing, annealing and polishing approach avoided the formation of through-through pinholes in the membrane. The membrane prepared using the plating, annealing and polishing approach showed no decline in the selectivity (H_2/He) leak development in the temperature range 300-450 °C for the total investigated time of 550 h.

In conclusions **(a)** The overpotential at which Ag was deposited in the case of the Pd-Ag sequential electroless deposition influenced the morphology and compactness of the deposits. The plating conditions favoring the low Ag overpotential deposition resulted in compact and uniform deposits, therefore were more suitable for the thin and selective Pd-Ag membrane synthesis **(b)** The multi layer sequential method was successfully utilized for the first time to synthesize thin (< 10 μm thickness) and H_2 selective Pd-Ag membranes using the plating conditions favoring the Ag deposition at low overpotential **(c)** The Pd-Ag membranes synthesized by the multi layer sequential method with Pd and Ag layers each in the thickness range of 2.0-3.0 μm or less were successfully annealed at 550 °C for 24 h **(d)** The Pd-Ag membranes showed lower activation energy for the H_2 permeation than the pure Pd membranes meaning that on decreasing the temperature, the H_2 permeation of the Pd-Ag membranes decreased at a lesser rate than that of the pure Pd membranes making Pd-Ag membranes more

effective at lower temperatures (e) The difference in the Pd and Ag deposition potentials had large impact on the properties of the obtained co-deposits. The large difference in the potentials (> 400 mV) resulted in the deposits showing non-uniform growth, inhomogeneous composition, poor substrate adhesion and the deposits were bimetallic requiring additional annealing step to synthesize the alloy membrane. The plating conditions favoring the deposition at lower potential (~ 250 mV) difference between Pd and Ag resulted in the deposits with alloy phase and homogeneous composition, therefore required no additional annealing step for the Pd-Ag alloy membrane synthesis (f) The voids present in the as plated Pd or Pd-Ag deposits were believed to be forming the pinholes in the membrane at higher temperatures (≥ 400 °C), therefore resulting in the decline in the selectivity (H_2/He) of Pd and Pd-Ag membranes. The voids present in the deposits were believed to agglomerate on heating and in a few of the cases, the voids agglomeration caused formation of the through-through pinholes in the membrane. The multi step plating, annealing and polishing approach prevented the formation of through-through pinholes in the membrane. The multi step plating, annealing and polishing approach resulted in the Pd and Pd-Ag membranes showing stable selectivity between 300-450 °C for more than 550 h. The membranes were at 450 °C in H_2 atmosphere for more than 200 h (> 8 days) out of 550 h.

Table of contents

Acknowledgements	ii
Abstract	iv
Executive summary	v
Table of contents	xii
List of figures	xvi
List of tables	xxv
1. Introduction	1
2. Literature Review	6
2.1. Pd-H system	6
2.2. Pd alloy-H system	8
2.3. Membrane Synthesis	14
2.3.1. <i>Substrate material, properties and treatment</i>	14
2.3.2. <i>Pd and Pd-alloy deposition techniques</i>	17
2.3.3. <i>Pd and Ag electroless deposition</i>	25
2.3.3.1. Pd plating	25
2.3.3.2. Ag plating.....	28
2.3.3.3. Pd-Ag co-plating	32
2.3.4. <i>H₂ permeation characteristics</i>	42
3. Experimental methods and procedures	46
3.1. Introduction	46
3.2. Substrate and treatment	46
3.2.1. <i>Substrate</i>	46
3.2.2. <i>Substrate pre-treatment</i>	47
3.3. Pd and Ag plating.....	50
3.4. Membrane polishing.....	52
3.5. Equipments used	53
3.5.1. <i>Membrane synthesis: He flux measurement</i>	53
3.5.2. <i>Gravimetric thickness</i>	53
3.5.3. <i>Bubble test</i>	55
3.5.4. <i>Ag electroplating set up</i>	55
3.5.5. <i>Membrane annealing and H₂ permeance characterization</i>	56
3.5.6. <i>SEM and EDX analysis</i>	58
3.5.7. <i>XRD analysis</i>	59
3.5.8. <i>Linear sweep (LSV) and cyclic voltammetry study</i>	59
4. H₂ interaction with Pd and Pd-Ag alloy	62
4.1. Introduction	62
4.2. H ₂ interaction with Pd	62
4.3. H ₂ interaction with Pd-Ag alloy	71

5. Pd-Ag sequential deposition: Relation between plating conditions and deposits morphology	78
5.1. Introduction	78
5.2. Experimental	81
5.2.1. <i>Plating conditions</i>	81
5.3. Results and discussions	85
5.3.1. <i>Single metal deposition</i>	85
5.3.2. <i>Pd-Ag sequential deposition</i>	88
5.3.3. <i>LSV polarization characteristics of Pd and Ag electroless baths</i>	91
5.3.3.1. Ag and Pd polarization characteristics	93
5.3.3.2. N_2H_4 polarization characteristics	97
5.3.4. <i>Morphology of the electroless Pd-Ag deposits</i>	97
5.4. Conclusion	110
6 Pd-Ag co-deposition: Conventional NH_3 and EDTA based bath chemistry	111
6.1. Introduction	111
6.2. Experimental	113
6.2.1. <i>Conventional NH_3 and EDTA bath and plating conditions</i>	113
6.2.2. <i>Pd and Ag LSV polarization study</i>	113
6.2.3. <i>Membrane synthesis</i>	115
6.2.4. <i>Deposit composition and crystalline structure</i>	115
6.3. Results and discussion	115
6.3.1. <i>Pd and Ag polarization characteristics using conventional NH_3 and EDTA bath</i>	115
6.3.2. <i>Effect of the total metal concentration (conventional bath)</i>	120
6.3.3. <i>Effect of N_2H_4 concentration (conventional bath)</i>	127
6.3.4. <i>Effect of NH_3 (conventional bath)</i>	129
6.3.5. <i>Effect of pH (conventional bath)</i>	133
6.3.6. <i>Temperature effect (conventional bath)</i>	135
6.3.7. <i>Effect of metal ratio (conventional bath)</i>	136
6.3.8. <i>Effect of substrate rotation (conventional bath)</i>	141
6.3.9. <i>Membrane synthesis-He flux decline (conventional bath)</i>	145
6.3.10. <i>Glycine influence on the Pd and Ag deposition</i>	147
6.3.10.1. Individual Pd and Ag polarization from glycine bath	147
6.3.10.2. Simultaneous Pd and Ag polarization characteristics from glycine bath	151
6.3.11. <i>Suitability of the complexing agents</i>	151
6.3.12. <i>N_2H_4 Oxidation</i>	154
6.4. Conclusion	157
7. Sequentially deposited Pd-Ag membranes and their annealing characteristics	159
7.1. Introduction	159
7.2. Experimental	160
7.2.1. <i>Plating conditions and substrate</i>	160
7.2.2. <i>Annealing and H_2 permeation measurement</i>	162
7.2.3. <i>SEM and EDX characterization</i>	163
7.3. Results and discussions	163
7.3.1. <i>The morphology of the Ag electrodeposits on PSS coupons</i>	163
7.3.2. <i>Synthesis of Pd-Ag membranes</i>	165
7.3.3. <i>Annealing characteristics</i>	167
7.3.4. <i>Post annealing H_2 permeation characteristics</i>	172
7.3.5. <i>SEM and EDX analysis</i>	180
7.3.6. <i>H_2/He selectivity ($\Delta P = 1 atm$)</i>	185
7.4. Conclusion	188

8. Characterization of Pd-Ag co-deposits and membrane synthesis	189
8.1. Introduction	189
8.2. Experimental	190
8.2.1. <i>Plating conditions and substrate</i>	190
8.2.2. <i>Coupon annealing</i>	192
8.2.3. <i>Membrane synthesis and characterization</i>	192
8.2.4. <i>Deposits morphology, compositional homogeneity and phase characterization</i>	194
8.3. Results and discussions	194
8.3.1. <i>Bath stability in the presence of N_2H_4</i>	194
8.3.2. <i>Deposits morphology, crystalline structure and compositional homogeneity</i>	195
8.3.3. <i>Annealing characteristics of the glycine based deposits</i>	210
8.3.3.1. <i>Annealing time estimation and characteristics</i>	210
8.3.3.2. <i>Pd-Ag particles size based on EDX EDX penetration depth</i>	219
8.4. Conclusion.....	221
9. He Leak mitigation in membranes	222
9.1. Introduction	222
9.2. Experimental	224
9.3. Results and discussions	226
9.3.1. <i>Possible leak mechanism</i>	226
9.3.2. <i>Effect of multi step plating, annealing and polishing on He leak</i>	231
9.3.3. <i>H_2/He selectivity characterization</i>	234
9.4. Conclusion.....	241
10. Conclusion	242
11. Recommendations.....	249
References	252
Nomenclature.....	263
A. Appendix: Pd and Ag equilibrium potential calculation.....	266
A.1. NH_3 as complexing agent.....	266
A.1.1. <i>NH_3 speciation water</i>	266
A.1.2. <i>Complexing reaction of Pd and Ag with NH_3</i>	266
A.2. EDTA as complexing agent	268
A.2.1. <i>EDTA speciation in water</i>	268
A.2.2. <i>Complexing reactions of EDTA with Pd and Ag</i>	268
A.3. Glycine as complexing agent	270
A.3.1. <i>Glycine speciation in water</i>	270
A.3.2. <i>Complexing reaction of Pd and Ag with glycine (gly)</i>	271
A.4. KCl as complexing agent	272
A.4.1. <i>Complexing reactions of Pd and Ag with Cl</i>	272
B. Appendix: LSV and CV scans of effect of different complexing agents on the Pd and Ag deposition.....	275
B.1. NH_3 influence on the Pd and Ag deposition.....	275
B.1.1. <i>Individual Pd and Ag polarization from NH_3 bath</i>	275
B.1.2. <i>Simultaneous Pd and Ag polarization characteristics from NH_3 bath</i>	278
B.2. EDTA influence on the Pd and Ag deposition	281

B.2.1.	<i>Individual Pd and Ag polarization from EDTA bath</i>	281
B.2.2.	<i>Simultaneous Pd and Ag polarization characteristics from EDTA bath.....</i>	284
B.3.	Glycine influence on the Pd and Ag deposition	284
B.3.1.	<i>Individual Pd and Ag polarization from glycine bath.....</i>	284
B.3.2.	<i>Simultaneous Pd and Ag polarization characteristics from glycine bath</i>	289
B.4.	KCl influence on the Pd and Ag deposition	291
B.4.1.	<i>Individual Pd and Ag polarization from KCl bath.....</i>	291
B.4.2.	<i>Simultaneous Pd and Ag polarization characteristics from KCl bath</i>	295
C.	Appendix: Electroless potential calculations for the Pd and Ag deposition using conventional NH₃+EDTA based bath	297
C.1.	Pd, Ag and N ₂ H ₄ bath polarization characteristics.....	297
C.2.	Kinetics parameter estimation for Pd, Ag and N ₂ H ₄ polarization	300
C.3.	Kinetics parameter estimation for Pd, Ag and N ₂ H ₄ polarization	307
D.	Appendix: List of membranes synthesized.....	313
E.	Appendix: He flow through the substrate	315
F.	Appendix: A case study of He leak in Pd membrane	319

List of Figures

Fig. 2.1. Equilibrium Isotherms of Pd-H system ($n = \text{atomic hydrogen/atomic Pd}$) in the temperature range of 0-298 °C by Wicke and Nernst[6].	9
Fig. 2.2. (a) Log P and C (H/Me) relationships for Pd-Cu alloy at 24 °C [26]. (b) Pressure-composition (P-C) relationships for Palladium/Silver alloys at 50 °C [30].	10
Fig. 2.3. Effect of alloying Pd with other elements on its H ₂ permeance (a) by Knapton [7], temp. = 350 °C and pressure = 21.5 atm (b) by Gryaznov [32] at 500 °C (c) alloying with more than one element [32] at 500 °C.	12
Fig. 2.4. Pore size distribution of porous stainless steel substrate with different media grade numbers measured by the mercury intrusion method.	18
Fig. 2.5. General schematic of the LSV polarization characteristics of electroless plating bath indicating the mechanism of deposition of metals Pore size distribution of porous stainless steel	22
Fig. 2.6. Effect of metal ratio in the bath on the plating rates and deposits composition (a) effect of the metal ratio in the bath and substrate nature on plating rate (b) effect of the metal ratio in the bath on the deposits composition.	34
Fig. 2.7. Effect of the silver content of the co-plating bath on the deposits plating rate and silver content. [metal] = 10 mM, [NH ₄ OH] = 9.8 mM, [N ₂ H ₄] = 10.2 mM and temperature = 50 °C Cheng Yeung [8].	36
Fig. 2.8 (a) Comparison of plating rate by the different seeding procedure, line a for seeding with Pd nano-particle and line b for seeding with PdCl ₂ and SnCl ₂ solutions (b) tuning of hydrazine conc. and ammonia conc. in the solution for the simultaneous deposition of Pd and Ag (Tanaka et al. [85]).	40
Fig. 3.1. Substrate pictures (a) Porous metal tube (b) Porous stainless steel coupon (c) Stainless steel wire.	48
Fig. 3.2. Schematic of He flux measurement set up in between membrane synthesis steps	54
Fig. 3.3. Membrane annealing and H ₂ permeation characterization set up	57
Fig. 3.4. EDX calibration curve for calculating the composition of Pd-Ag deposits	60
Fig. 4.1. The interaction of H ₂ with the Pd foil (a) steps involved in the H ₂ permeation through the Pd foil (b) potential energy diagram of H atom during the permeation steps through the Pd foil (c) fluxes associated with various steps involved in the H atom permeation at the H ₂ gas and	

Pd film interface (see the nomenclature in the end of the chapter for definition of the symbols used in the figure).....	64
Fig. 4.2. Diffusivity of hydrogen in Pd-Ag alloy (a) by Holleck [95], foil area = 3.14 cm ² , pressure range = 0.04- 0.66 atm and thicknesses = 800-2025 μm (b) by Pugachev et al. [94], foil area = 23 cm ² , pressure range = 0-1 atm, and thickness = 100-150 μm.....	72
Fig. 4.3. Solubility of hydrogen in Pd-Ag alloy (a) calculated from data given by Pugachev et al. [94], foil area = 23 cm ² , pressure range = 0-1 atm, and thickness = 100-150 μm (b) by Holleck [95], foil area = 3.14 cm ² , pressure range = 0.04- 0.66 atm and thicknesses = 800-2025 μm (c) by Sieverts et al.[89],Pressure = 1 atm and sample size = 100 g Pd-Ag alloy powder.....	73
Fig. 4.4. Relative H ₂ permeance of Pd-Ag alloy with respect to pure Pd, pressure range = 0.04-0.66 atm Holleck [95], 0-1 atm Pugachev et al. [94], 0-21.5 atm Knapton [7](a) at 500 °C (b) at 350 °C (c) at 250 °C.....	75
Fig. 4.5. The H ₂ permeability of pure Pd and Pd-Ag alloy in the optimum Ag concentration range at 300 °C, pressure range used: Ackerman and Koskinas [99] = 1-7.8 atm, Jemma et al.[112] = 1.4-4.4 atm, Serra et al.[103] = 0-1.1 atm, Holleck [102] = 0.04-0.66 atm, Morreale et al. [97] = 1-27 atm, Howard et al. [104] = 1-27.6 atm, Davis [105] = 0-0.99 atm and Pugachev et al. [101] = 0-1 atm..	76
Fig. 5.1. Schematic of the deposit growth on the substrate immersed in the plating solution, deposits pore penetration and its significance from the substrate pores coverage point of view ..	80
Fig. 5.2. Initial deposition characteristics of single metal deposits on PSS coupon surface (plating solution volume = 50 ml, sample surface area = 2 cm ² , bath temp. = 60 °C, pH = 11) (a) Pd deposits and plating time = 15 min, (b) Ag electroless condition 1 and plating time = 45 min.	86
Fig. 5.3. XRD pattern of the initial single metal deposits obtained on PSS coupon surface (plating solution volume = 50 ml, sample surface area = 2 cm ² , bath temp. = 60 °C, pH = 11) (a) Pd deposits and plating time = 15 min, (b) Ag electroless condition 1 and plating time 45 = min.	87
Fig. 5.4. Cross section of the PSS coupons with single metal deposits thickness > 3μm (plating solution volume = 50 ml, sample surface area = 2 cm ² , bath temp. = 60 °C and pH = 11) (a) Pd electroless deposits and plating time = 45 min,(b) Ag electroless deposits and plating time = 300 min.	89
Fig. 5.5. The Pd-Ag sequential deposits obtained on the PSS surface with total four sequence of Pd-Ag plating. The Pd plating time = 15 min and Ag plating time = 30 min was used in each sequence (for each plating, solution volume = 50 ml, sample surface area = 2 cm ² , bath temp. = 60 °C, pH = 11).....	90
Fig. 5.6. Polarization curve obtained on the Pd or Ag coated stainless wires (plating solution volume = 50 ml, temp. = 60 °C, pH =11 and sample surface area = 0.63 cm ²) (a) Ag solution on the Ag surface, (b) Pd solution on the Pd surface.	94

Fig. 5.7. Polarization curve obtained on Pd or Ag coated stainless steel wires (plating solution volume = 50 ml, temp. = 60 °C, pH = 11 and sample surface area = 0.63 cm ²) (a) Ag solution on the Ag and Pd surface, (b) Pd solution on the Ag and Pd surface.	96
Fig. 5.8. LSV scan of the oxidation of N ₂ H ₄ on the Pd or Ag coated stainless steel wires (plating solution volume = 50 ml, temp. = 60 °C, pH = 11 and sample surface area = 0.63 cm ²) (a) Ag surface, (b) Pd surface.	98
Fig. 5.9. Schematic of the Pd-Ag sequential deposits morphology evolution under Ag plating condition 1.	101
Fig. 5.10. Ag deposition on PSS coupons surface (plating solution volume = 50 ml, sample surface area = 2 cm ² , bath temp. = 60 °C, pH = 11) (a) condition 2 and 45 min plating, (b) condition 3 and 45 min plating, (c) condition 4 and 150 min plating.	103
Fig. 5.11. Ag plating on Pd (20 min plating) plated surface (plating solution volume = 50 ml, sample surface area = 2 cm ² , bath temp. = 60 °C, pH = 11) (a) condition 1, 90 min plating (b) condition 2, 90 min plating (c) condition 3, 90 min plating (d) condition 4, 270 min plating. ...	104
Fig. 5.12. X-ray diffraction pattern of samples with Ag plating on Pd (20 min) plated surface (a) condition 1 (90 min Ag plating) (b) condition 2 (90 min Ag plating) (c) condition 3 (90 min Ag plating) (d) condition 4 (270 min Ag plating).	106
Fig. 5.13. Pd-Ag sequential deposits with two alternate layers of Pd (12 min) and Ag each a. Ag plating condition 1 (Ag plating time 45 min) b. Ag plating condition 2 (Ag plating time 45 min) c. plating condition 3 (Ag plating time 45 min) d. Ag plating condition 4 (Ag plating time 150 min)	107
Fig. 5.14. The sequential Pd-Ag deposits obtained using the Ag plating condition 2 on the PSS surface. Total five sequences of Pd-Ag plating were used with Pd plating time = 15 min and Ag plating time = 20 min for each sequence. For each plating, the solution volume = 50 ml, bath temp. = 60 °C, and pH = 11 were maintained.	109
Fig. 6.1. Pd and Ag polarization characteristics of the co-deposition bath (a) on the Pd surface (b) on the Ag surface.	118
Fig. 6.2. XRD pattern of Pd-Ag co-deposits. Bath composition; total metal conc. = 4 mM, Ag (at%) = 10, N ₂ H ₄ = 6 mM, NH ₃ = 3 M, Na ₂ EDTA = 0.1 M, pH = 11 and Temp. = 60 °C.	121
Fig. 6.3. Effect of the total metal concentration on the average total plating rate and the composition of the deposit. Bath composition; Ag (at%) = 10, N ₂ H ₄ = 6 mM, NH ₃ = 3 M, Na ₂ EDTA = 0.1 M, pH = 11 and Temp. = 60 °C.	122
Fig. 6.4. Effect of the total metal concentration on the morphology of the Pd-Ag deposit. Bath composition; Ag (at%) = 10, N ₂ H ₄ = 6 mM, NH ₃ = 3 M, Na ₂ EDTA = 0.1 M, pH = 11 and Temp. = 60 °C.	124

Fig. 6.5. Typical Pd and Ag distribution obtained in the deposits. Bath composition; total metal conc. = 4 mM, Ag (at%) = 10, N ₂ H ₄ = 6 mM, NH ₃ = 3 M, Na ₂ EDTA = 0.1 M, pH = 11 and Temp. = 60 °C.....	126
Fig. 6.6. Effect of the N ₂ H ₄ concentration on the average plating rate and deposit composition. Bath composition; Total metal conc. = 4 mM (10 at% Ag), NH ₃ = 3 M, Na ₂ EDTA = 0.1 M, pH = 11 and Temp. = 60 °C.....	128
Fig. 6.7. Effect of the N ₂ H ₄ concentration on the morphology of the deposit. Bath composition; Total metal conc. = 4 mM (10 at% Ag), NH ₃ = 3 M, Na ₂ EDTA = 0.1 M, pH = 11 and Temp. = 60 °C.....	130
Fig. 6.8. Effect of the NH ₃ concentration on the average plating rates and deposit composition. Bath composition; Total metal conc. = 4 mM (10 at% Ag), N ₂ H ₄ = 6 mM, Na ₂ EDTA = 0.1 M, pH = 11 and Temp. = 60 °C.....	131
Fig. 6.9. Effect of the NH ₃ concentration on morphology of the deposits. Bath composition; Total metal conc. = 4 mM (10 at% Ag), N ₂ H ₄ = 6 mM, Na ₂ EDTA = 0.1 M, pH = 11 and Temp. = 60 °C.....	132
Fig. 6.10. Effect of pH on the average plating rate and deposit composition. Bath composition; Total metal conc. = 4 mM (10 at% Ag), N ₂ H ₄ = 6 mM, NH ₃ = 3 M, Na ₂ EDTA = 0.1 M and Temp. = 60 °C.....	134
Fig. 6.11. Effect of pH on the morphology of the deposit. Bath composition; Total metal conc. = 4mM (10 at% Ag), N ₂ H ₄ = 6 mM, NH ₃ = 3 M, Na ₂ EDTA = 0.1 M and Temp. = 60 °C.....	136
Fig. 6.12. Effect of temperature on the average plating rate and the deposit composition. Bath composition; Total metal conc. = 4 mM (10 at% Ag), N ₂ H ₄ = 6 mM, NH ₃ = 3 M, Na ₂ EDTA = 0.1 M and pH = 11.....	137
Fig. 6.13. Effect of temperature on the morphology of the deposits. Bath composition; Total metal conc. = 4 mM (10 at% Ag), N ₂ H ₄ = 6 mM, NH ₃ = 3 M, Na ₂ EDTA = 0.1 M and pH = 11.....	139
Fig. 6.14. Effect of at% Ag on the deposit composition and average total metal plating rate. Bath composition; Total metal conc. = 4 mM, N ₂ H ₄ = 6 mM, NH ₃ = 3 M, Na ₂ EDTA = 0.1 M and pH = 11.	140
Fig. 6.15. Effect of the substrate rotation on the phase composition of the deposits; Bath composition: Total metal conc. = 4 mM (10 at% Ag), N ₂ H ₄ = 6 mM, NH ₃ = 3 M, Na ₂ EDTA = 0.1 M and pH = 11.....	142
Fig. 6.16. Effect of the substrate rotation on the morphology of the deposits; Bath composition: Total metal conc. = 4 mM (10 at% Ag), N ₂ H ₄ = 6 mM, NH ₃ = 3 M, Na ₂ EDTA = 0.1 M and pH = 11.....	143
Fig. 6.17. He flux (at ΔP = 1 atm) during synthesis of membranes a. Pure Pd membrane b. Pd-Ag co-deposited membrane (Total metal conc. = 4 mM with 15 at% Ag).....	146

<u>Fig. 6.18.</u> Pd polarization characteristics in the presence of glycine at temp. = 60 °C and Pd conc. = 10 mM in the bath (a) on the Pd surface (b) on the Ag surface	148
<u>Fig. 6.19.</u> Ag polarization characteristics in the presence of glycine at temp. = 60 °C and Ag conc. = 3 mM (a). on the Ag surface (b). on the Pd surface.....	150
<u>Fig. 6.20.</u> Pd and Ag polarization characteristics in the presence of glycine at temp. = 60 °C, Pd conc. =10 mM and Ag conc. = 3mM (a) on the Pd surface (b) on the Ag surface.....	152
<u>Fig. 6.21.</u> N ₂ H ₄ polarization characteristics in the presence of different complexing agents investigated in this study (a) on the Pd surface (b) on the Ag surface	155
<u>Fig. 7.1.</u> The deposition characteristics of the Ag electrodeposits (a) initial 1 μm characteristics for thickness < (b) cross-section of the deposits, thickness >3 μm (c) sequential Pd electroless and Ag electrodeposits	164
<u>Fig. 7.2.</u> He permeance of the substrates during the pre-treatment steps of cleaning and filling the substrate pores with alumina powder.	166
<u>Fig. 7.3.</u> H ₂ permeance of the membranes during the temperature ramp from 400 to 550 °C and annealing step at 550 °C.	169
<u>Fig. 7.4.</u> H ₂ permeance of the membranes measured during the temperature ramp between 400 and 550 °C before and after the annealing step at 550 °C.....	171
<u>Fig. 7.5.</u> Sieverts' plot for the H ₂ permeation between 250 and 500 °C without accounting the pressure drop through the substrate (a) R-06 (b) R-10 (c) R-11 (d) R-13a.	173
<u>Fig. 7.6.</u> Schematic of H ₂ permeation through the composite membrane.	174
<u>Fig. 7.7.</u> Sieverts' plot for the H ₂ permeation between 250 and 500 °C with accounting the pressure drop through the substrate (a) R-06 (b) R-10 (c) R-11 (d) R-13a.	176
<u>Fig. 7.8.</u> Arrhenius plot for H ₂ permeance (250-500 °C) of the membranes	177
<u>Fig. 7.9.</u> Activation energy for the H ₂ permeation in Pd-Ag alloy with different wt% Ag.....	179
<u>Fig. 7.10.</u> H ₂ permeance of the membranes relative to the pure Pd foils with the thickness same as that of the membranes.	181
<u>Fig. 7.11.</u> SEM image of the membrane cross- section (a) R-06 (b) R-10 (c) R-11	182
<u>Fig. 7.12.</u> EDX line scans of the membranes cross-section (a) R-06 (b) R-10 (c) R-11	184
<u>Fig. 8.1.</u> SEM images of the Pd-Ag co-deposits obtained at total metal concentration = 4 mM (10 at% Ag), temp. = 60 °C and N ₂ H ₄ = 5 mM in the bath (a) NH ₃ bath, pH = 11 (b) Glycine bath, pH = 11 (c) EDTA bath, pH = 9.5	197

Fig. 8.2. XRD pattern of the Pd-Ag co-deposits obtained at total metal concentration = 4 mM (10 at% Ag), temp. = 60 °C and N ₂ H ₄ = 5 mM in the bath (a) NH ₃ bath, pH = 11 (b) Glycine bath, pH = 11 (c) EDTA bath, pH = 9.5	200
Fig. 8.3. SEM images of the deposits obtained from KCl bath (pH~1.5) with HCHO (60 mM) as the reducing agent and bath temperature = 60 °C. Total metal concentration was 10 mM with 20 at% Ag in the bath (a) with HCHO in solution (b) without HCHO in solution	201
Fig. 8.4. The X-ray diffraction patterns of the deposits obtained from KCl bath (pH~1.5) with HCHO (60 mM) as the reducing agent and bath temperature = 60 °C. Total metal concentration was 10 mM with 20 at% Ag in the bath (a) with HCHO in solution (b) without HCHO in solution	203
Fig. 8.5. EDX spot scans of the Pd-Ag co-deposits obtained at total metal concentration = 4 mM (10 at% Ag), temp. = 60 °C and N ₂ H ₄ = 5 mM in the bath (a) NH ₃ bath, pH = 11 (b) Glycine bath, pH = 11 (c) EDTA bath, pH = 9.5	204
Fig. 8.6. EDX spot scans of the deposits obtained from KCl bath (pH~1.5) with HCHO (60 mM) as the reducing agent and bath temperature = 60 °C. Total metal concentration was 10 mM with 20 at% Ag in the bath (a) with HCHO in solution (b) without HCHO in solution.....	206
Fig. 8.7. SEM and EDX analysis of the Pd-Ag deposits obtained on the Pd foil from the KCl bath (pH~1.5) with HCHO (60 mM) as the reducing agent and bath temperature = 60 °C. Total metal concentration was 10 mM with 20 at% Ag in the bath (a) SEM image of the foil immersed in the KCl bath without HCHO presence (b) SEM image of the deposits obtained in the presence of HCHO (c) EDX spot scan of the deposits obtained in the presence of HCHO and (d) corresponding Pd and Ag spot composition.....	208
Fig. 8.8. XRD patterns of the deposits obtained on the Pd foil from the KCl bath (pH~1.5) with HCHO (60 mM) as the reducing agent and bath temperature = 60 °C. Total metal concentration was 10 mM with 20 at% Ag in the bath.....	209
Fig. 8.9. XRD patterns of the glycine based Pd-Ag deposits with approximate Ag wt% in the deposits = 10 (a) as deposited (b) after treatment at 400 °C for 10 h in H ₂ (c) after treatment at 500 °C for 10 h in H ₂	211
Fig. 8.10. H ₂ permeation and annealing characteristics membranes synthesized using the glycine based bath (a) R-09 (b) R-12.....	213
Fig. 8.11. He leak and selectivity decline of the membranes during annealing and H ₂ permeation characterization (a) R-09 (b) R-12.....	214
Fig. 8.12. Sieverts' plot for the H ₂ permeance of R-12 between 250-400 °C (a) during heating up membrane from 250 to 400 °C, the data was taken after the H ₂ permeance reached to steady state at each temperature (b) during cooling the membrane from 400 to 250 °C.	216
Fig. 8.13. The EDX analysis of the cross section of membrane R-12 after annealing between 250 and 400 °C.	218

Fig. 9.1. SEM images of Pd and Ag films (a) fresh plated Pd film (b) Pd film heated at 700 °C (c) fresh plated Ag film (d) Ag film heated at 700 °C	227
Fig. 9.2. Schematic of voids present in the film (a) as deposited Pd film (b) Pd film heat at high temperature (c) Pd films subjected to repeated sequence of plating and heating	229
Fig. 9.3. He leak progression on multi step plating, annealing and mechanical polishing steps (a) for R-13 (b) for R-14	232
Fig. 9.4. Effect of repeated steps of plating, annealing and polishing on H ₂ permeance of membranes (a) R-13 (b) R-14.....	235
Fig. 9.5. H ₂ permeance and H ₂ /He selectivity of membranes between 300-450 °C for 550 h (a) R-13b (b) R-14	236
Fig. 9.6. The typical EDX line scans of the membrane cross-sections after the H ₂ permeance and selectivity characteristics study in the temperature range 300-450 °C for more than 550 h (a) R-13b (b) R-14	238
Fig. 9.7. Arrhenius plot of the H ₂ permeance of the membranes (synthesized by multi step plating, annealing and polishing steps) between 300-450 °C for R-13b and R-14.....	239
Fig. B.1. Pd polarization characteristics in the presence of NH ₃ (for bath composition see Chapter 6, Section 6.2) (a). LSV scan on the Pd surface (b). CV scan on the Pd surface (c). LSV scan on the Ag surface (d). CV scan on the Ag surface	276
Fig. B.2. Ag polarization characteristics in the presence of NH ₃ (for bath composition see Chapter 6, Section 6.2) (a). LSV scan on the Ag surface (b). CV scan on the Ag surface (c). LSV scan on the Pd surface (d). CV scan on the Pd surface	277
Fig. B.3. Pd and Ag polarization characteristics in the presence of NH ₃ (for bath composition see Chapter 6, Section 6.2) (a). LSV scan on the Pd surface (b). CV scan on the Pd surface (c). LSV scan on the Ag surface (d). CV scan on the Ag surface.....	279
Fig. B.4. Pd polarization characteristics in the presence of EDTA (see Chapter 6, Section 6.2 for bath composition) (a). LSV scan on the Pd surface (b). CV scan on the Pd surface (c). LSV scan on the Ag surface (d). CV scan on the Ag surface	282
Fig. B.5. Ag polarization characteristics in the presence of EDTA (see Chapter 6, Section 6.2 for bath composition) (a). LSV scan on the Ag surface (b). CV scan on the Ag surface (c). LSV scan on the Pd surface (d). CV scan on the Pd surface.....	283
Fig. B.6. Pd and Ag polarization characteristics in the presence of EDTA (see Chapter 6, Section 6.2 for bath composition) (a). LSV scan on the Pd surface (b). CV scan on the Pd surface (c). LSV scan on the Ag surface (d). CV scan on the Ag surface	285

Fig. B.7. Pd polarization characteristics in the presence of glycine (see Chapter 6 for bath composition) [a]. LSV scan on the Pd surface [b]. CV scan on the Pd surface [c]. LSV scan on the Ag surface [d]. CV scan on the Ag surface 286

Fig. B.8. Ag polarization characteristics in the presence of glycine (see Chapter 6, Section 6.2 for bath composition) (a). LSV scan on the Ag surface (b). CV scan on the Ag surface (c). LSV scan on the Pd surface (d). CV scan on the Pd surface..... 287

Fig. B.9. Pd and Ag polarization characteristics in the presence of glycine (see Chapter 6, Section 6.2 for bath composition) (a). LSV scan on the Pd surface (b). CV scan on the Pd surface (c). LSV scan on the Ag surface (d). CV scan on the Ag surface..... 290

Fig. B.10. Pd polarization characteristics in the presence of KCl (see Chapter 6, Section 6.2 for bath composition) (a). LSV scan on the Pd surface (b). CV scan on the Pd surface (c). LSV scan on the Ag surface (d). CV scan on the Ag surface 292

Fig. B.11. Ag polarization characteristics in the presence of KCl (see Chapter 6, Section 6.2 for bath composition) (a). LSV scan on the Ag surface (b). CV scan on the Ag surface (c). LSV scan on the Pd surface (d). CV scan on the Pd surface..... 294

Fig. B.12. Pd and Ag simultaneous polarization characteristics in the presence KCl (see Chapter 6, Section 6.2 for bath composition) (a). LSV scan on the Pd surface (b). CV scan on the Pd surface (c). LSV scan on the Ag surface (d). CV scan on the Ag surface..... 296

Fig. C.1. Fitting the LSV scan data obtained on Ag and Pd solution to the Butler-Volmer equation in order to determine the kinetic parameters for the charge transfer reaction associated with Ag and Pd reduction. (a) the LSV polarization curve with the net current for Ag (b) fitting the Ag LSV polarization curve to the Butler-Volmer equation (c) the LSV polarization curve with the net current for Pd (d) fitting the Pd LSV polarization curve to the Butler-Volmer equation 302

Fig. C.2. Fitting the N_2H_4 LSV polarization data to the high overpotential approximation Butler-Volmer equation. (a) LSV polarization curve with the net current associated with the oxidation of N_2H_4 [3 mM] on the Ag surface (b) Fitting the N_2H_4 oxidation polarization data on the Ag surface to the high field approximation of Butler-Volmer equation (c) LSV polarization curve with the net current associated with the oxidation of N_2H_4 [3 mM] on the Pd surface (d) Fitting the N_2H_4 oxidation LSV polarization data on the Pd surface to the high field approximation of Butler-Volmer equation. n on the Ag surface 305

Fig. C.3. Overall Pd and Ag electroless plating polarization characteristics. (a)Ag deposition on the Ag surface (b) Ag deposition on the Pd surface (c) Pd deposition on the Pd surface (d) Pd deposition on the Ag surface [Ag] = 3mM, [Pd] = 3 mM and [N₂H₄] = 3 mM and electrode area = 0.63 cm² 309

Fig. C.4. Overall Pd-Ag electroless co- plating polarization characteristics. (a)Pd-Ag co-deposition on the Pd surface (b) Pd-Ag deposition on the Ag surface (c) Pd-Ag co-deposition on the Pd surface when Ag is depositing under the mass transfer controlled conditions (d) Pd deposition on the Ag surface [Ag] = 3mM, [Pd] = 3 mM and [N₂H₄] = 3 mM and electrode area = 0.63 cm² 310

Fig. E.1. The typical He permeance vs. average pressure (average of the pressures on the higher pressure end and lower pressure end) data of the substrate (measured at room temperature) used in this study for the Pd and Pd-Ag membrane preparation..... 316

Fig. F.1. Typical SEM images of the membranes surface after annealing and H₂ permeation characteristics study in the temperature range of 250-550 °C (see Chapter 7, Section 7.3.3 and 7.3.4) (a) R-06 (b) R-10 (c) R-11. 325

List of tables

Table 2.1. Pd electroless plating bath developed by (a) Rhoda [75] (b) Pearlstein and Weightman [78].....	26
Table 2.2. Ag plating bath composition used by Shu et al. [41]	29
Table 2.3. Compositions of the electroless plating baths used for the Pd-Ag co-deposition in the literature	33
Table 2.4. Example of variation in the H ₂ permeance of composite membranes.....	44
Table 3.1. Basic solution composition used for the cleaning of the substrate.....	48
Table 3.2. Pd electroless, Ag electroless and Ag electroplating bath compositions.....	51
Table 5.1. Composition of Pd and Ag plating solutions.....	82
Table 5.2. Different plating conditions used for the Ag deposition. Condition 1 represented the typical plating conditions used for the deposition of Ag in the literature [49, 87] and conditions 2, 3 and 4 represented the different modifications to condition 1.....	84
Table 6.1. NH ₃ and EDTA based Pd-Ag co-deposition bath.....	114
Table 6.2. Complexing agents and their bath composition.....	116
Table 6.3. Summary of the deposition potential in the presence of various complexing agents	153
Table 7.1. Summary of Pd and Ag plating conditions and obtained deposit characteristics investigated in Chapter 5.....	161
Table 7.2. Gravimetric thicknesses of the sequentially deposited Pd-Ag layers.....	168
Table 7.3. The Ag wt% measured by EDX area scan.....	186
Table 8.1. KCl bath composition	191
Table 8.2. Stability checking for the KCl bath with 20 wt% Ag and 2 mM concentration of reducing agent.....	196
Table A.1. Fraction of NH ₃ at different pH in water	266
Table A.2. Fraction of EDTA ⁻⁴ (Y ⁻⁴) as function of pH in water.....	269
Table A.3. Fraction of the total glycine added in the form of gly ⁻ at different pH in water	270

<u>Table A.4.</u> The calculation of the equilibrium potentials of Pd and Ag in the presence of different complexing agents for [Pd] = 10 mM and [Ag] = 3 mM in the bath.....	274
<u>Table C.1.</u> Kinetics parameter obtained after fitting the LSV curves for the Ag reduction, Pd reduction and the N ₂ H ₄ oxidation	306
<u>Table D.1.</u> Substrates and their pre-treatment before the plating step.....	313
<u>Table D.2.</u> Membrane plating steps and their description.	314
<u>Table E.1.</u> Average pore size of some of the substrates used in this study for the Pd and Pd-Ag membrane preparation.....	318
<u>Table F.1.</u> He flow through the Pd film in the case when all the defects contribute to the pinholes formation	321
<u>Table F.2.</u> He leak formation in composite Pd membrane (Substrate + Pd film) due to the voids present in the electroless deposited Pd film.....	322

1. Introduction

The world energy demand is increasing day by day. The main source of energy used today is based on fossil fuels which cause a number of environmental concerns. The reserves of fossil fuels have limited life [1] and the future energy dependence will have to be on other sources such as solar, biomass, wind and nuclear energy. H₂ being very clean energy carrier has potential to play an important role in the future energy scheme, in which H₂ produced using sources such as solar, nuclear, biomass and wind power needs to be transported to different locations of use demanding huge H₂ supply network [2]. In the transition to the future hydrogen economy and in the present scenario, H₂ could be produced by the reforming of fossil fuels and the infrastructure for the future economy could be initiated. Also the by-product of reforming, the greenhouse CO₂, could be captured and handled more efficiently to deal with the environmental effects of using fossil fuels. The H₂ produced by the reforming of hydrocarbons in the fossil fuel then can be used in the fuel cell. A fuel cell operates at an efficiency of 50-60% [3], while the efficiency for steam power plant and internal combustion engines is 35% and 15-20% [3] respectively, therefore the use of H₂ as the energy carrier could also prolong the life of fossil fuels available today. In addition to using H₂ as an energy carrier, it also finds use for synthesizing ammonia, methanol, refined metals, semiconductors and refining crude oil.

The future demand of hydrogen is expected to rise because of the increasing demand for hydrodesulfurisation of heavy sour crude (e.g., from 480 ft³ to 645 ft³/barrel between 2001 and 2006, an increase of 34%), fuel cells for both stationary and mobile applications and other chemical applications [4]. The growing demand for hydrogen can

be achieved by the use of membrane reactors. The conventional technique for hydrogen production is steam reforming of natural gas (CH_4) at higher temperatures (800 °C or even higher) [5] and pressures (25-30 atm) followed by the water gas shift reaction. The H_2 gas in the product mixture from the water gas shift reaction is purified further by removing impurities such as CO_2 , CO, methane and water using the pressure swing adsorption (PSA) technique. The use of membrane reactor technique offers advantage of combining production and separation in a single step. The simultaneous removal of the product also enhances the overall conversion of the steam reforming reaction at lower temperatures than 800 °C. Therefore, the use of the membrane reactor technique has the potential of producing relatively cheaper H_2 than the existing steam reforming technology.

The membranes used for the purification of H_2 in the membrane reactor assembly are classified into three groups; ceramic, polymer and metal membranes. Porous ceramic membranes have high thermal stability and mechanical strength but are brittle and the selectivity is poor. On the other hand, polymer membranes exhibit high selectivity but can only be used in low temperature ranges, therefore are not suitable for use in the steam reforming conditions. Metal membranes, particularly, the Pd based membranes show high selectivity and thermal stability making them attractive for use in the high temperature membrane reactor applications.

The Pd-H system shows $\alpha \rightarrow \beta$ phase transformation at temperatures below 300 °C. This phase change is characterized by the increase in the H_2 concentration in Pd without pressure increase [6]. The transition from $\alpha \rightarrow \beta$ phase causes the expansion of the Pd lattice. This lattice expansion is accompanied by severe lattice strain in Pd. Therefore when pure Pd membranes are exposed to thermal cycling, at least one temperature being

lower than the critical temperature (~ 300 °C), in the presence of H_2 , the membranes develop cracks and lose their selectivity.

The critical temperature for the $\alpha \rightarrow \beta$ phase transition can be lowered by alloying Pd with Ag. Alloying Pd with Ag not only provides the membrane with the property to withstand thermal cycling in the presence of H_2 but also improves the H_2 permeability when the alloy is in a specific composition range [7]. In addition to the above mentioned advantages, Ag has lower cost than Pd, therefore Pd-Ag membranes with the same thickness cost less than pure Pd membranes.

The minimum range of the thickness for the pure Pd or alloy membranes in the form of free standing sheets or foils by the cold rolling method is limited to ~ 20 - 30 μm . Thicker membranes have low H_2 permeance because in the temperature range of 300 - 500 °C, generally the bulk diffusion through the Pd and Pd-Ag membrane is the rate controlling process and the permeance is inversely proportional to the thickness of the membrane. This limitation in the thickness of the membrane in the form of foil can be overcome by the concept of a composite membrane. The composite membrane consists of a porous substrate on top of which a H_2 selective layer of Pd or Pd-Ag alloy is deposited. The substrate provides the desired mechanical strength to the H_2 selective layer and therefore membranes with thickness as low as a few micrometers can be achieved.

The commonly used substrate materials are Vycor glass [8], porous alumina [9] and porous metal such as stainless steel and inconel [10, 11]. Porous stainless steel and inconel as the substrate material are preferred over other material because of their resistance to cracking, matching coefficient of thermal expansion, easy module fabrication and integration with the reaction system. The synthesis of a composite Pd

based membrane consists of depositing the H₂ selective layer of Pd or Pd-Ag alloy on the substrate. The commonly used deposition techniques are physical vapor deposition, chemical vapor deposition, electroplating and electroless plating [12]. Among these techniques, electroless plating holds advantages of being simple and economical, easy to form a uniform layer on any shape, easy to scale up to the large size substrate and therefore is more suitable as the deposition method for the industrial applications.

The electroless deposition procedure in the case of Pd-Ag alloy membranes consists of either depositing both elements simultaneously (co-deposition) or sequentially (layer by layer). In the sequential deposition approach, alternate layers of Pd and Ag are deposited from their individual plating baths. The Pd and Ag layers are then annealed at higher temperatures to obtain a uniform alloy film. The simultaneous or co-deposition uses a single plating bath for depositing both elements. The annealing step in the case of the co-deposition method depends up on the phase structure of the co-deposits (alloy or bimetallic). The co-deposits with alloy phase do not require the annealing step and the overall membrane synthesis procedure becomes significantly simple. The bimetallic deposits, depending on the particles size of the two metals, could be annealed using more mild time and temperature conditions than those required for the sequential deposition method.

The properties of electroless deposits such as uniformity, compactness in the case single metal deposition and sequential deposition play a very important role in the synthesis of thin and H₂ selective homogenous Pd-Ag alloy composite membranes. In the case of co-deposition, additional properties such as the deposit phase structure, compositional homogeneity and particle sizes of individual metals (if the co-deposits are bimetallic) are also very important for the synthesis of homogeneous Pd-Ag alloy

membranes. The deposit properties described above are highly dependent on the electroless bath components and plating conditions.

This study focused on the synthesis of Pd-Ag composite membranes supported on porous metal substrates using the electroless deposition method. Both sequential and co-deposition methods were investigated. The main objectives of the study were:

- *To understand the effect of addition of Ag into Pd on the H₂ permeation characteristics of the Pd membrane.*
- *To understand how the electroless plating solution components and plating conditions affected the properties of single Pd, Ag metal deposits and sequential Pd-Ag deposits. The deposits properties ((important from membrane synthesis point of view) investigated were morphology and compactness of the deposits.*
- *To gain understanding of the effect of electroless plating bath components and plating conditions on the properties of co-deposits (important from membrane synthesis point of view) and further characterize the co-deposits in terms of their phase structure, particles size in the case of bimetallic structure of the co-deposits. The deposits properties, important from membrane synthesis point of view, investigated were morphology, compactness, phase structure and the compositional homogeneity of the deposits.*
- *To synthesize the Pd-Ag composite membranes based on the obtained results described in items 2 and 3 above and to further study the annealing and H₂ permeation characteristics of the synthesized membranes.*
- *To gain understanding of the leak formation in Pd and Pd-Ag membranes and develop synthesis procedure to enhance the leak stability of Pd and Pd-Ag membranes.*

2. Literature Review

2.1. Pd-H system

The ability of Palladium (Pd) to absorb H_2 was first pointed out by Graham in 1866 [13]. Since then the Pd-H system has been studied in great detail because of its application in the separation of H_2 from gaseous mixtures. When two sides of a Pd metal piece are exposed to the gaseous mixtures having different partial pressures of H_2 , the H_2 gas permeates from the high to the low pressure side due to the difference in the H_2 chemical potential. The following steps are involved during the H_2 permeation from the high pressure side to the low pressure side [14-16].

At the high pressure side:

- The diffusion of H_2 from the bulk to the surface of the membrane
- The dissociative chemisorption of H_2 on the surface of Pd
- The dissolution of atomic H into the bulk of Pd
- The diffusion of atomic H in the bulk of Pd

At the low pressure side:

- Movement of H atom from the bulk to the surface.
- Associative desorption of H in the form of H_2 from the surface
- Diffusion of H_2 from the surface of Pd into the bulk of the gas mixture

When the diffusion of hydrogen in palladium is the rate controlling step (see Chapter 4, Section 4.2 for more details), the flux $j_{diff}(H_2)$ ($\text{mol}/\text{m}^2\text{-s}$) of H_2 is given by Fick's law [14].

$$j_{diff}(H_2) = \frac{DC}{2z}(n_1 - n_2) \quad 2.1$$

Where D , z , n_1 , n_2 and C stand for the diffusivity of H atom through Pd metal (m^2/s), thickness of Pd metal (m), the H atom to Pd atom ratio on the higher pressure side, the H atom to Pd atom ratio on the low pressure side and molar density of Pd metal ($mole/m^3$) respectively. As can be observed from Eqn. 2.1, the H_2 flux is inversely proportional to the Pd membrane thickness, therefore, thinner membranes are desired for the high H_2 flux. Another way of altering the H_2 flux in the Pd membrane is to alter the value of diffusivity, D and solubility, n (see Eqn. 2.1) of H in Pd. The addition of an alloying element into Pd affects the diffusivity and solubility of H in the Pd metal and therefore affects the permeation rate of H_2 in Pd [7, 12, 17-19]. The effect of addition of various elements into Pd on the diffusivity and solubility of H in Pd is discussed in Section 2.2.

One drawback of using the pure Pd metal for the H_2 separation application is the phase transition in the Pd-H system below the critical temperature of 298 °C and pressure of 20 atm [6]. Below the critical conditions, the low solubility phase (α phase) transforms into the higher solubility phase (β phase) as pressure is increased [6, 20-22]. The phase transition is accompanied by the expansion in the host lattice while the structure (fcc) still remains the same [23, 24]. Therefore if a pure Pd metal membrane is exposed to the temperatures below the critical temperature (i.e. 298 °C), the transition between α and β phase could cause cracking of the Pd metal [17], hence resulting in the loss of the membrane selectivity for H_2 . The phase transition in the Pd-H system was reported by Wicke and Nerst [6] by plotting the equilibrium isotherms for the Pd-H system as shown in Fig. 2.1. As can be seen from Fig. 2.1, for 1 atm pressure of H_2 , the

Pd membrane cannot be exposed to temperatures less than 160 °C without the transformation of the α phase to the β phase. The high critical temperature for the phase transition in the Pd-H system is a drawback of the Pd membranes from the industrial application point of view. Unexpected power shut downs in the industrial scenario could cause serious damage to the Pd membranes.

2.2. Pd alloy-H system

The alloying of Pd with other metals suppresses the α to β phase transition temperature in the Pd-H system. The addition of the alloying metal into Pd changes the lattice sizes and the number of vacant d-band holes in Pd [25]. As a result, the hydrogen solubility in different phases (α and β) and the extent of the α to β phase transition in the Pd-H system changes from alloy to alloy. The addition of metal such as Ag, Cu, Pt, Ni, Rh, Au is reported to lower the α to β phase transition temperature in the Pd-H system [25-30]. The alloying of Cu with Pd increased the resistance for the α to β phase transition in Pd-H system [26]. The presence of more than 8 wt% Cu in Pd eliminated the phase transition in the Pd-H system even at room temperature (Fig. 2.2a) [26]. The addition of Pt [28], Ni [29] and Rh [29] into Pd had the effect similar to that of the Cu addition into Pd, i.e., the addition of Pt, Ni and Rh increased the resistance for the α to β phase transition. Brodowsky and Poeschel [30] studied the effect of addition of Ag into Pd on the α to β phase transition in the Pd-H system. The introduction of Ag into Pd increased the resistance for the α to β phase transition. The resistance for the α to β phase transition increased with increased Ag concentration (Fig. 2.2b) and more than 20-30 wt% Ag in Pd resulted in the disappearance of α to β phase transition at 50 °C (Fig. 2.2b). The addition of 19 wt% Ni into Pd lowered the critical

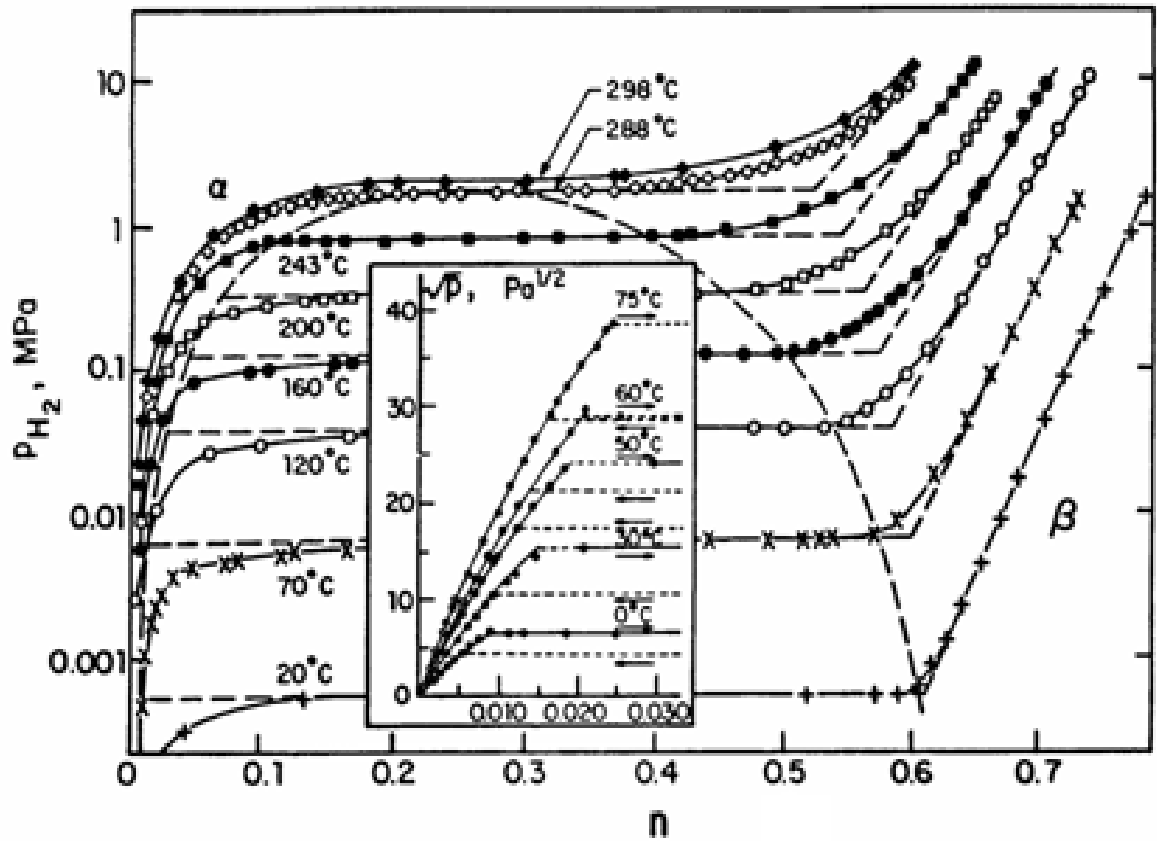


Fig. 2.1. Equilibrium Isotherms of Pd-H system ($n = \text{atomic hydrogen/atomic Pd}$) in the temperature range of 0-298°C by Wicke and Nernst [6].

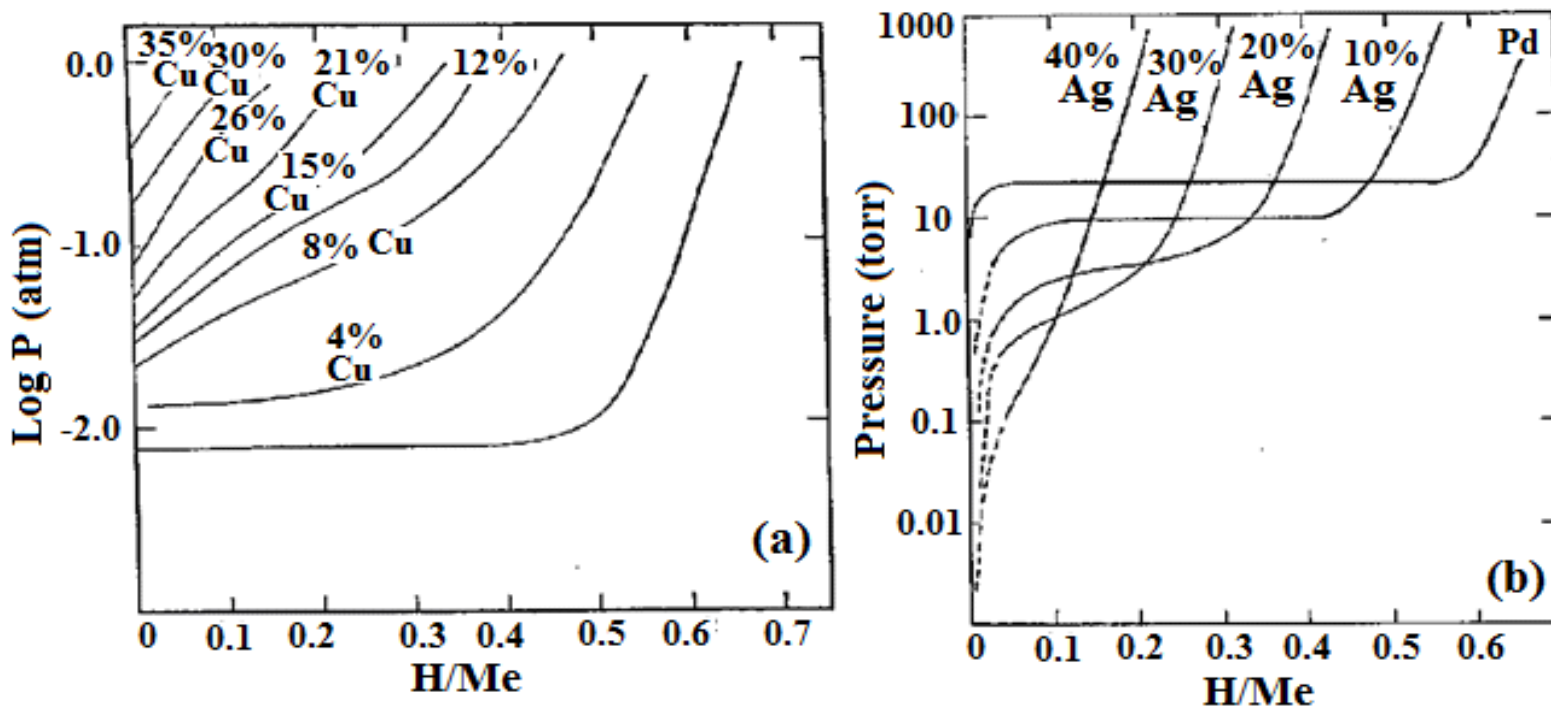


Fig. 2.2. (a) $\text{Log } P$ and H/metal ratio relationships for Pd-Cu alloy at 24°C [26]. (b) pressure-composition (P - H/metal ratio) relationships for Palladium/Silver alloys at 50°C [30].

temperature for the α to β phase transition to 25 °C [29]. The presence of Au in Pd suppressed the α to β phase transition in Pd-H system [27]. According to Rodina et al., [27] the mechanical deformation in the Pd-Au (8 wt%) foil due to the α to β phase transition was observed only after 200 repeated thermal cycling between 20-520 °C, but the pure Pd foil showed mechanical deformation only after 20-30 repeated thermal cycles.

Alloying Pd with various metals also changes the diffusivity and solubility of H in Pd and subsequently the H₂ permeability of Pd. According to Knapton [7], the binary alloys of metals, such as Ag (0-23 wt%), Cu (40 wt%), Ce (0-8 wt%) and Y (0-12 wt%), with Pd had the positive effect on the H₂ permeability (see Fig. 2.3a). Kikuchi and Uemiya [31] reported the effect of the addition of Ag on the H₂ permeability of Pd similar to that observed by Knapton [7]. The H₂ permeability increased up to 23 wt% Ag in Pd and then decreased on further increasing the Ag concentration [31]. The effect of the Ag addition on the H₂ permeability of Pd reported by Gryaznov [32] (see Fig. 2.3b) was significantly different from that reported by Knapton [7] and Kikuchi and Uemiya [31] after alloying 23 wt% concentration of Ag into Pd. According to Knapton [7] and Kikuchi and Uemiya [31], the permeability of H₂ increased with the addition of Ag into Pd up to 23 wt% Ag and then decreased on further addition of Ag. However, according to Gryaznov [32], the permeability of H₂ continuously increased on the addition of Ag into Pd (reported up to 40 wt% Ag, see Fig. 2.3b). The H₂ permeability is very sensitive to the factors such as the level of membrane surface cleanliness and the purity of the H₂ gas used for the permeation measurements. The difference in the factors (membrane surface cleanliness, H₂ gas purity) mentioned above affecting the H₂ permeation measurements could be responsible for the discrepancy between the results

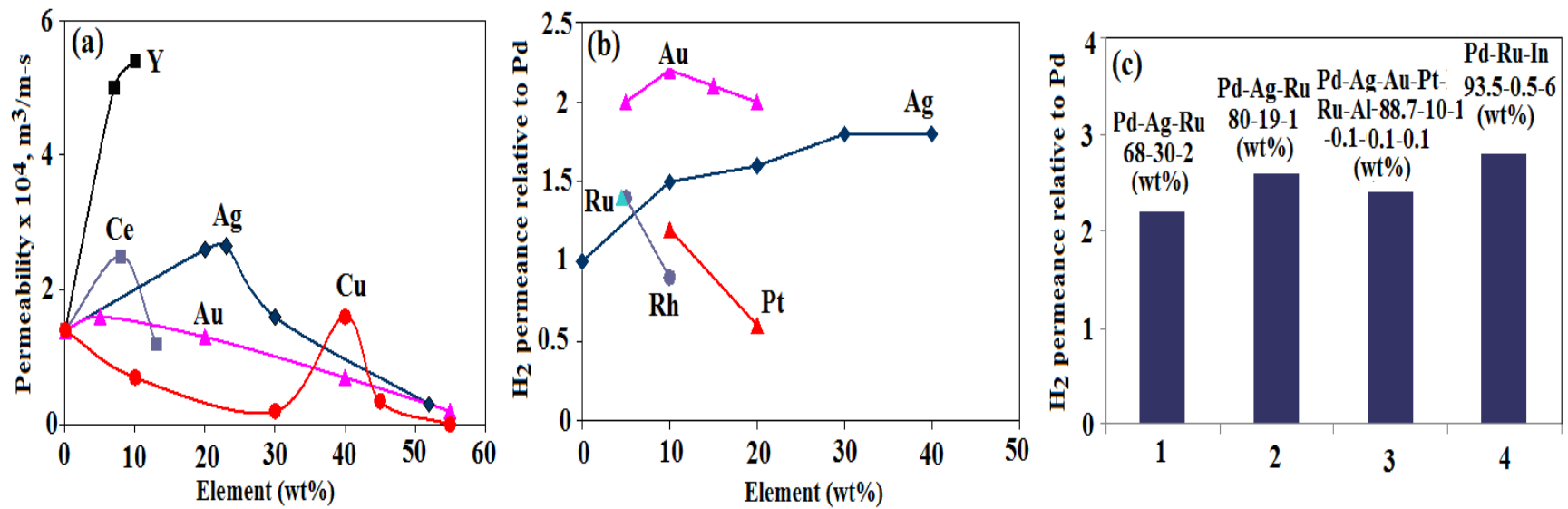


Fig. 2.3. Effect of alloying Pd with other elements on its H₂ permeance (a) by Knapp [7], temp. = 350 °C and pressure = 21.5 atm (b) by Gryaznov [32] at 500 °C (c) alloying with more than one element [32] at 500 °C.

reported by Knapton [7] and Gryaznov [32]. The effect of the addition of Ag on the H₂ permeability of Pd is discussed in details in Chapter 4 (Section 4.3). There are conflicting reports regarding the effect of the addition of Au on the H₂ permeability of Pd. According to Knapton [7], Rodina et al. [27] and McKinley [33], the addition of Au into Pd did not show any significant increase in the H₂ permeance, however according to Gryaznov (see Fig. 2.3b) [32], Pd-Au alloy (0-20 wt% Au) had the H₂ permeance more than two times that of pure Pd (Fig. 2.3b). Gryaznov [32] also reported that ternary alloy of Ru, Ag, Pd and Ru, In, Pd showed twice the permeance in comparison to pure Pd (see Fig. 2.3c). Binary alloy of Cr (0-24 wt%) with Pd decreased both diffusion coefficient and solubility of H₂ in Pd and resulted in a lower H₂ permeance than that of Pd [34]. The decline in the H₂ permeance was also reported on alloying Pd with V [35] and Fe [35] and the decline was due to the drop in the H₂ diffusivity [34, 35].

Beside Pd, several other pure metals have been investigated for their H₂ permeability [36-38]. Pure Rh and Ir membranes showed the H₂ permeance comparable to pure Pd membranes (500 °C and $\Delta P = 0.97$ atm) [36]. V and Ta foils had the H₂ permeation rate higher than Pd foils [37, 38]. The surface of V and Ta oxidized easily in air at room temperature and inhibited the surface reaction, i.e. dissociation and association of H₂, limiting the practical use of V and Ta for H₂ separation. Covering the Ta and V surface with a thin Pd layer prevented the surface oxidation and the resulting foils had H₂ fluxes higher than Pd foils [37, 38]. Although Pd covered Ta and V foils showed higher fluxes than the pure Pd, but exposure of the foils to higher temperatures resulted in the inter diffusion of the metals and sharp decline in the H₂ permeance [39].

2.3. Membrane Synthesis

Pd and Pd-alloy for the H₂ separation could be used in the form of foils or composite membranes, i.e., Pd or Pd-alloy film supported on a porous substrate. The reactions, such as methane steam reforming and water gas shift reactions for the production of H₂, require temperature in the range of 300-800 °C (300-400 °C for the water gas shift reaction and 500-800 °C for the methane steam reforming reaction) and pressure as high as 20-30 atm [5, 12, 40, 41]. Under the high temperature reaction conditions, the process of the H₂ permeation through Pd or Pd-alloy is controlled by its diffusion through the lattice, therefore the low membrane thickness is desired for high H₂ fluxes. The lower limit for the thickness of the Pd and Pd-alloy foils prepared by the cold rolling method is limited to roughly 25 µm. The lower limit of foils thickness subsequently restricts the highest H₂ fluxes attainable by Pd or Pd-alloy foils. The concept of a composite membrane, i.e. Pd or Pd-alloy film supported on a porous substrate where the substrate provides the mechanical strength, overcomes the thickness drawback of Pd or Pd-alloy foils.

The major steps in the synthesis of a composite membrane consists of selecting a suitable substrate material, the treatment of the substrate before the deposition of the Pd or Pd-alloy film, the deposition of the Pd or Pd-alloy layer on the support surface.

2.3.1. Substrate material, properties and treatment

The common substrate materials used in the literature are porous stainless steel [10, 42, 43], Vycor glass [8, 44-47], alumina [9, 48-50], hastelloy, inconel [11, 51] and Ni [52]. Among these materials, the metallic substrate (stainless steel, hastelloy and inconel) offer certain advantages including ease of fabrication, matching coefficient of

thermal expansion with Pd metal and resistance to cracking. However at high temperatures, the metal substrates suffer from the phenomenon of intermetallic diffusion, i.e., diffusion of the substrate components into the supported Pd or Pd-alloy film, thereby reducing the membrane permeability [10, 11, 43, 51]. Ceramic and glass substrates do not contaminate the supported Pd or Pd-alloy film but have drawbacks of low cracking resistance, structural instability of membrane (the low adhesion between metallic Pd film and non-metallic substrate may cause detachment of the Pd film) during the thermal cycling and problems associated with integration of the membrane into the overall reactor assembly.

The metallic substrates require some form of surface treatment to prevent intermetallic diffusion between the substrate and the Pd or Pd-alloy film. Several materials have been used as an intermediate layer for the intermetallic diffusion barrier between Pd or Pd-alloy film and the metal substrate [43, 53-56]. Gryaznov et al. [53] observed twofold decline in the H₂ permeability of a 10 μm thick Pd-Ru (6 wt%) alloy film supported on the porous stainless steel (PSS) substrate after 1000 h at 800 °C. XPS spectra revealed the penetration of stainless steel components into Pd-Ru alloy film causing the decline in the H₂ permeability. The authors then further tested intermediate layers of molybdenum (0.08 μm), tungsten (0.8 μm), tantalum oxide (0.1 μm), magnesia (0.5 μm), alumina (1.2 μm) and zirconia (1.0 μm) deposited by sputtering method as the intermetallic diffusion barrier between the stainless steel and the Pd-Ru alloy film. Among these materials tested, only tungsten, tantalum oxide, magnesia and zirconia provided the 100% structural stability for the membrane for 1000 h at 800 °C. A thin titanium nitride (0.1 μm thick) layer avoided the contamination of Pd layer by the stainless steel substrate components and the membrane was structurally stable at

temperatures as high as 700 °C [43]. In a different approach, the in situ formation of an oxide layer as the intermetallic diffusion barrier by heating the stainless steel support in the presence of air was given by Ma et al. [54]. The oxidation method by Ma et al. [54] was very simple and cost effective as compared to sputtering method used by Gryaznov et al. [53] which involved costly equipment. Nam and Lee [55] deposited a thin layer of silica using sol-gel method to avoid the contact between the stainless steel and Pd-Cu alloy layer. The membrane showed structural stability at 450 °C. An Ag layer of 0.3 μm thickness on the porous stainless steel tube was used to protect the H₂ selective layer consisting of the Pd layer (3 μm) and the Pd-Ag alloy layer (2 μm) [56]. The membrane was subjected to temperature of 500 °C for 75 h and based on the EDS analysis of the membrane cross-section, no penetration of the PSS components into the Pd layer was detected. There exist several methods for the formation (as can be noted from this paragraph) of the intermetallic diffusion barrier between the metal substrate and the Pd or Pd alloy film in the literature. However, methods such as in situ oxidation [54], sol gel method [55] involve less expensive equipments than that required for the sputtering method [53] and could be more preferred from the industrial application viewpoint.

In addition to the structural thermal stability of the substrate against the intermetallic diffusion, other properties desired in a substrate are small pore size, uniform pore size distribution (for the thin membrane synthesis), high porosity (for least substrate resistance for the H₂ flow). In comparison to the ceramic and glass substrates, the PSS substrate lacked the uniform distribution of pore size, which was demonstrated using the mercury intrusion method by Mardilovich et al. [57] with 0.1 μm, 0.2 μm and 0.5 μm media grade substrates obtained from Mott Metallurgical Corporation (Farmington, Connecticut). According to the manufacturer, the media grade of the substrate was

based on its filtration ability towards well characterized particles e.g., 0.5 μm grade substrate rejected a minimum of 95% of particles of sizes equal or greater than 0.5 μm . The maximum size of pores ranged between 4-5 μm , 6-7 μm and 11-12 μm for substrate with media grade of 0.1 μm , 0.2 μm and 0.5 μm respectively (see Fig. 2.4). The thickness of the membrane is determined by the maximum size of the substrate pores. The thickness of the Pd layer required to achieve a He tight membrane was approximately 3 times the diameter of the largest pores in the substrate [57, 58]. Different types of approaches such as shot pinning of iron particles into pores [59], filling pores with alumina powder [60, 61], aluminum hydroxide gel [56, 62] and use of asymmetric substrate [42], have been adopted to narrow down the substrate pores size. In the case of the asymmetric substrate approach, the substrate consists of two layers. The first layer has large porosity and pore size and is followed by relatively thinner layer with narrow pore size on its top. The filling of the substrate pores also introduces the resistance for H_2 diffusion in the substrate. If in a case where the diffusion of H_2 through the substrate is the rate controlling step for the H_2 permeation, the pore filling approach might not be desired.

2.3.2. Pd and Pd-alloy deposition techniques

Varieties of methods are available for the deposition of Pd or Pd-alloy film for the synthesis of composite membranes. Among these, sputtering [63], vapor deposition process [64, 65], chemical vapor deposition [64, 66], electroplating [67] and electroless plating [68] have been extensively used for the Pd and Pd-alloy deposition. The desired properties in a deposition technique include high deposition rate, good control over the deposition rate, uniform deposition, good composition control in the case of alloy

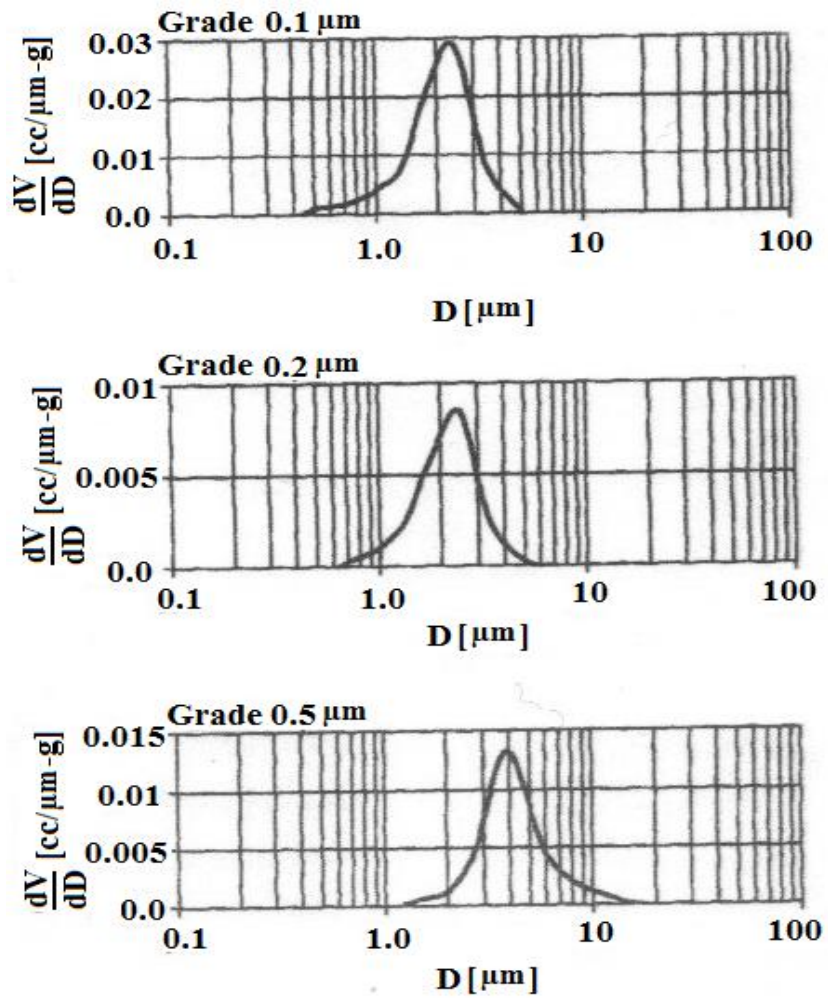


Fig. 2.4. Pore size distribution of porous stainless steel substrate with different media grade numbers measured by the mercury intrusion method [57].

deposition, high purity of the deposits, easy scale up and the low cost of deposition.

The sputtering method involves applying high voltage across the low pressure gas usually Ar. The high voltage ionizes the Ar gas. The positive Ar ion then bombards the cathodic target. The atoms of the cathodic target material, which is Pd or Pd-alloy to be deposited, are ejected in all directions and gets deposited on whatever comes in their way including the substrate. Xomeritakis and Lin [63] prepared Pd-Ag membranes supported on the asymmetric porous alumina supports using the sputtering method. Pd-Ag (25 wt%) alloy was used as the target. Membranes with thicknesses 0.1-1.5 μm were achieved and selectivity ranged from 20-300 at 300 $^{\circ}\text{C}$. The deposition rate as high as 9 $\mu\text{m}/\text{h}$ was achieved and the deposits formed were alloy with the same composition as the target. In a similar study, Chechetto et al. [69] used the sputtering method to deposit Pd on the porous stainless steel (PSS) support covered with the polycarbonate layer. The deposition rate of 9 $\mu\text{m}/\text{h}$ was observed at their operating conditions. The sputtering technique could be used to deposit any metal or alloy with easy control over the deposit composition with high deposition rate but suffered from the disadvantages like high cost of the deposition set up and operating cost [63, 69, 70].

The physical vapor deposition technique is very similar to the sputtering with the difference that the target atoms are ejected by heating in the case of the physical vapor deposition [70].

The chemical vapor deposition technique (CVD) involves organometallic precursor of the metal to be deposited. The metal precursor is made to evaporate and then come into contact of the heated substrate. The precursor decomposes at the substrate surface resulting in the metal deposition [70]. Several researchers have used the CVD technique to prepare Pd based composite membranes [63, 64, 71]. Xomeritakis and Lin [63]

deposited Pd on asymmetric porous alumina supports using the CVD method. Pd(II) acetylacetonate was used as the precursor. The deposition was performed between 250-350 °C and the deposition rate ranged from 0.5 to 2 μm/h. The complete He dense membranes were achieved within 1-1.5 μm thickness of the Pd deposits. The CVD method suffers from drawbacks such as costly set up, lack of precursors in the case of alloy deposition and deposits contamination by the organic precursor [70].

The electroplating method requires less expensive set up in comparison to the sputtering and CVD method. The method involves a cathode i.e., substrate, an anode and direct current (DC) power supply. The electrical potential is applied across the electrodes of the plating system such that the reduction of the metal ions takes place on the substrate. The electrodeposition method was used for the Pd-Cu [55], Pd-Ni [72] and Pd-Ag [56] membrane synthesis supported on the PSS substrate. The method has the main disadvantage that it requires electrical conductive surface which restricts the choice of the substrate material and its pretreatment before the deposition. For example, as mentioned in the previous section that the PSS substrate lacked uniform pore size distribution and require pretreatment such as filling the pores with alumina powder. The alumina powder is electrically non-conductive surface, therefore the electrodeposition will not occur on alumina powder and the advantage of pore filling by the electrically non-conductive surface cannot be achieved by using the electroplating method. The control over the deposition rate in the case of the electroplating method can easily be achieved by controlling the amount of the current passed through the electroplating cell. The co-deposition of two metals becomes difficult when the difference between the standard electrode potential of two metals is more than one volt. However, with the suitable combination of metal complexes, electrolyte and operating conditions, the

deposition potential of the two metals can be brought closer and the co-deposition can be realized [67].

The electroless plating is a widely used method for obtaining a thin metallic film on different substrates (metals, ceramics and plastics) by just immersing the substrate into an electrolyte solution. The method (electroless) works on the similar mechanism as electroplating method with the difference that no external source of electron is required [73]. An electrolyte solution containing metallic ions, reductants, complexing agents and other minor components constitute the typical electroless plating bath. The electroless metal plating mainly involves two redox reactions. The first redox reaction is associated with the metal ions and the second is associated with the reducing agent in the bath. Both cathodic and anodic reactions occur at the substrate surface according to the following generalized reactions.

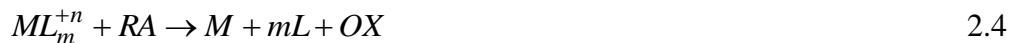
Cathodic:



Anodic:



Overall:



Where M , L , RA , OX and e indicate metal to be deposited, complexant, reducing agent, oxidation product of reducing agent and electron respectively. Fig. 2.5 shows the generalized polarization characteristics of the redox reactions associated with electroless plating. Curve 1 and curve 2 in Fig. 2.5 represent the polarization

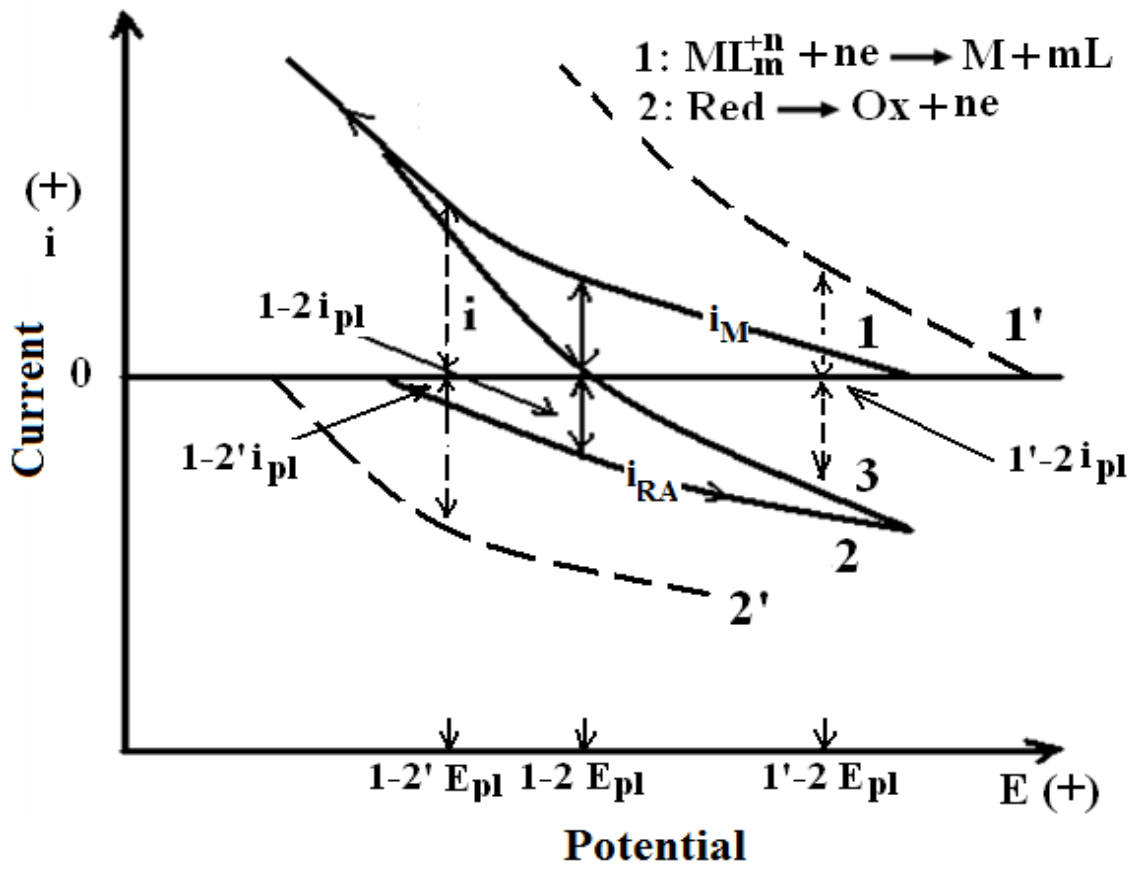


Fig. 2.5. General schematic of the LSV polarization characteristics of electroless plating bath indicating the mechanism of deposition of metals.

characteristics of the metal ions and the reducing agent respectively. i_M and i_{RA} in Fig. 2.5 are the currents associated with curve 1 and curve 2 respectively. For the metal deposition, the following conditions are very important.

1. The equilibrium electrode potential of the metal ions must be higher than that of the reducing agent. The reducing agent will polarize the metal ions reaction in the cathodic direction (resulting in metal deposition) only if the equilibrium electrode potential of metal ions is higher than the equilibrium electrode potential of the reducing agent in the bath.
2. The surface of metal to be deposited should show good catalytic activity for the oxidation of the reducing agent [74]. The poor catalytic activity of the metal surface for the oxidation of the reducing agent would lead to very slow metal deposition rate making the method impractical for the industrial use.
3. The plating conditions should be such that the homogeneous reaction between the metal ions and the reducing agent in the solution is suppressed.

According to the mixed potential theory [73, 75], the electroless plating occurs at the electrode potential where i_M is equal to i_{RA} (because the net external current for the electroless plating is zero). For the plating conditions corresponding to curve 1 and curve 2 (Fig. 2.5), the electrode potential for the electroless plating (i.e. electroless plating potential) is $1-2E_{pl}$ (see Fig. 2.5). The electroless plating potential is highly dependent on bath components and their concentration. For example, if the metal ions concentration in the bath corresponding to curve 1 and curve 2 is increased, then curve 1 will shift towards anodic potential (curve 1'). The electroless potential corresponding to curve 1' ($1'-2 E_{pl}$) will become more anodic than $1-2E_{pl}$. On the other hand if the concentration of the reducing agent is increased in the bath (relative to the plating

conditions corresponding to curve 1 and curve 2), the curve 2 will shift towards cathodic direction (see curve 2', Fig. 2.5) and the electroless plating potential (1-2' E_{pl}) will become more cathodic than 1-2 E_{pl} . The complexing agent in the plating bath has huge impact on the polarization characteristics of the metal ions i.e. on the characteristics of metal ions reduction, curve 1. The complexing agent binds with the metal ions and reduces the equilibrium of potential of the metal ions in the bath. The stronger the binding power of the complexing agent, the larger is the shift of the polarization curve towards the cathodic potential. The complexing agent can also influence the polarization characteristics of the metal ions [76] and the reducing agent by simply adsorbing on the metal surface.

The polarization curves of the overall plating bath do not provide insight into the individual contribution of the metal ions and the reducing agent on the overall characteristics of the plating bath. According to the mixed potential theory [73, 75], the polarization characteristics of metal ions and the reducing agent can be summed up to know the overall plating bath polarization characteristics. The polarization characteristics of metal ions and the reducing agents provides important information such as the overpotential associated with the metal deposition and the suitability of the reducing agent for the metal reduction [77]. The overpotential associated with the metal deposition has an important effect on the metal growth characteristics (e.g., morphology, deposits compactness) [78, 79]. Therefore polarization characteristics of the electroless plating bath components could be very helpful in developing the electroless plating bath composition producing the metal deposits with the desired growth characteristics. In the case of simultaneous deposition of two metals, the polarization curves of the individual metal ions can indicate the difference in the

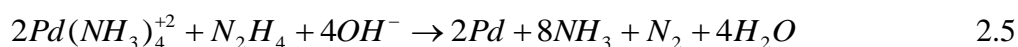
deposition potential and the feasibility of the simultaneous deposition of the metal ions. For the simultaneous deposition of two metals to occur, their deposition potentials should be close to each other [67]. The important challenge in the case of the electroless plating lies in finding the suitable plating conditions especially in the case of simultaneous deposition of two metals.

Since no sophisticated equipment is required, simplicity is the biggest advantage of the electroless plating method. The other important advantages of the electroless plating method are ability to deposit on electrically non-conductive surface, easy scale up, uniform deposition on the complex substrate surface geometry and simple operating conditions. The electroless plating is the most used deposition method for the synthesis of Pd based composite membranes [9, 11, 48-51]. Since this thesis is related to synthesis of the Pd-Ag alloy membranes by the electroless method, the focus is given here more for the Pd and Ag electroless bath chemistry and related information available in the literature.

2.3.3. Pd and Ag electroless deposition

2.3.3.1. Pd Plating

The first electroless plating bath for Pd was reported by Rhoda [80] and its composition is shown in Table 2.1. N_2H_4 in the bath acted as the reducing agent. The overall plating reaction was believed to be represented by



The Pd bath produced deposits of high purity. Since its development, the Pd bath reported by Rhoda has gone through minor changes but the bath to large extent has

Table 2.1. Pd electroless plating bath developed by (a) Rhoda [80] (b) Pearlstein and Weightman [83]

Bath component (a)	Composition (a)	Bath component (b)	Composition (b)
Pd(NH ₃) ₄ Cl ₂	5.4 g/l	PdCl ₂	2 g/l
Na ₂ EDTA	33.6 g/l	HCl (38%)	4 ml/l
NH ₄ OH	350 g/l	NH ₄ OH (28%NH ₃)	160 ml/l
N ₂ H ₄	0.8 g/l	NH ₄ Cl	27 g/l
Temp. °C	80	NaH ₂ PO ₂ .H ₂ O	10 g/l
pH	11.0	pH	9.8 ⁺ 2.0
Plating area, cm ² /l	100	Temperature, °C	50-60

remained the same. The bath has been used in almost all cases for the Pd membrane synthesis [8, 9, 11,46-52] by electroless plating method on a variety of substrates ranging from electrically non-conductive substrates (glass [8, 44, 46, 47], alumina [9, 48-50], zirconia [81]) to electrically conductive substrates (porous stainless steel [10, 11, 51], porous nickel [52], porous inconel [11, 51], porous hastelloy [11, 51]). Uemiya et al. [44] used the bath for the Pd membrane synthesis supported on the porous glass tubes (average pore size = 0.30 μm). The glass tube became Ar tight with a 13 μm thick layer of Pd. The activation energy for the H_2 permeation through the membrane was calculated to be 11.7 kJ/mole in the temperature range of 400-500 $^\circ\text{C}$. The value of the activation energy for the H_2 permeation was close to that reported by Hurlbert et al. [82] for the pure palladium foils supporting the high purity of the obtained deposits from the Pd bath by Rhoda [80]. Pearlstein and Weightman [83] used different Pd electroless bath than that of Rhoda [80] (see Table 2.1). Hypophosphite was used instead of N_2H_4 as the reducing agent. The deposits obtained were not pure Pd and phosphorous content as high as 2 at% was co-deposited with Pd. The bath developed by Pearlstein and Weightman [83] was further studied by Cheng and Yeung [47] for the membrane synthesis. The Pd deposits obtained showed a large number of cracks and hence were not suitable for the preparation of the H_2 selective membrane. The cracks in the deposits were reported to be due to the H_2 gas evolution which was the product of oxidation of the reducing agent used. The bath developed by Pearlstein and Weightman [83] is an example of difficulty involved in finding a suitable electroless bath for the metal deposition from the membrane synthesis perspective. The requirements associated with the deposits from the membrane synthesis perspective include e.g., high purity of the deposits, good adhesion with the substrate surface, high enough deposition rate from practical application point of view, uniform deposition all over the substrate

surface and high compactness of the deposits.

2.3.3.2. Ag Plating

The electroless Ag plating bath used in the literature for the membrane synthesis has been similar to the Pd plating bath [9, 41, 49, 84-87]. Table 2.2 shows the typical Ag bath composition reported in the literature [41]. Shu et al. [41] deposited Ag on PSS substrate using the bath shown in Table 2.2. According to the authors, the Ag bath showed more tendencies to have homogeneous precipitation than the Pd bath, therefore the concentration of Ag (3 mM) was kept much lower than that of Pd (16 mM) in the bath. The Ag deposits lacked uniform deposition over the entire surface of porous stainless steel substrate [41]. The deposits showed preferential deposition on the top of the substrate pores than the inside of the pores. Similar characteristics of the preferential Ag deposition on the top of the substrate pores was observed by Keuler et al. [84] on the γ -Al₂O₃ and ZrO₂ support stabilized with Y₂O₃. The factors responsible for the preferential deposition of Ag on the top of the substrate pore than inside the pore was not investigated by the authors (Shu et al. [41], Keuler et al. [84]) and require further study. The Ag bath shown in Table 2.2 has been used to prepare the Pd-Ag membranes using only the bi-layer sequential deposition method [9, 41, 49, 85, 87]. The bi-layer method consisted of depositing a thick layer of Pd (4.5-10 μ m) already selective to H₂ followed by the Ag layer on the top. The bi-layer was annealed at high temperature to form the Pd-Ag alloy. Uemiya et al., [9] synthesized Pd-Ag membranes on alumina substrates (0.2 μ m grade) using the sequential bi-layer deposition method. The Pd-Ag bi-layer consisted of a Pd layer (~4.3 μ m thick) and an Ag layer (~1.45 μ m thick) on the

Table 2.2. Ag plating bath composition used by Shu et al. [41]

Bath component	Concentration (M)
AgNO ₃ (source of silver ions in the bath)	0.003
Na ₂ EDTA (complexing agent and buffer in the bath)	0.11
NH ₃ (28%) (complexing agent in the bath)	3.17
N ₂ H ₄ .H ₂ O (reducing agent in the bath)	0.0056
Temp. °C	60
pH	10.4

top. The resulted bi-layer deposits were then annealed at temperatures of 500 and 900 °C for 12 h in Ar atmosphere. The temperature of 500 °C was not sufficient for the annealing of the Pd-Ag bi-layer. After annealing at 500 °C, the H₂ flux of the membrane (measured at 400 °C) was only 14.3 m³/m²-h compared to 38.1 m³/m²-h (measured at 400 °C) obtained after annealing at 900 °C. The EDX cross-section line scan analysis revealed complete homogenization of the bi-layer after 900 °C annealing.

Shu et al. [43] deposited Pd (5 µm) and Ag (1.4 µm) bi-layer on the dense stainless steel substrate. The Pd and Ag layers were annealed at different temperatures for 5 h in H₂ atmosphere. It was estimated that Ag penetrated into the palladium layer only to the depth of 0.88, 1.02 and 1.07 µm at temperature of 400 °C, 500 °C and 600 °C respectively. The depth with 10 at% Ag concentration was considered as penetration depth in all the cases. The significant penetration of Fe from the substrate into the Pd-Ag layer was also observed at 600 °C.

Keuler et al. [87] annealed Pd-Ag bi-layer with the total thickness between 1.54 µm and 2.14 µm supported on an alumina tube and annealed the layer at 540 °C in H₂ atmosphere for 30 h. The H₂ permeance increased from 33.5 m³/m²-atm-h at time 0 h to steady value of 46.6 m³/m²-atm-h after 30 h during the annealing step at 540 °C. According to Keuler et al. [87], it was possible to completely anneal thin layers of Pd and Ag (1-1.5 µm thickness) in reasonable time (25-30 h) at 540 °C in H₂ atmosphere. Nair et al. [85] attempted to anneal Pd (10 µm) and Ag (1 µm) bi-layer (~ 12 wt% Ag) supported on alumina substrate at 550 °C for 10 h in H₂ and N₂ (1:1) mixture. According to the authors [85], annealing conditions resulted in the Pd-Ag alloy formation measured by the X-ray (Cu Kα) diffraction analysis of the deposits. It is important to mention here that X-rays penetrate only to a depth between 2-3 µm in the

case of Pd and Ag metals, therefore the XRD analysis revealed the annealing information of the bi-layer limited to the penetration depth of the X-rays. Based on the study by Keuler et al. [87], Shu et al. [43] and Uemiya et al., [9], it appears highly unlikely that such a thick bi-layer of Pd-Ag (11 μm) obtained by Nair et al. [85] could be annealed at 550 $^{\circ}\text{C}$ for 10 h. No EDX cross-section line analysis of the bi-layer was done by Nair et al. [85] which would have clearly indicated the distribution of Pd and Ag across the cross-section of the bi-layer.

The diffusion of the substrate components into the H_2 selective Pd-Ag layers limits the annealing temperature in the case of porous metal substrates [43, 54]. The annealing temperature can be reduced by using the multi-layer sequential deposition approach. The multi-layer sequential deposition approach allows deposition of very thin layers (1-2 μm) of Pd and Ag which then could be annealed using the short time and lower temperature than that required for the bi-layer approach.

The study on the Pd-Ag membrane synthesis by the multi-layer sequential deposition method is lacking in the literature and was one of the main areas of focus in this study. The deposits (single metal as well as sequential deposits) properties such as the morphology and compactness affect the synthesis of thin and H_2 selective Pd and Pd-Ag membranes. There exists very limited study in the literature relating the electroless plating conditions to the deposits properties (important from membrane synthesis viewpoint). The focus of this study, therefore was to understand the effect of the plating conditions on the properties of the single metal (Pd as well as Ag) and sequential multilayer Pd-Ag deposits.

2.3.3.3. Pd-Ag co-plating

An alternate way to the sequential deposition method is the co-deposition method for the preparation of the Pd-Ag membranes. The co-deposition method simplifies the plating steps involved in the Pd-Ag deposition and if the co-deposits have small size Pd and Ag particles, the annealing of the membrane also becomes relatively easier. Shu et al. [88] did the pioneering work of developing an electroless plating bath for the Pd-Ag co-deposition. The authors [88] showed for the first time that Pd and Ag could be deposited simultaneously from the mixed metal electroless plating bath. The NH_3 +EDTA mixed metal or co-deposition bath had bath components similar to Pd or Ag single metal baths described in the Sections 2.3.3.1 and 2.3.3.2.. Table 2.3 shows the plating bath compositions used by Shu et al. [88] and several other authors [8, 89, 90] for the Pd-Ag co-deposition. The main focus in the literature has been on investigating the effect of the co-plating conditions (such as concentration of bath components, temperature, nature of the substrate) on the plating rates and the phase composition of the deposits.

Shu et al. [88] studied the effect of the Pd and Ag metal ratio in the bath and nature of the substrate surface on the plating rates and the deposit composition. Ag had passivating effect on the Pd deposition. The Pd-Ag co-deposition occurred only for 0-20 wt% Ag in the bath on the Pd activated PSS substrate. For the Ag concentration more than 20 wt% in the bath, only the Ag deposition occurred. The plating rate dropped suddenly after 20 wt% Ag in the bath (Fig. 2.6a). The Ag passivating effect was explained on the basis of the electrode potential of the metal ions in the bath. For 0-20 wt% Ag range, the electrode potential of the Ag ions was less than that of Pd and after 20 wt% Ag in the bath, the Ag electrode potential became higher than that of Pd. The

Table 2.3. Compositions of the electroless plating baths used for the Pd-Ag co-deposition in the literature

Bath component	Conc.			
	Shu et al. [88]	Cheng and Yeung. [8]	Huang et al. [89]	Tanaka et al. [90]
Pd(NH ₃) ₄ Cl ₂ .H ₂ O	0-1.8 mM	-	-	-
Pd(NH ₃) ₄ (NO ₃) ₂	-	1.2-50.4 mM	-	-
Pd-acetate	-	-	-	9 mM
PdCl ₂	-	-	1.7 mM	-
AgNO ₃	0-1.8 mM	0.2-4.6 mM	0.2-0.5 mM	1 mM
Na ₂ EDTA	0.1 M	0.1 M	0.1 M	0.1 M
NH ₃ (28%)	3.2 M	3-9 M	3.2 M	4 M
N ₂ H ₄	5.6 mM	5-20 mM	5.6 mM	14 mM
Temp., °C	60	50-60	60	60
Loading, cm ³ /cm ²	-	60/21	16.7	-

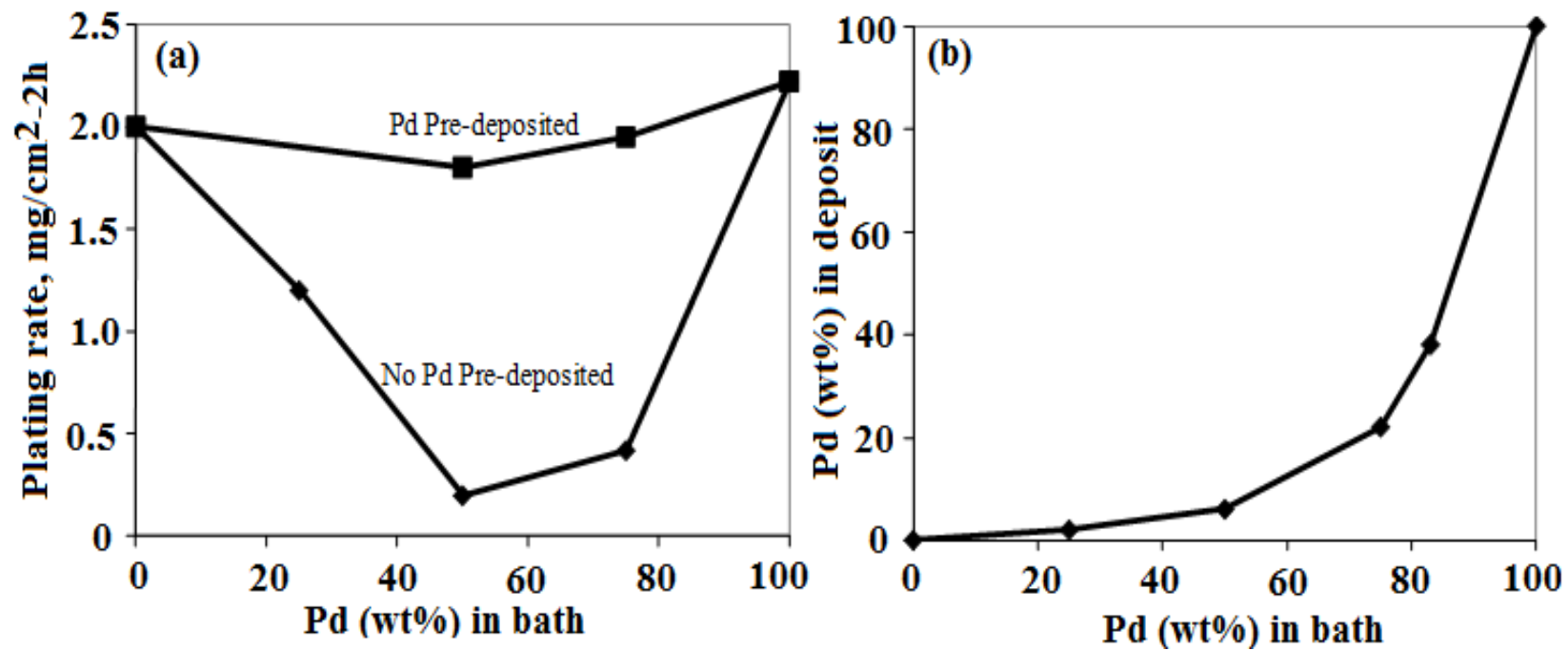


Fig. 2.6. Effect of metal ratio in the bath on the plating rates and deposits composition [88] (a) effect of the metal ratio in the bath and substrate nature on plating rate (b) effect of the metal ratio in the bath on the deposits composition

plating bath contained both EDTA and NH_3 (see Table 2.3), however only EDTA was considered as the complexing agent for the electrode potential calculation. The Pd pre-plating of the PSS substrate avoided the passivating effect and co-deposition occurred up to 80 wt% Ag concentration in the bath (Fig. 2.6b). The Pd pre-plating of the PSS substrate also avoided the drop in the plating rate (Fig. 2.6a) observed on the Pd activated PSS substrate after 20 wt% Ag in the bath. The substrate effect on the Pd and Ag deposition indicated that the electrode potential of the metal ions was not the sole factor influencing the co-deposition. According to Shu et al. [88], the co-deposits were bi-metallic in phase (the deposits were individual particles of the two metals) and required further annealing step for the alloy formation. The additional co-deposits properties (important from membrane synthesis viewpoint) such as morphology and Pd and Ag homogeneity were not investigated. Although the authors (Shu et al. [88]) were successful in obtaining the plating conditions favoring the Pd-Ag co-deposition but no membrane was synthesized using the co-plating bath.

Cheng and Yeung [8] also observed the passivating effect of Ag on the Pd plating on the Vycor glass substrate (5 nm pore size) similar to that reported by Shu et al. [88]. The Pd passivation was affected by the bath composition and the nature of the substrate surface. The higher N_2H_4 to total metal concentration ratio in the bath favored the Pd deposition (Cheng and Yeung [8]). According to Shu et al. [88], the Pd pre-plating of the PSS surface favored the Pd deposition. Shu et al. [88] used the Pd nuclei activated PSS surface and N_2H_4 to metal ratio of 5.6 mM/1.8 mM in the bath. The Pd passivation started at 20 wt% (~ 20 at%) Ag in the bath (Shu et al. [88]). Cheng and Yeung [8] reported the Pd passivation at 3 at% Ag for the N_2H_4 /metal ratio = 10.2 mM/10 mM in the bath on the Pd activated Vycor glass surface (see Fig. 2.7). The

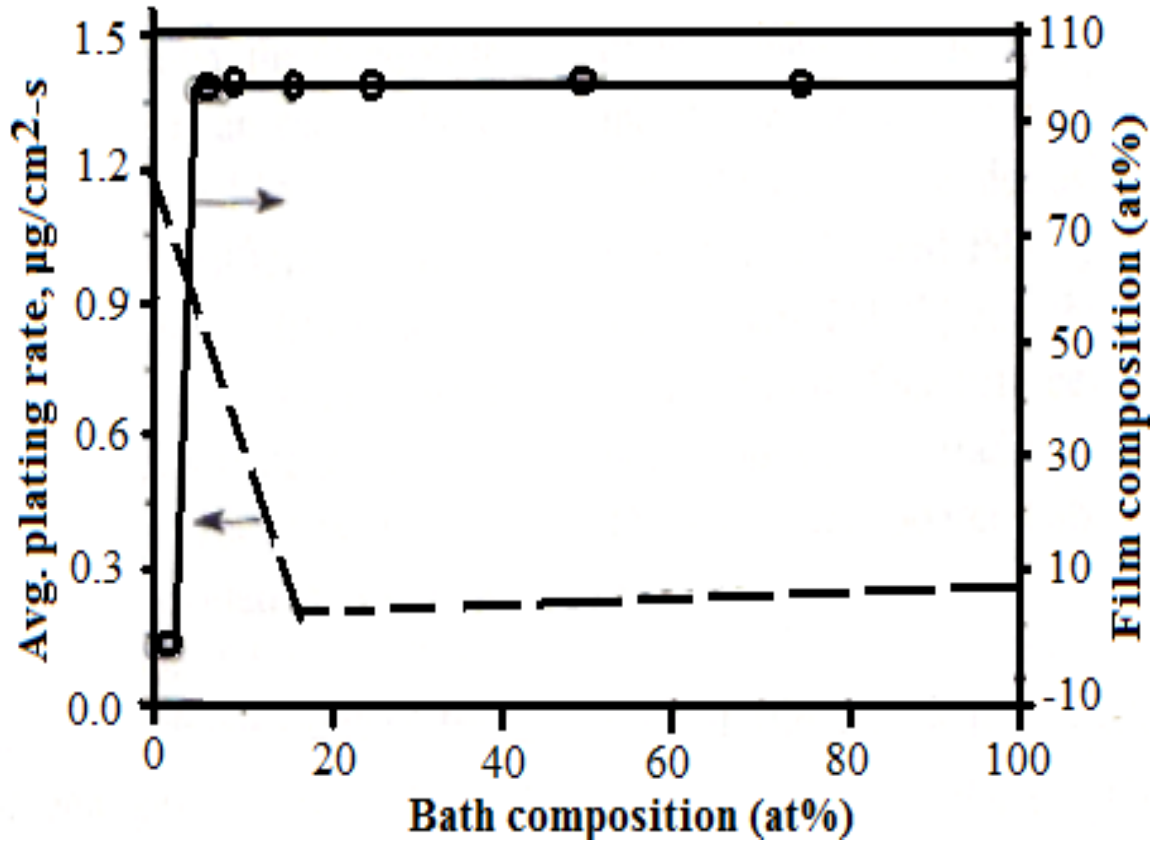


Fig. 2.7. Effect of the silver content of the co-plating bath on the deposits plating rate and silver content. $[\text{metal}] = 10 \text{ mM}$, $[\text{NH}_4\text{OH}] = 9.8 \text{ mM}$, $[\text{N}_2\text{H}_4] = 10.2 \text{ mM}$ and temperature = 50°C (Cheng and Yeung [8]).

different amount of Pd nuclei on the PSS surface and higher N_2H_4 to metal ratio in the bath (in the case of Shu et al. [88] study) could be responsible for the Pd passivation starting at 20 wt% (~ 20 at%) Ag as compared to 3 at% Ag reported by Cheng and Yeung [8]. The characteristics of the effect of the Ag concentration in the bath on the plating rate observed by Cheng and Yeung [8] (see Fig. 2.7) was different from that reported by Shu et al. [88] (see Fig. 2.6a). According to Cheng and Yeung [8], the plating rate did not increase when the Ag concentration was increased after the 3 at% Ag in the bath (note: after 3 at% Ag in the bath, only the Ag deposition occurred (see Fig. 2.7)). The Ag concentration effect on the plating rate was contrary to the previous study by Yeung et al. [46], where increasing the concentration of Ag in the bath resulted in the increase in the Ag plating rate. Shu et al. [88] also reported increase in the Ag plating rate (contrary to the Cheng and Yeung [8], who after the passivation effect reported no significant effect on the Ag plating rate with the increase in the Ag concentration in the bath) with the increase in the Ag concentration in the bath after the concentration at which the Pd passivation started i.e. 20 wt% (~ 20 at%) Ag in the bath. No increase in the Ag plating rate with the increase in the Ag concentration in the bath (after the passivation effect) reported by Cheng and Yeung [8] appears to be due to some experimental error. There existed considerable doubt in the data reported by Cheng and Yeung [8]. For the same set of the plating conditions in their (Cheng and Yeung [8]) two separate figures, the difference in the metal plating rates and the Ag concentration in the deposits was as large as 40%. According to Cheng and Yeung [8], the Pd passivation effect was reduced by decreasing the NH_3 concentration, increasing the N_2H_4 concentration and the temperature in the bath. Cheng and Yeung [8] also reported the SEM images of the morphology of the obtained deposits. However, the deposits thickness was less than 1 μm and the trends in the morphology were not clear

at such low thickness. According to Lbl and Schadegg [91], there was a minimum thickness required (0.3-1.5 μm , depending on the plating conditions particularly the overpotential at which a metal was deposited) of the deposits above which the effect of the plating conditions on the deposits morphology became clear. Even the plating conditions favoring powder or dendritic deposits formation produced compact deposits up to some thickness and then started showing powdery or dendritic growth. It is worth mentioning here that the Vycor glass substrate used by Cheng and Yeung [8] had pore size of 5 nm. The He dense membrane was prepared merely by depositing a 1.2 μm thick Pd-Ag (12.5 wt% Ag) layer. For such low pore size substrates, the deposits morphology had very little influence on the preparation of He gas tight membrane (as mentioned above, a certain minimum thickness was needed for the clear evolution of the deposits morphology [91]).

The co-deposits obtained by Cheng and Yeung [8] were bimetallic in phase and required the annealing step to form the Pd-Ag alloy. The Pd-Ag (12.5 wt% Ag, 1.2 μm thick) membrane supported on porous Vycor glass tube (OD = 10 mm, ID = 7 mm and 5 nm pore size) was therefore annealed, first at 400 $^{\circ}\text{C}$ and then at 500 $^{\circ}\text{C}$ for 8 h in H_2 . The H_2 permeance of the membrane after annealing at 500 $^{\circ}\text{C}$ was 50% higher than the permeance after annealing at 400 $^{\circ}\text{C}$, indicating 400 $^{\circ}\text{C}$, 8 h was not sufficient for the alloy formation. The XRD analysis of the membrane after 500 $^{\circ}\text{C}$ annealing showed single alloy phase. The membrane showed H_2 permeance of $0.84 \text{ m}^3/\text{m}^2\text{-h-atm}^{0.5}$ ($1.4 \text{ cm}^3/\text{cm}^2\text{-min-bar}^{0.5}$) at 350 $^{\circ}\text{C}$ after annealing at 500 $^{\circ}\text{C}$. A pure Pd film with thickness 1.2 μm at 350 $^{\circ}\text{C}$ would show H_2 permeance of $250 \text{ m}^3/\text{m}^2\text{-h-atm}^{0.5}$ [11]. There was no explanation provided by Cheng and Yeung [8] for such a low H_2 permeance of their membrane. Due to the limited information available, it was hard to find the factors

responsible for the low H₂ permeance. The substrate used by Cheng and Yeung [8] had very small pore size (5 nm) and the higher substrate resistance for the H₂ permeation could be one of the factors causing the low H₂ permeance.

Huang et al. [89] studied the Pd-Ag co-deposition using the NH₃+EDTA (Table 2.3) bath on the α -alumina and γ -alumina substrates. Similar to Shu et al. [88], Huang et al. [89] also reported the significant influence of the substrate nature on the Pd-Ag co-deposition. The α -alumina and γ -alumina substrates activated with the Pd nuclei following exactly the same procedure showed different metal deposition rate. The difference could be due to the different amount of Pd nuclei on the two substrates. The co-deposition bath was used to prepare a membrane supported on the α -alumina (0.1 μm grade) substrate (Huang et al. [89]). The co-deposits showed the difficulty in preparing a N₂ gas tight membrane even after depositing a 20 μm thick layer. The authors [89] did not cite any specific reason for the N₂ leak in the membrane. Uemiya et al. [9] prepared N₂ gas tight pure Pd membrane by depositing a 4.7 μm thick Pd layer on the α -alumina substrate (0.2 μm grade). The pore size of the substrate (0.1 μm grade) used by Huang et al. [89] was smaller than that used by Uemiya et al., [9], still the 20 μm thick Pd-Ag co-deposits layer could not produce N₂ gas tight membrane. The difficulty of the co-deposits to produce N₂ gas tight membrane [89] could be due to the non-uniform morphology of the deposits or the large defects present in the substrate.

Tanaka et al. [90] prepared several Pd-Ag membranes supported on α -alumina tubes (0.15 μm grade) using the NH₃+EDTA co-deposition bath (see Table 2.3 for the bath composition). According to the authors, the amount of Pd nuclei (see Fig. 2.8a) on the substrate surface had significant effect on the metal deposition rate, similar to the observation of Shu et al. [88] and Huang et al. [89]. The effect of N₂H₄ and NH₃ in

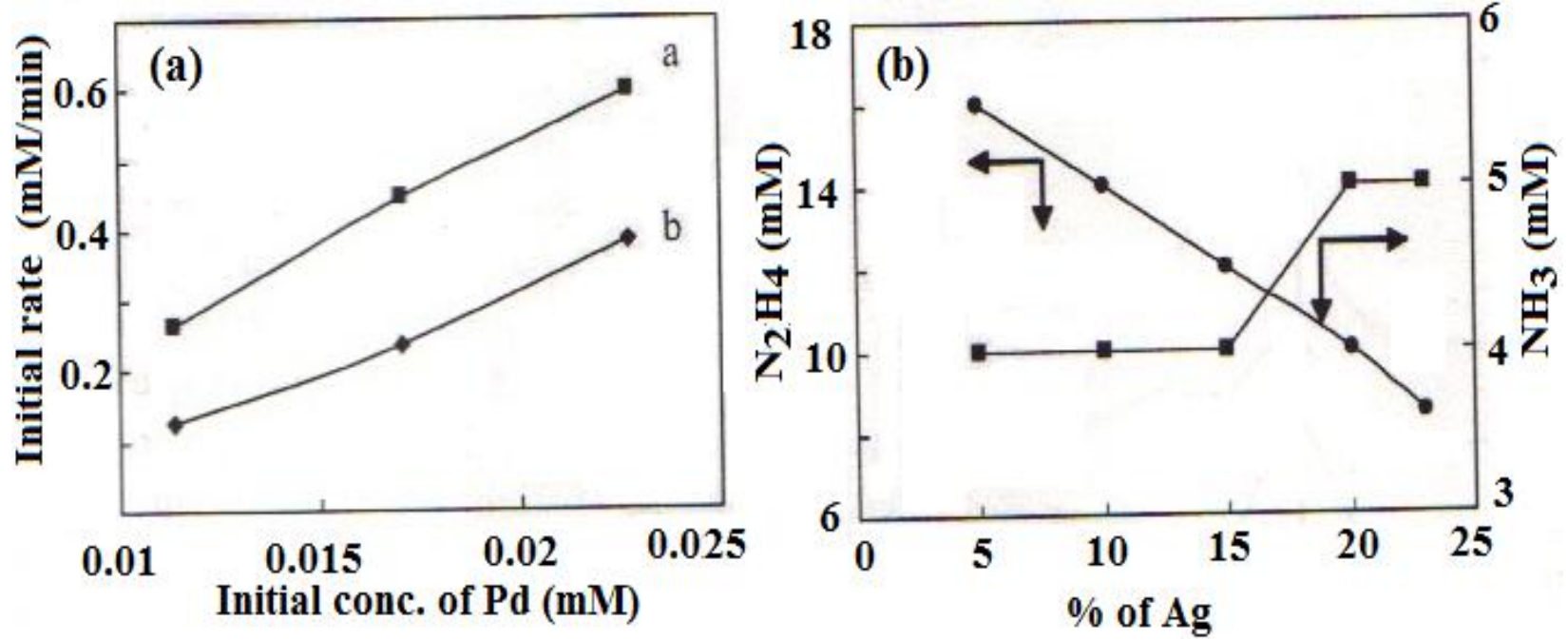


Fig. 2.8. (a) Comparison of plating rate by the different seeding procedure, line a for seeding with Pd nano-particle and line b for seeding with PdCl₂ and SnCl₂ solutions (b) tuning of hydrazine conc. and ammonia conc. in the solution for the simultaneous deposition of Pd and Ag (Tanaka et al. [90]).

the bath on the Pd-Ag co-deposition was opposite to that reported by Cheng and Yeung [8]. The increasing N_2H_4 concentration and decreasing NH_3 concentration in the bath favored the Ag deposition (Tanaka et al. [90]) while reverse trend was reported by Cheng and Yeung [8]. The thickness of Pd-Ag membranes ranged between 4 and 5 μm (Tanaka et al. [90]) and the Ag wt% ranged between 5 and 23. The Pd-Ag co-deposits obtained were bi-metallic in nature. Alloying of the Pd-Ag deposits was achieved at 500 $^\circ\text{C}$ for 4 h. The Pd-Ag membrane (20 wt% Ag, and 4.5 μm thick) after annealing showed H_2 permeance of 37 $\text{m}^3/\text{m}^2\text{-h-atm}^{0.5}$ ($1.44 \times 10^{-3} \text{ mol}/\text{m}^2\text{-s-Pa}^{0.5}$) and H_2/N_2 selectivity of 92 ($\text{H}_2/\text{He} = 34$, based on Knudson flow assumption of the N_2 gas through the defects in the membrane) at 300 $^\circ\text{C}$. The pure Pd foil with the same thickness (4.5 μm) would show the H_2 permeance of 52 $\text{m}^3/\text{m}^2\text{-h-atm}^{0.5}$ at 300 $^\circ\text{C}$ [11]. The reason for the relatively lower permeance was not clear from the article by Tanaka et al. [90]. The selectivity (H_2/N_2) of the membranes after 4 h treatment at 500 $^\circ\text{C}$ ranged between 90 and 680 ($\text{H}_2/\text{He} = 27\text{-}220$ based on the Knudson flow mechanism for the inert gas) measured at 300 $^\circ\text{C}$ and the pressure difference of 100 kPa. The reason for the low selectivity of the membrane was attributed to the defects present in the deposits, however no details were provided. The low selectivity of the membranes could be due to the non-uniform morphology of the obtained co-deposits.

As can be seen from the literature (previous paragraphs in this section), there were data available on the effects of plating parameters on the deposits composition and the deposition rate, however there was a lack of the clear understanding of the influence of the plating parameters on the plating rate and deposits composition. Also, no study was available in the literature mentioning the effects of plating parameters on the deposits morphology, Pd and Ag particles size and the compositional homogeneity of the

deposits (important properties from membrane synthesis viewpoint). Therefore, studying the effect of the co-plating bath parameters on the deposits properties was one of the main objectives of this study.

2.3.4. H₂ permeation characteristics

The fact that the H₂ selective layer of Pd or Pd-alloy is supported on the porous support makes the H₂ permeation characteristics of the composite membranes different from the membranes in the form of foils. The difference arises from factors such as the resistance for H₂ flow through the porous substrate and the interaction of support surface with the H₂ selective layer. The permeation of H₂ through the composite membrane is controlled by several factors such as support characteristics, support surface treatment, Pd or Pd- alloy deposition method and conditions and post deposition treatment of the membrane. All these factors make the H₂ permeation characteristics of the composite membranes different from one another. This section discusses a few Pd and Pd-alloy membranes reported in the literature along with their reported H₂ permeance (see Table 2.4 for summary). The idea of the discussion is to give a perspective of the several variables involved influencing the H₂ permeance and making it difficult to compare membranes prepared from different laboratories.

Mardilovich et al. [10] prepared Pd composite membranes using the PSS substrate with a maximum size of pores up to 8 μm. The authors showed that the thickness of the dense Pd layer depended on the size of the largest pores. Mechanical treatment (filing, use of sand paper) was applied to reduce the size of the largest pores and the thickness of the dense Pd layer. Above 550 °C, the membrane permeability decreased due to the intermetallic diffusion and also the selectivity of the membranes decreased. This

decrease in the selectivity was attributed by Mardilovich et al. [10] to the re-adjustment of the Pd layer resulting in the formation of pinholes. The activation energy of 16.4 kJ/mole was reported for the H₂ permeation between 350 °C and 550 °C. At 350 °C, the membrane showed stable behavior in terms of the H₂ flux and selectivity for 1100 h. The 20 μm thick membrane showed the H₂ permeance of 8 m³/m²-atm^{0.5}-h at 350 °C.

Li et al. [42] prepared a 10 μm thick Pd membrane on the PSS substrate (0.1-0.2 μm grade) by the electroless deposition combined with osmosis. The membrane showed the H₂ permeance of 7 m³/m²-atm^{0.5}-h at 380 °C and the selectivity (H₂/N₂) increased with temperature and was over 1000 above 400 °C. The membrane prepared by Mardilovich et al. [10] had double the thickness in comparison to that of membrane prepared by Li et al. [42] but both the membranes (Mardilovich et al. [10] and Li et al. [42]) showed similar value of H₂ permeance.

Uemiya et al. [44] prepared the composite membrane on the porous glass tube with 0.31 μm average pore size by depositing 13 μm Pd layer using the electroless plating. The membrane showed the hydrogen flux of 16.7 and 21.4 m³/m²-h-atm^{0.5} at temperature of 400 °C and 500 °C respectively. The activation energy for the hydrogen permeation in this temperature range (400-500 °C) was 10.7 kJ/mole which was lower than that reported by Mardilovich et al. [10]. The low activation energy could be due to the substrate resistance playing an important role in the overall permeation of the membrane reported by Uemiya et al. [44], however, due to the lack of the inert gas flux data of the substrate prior to the Pd deposition, it was not possible to verify the effect of the substrate resistance.

Uemiya et al. [9] prepared a 5.8 μm thick Pd-Ag (23 wt%) membrane, which was synthesized using the bi layer sequential approach and supported on porous alumina

Table 2.4. Example of variation in the H₂ permeance of composite membranes

Ref.	Pd-Ag (wt%)/substrate	thickness (μm)	Temp. ($^{\circ}\text{C}$)	Permeance, $\text{m}^3/\text{m}^2\text{-h-}$ $\text{atm}^{0.5}$	Permeability, $\text{m}^3\text{-}\mu\text{m}/\text{m}^2\text{-h-}$ $\text{atm}^{0.5}$	Selectivity (H ₂ /He)
[10]	Pd/PSS	20	350	8	160	5000
[42]	Pd/PSS	10	380	7	70	>300
[44]	Pd/glass	13	400	16.7	217	∞
[9]	Pd-Ag(23) /alumina	5.8	400	53.4	309	∞
[49]	Pd-Ag(25) /alumina	5.5	400	26.3	144.6	>1700

0.2 μm) tube. The membrane showed H₂ permeance of 53.4 m³/m²-atm^{0.5}-h at 400 °C. The membrane was annealed at 900 °C and 100% selectivity was reported at 400 °C after the annealing step.

Hou and Hughes [49] used the sequential electroless plating based on N₂H₄ bath for synthesizing the Pd-Ag membranes on an α-alumina support (0.18 μm). From the XRD pattern of the Pd-Ag deposits, the composition of the Pd-Ag film was roughly 25 wt% Ag. The Pd-Ag film with a total thickness of 5.5 μm formed was annealed above 600 °C for the alloy formation in the H₂ atmosphere. The H₂ permeance was measured in the temperature range of 277-347 °C. Based on the activation energy for the H₂ permeance between 277 and 347 °C, the value of H₂ permeance extrapolated to 400 °C was 26.2 m³/m²-h-atm^{0.5}. The membranes showed H₂/N₂ selectivity of 4500 at 225 °C and pressure difference of 1 atm.

3. Experimental methods and procedures

3.1. Introduction

The experimental procedures and methods common to all chapters in the thesis are mentioned in this chapter, however some procedure limited to a particular chapter are detailed in that chapter, especially the plating conditions used and procedure adopted for the plating. This chapter is divided basically into three broad sections. The first section gives details of substrates used and their treatment steps before performing the actual Pd, Ag and Pd-Ag deposition. The second section describes the Pd plating conditions common to all the chapters and the third section describes the experimental techniques used for the membrane characterization.

3.2. Substrate and treatment

3.2.1. Substrate

The substrates used were either in the form of coupons (1 x 1 cm plates) or porous metal tubes (1.27 cm diameter and 5.9 cm length, approximate porous part area = 23 cm²). The porous metal tubes were either stainless steel (PSS, 316L) or inconel. One end of the porous part of the tube was welded to a non-porous stainless steel of the same diameter and the other end of the porous tube was sealed with a non-porous stainless steel cap. Both coupons and tubes were supplied by Mott Metallurgical Corporation, Farmington, CT. All the porous coupons and porous tubes used were available in 0.1 μm media grade. For the electrochemical study of the plating

solutions, the substrate used were in the form of very smooth stainless steel wires (316L) with 0.2 cm diameter and 1 cm length. The surface area of the wire was kept 0.63 cm^2 . Fig. 3.1 shows the photographs of the substrates used.

3.2.2. Substrate pre-treatment

Prior to any plating experiment, the substrates were cleaned in the basic solution. The purpose of the cleaning step was to remove any unwanted contaminants such as grease, oil and dirt on the substrate surface. The composition of the basic solution is shown in Table 3.1. For cleaning, the substrate dipped in the basic solution was kept in the ultrasonic bath (40-45 °C) for 90 min. The substrate after the basic solution cleaning was thoroughly rinsed with Di water to remove any solution trapped in the pores and dried at 120 °C in air for minimum 2 h.

The porous metal tubes after cleaning were either oxidized in the air or deposited with γ -alumina layer by the sol gel process to introduce the intermetallic diffusion barrier between the tube components and the Pd or Pd-Ag layer. The oxidation temperature required for the formation of the intermetallic diffusion barrier increased with the increase in the temperature that the membrane was to be used [92, 93]. The thickness of the oxidation layer formed increased with the increase in the oxidation temperature [92]. According to Engwall et al. [93], the oxidation barrier layer might increase significant mass transfer resistance for the diffusion of He gas through the substrate (depending on the grade of the substrate) and the mass transfer resistance increased with the increase in the oxidation temperature. Therefore, substrate for the membranes exposed to higher than 500 °C, the oxidation temperature for the formation

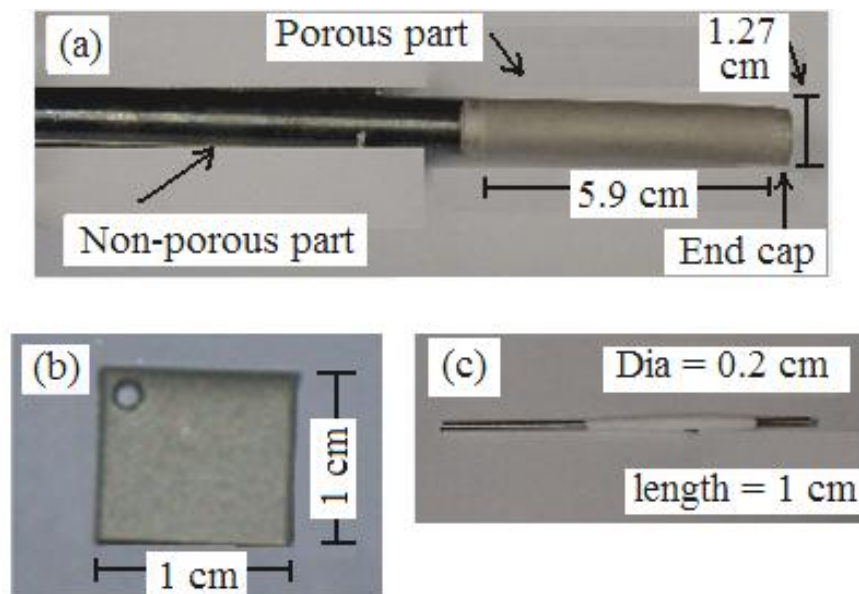


Fig. 3.1. Substrate pictures (a) porous metal tube (b) porous stainless steel coupon (c) stainless steel wire

Table 3.1. Basic solution composition used for the cleaning of the substrate

Component	Conc. (M)
$\text{Na}_3\text{PO}_4 \cdot 12\text{H}_2\text{O}$	0.12
Na_2CO_3	0.6
NaOH	1.12
Saturated Alcojet	
detergent solution	5 ml/L

of the intermetallic diffusion barrier required was expected to be high (800 °C or higher) causing large mass transfer resistance for the H₂ gas diffusion through the substrate. For all the membranes exposed to temperatures higher than 500 °C, the γ -alumina layer was used as the intermetallic diffusion barrier in the current study. The substrates were simply oxidized in air for the intermetallic diffusion barrier for the membranes exposed to 500 °C or lower. The oxidation temperature used was either 500 or 700 °C (10 h). The air oxidation procedure (700 °C, 10 h air treatment) was also adopted for the coupons exposed to the high temperature treatment for the introduction of the intermetallic diffusion barrier between the coupon components and the deposited Pd or Pd-Ag layer on the top. In the case of the γ -alumina layer, the porous metal tubes after the deposition of thin γ -alumina layer were calcined at 550 °C for 10 h in air.

The sol for the γ -alumina layer deposition was prepared by heating the deionized water to a temperature of 80-90 °C and aluminum sec-butoxide (Al[O(CH₃)CHC₂H₅]₃, 95% from Alfa Aesar) was added into the hot water. After 15 min of the addition of aluminum sec-butoxide, 2.70 ml of HCl (10 M) was added drop by drop into the solution. Two minutes after the addition of HCl, the solution was kept boiling for 6-8 h with total reflux. The water to aluminum molar ratio [H₂O/Al] of 200 and the acid to aluminum molar ratio [HCl/Al] ratio of 0.1 were kept in the solution.

After the oxidation or the γ -alumina layer deposition step, in some cases, the pores of the tubes were filled with γ -alumina powder (0.3 μ m size powder from Alfa Aesar) by simply hand rubbing the powder slurry on the substrate surface. The purpose of the pore filling with γ -alumina powder was to narrow the pore size distribution of the tubes in order to achieve He gas tight tubes with the minimum thickness of Pd or Pd-Ag layer. After the alumina powder pore filling, the tubes were dried at 120 °C in air for a

minimum of 2 h. Appendix D summarizes all the membranes synthesized in this study along with the treatment of the substrates before the plating step.

Before performing the Pd or Ag or Pd-Ag deposition, the substrate was activated with Pd nuclei to initiate the electroless deposition process. The Pd nuclei activation step consisted of dipping the substrate in the $\text{SnCl}_2 \cdot 2\text{H}_2\text{O}$ (4.4 mM) solution (5 min) followed by dipping in the DI water (1 min), PdCl_2 (0.56 mM) solution (5 min) and HCl (0.01 M) solution (1 min). The procedure was repeated a minimum of four times or more until the substrate surface showed dark brown color. After the activation with Pd nuclei step, the substrate was always dipped in the plating solution with no more than 1 h intervals. In the case where the Ag electrodeposition was performed, no Pd activation of the substrate was performed.

3.3. Pd and Ag plating

Different Pd and Ag plating solution compositions were used, however the typical plating solution composition for the Pd and Ag deposition used in the lab is shown in Table 3.2 and referred as regular Pd or Ag plating solution. The NH_3 and EDTA both acted as complexing agents and buffers in the solution. N_2H_4 acted as the reducing agent. All the chemicals used were purchased from Alfa Aesar and had purity more than 99%.

The procedure adopted for preparing one liter of Pd or Ag solution comprised of adding 198 ml of NH_4OH (28 wt%) into 300 ml of DI water then followed by adding Pd or Ag salt and completely dissolving the salt. After the Pd or Ag salt dissolution, Na_2EDTA (40 g) was added and the solution was shaken to completely dissolve

Table 3.2. Pd electroless, Ag electroless and Ag electroplating bath compositions

Bath component	Conc. (M)		
	Pd electroless	Ag electroless	Ag electroplating
Pd(NH ₃) ₄ Cl ₂ ·H ₂ O	0.016	-	-
AgNO ₃	-	0.003	0.1
NH ₃	3.1	3.1	-
Na ₂ EDTA	0.1	0.1	-
N ₂ H ₄	0.0056	0.0056	
C ₄ H ₅ O ₂ N	-	-	1.26
H ₃ BO ₃	-	-	0.5
PEI	-	-	0.0008
Temp.(°C), pH	60, 11	60, 11	20, 10**

**Note: pH in the case of Ag electroplating solution was adjusted by KOH

Na₂EDTA. The solution was then made one liter by adding the rest of the DI water. The prepared Pd and Ag solution could be stored for long (2-3 months) time without any degradation of the solution. The general procedure for the Pd or Ag plating included adding N₂H₄ into the Pd or Ag solution at room temperature and then heating the solution to 60 °C before dipping the activated substrate into the solution.

The bath composition used for Ag electroplating is shown in Table 3.2. No Pd activation procedure was required for the substrate before Ag electroplating. The pH of the electroplating solution was adjusted using KOH and H₃BO₃. Succinimide (C₄H₅O₂N) acted as complexing agent and polyethyleneimine (PEI) acted as brightener in the bath.

The amount of Pd or Ag deposited was calculated gravimetrically i.e., by measuring the weight of the substrate before and after plating. For the thickness of the Pd or Ag layer, the weight added was divided by the plated substrate surface area and the density of Pd or Ag respectively.

3.4. Membrane polishing

The membrane surface was polished using the SiC (1200 grit) paper either using gentle hand rubbing or the lathe machine. For the lathe machine polishing, the membrane was held in the lathe machine at the non-porous part and rotated at approximately the speed of 300 rpm. The SiC paper was mildly thumb pressed against the membrane surface and moved over the entire membrane surface. The polishing step was assumed to be complete when the membrane surface visually appeared smooth and shiny. The membrane thickness reduced in the polishing step ranged between 0.7-3 μm. After the polishing step, the membrane surface was cleaned with 1 M HCl solution.

3.5. Equipments used

3.5.1. Membrane synthesis: He flux measurement

In between various steps during the membrane synthesis, the He flux of the membrane was measured to check the gas tightness of the membrane. Before measuring the He flux, the membrane was thoroughly cleaned with hot DI water (~60 °C) and dried at 120 °C for a minimum of 2 h. The He flux measurement set up was the same as that described by Ayrtuk [51]. He gas was introduced into the shell side at a pressure ranging between 2-5 atm and the gas permeated to the tube side, which was kept at 1 atm. The He gas flow was measured using the wet test meter (maximum flow 13 l/min) or digital flow meter (maximum flow 0.3 l/min) or bubble flow meter (flow rate < 0.01 l/min) depending upon the flow rate. Fig. 3.2 shows the schematic of the He flow rate measurement set up. When the membranes were He gas tight or with a very low He flow rate, the deposition of Pd, Ag or Pd-Ag was stopped and the membrane was assumed to be ready for the next step.

3.5.2. Gravimetric thickness

During the Pd, Ag or Pd-Ag synthesis step, the plating was stopped and the membrane was thoroughly cleaned with hot water (60 °C). The membrane was then next dried at 120 °C (> 2 h) and the weight of the membrane was measured. The difference of the weight before and after the plating step was then used to calculate the thickness of the deposited Pd, Ag or Pd-Ag layer. The uncertainty in the membrane thickness measurement was 0.3-0.4 µm due to the sensitivity of the balance used for the weight measurement. Additional potential sources of error in the measurement of

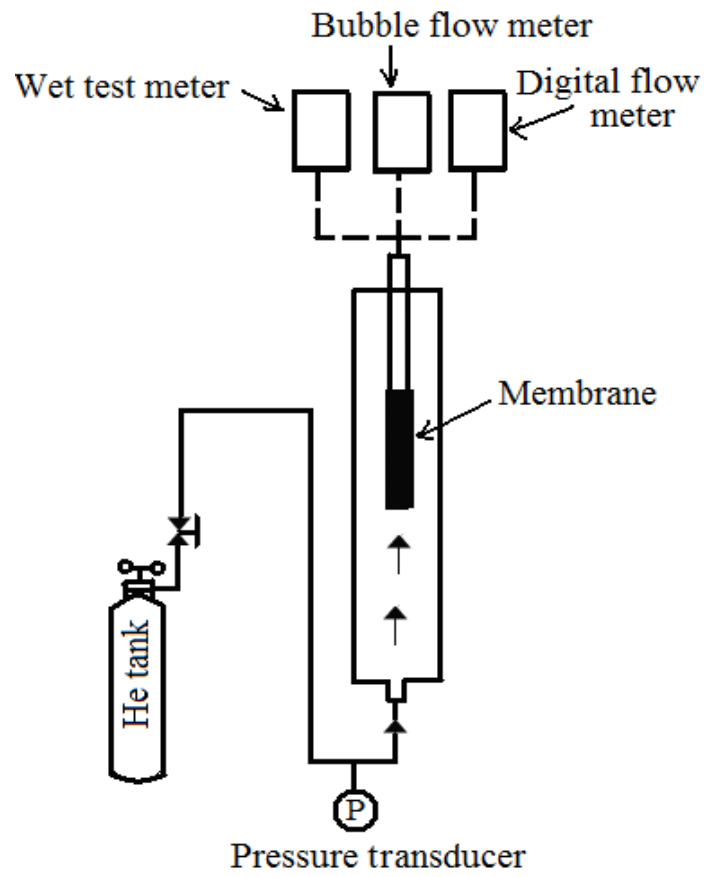


Fig. 3.2. Schematic of He flux measurement set up in between membrane synthesis steps

the thickness by the gravimetric method included improper cleaning and drying of the membranes in between the steps of the Pd or Ag deposition.

3.5.3. Bubble test

During the membrane synthesis and post annealing or H₂ permeation characterization step, the location of the defects causing the He leak in the membrane was detected by the bubble test procedure similar to that described by Ayrtuk [51] and Guazzone [11]. The set up used for bubble test was the same as that for He flux measurement with slight modification. The He gas was introduced into the tube side (pressure > 2.5 atm) and the membrane was then dipped into water. The location of He gas bubbles indicated the defective areas in the membrane and the information were also sometime used during the membrane synthesis step to plate only the defective area.

3.5.4. Ag electroplating set up

The Ag electroplating on the substrate (both coupons and inconel tube) was performed by using the set up consisted of a DC power source (manufactured by EICO, model-1064) with ranges of 0-20 V and 0-20 A for the voltage and the current respectively, a digital meter manufactured by Amprobe Instruments (AM-32) for the current measurements. Four silver wires of 0.1 cm diameter (length = 2 cm for coupons and 6 cm for inconel tube) purchased from Alfa Aesar (99.9 wt %) acted as anode and were placed symmetrically around the substrate and the distance of 1 cm was kept between the anode and sample surface. The current density of 2 mA/cm² was used in all the experiments.

3.5.5. Membrane annealing and H₂ permeance characterization

For the membrane annealing and H₂ permeation measurements, the set up similar to the one reported by Mardilovich et al. [10] and Guazzone et al. [94] was used and is shown in Fig. 3.3. The set up consisted of a stainless steel reactor, which housed the membrane tube, surrounded by a furnace supplied by Watlow (60V, 275W) for heating the reactor. The membrane tube was connected to the inlet and the outlet tubing using the Swagelok compression fittings and graphite ferrules. The temperature of the membrane was regulated by using the temperature controller (Omega-CN4800) and two K-type thermocouples. The membrane tube temperature was measured by the thermocouple placed inside the tube and the second thermocouple measured the stainless steel reactor temperature which in combination with the temperature controller regulated the furnace heating to obtain the desired temperatures. H₂ was introduced on the shell side and the permeated gas on the tube side was measured by either the H₂ flow meter (MKS) with the maximum flow rate capacity of 1 L/min or wet test meter (maximum capacity = 13 L/min) depending upon the flow rate. The pressure on both sides of the tube was measured by using the pressure transducers. The shell side pressure was varied between 0.3 to 6 atmospheres while the tube side pressure was kept constant and equal to atmospheric pressure to obtain different pressure differences across the membrane tube. The membranes were heated from room temperature to the temperature range between 200-400 °C in the He atmosphere at 1 °C/min and then switched to the H₂ atmosphere. The temperature that the membranes were exposed to the H₂ atmosphere ranged between 200-550 °C and varied from membrane to membrane. At various stages during the membrane annealing and characterization steps, the system was also switched from H₂ to He gas in order to measure the He flux of the membrane, using the bubble or digital flow meter, to determine the H₂/He selectivity of.

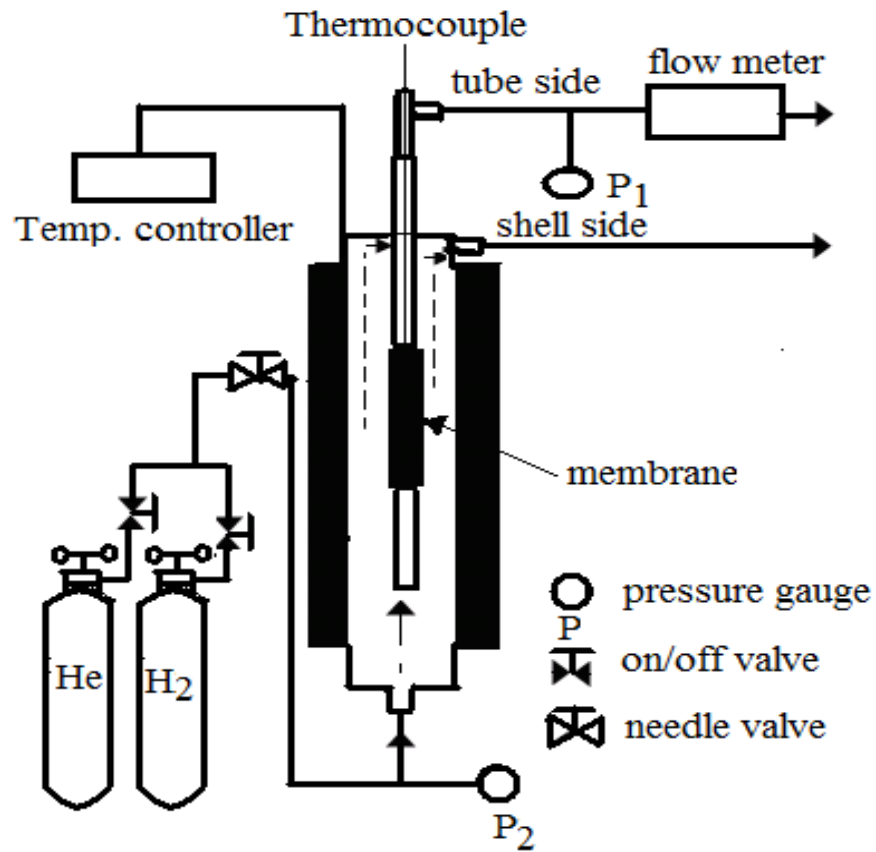


Fig. 3.3. Membrane annealing and H₂ permeation characterization set up

the membrane.

The set up described in Fig. 3.3 was connected to a computer installed with LabView 7.1 software via the data acquisition board purchased from National Instruments. The system temperature, pressure and H₂ flow rate were continuously recorded by the computer.

3.5.6. SEM and EDX analysis

For the surface analysis of the samples, Amray 1610 turbo scanning electron microscope (SEM) equipped with energy dispersive analysis (EDX) from Princeton Gamma-Tech Instruments Inc., NJ was used. The EDX detector had beryllium window and was sensitive to elements with atomic weight as low as that of carbon. For the cross-section analysis, samples were mounted on a phenolic resin holder. The samples were then polished using silicon carbide paper and 1 μm diamond suspension (Buehler) to expose the fresh and smooth cross section. For the EDX line scans, the samples were sputtered with a very thin Pd layer to avoid the electron charging during the line scan acquisition. For most of the SEM and EDX analysis, the beam voltage was kept 15 kV.

For the Pd-Ag deposit composition by the EDX area analysis, the EDX was calibrated with Pd and Ag powder mixture with particle size ranging from 0.3-0.5 μm. In order to obtain a Pd-Ag powder mixture of a certain composition, the Pd and Ag powder (Alfa Aesar, 99.99 wt% purity) were weighed separately in proportional amount and then mixed in acetone by strongly stirring the slurry for 30 minutes. For each sample, the total weight of approximately 100 mg was maintained. After the stirring, the slurry was dried at 80 °C for 24 h to let all the acetone evaporate to obtain completely

dried Pd-Ag powder. For example, in order to prepare a Pd-Ag powder with 50 wt% Ag, 50 mg of Pd and Ag powder each were weighed separately and poured into acetone and then the solution was stirred strongly for 30 minutes. The slurry was then heated to obtain completely dried Pd-Ag powder. For both Pd and Ag, the L_{α} line (Pd=2.838 kV, Ag=2.984 kV) was considered for the quantification purpose. The net counts (gross counts-background counts) under the half of the FWHM (full width at half maximum) of L_{α} line were considered for the Pd-Ag composition calibration of the EDX. Fig. 3.4 shows the obtained calibration curve by plotting wt% of Ag in the powder against the ratio of net counts of Pd L_{α} to Ag L_{α} line. The ratio of net counts of Pd (L_{α})/Ag(L_{α}) obtained from the EDX area scan of a sample were used in the fitted equation shown in Fig. 3.4 to calculate the Ag wt% in the sample

3.5.7. XRD analysis

The phase analysis of the samples was performed using Rikagu X-ray diffractometer with CuK_{α} ($\lambda=1.542 \text{ \AA}$) radiation source and a nickel filter was used. The voltage was set at 37.5 kV and current at 27 mA.

3.5.8. Linear sweep (LSV) and cyclic voltammetry study

For the electrochemical study of the electroless plating baths, the linear sweep voltammetry (LSV) and cyclic voltammetry scans were obtained using the BAS 110B/W electrochemical station with conventional three-electrode system. The electrochemical station consisted of a potentiostat and a computer equipped with BAS software. Ag/AgCl (3 M NaCl), BAS model-MF 2052, was used as a reference

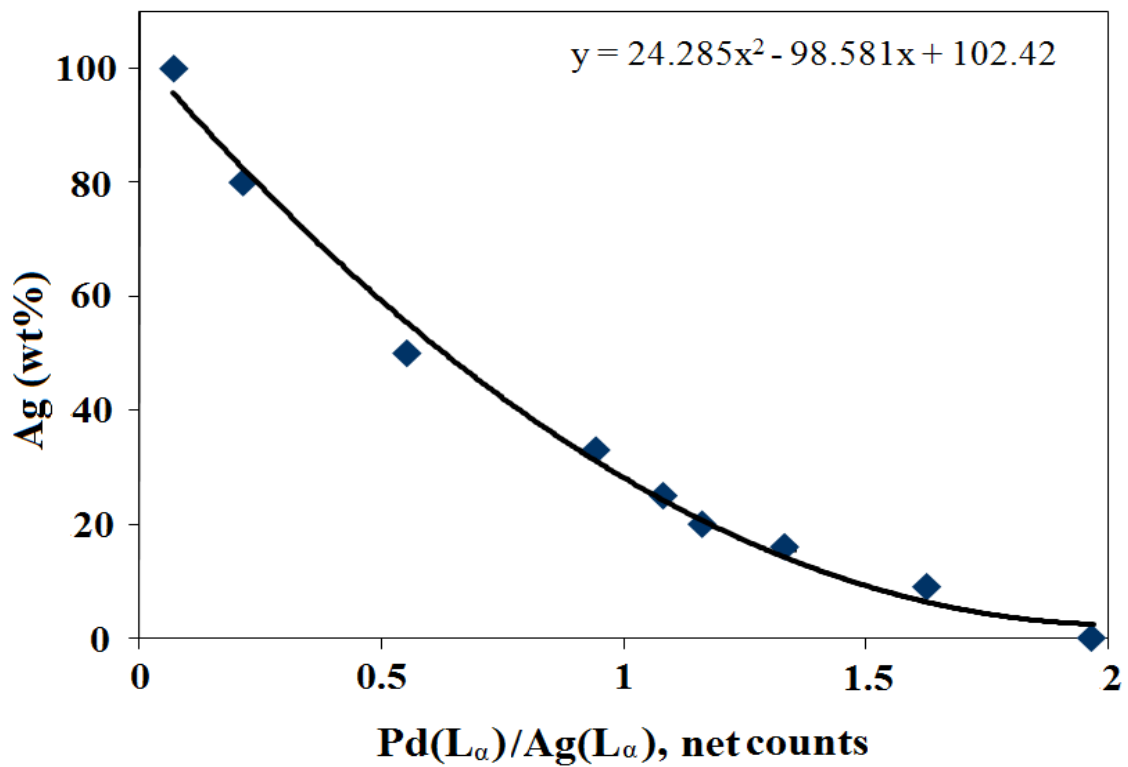


Fig. 3.4. EDX calibration curve for calculating the composition of Pd-Ag deposits

electrode and Ag or Pd wire (0.1 cm diameter and 3 cm length) functioned as counter electrode. Stainless steel wires (0.2 cm diameter and 1 cm length) with very smooth and shiny surface covered with electroless plated Ag or Pd deposits (approximate thickness 2 μm) acted as the working electrode. The stainless steel wires were cleaned with the basic solution described in the Section 3.2.2 before the Pd or Ag deposition. The distance of 0.5 cm was maintained between the working and reference electrode. All the scans were obtained at the rate of 10 or 25 mV/s with the sensitivity of 1 mA/V.

4. H₂ interaction with Pd and Pd-Ag alloy

4.1. Introduction

The understanding of the interaction of H₂ with Pd and Pd-Ag alloy is important for the understanding of the overall permeation characteristics of Pd and Pd-Ag composite membranes. The permeation in the case of composite membranes is affected by both the substrate and the Pd or Pd-Ag alloy layer deposited on the top of the substrate. The knowledge of the H₂ interaction with the Pd or Pd-Ag alloy film, therefore, could be utilized to gain better insight into the role played by both the substrate and the deposited Pd or Pd-Ag layer. The majority of the studies reported in the literature involving H₂ and Pd or Pd-Ag alloy interaction used Pd or Pd-Ag alloy in the form of foils (> 25 μm) [6, 8, 82, 95-105]. The foils were prepared by the casting and rolling method i.e., melting the raw material, casting into thick sheets and cold rolling and annealing down to the desired thicknesses. The fact that the alloying components, Pd and Ag, were melted in the case of the casting and rolling method lead to the alloy foils with high compositional homogeneity.

4.2. H₂ interaction with Pd

The permeation of H₂ through the Pd film involves the following steps (also see Fig. 4.1a). 1. dissociative adsorption on the higher H₂ pressure side of Pd film. 2. transfer of the H atom from the surface into the bulk. 3. interstitial diffusion of the H atom in the bulk Pd. 4. transfer of the H atom from bulk to the Pd surface. 5. associative desorption from the Pd surface on the low H₂ pressure side. Step 4 and step 5 are the reverse of

step 2 and step 1 respectively [14, 16]. In fact all the steps mentioned (step 1, 2, 4 and 5) previously for the H₂ permeation occurs on both side (high pressure side as well as low pressure side) of the Pd film. The step 1 and step 2 have higher rates than the step 5 and step 4 on the higher pressure side and the opposite is true for the lower pressure side. Fig. 4.1c shows the schematic of all the steps occurring on one side of the Pd film surface. The same schematic (Fig. 4.1c) holds true for the opposite side also. When the Pd film is exposed to different pressures of H₂ on its opposite sides (see Fig. 4.1a), the Step 1 and step 2 have higher rate than step 5 and step 4 respectively on the higher pressure side, therefore resulting in the net flow of H₂ into the Pd foil on the higher pressure side. The opposite is true on the low pressure side of the Pd film (i.e., step 5 and step 4 have higher rates than step 1 and step 2 respectively), resulting in the net flow of H₂ out of the Pd foil.

Step 1, the dissociative adsorption of H₂ on the Pd surface can be written as

$$j_{ad} = 2\tau s(1-\theta)^2 \quad 4.1$$

j_{ad} = flux of dissociated H atoms at the Pd surface (mole/m²-s)

τ = flux of H₂ molecules impinging on the Pd surface (mole/m²-s)

s = sticking probability of H₂ molecules impinging on the Pd surface or the fraction of H₂ molecules striking the Pd surface and getting dissociatively adsorbed

θ = surface coverage of H atoms or the ratio of H atoms/Pd atoms on the Pd surface

(note: two adjacent vacant sites are required for the adsorption step)

Eqn. 4.1 is valid for the low value of θ when the interaction between the adsorbed H atoms is weak which is generally the case for temperatures above the room temperature. The sticking probability for the clean Pd surface has been reported to be 1

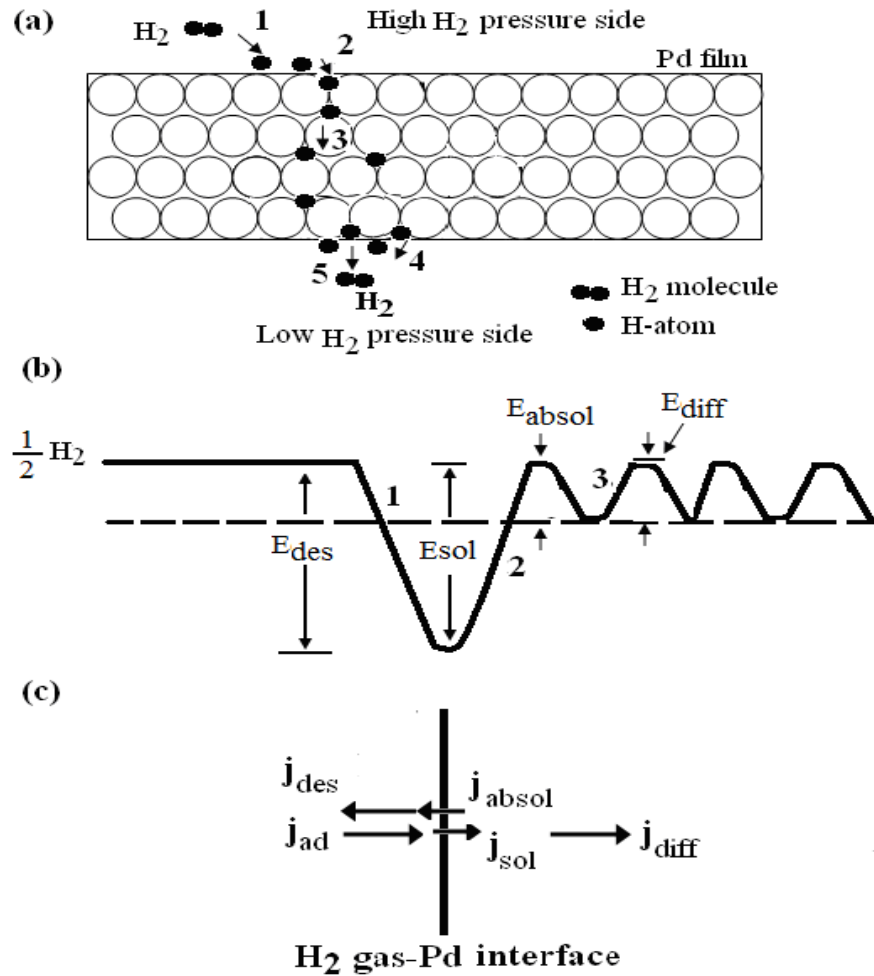


Fig. 4.1. The interaction of H₂ with the Pd foil (a) steps involved in the H₂ permeation through the Pd foil (b) potential energy diagram of H atom during the permeation steps through the Pd foil [14, 16] (c) fluxes associated with various steps involved in the H atom permeation at the H₂ gas and Pd film interface [16] (see the Nomenclature at the end for the definition of the symbols used in the figure)

especially for the low value of θ , i.e. no activation energy barrier exists for the adsorption step of H₂ molecule on the clean metal surface [106, 107] (see Fig. 4.1b for the potential energy associated with various steps involved in H₂ permeation through Pd metal). The flux of H₂ molecules impinging on the Pd surface (assumption: the H₂ gas phase follows ideal gas law) can be written as [16]

$$\tau = k \frac{P}{T^{0.5}} \quad 4.2$$

τ = flux of H₂ molecules impinging on the Pd surface, mole/m²-s

k = constant relating the H₂ gas pressure and temperature to the flux of H₂ molecules impinging on the Pd surface

p = pressure (atm)

T = Temperature (K)

The flux of H₂ molecules impinging on the Pd surface is directly proportional to the H₂ gas pressure as can be seen from Eqn. 4.2. The dissociative desorption flux of H atoms, j_{des} (mole/m²-s) from the Pd surface (step 5) (note: Eqn. 4.3 holds true for the low value of θ when the second order kinetics for desorption is valid and very little interaction occurs between the adsorbed atoms [108, 109]) is given by

$$j_{des} = 2K_{des}\theta^2 \quad 4.3$$

j_{des} = dissociative desorption flux of H-atoms from the Pd surface, mole/m²-s

K_{des} = rate constant for the dissociative desorption of H-atoms from the Pd surface, mole/m²-s

θ = fraction of Pd surface covered by H-atoms

Where the desorption rate constant, K_{des} is given by

$$K_{des} = K_{des}^0 e^{-\frac{2E_{des}}{RT}} \quad 4.4$$

$K_{des}^0 = H$ atom desorption rate constant pre-exponential factor, mole/m²-s

E_{des} = activation energy barrier for the H atom desorption from the Pd surface,
kJ/mole

R = gas constant, kJ/mole-K

Eqns. 4.3 and 4.4 show that the simultaneous desorption of two adjacent H atoms on the Pd surface is required for the successful desorption of H₂ from the Pd surface. The desorption rate constant also accounts for the probability of two H atoms simultaneously overcoming the desorption activation barrier, E_{des} (Eqn. 4.4). It is important to know that Eqns. 4.1 and 4.3 are valid only for the clean Pd metal surface. The presence of impurities on the metal surface increases the activation energy barrier for the hydrogen dissociation and association [110, 111] and generally less than one monolayer of the impurity atoms completely masks the interaction between hydrogen and the metal surface.

The transfer of the H atom from the Pd surface into the Pd bulk depends both on the surface concentration of the H atom and the concentration of the interstitial site available for the occupancy of the H atom in the Pd lattice. The flux of the H atom, j_{sol} (mole/m²-s) from the surface into the bulk (step 2) is given by

$$j_{sol} = K_{sol}\theta(1-n) \quad 4.5$$

K_{sol} = rate constant for the solution step, mole/m²-s

n = ratio of H atom to Pd atom in the bulk Pd

The rate constant, K_{sol} for the dissolution step is given by

$$K_{sol} = K_{sol}^0 e^{\frac{-E_{sol}}{RT}} \quad 4.6$$

K_{sol}^0 = pre-exponential factor for the rate constant for the solution step, mole/m²-s

E_{sol} = activation energy for the dissolution step, kJ/mole

The opposite of step 2 (transfer of the H atom from the Pd surface into the Pd bulk) is absorption of the H atom from the Pd bulk to the Pd surface (step 4). The flux of the H atom from the Pd bulk to the surface, j_{absol} is given by

$$j_{absol} = K_{absol}(1-\theta)n \quad 4.7$$

j_{absol} = flux of the H atom from the Pd bulk to the Pd surface, mole/m²-s

K_{absol} = rate constant for the H atom movement from the Pd bulk to the Pd surface (step 4), mole/m²-s

The rate constant K_{absol} is given by

$$K_{absol} = K_{absol}^0 e^{\frac{-E_{absol}}{RT}} \quad 4.8$$

K_{absol}^0 = pre-exponential factor for K_{absol} , mole/m²-s

E_{absol} = activation energy for the H atom movement from Pd bulk to the Pd surface (step 4), kJ/mole

Eqns. 4.5 and 4.7 are valid when the value of n is low and the dissolved H atoms mainly interact with Pd atoms. In the case of the concentration gradient in the Pd bulk, the diffusion flux of the atomic H, $j_{diff}(H)$ (mole/m²-s) can be written as

$$j_{diff}(H) = -D \frac{d}{dz}(Cn) \quad 4.9$$

D = diffusivity of H in Pd, m²/s

C = density of Pd, mole/m³

z = distance along the thickness of Pd film from the higher H₂ pressure side, m

n = ratio H atom to Pd atom in the Pd bulk

The diffusivity of the H atom in Pd, D is given by

$$D = D_o e^{\frac{-E_{diff}}{RT}} \quad 4.10$$

D_o = Pre-exponential factor for D , m²/s

E_{diff} = activation energy for the H atom diffusivity in Pd, kJ/mole

At equilibrium, i.e., when the Pd film surface is exposed to the same H₂ pressure on both sides (no H concentration gradient exists in the Pd bulk), all the steps are equal and

$j_{ad} = j_{des}$ (step 1 = step 5), i.e.,

$$2\tau(1-\theta)^2 = 2K_{des}\theta^2 \text{ or } \frac{\theta^2}{(1-\theta)^2} = \frac{2\tau}{2K_{des}} \quad 4.11$$

and

$j_{sol} = j_{absol}$ (step 2 = step 4), i.e.,

$$K_{sol}\theta(1-n) = K_{absol}(1-\theta)n \text{ or } \frac{\theta}{(1-\theta)} = \frac{K_{absol}}{K_{sol}} \frac{n}{(1-n)} \quad 4.12$$

Further manipulation of Eqn. 4.2, Eqn. 4.11 and Eqn. 4.12 gives

$$\frac{(K_{absol})^2}{(K_{sol})^2} \frac{n^2}{(1-n)^2} = \frac{2\tau}{2K_{des}} = \frac{\tau}{K_{des}} \quad 4.13$$

or

$$\frac{n}{1-n} = \frac{K_{sol}}{K_{absol}\sqrt{K_{des}}} \sqrt{\tau} \sqrt{p} \quad 4.14$$

When n is $\ll 1$ which is generally the case at high temperatures and low H₂ pressures [6, 14, 16, 96, 102].

$$\begin{aligned}
 n &= \frac{K_{sol}}{K_{absol}\sqrt{K_{des}}} \sqrt{\tau} \sqrt{p} = \sqrt{\tau} \frac{K_{sol}^o}{K_{absol}^0\sqrt{K_{des}^0}} e^{\frac{-E_{sol}+E_{absol}+E_{des}}{RT}} \sqrt{p} \\
 &= \sqrt{\tau} \frac{K_{sol}^o}{K_{absol}^0\sqrt{K_{des}^0}} e^{\frac{-\Delta H}{RT}} \sqrt{p} = K_{Sievevts} \sqrt{p}
 \end{aligned} \tag{4.15}$$

Where

$$K_{Sievevts} = \sqrt{\tau} \frac{K_{sol}^o}{K_{absol}^0\sqrt{K_{des}^0}} e^{\frac{-\Delta H}{RT}} = \text{Sieverts' constant (relating } n, \text{ the H/Pd ratio, with } p, \text{ the H}_2 \text{ pressure in the gas phase [106]), atm}^{-0.5}$$

ΔH = enthalpy change associated with the H atom dissolution from H₂ gas phase into the Pd bulk, kJ/mole H-atom

At a fixed temperature, all the parameters relating the H₂ gas pressure to the n in Eqn. 4.15 are constant and when combined becomes the Sieverts' constant ($K_{Sievevts}$). $-\Delta H$ (summation of $-E_{sol} + E_{absol} + E_{des}$, see Fig. 4.1b) is the enthalpy associated with the transfer of the H atom from the H₂ gas phase into the bulk of Pd. The activation energy barrier associated with surface reactions (step 5) and transfer of H atom between the surface and Pd bulk just beneath the surface (step 2) is higher than the activation barrier associated with the diffusion of H in the Pd bulk (step 3). As the temperature increases when H₂ is permeating through Pd, the step 5 and step 2 increases at faster rate than step 3 and at some temperature, step 3 (diffusion of H atom in Pd) becomes the rate controlling step for the H₂ permeation. In the case of steady state and the diffusion being the rate controlling step, the dissolved H atoms just beneath the Pd film surface on both sides exposed to different H₂ pressure are in equilibrium with the gas phase H₂ and the H₂ permeation rate through the film is given by Fick's law (Eqn. 4.9).

$$j_{diff}(H) = -D \frac{d(Cn)}{dz} = D \frac{C(n_1 - n_2)}{z} = D \frac{S_1 - S_2}{z} = \frac{DCK_{Sievevts}(\sqrt{P_1} - \sqrt{P_2})}{z} \quad 4.16$$

S_1 = solubility of H atom on higher pressure side, mole/m³

S_2 = solubility of H atom (mole/m³) on lower pressure side, mole/m³

For the Pd film with unit thickness, the flux of H-atoms through the film becomes

$$j_{diff}(H) = D(S_1 - S_2) = DCK_{Sievevts}(\sqrt{P_1} - \sqrt{P_2}) \quad 4.17$$

Since the molecular flux of H₂, $j_{diff}(H_2)$, is half of the flux of H-atoms, $j_{diff}(H)$, the H₂ flux for the Pd film with unit thickness could be written by simple modification of Eqn. 4.17, as shown in Eqn. 4.18

$$j_{diff}(H_2) = \frac{1}{2} j_{diff}(H) = \frac{D(S_1 - S_2)}{2} = \frac{DCK_{Sievevts}(\sqrt{P_1} - \sqrt{P_2})}{2} \quad 4.18$$

Eqn. 4.18 shows that the flux of H₂ in the case of diffusion through the Pd film (with unit thickness) being the rate controlling step, is simply controlled by the product of diffusivity (D) of H-atoms and solubility of H-atoms in Pd per unit square root of the H₂ pressure ($CK_{Sievevts}$, mole/m³-atm^{0.5}) and the difference of the square root of the H₂ pressures on the two sides of Pd film. Therefore the effect of the addition of the alloying element into Pd on the H₂ flux could simply be indicated by how the diffusivity and solubility of H-atoms in Pd (in case the pressures on the two sides of film are fixed) is affected by the addition of the alloying element. In all the chapters from here on, the flux or the permeance of hydrogen through the Pd or Pd-alloy membrane is represented in terms of molecular (H₂) flux or permeance.

4.3. H₂ interaction with Pd-Ag alloy

The addition of Ag into Pd alters the diffusivity and solubility of H-atoms in Pd and consequently affects the H₂ permeation through Pd. The addition of Ag decreased the diffusivity of hydrogen in Pd (see Fig. 4.2) [101, 102]. The decline in the diffusivity showed in two regions. The first region (up to 20-25 Ag wt%) showed relatively slower decrease in the diffusivity with the addition of Ag and the diffusivity of hydrogen did not differ much from pure Pd. In the second region (after 20-25 Ag wt%), the hydrogen diffusivity decreased relatively faster on the addition of Ag. The diffusivity of hydrogen in Pd-Ag alloy up to 20 wt% did not show any significant sensitivity to temperature. For example, at 500 °C, the diffusivity decreased between 0 and 20 wt% Ag only by a factor of 0.75 [102] and at 250 °C, the diffusivity decreased by a factor of 0.73 between 0 and 20 wt% Ag [102].

Contrary to the hydrogen diffusivity, the solubility of hydrogen in the Pd-Ag alloy increased with the addition of Ag (Fig. 4.3). There are differences in the characteristics trend of the hydrogen solubility in Pd-Ag alloy in the literature. According to Holleck [102], the solubility in the Pd-Ag alloy (Fig. 4.3a) increased with the addition of Ag, went through a maximum between 30-40 wt% Ag and declined afterward. The solubility trend observed by Sieverts et al. [96] (Fig. 4.3c) were very similar to that of Holleck [102] but with the difference that the solubility maximum lied between 20-30 wt% Ag. In contrast to the observation of Holleck [102] and Sieverts et al. [96], Pugachev et al. [101] reported no maximum in the solubility (Fig. 4.3c) in Pd-Ag alloy and the solubility of hydrogen increased monotonically up to 40 wt% Ag (the maximum wt% Ag used in the study was 40). The solubility of hydrogen in Pd-Ag alloy showed relatively higher sensitivity to Ag content at lower temperatures.

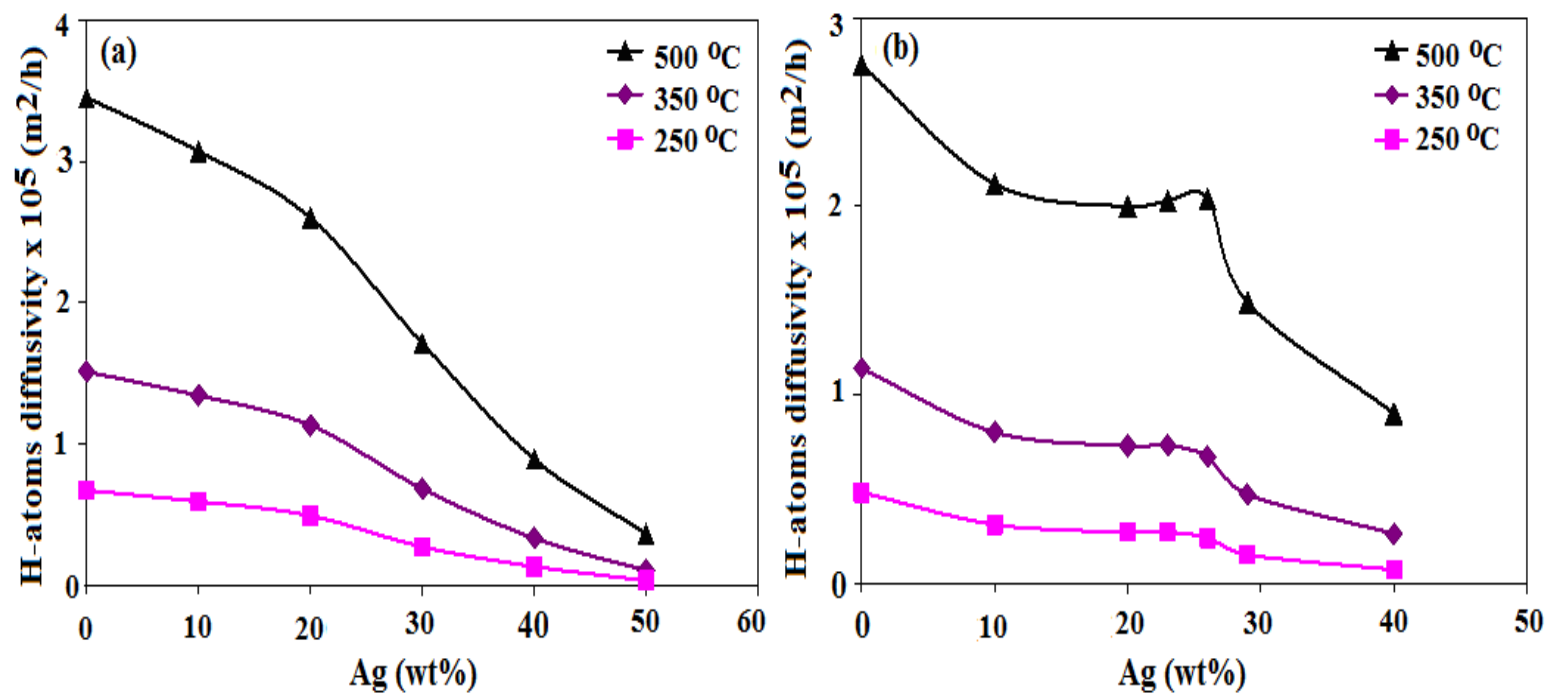


Fig. 4.2. Diffusivity of hydrogen in Pd-Ag alloy (a) by Holleck [102], foil area = 3.14 cm², pressure range = 0.04- 0.66 atm and thicknesses = 800-2025 μ m (b) by Pugachev et al. [101], foil area = 23 cm², pressure range = 0-1 atm, and thickness = 100-150 μ m

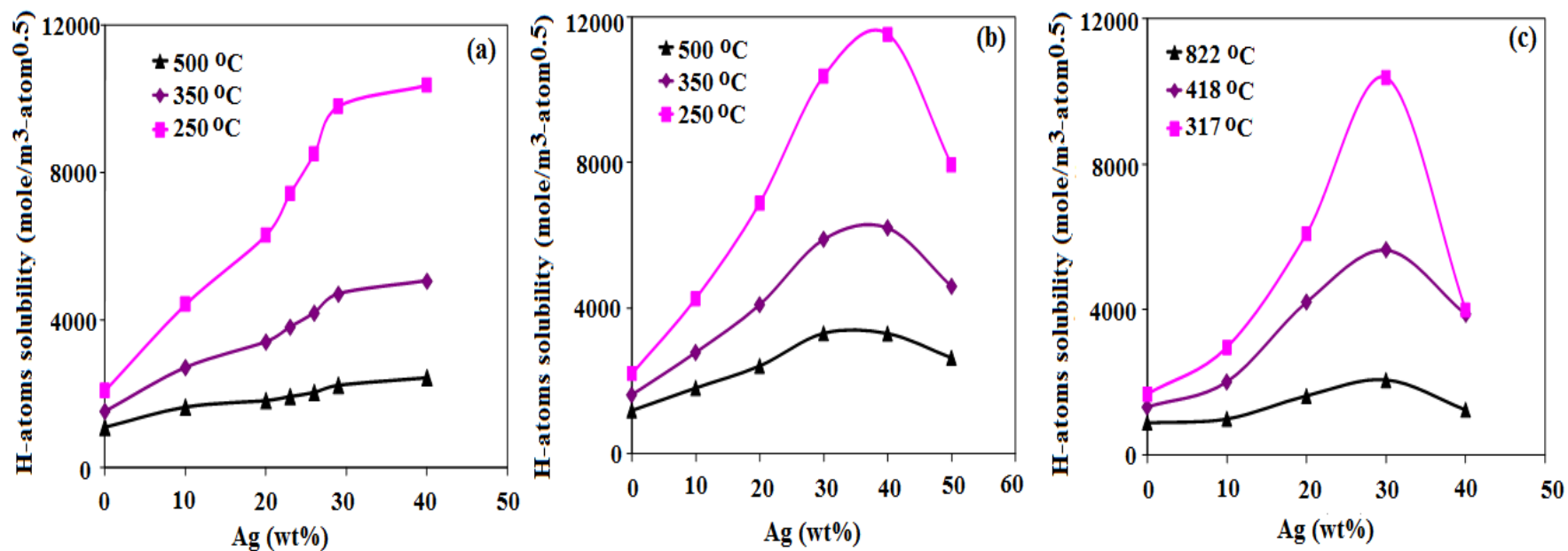


Fig. 4.3. Solubility of hydrogen in Pd-Ag alloy (a) calculated from data given by Pugachev et al. [101], foil area = 23 cm², pressure range = 0-1 atm, and thickness = 100-150 μm (b) by Holleck [102], foil area = 3.14 cm², pressure range = 0.04- 0.66 atm and thicknesses = 800-2025 μm (c) by Sieverts et al.[96], Pressure = 1 atm and sample size = 100 g Pd-Ag alloy powder

For example, at 500 °C, the solubility of H-atoms in Pd at 1 atm was 1181 mole/m³ and reached 2416 mole/m³ for Pd-Ag (20 wt%) alloy, an increase by a factor of 2.05 [101], however at 250 °C, the solubility at 1 atm for Pd was 2200 mole/m³ and increased to 6895 mole/m³ for the Pd-Ag (20 wt%) alloy, an increase by a factor of 3.14.

As is shown in Eqn. 4.18, the permeation rate of H₂ in Pd is proportional to the product of the diffusivity and solubility of H-atoms. The solubility of H-atoms in Pd increased with the addition of Ag up to 30-40 wt% Ag [96, 102] and the diffusivity decreased with increasing Ag wt% [101, 102]. Therefore the net result of the addition of Ag was the increase in the H₂ permeation rate of Pd. Fig. 4.4 shows the effect of the addition of Ag into Pd on the relative H₂ permeance with respect to Pd. The H₂ permeance reached maximum between 20-25 wt% Ag and then decreased afterward. The optimum concentration range remained the same for the wide variation in the pressure measurement conditions. For example, Holleck [102] and Pugachev et al. [101] used the pressure range 0.04-0.66 atm and 0-1 atm respectively in their study while Knapton [7] used the pressure range 0-21.5 atm. Despite the large variation in the pressure range used by different authors, the range of Ag wt% for the maximum relative permeance remained little affected (Fig. 4.4b). The range of Ag wt% which showed the maximum relative H₂ permeance remained the same between 250-500 °C (Fig. 4.4). The H₂ relative permeance for 20-25 wt% Ag alloy with respect to pure Pd increased with decreasing temperature.

Fig. 4.5 shows the absolute value of the H₂ permeability in pure Pd and Pd-Ag alloy in the optimum Ag concentration range (20-25 wt%). It can be examined from the figure that there existed large variation in the absolute value of H₂ permeability reported by different authors for pure Pd and Pd-Ag alloy (20-25 wt%). The large variation in the

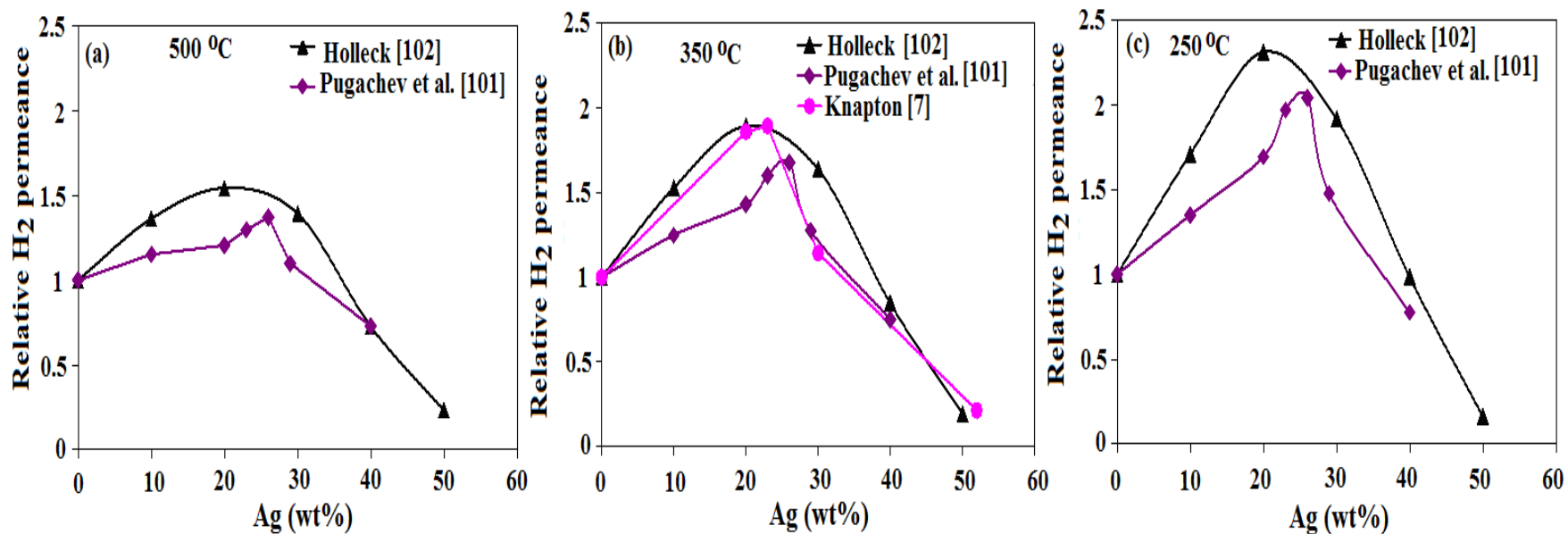


Fig. 4.4. Relative H_2 permeance of Pd-Ag alloy with respect to pure Pd, pressure range = 0.04-0.66 atm Holleck [102], 0-1 atm Pugachev et al. [101], 0-21.5 atm Knapton [7](a) at 500 °C (b) at 350 °C (c) at 250 °C

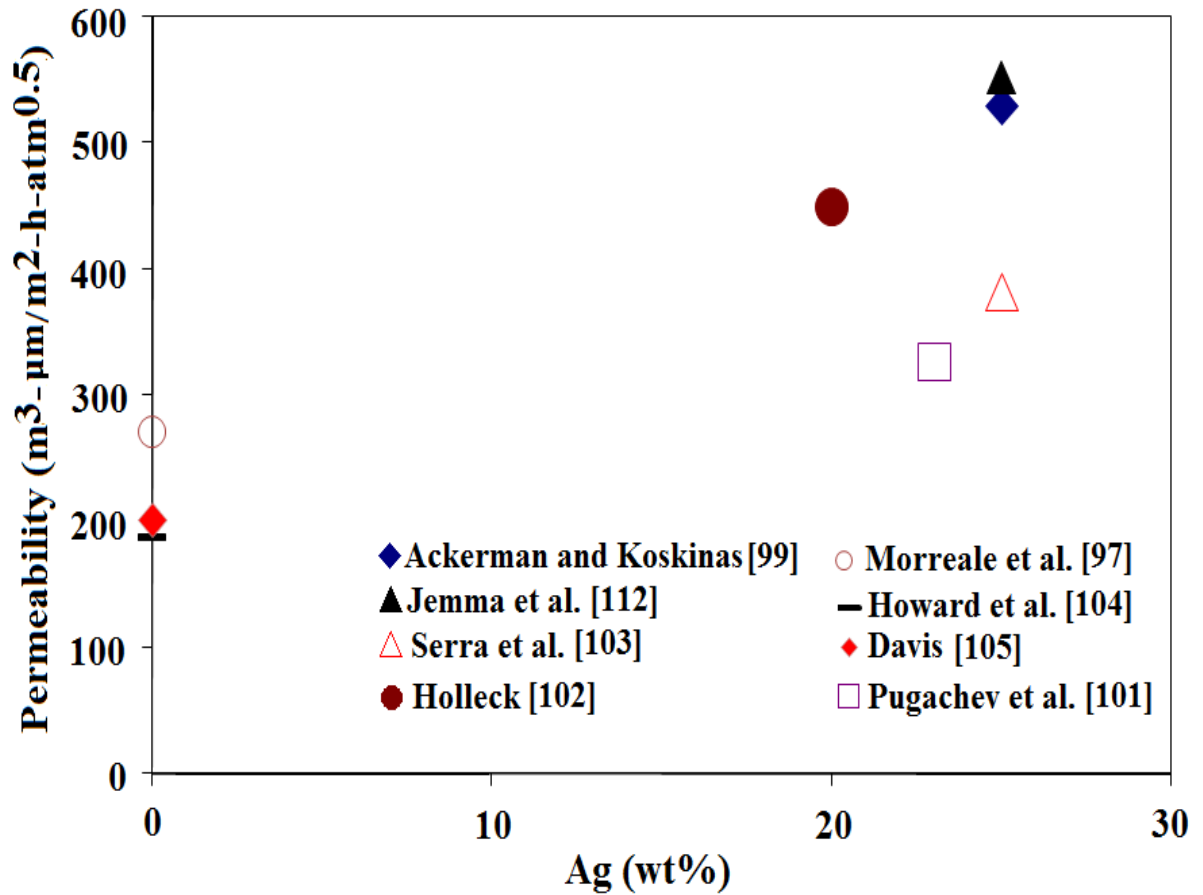


Fig. 4.5. The H_2 permeability of pure Pd and Pd-Ag alloy in the optimum Ag concentration range at 300 °C, pressure range used: Ackerman and Koskinas [99] = 1-7.8 atm, Jemma et al. [112] = 1.4-4.4 atm, Serra et al. [103] = 0-1.1 atm, Holleck [102] = 0.04-0.66 atm, Morreale et al. [97] = 1-27 atm, Howard et al. [104] = 1-27.6 atm, Davis [105] = 0-0.99 atm and Pugachev et al. [101] = 0-1 atm.

absolute value of permeability of Pd or Pd-Ag alloy could be due to the difference in the pressure ranges used and the level of surface cleanliness of the membrane surface and the purity level of H₂ gas used in the study [111, 113].

5. Pd-Ag sequential deposition: Relation between plating conditions and deposits morphology

5.1. Introduction

One way to synthesize Pd-Ag composite membranes is to use the sequential deposition approach in which Pd and Ag layers are deposited on top of each other and then annealed further to form the Pd-Ag alloy. The general practice for the synthesis of Pd-Ag membranes by the sequential deposition was the bi-layer approach [41, 45, 49]. The preparation method consisted of the deposition of a thick layer of Pd already selective to hydrogen followed by an Ag top layer. The thick Pd-Ag bi-layer, the thick Pd layer and the Ag layer on the top of the Pd layer, required high temperatures (generally 600 °C or higher) to form the Pd-Ag alloy [9, 43, 86]. However, in the case of porous metal substrate, the annealing temperature was limited because of the diffusion of the substrate components into the Pd and Ag layers [43, 55] (see Chapter 2, Section 2.3.1). The limitation of the annealing temperature in the case of porous metal substrate therefore demands very thin multi alternate layers of the two metals to be deposited to reduce the annealing time for the alloy formation. Furthermore, thinner Pd-Ag membranes are desired from the high H₂ permeance point of view.

The morphology of the Pd-Ag deposits plays an important role in the synthesis of the thin H₂ selective membrane. The important morphological aspects are compactness of the deposits and good substrate pores coverage. The one attribute to judge the good pores coverage is equal growth of the deposits in the direction perpendicular and lateral

to the substrate surface and is referred to as deposits with uniform growth in this study. Furthermore, the lateral growth of the deposits could be judged by the substrate pore penetration of the deposits. For example, Fig. 5.1 shows the schematic of the deposit growing on the substrate surface. Point A (closure to the solution side) and point B (relatively farther away from the solution side) represent two locations in the deposits growing on the substrate surface. In order to cover the pores of the substrate to form the thin H₂ selective membrane, the deposition rate at point B should be more or less equal to that at point A. The deposition at point B will lead to the deposits growth in the lateral direction to the substrate surface and therefore to the substrate pores coverage. The ability of the deposits to cover the substrate pores therefore could be judged by how equally the deposits grow at points closer to the solution and at points relatively farther away from the plating solution. In the case where the deposits growth at point A is much higher than the growth at point B, the deposits will grow mainly in the perpendicular direction without showing any substrate pores coverage. The higher growth in the perpendicular direction therefore will result in thicker membranes without complete selectivity towards H₂.

The top of the substrate (tip of the particle) and the neck of the substrate (see Fig. 5.1) are the points on the substrate very similar to points A and B (see Fig. 5.1) respectively in terms of their location with respect to the plating solution. The top of the substrate (similar to point A) is closer to the plating solution and the neck of the substrate is relatively farther away from the solution (similar to point B). As mentioned previously in this section, for the good lateral growth (required for the substrate pores coverage), the top of the substrate (point closer to the plating solution) and neck of the substrate (point farther away from the plating solution) should show more or less equal

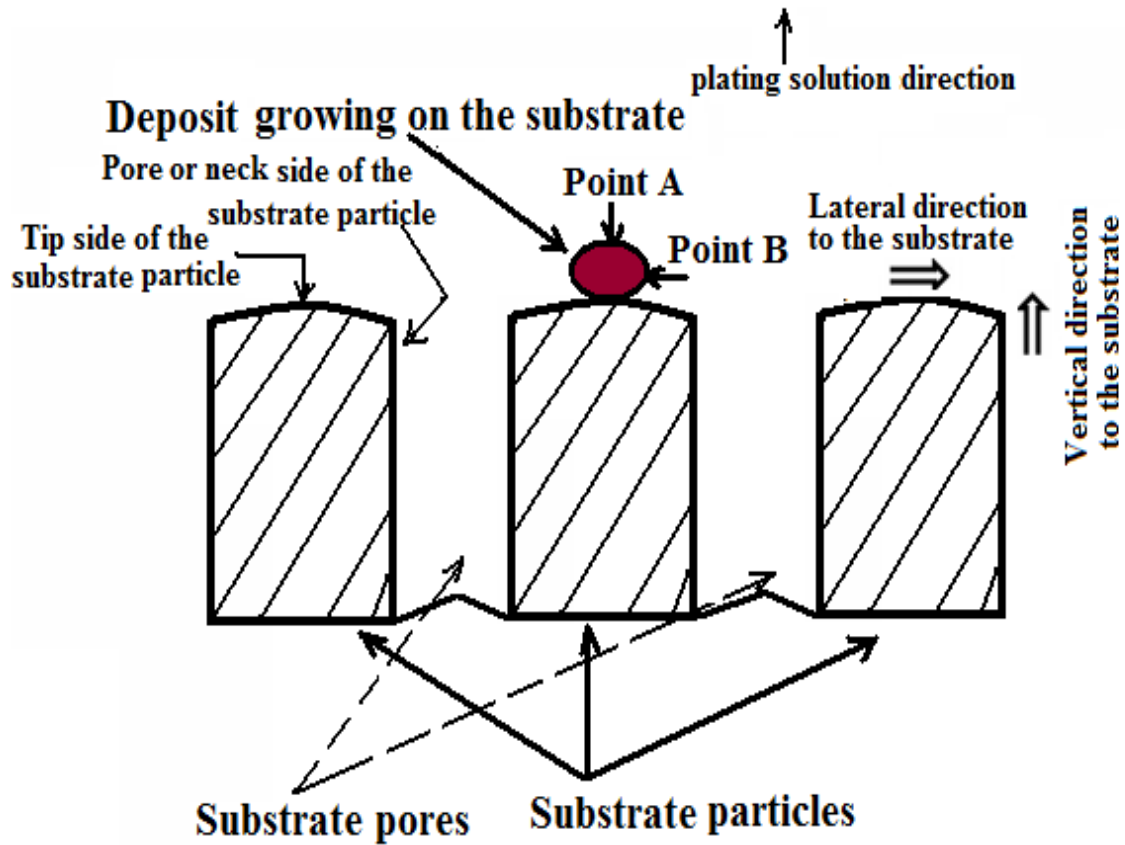


Fig. 5.1. Schematic of the deposit growth on the substrate immersed in the plating solution, deposits pore penetration and its significance from the substrate pores coverage point of view

deposition rate. Therefore, the deposits substrate pores coverage could be judged by the deposits growth at the neck side of the substrate or by the pore penetration (i.e. deposition inside the pores) of the deposits. The good substrate pore penetration or good growth at the neck side of the substrate therefore is indicative for the deposits ability to cover the substrate pores.

The plating techniques and conditions have radical effects on the deposits growth characteristics or the deposits morphology. Therefore, the objective of the study in this chapter was to investigate the effect of plating conditions on the morphology of Pd-Ag deposits for the synthesis of Pd-Ag composite membranes using the multilayer sequential approach.

5.2. Experimental

5.2.1. Plating conditions

Porous stainless steel (PSS) coupons were used for studying the effect of plating conditions on the morphological characteristics of the Pd and Ag deposits.

For the electrochemical study of the electroless plating baths, the linear sweep voltammetry (LSV) scans were obtained using the BAS 110B/W electrochemical station described in Chapter 3, Section 3.5.2. For all the scans, the Pd, Ag and N_2H_4 concentration of 3 mM was maintained in the bath and the solution volume of 50 ml was used. All the scans were obtained at 60 °C, which was the actual plating bath temperature used during the deposition. Table 5.1 shows the bath compositions and plating conditions investigated.

Table 5.1. Composition of Pd and Ag plating solutions

Component	Conc. (M)	
	Pd	Ag
Pd(NH ₃) ₄ Cl ₂ .H ₂ O	0.016	-
AgNO ₃	-	0.003- 0.02
NH ₃	3.1	3.1
Na ₂ EDTA	0.1	0.1
N ₂ H ₄	0.0056	0.004 - 0.0056
Temp., °C, pH	60, 11	60, 11
substrate rotation (rpm)	0	0-500

Based on the LSV polarization curve of the Ag electroless plating bath obtained, it was observed that Ag showed fast reduction kinetics and the overall Ag deposition process could be limited by the diffusion of Ag ions to the substrate surface. Therefore the electroless Ag deposition was performed at four different bath conditions. The four Ag bath conditions have been designated as condition 1, 2, 3 and 4 (see Table 5.2).

The condition 1 represented 3 mM of Ag and 5.6 mM of N_2H_4 concentration which was the typical composition of the electroless Ag plating bath used in the literature [49, 87] for the membrane synthesis. In order to further reduce the concentration gradient of Ag ions in the solution relative to the condition 1, the condition 2 corresponded to a higher concentration ratio of Ag ions to N_2H_4 in the bath, i.e. 20 mM of Ag and 4 mM of N_2H_4 and the condition 3 used the same Ag ions to N_2H_4 ratio as that of the condition 1 but the substrate was rotated at 500 rpm. In the condition 4, the higher ratio of Ag to N_2H_4 in the bath was achieved by maintaining the Ag concentration the same as the condition 1 but the concentration of N_2H_4 was lowered from 5.6 mM to 1 mM. For all the experiments, the solution volume of 50 ml was used.

Prior to any plating experiment, the substrate was cleaned in a basic solution. The procedure adopted for cleaning was the same as that described in Chapter 3, Section 3.2.2. The morphology of the deposits was characterized using scanning electron microscope (SEM) equipped with EDX. The examination of the crystalline structure of the deposits was performed using Rikagu X-ray diffractometer.

Table 5.2. Different plating conditions used for the Ag deposition. Condition 1 represented the typical plating conditions for the Ag deposition used in the literature [49, 87] and conditions 2, 3 and 4 represented different modification to condition 1.

Plating condition	[Ag]/[N ₂ H ₄]	Substrate rotation	Comments
Condition 1	3 mM/5.6 mM	0 rpm	Typical conditions used for Ag plating in the literature [49, 87]
Condition 2	20 mM/4 mM	0 rpm	Represented higher Ag/N ₂ H ₄ ratio than the condition 1
Condition 3	3 mM/5.6 mM	500 rpm	Same as condition 1 but substrate stirring used to enhanced the Ag diffusion in the solution
Condition 4	3 mM/1 mM	0 rpm	Represented higher Ag/N ₂ H ₄ than the condition 1

5.3. Results and discussions

5.3.1. Single metal deposition

The initial deposits with a thickness less than 1 μm showed difference in the growth characteristics for Pd and Ag. Fig. 5.2 shows the SEM images of the Pd and Ag deposits. The Pd deposits showed a uniform deposition over the entire substrate surface as shown in Fig. 5.2a. The deposits showed equal growth on the top and inside the pores of the substrate, which was a desired deposit characteristic from the synthesis of thin and hydrogen selective membranes point of view. In the case of the Ag deposition (condition 1), the SEM image of the sample as shown in Fig. 5.2b revealed that the Ag deposits showed lesser tendencies to penetrate into the substrate pores than the Pd deposits. Shu et al. [88] also reported more Ag deposition on the top than inside the pores of the PSS substrate using similar bath conditions. The non-uniformity of the obtained Ag deposits using the similar Ag electroless plating conditions was also observed on $\gamma\text{-Al}_2\text{O}_3$ and ZrO_2 substrates [84].

The XRD pattern of the obtained Pd deposits is shown in Fig. 5.3a. The deposits were crystalline structure and did not show any preferred crystal orientation which was consistent with the observation of Shu et al. [114] who used the similar plating conditions for the Pd deposition on the PSS substrate. Similar to the Pd deposits, Ag electroless deposits (Fig. 5.3b) obtained were also crystalline in nature. The deposits showed fcc structure and the order of relative intensity ratio of the peaks obtained for the different planes matched with the standard Ag pattern signifying no preferred crystalline orientation of the deposits.

The deposition characteristics for both Pd and Ag deposits continued with the trend

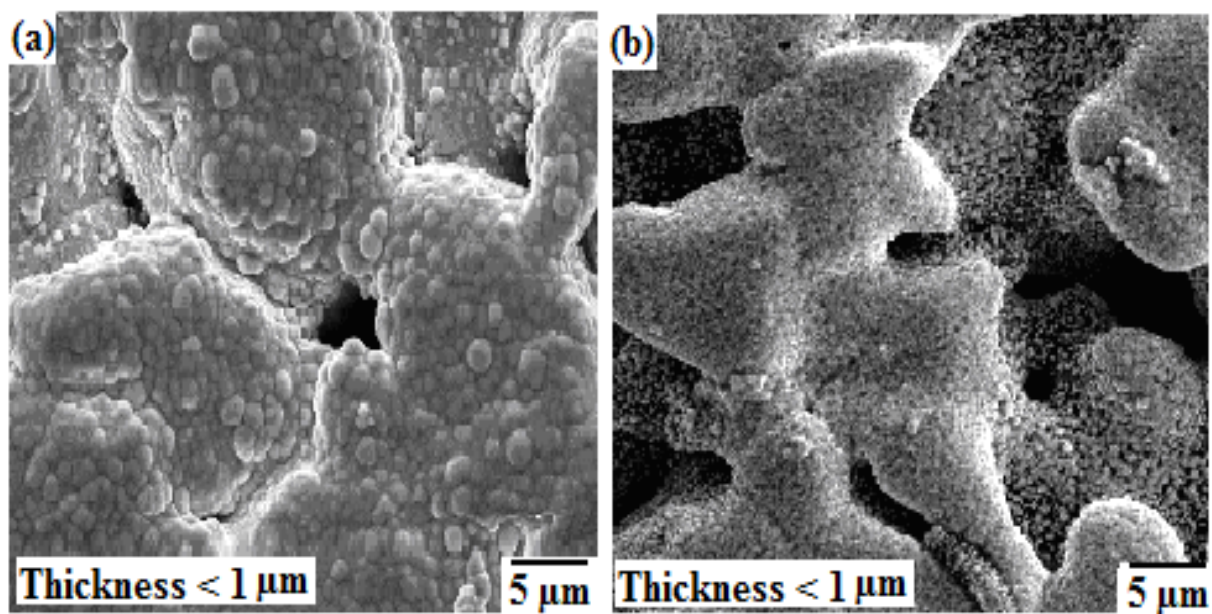


Fig. 5.2. Initial deposition characteristics of single metal deposits on PSS coupon surface (plating solution volume = 50 ml, sample surface area = 2 cm², bath temp. = 60 °C, pH = 11) (a) Pd deposits and plating time = 15 min, (b) Ag electroless plating condition 1 and plating time = 45 min.

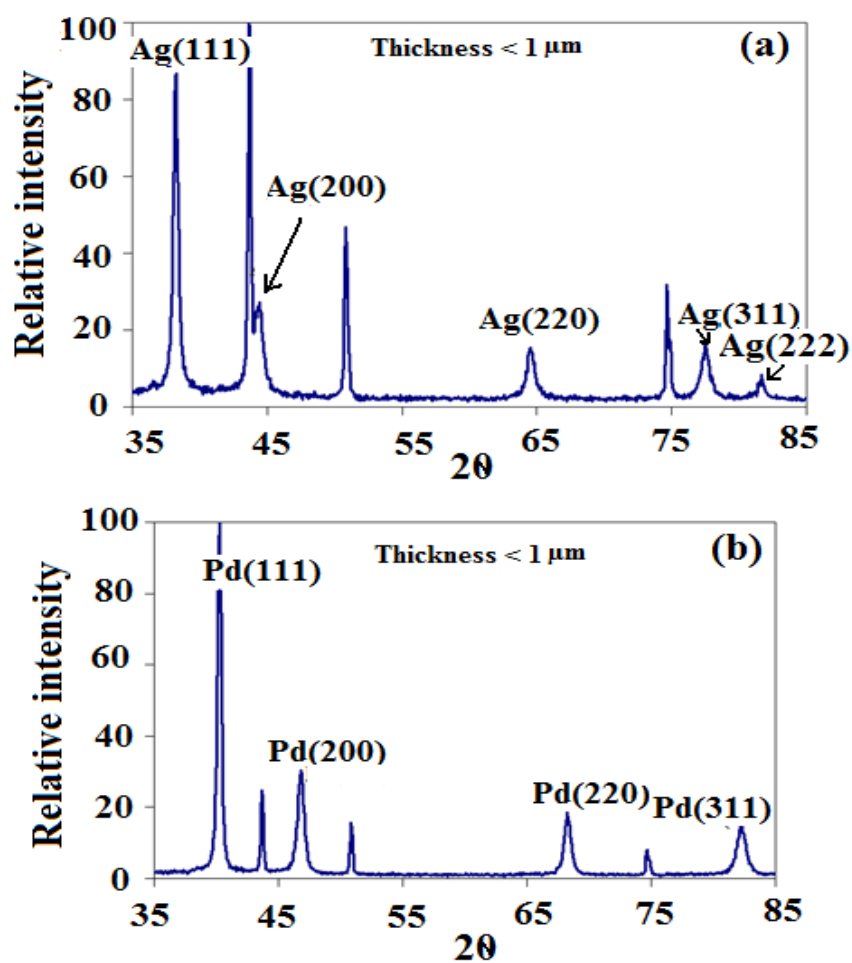


Fig. 5.3. XRD pattern of the initial single metal deposits obtained on PSS coupon surface (plating solution volume = 50 ml, sample surface area = 2 cm^2 , bath temp. = 60°C , pH = 11) (a) Pd deposits and plating time = 15 min, (b) Ag electroless plating condition 1 and plating time 45 = min.

similar to the initial deposits as the thickness increased. Fig. 5.4 shows the SEM images of the cross-section of the deposits with the thickness greater than 3 μm . Pd continued depositing with the characteristics similar to that observed for the initial deposition for the extended plating time (Fig. 5.4a). Keuler et al. [7] also reported similar trend for the Pd deposition on $\gamma\text{-Al}_2\text{O}_3$ and ZrO_2 substrates. The Ag electroless deposits, on the other hand, showed non-uniform thickness, higher at the top of the substrate than at the neck of the pores (Fig. 5.4b). Under the plating conditions studied, the average Pd plating rates, based on the initial 45 min deposition, ranged between 6 and 6.5 $\mu\text{m/h}$ and no more than 15 wt% of Pd in the solution was consumed during the deposition. Therefore, approximately constant plating conditions (close to the initial conditions) were maintained for the entire plating period. For the Ag electroless plating (condition 1), the average plating rates ranged between 1.1 and 1.3 $\mu\text{m/h}$ for the first 45 minutes of plating and again no more than 15 wt% Ag in the solution was consumed during this period.

5.3.2. Pd-Ag sequential deposition

Fig. 5.5 shows the SEM images of the cross-section of Pd-Ag sequential deposits obtained. As can be seen in the figure, the Pd-Ag deposits showed drastic differences in the morphology when the Pd and Ag layers were deposited on top of each other as compared to the morphology of the single metal deposits. The morphology of the sequential deposits was highly non-uniform and showed dendritic structure (Fig. 5.5) as compared to the morphology that was expected from the morphology of single metal deposits (Fig. 5.4), simply layered on top of each other (note: the Pd and Ag single metal deposits did not show any dendritic morphology (Fig. 5.4)) and based on the

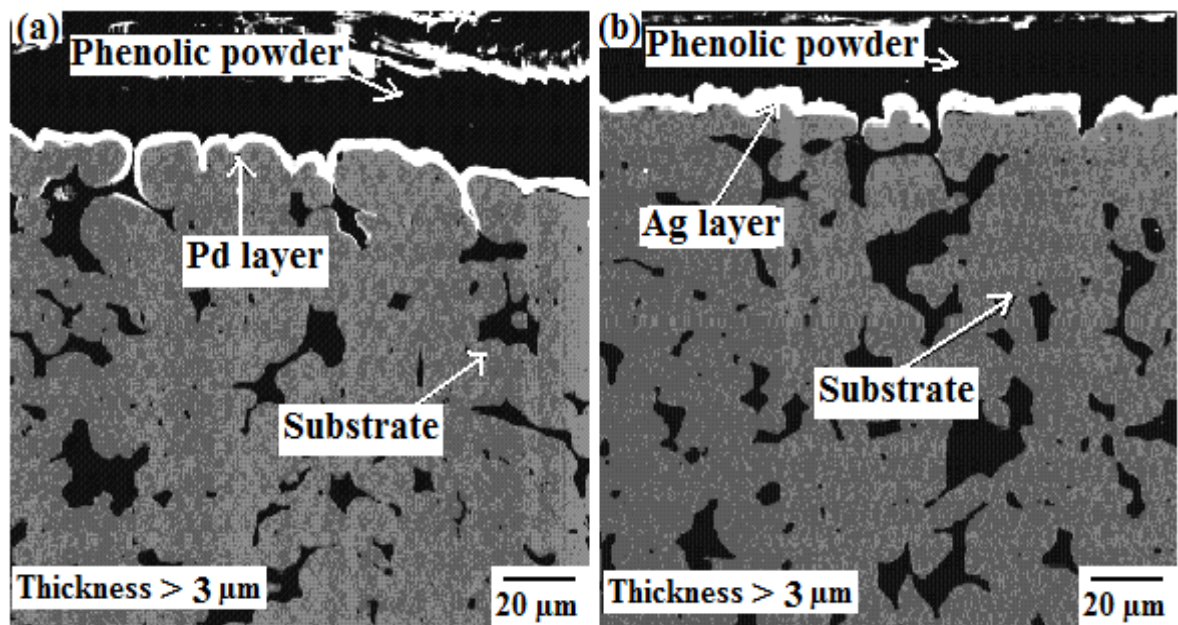


Fig. 5.4. Cross section of the PSS coupons with single metal deposits thickness $> 3 \mu\text{m}$ (plating solution volume = 50 ml, sample surface area = 2 cm^2 , bath temp. = 60°C and $\text{pH} = 11$) (a) Pd electroless plating deposits and plating time = 45 min, (b) Ag electroless plating deposits and plating time = 300 min.

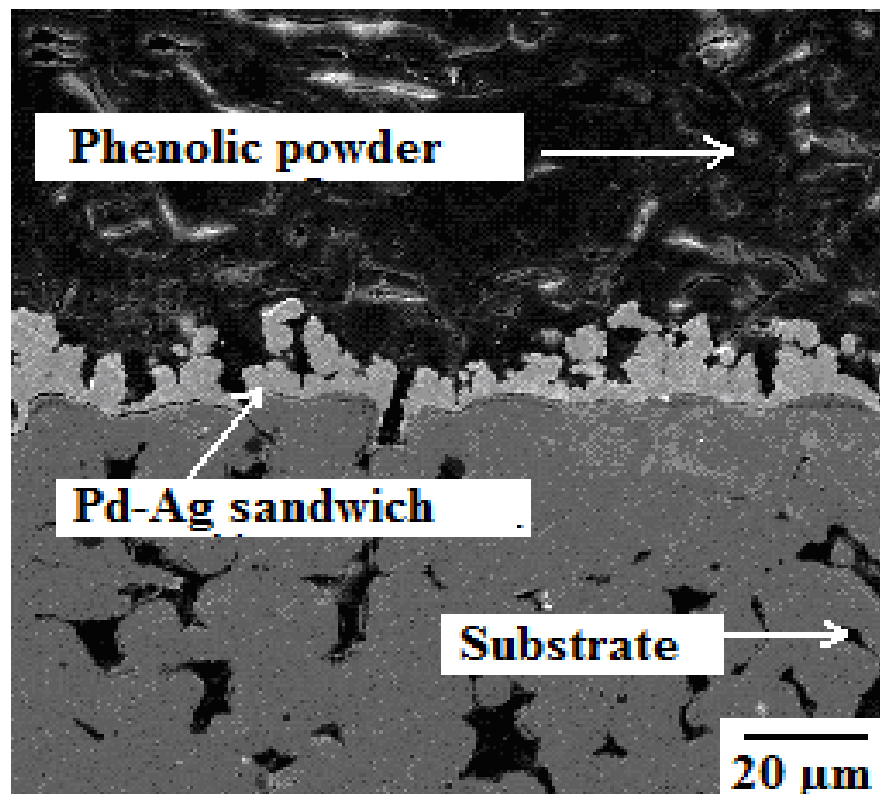


Fig. 5.5. The Pd-Ag sequential deposits obtained on the PSS surface with total four sequence of Pd-Ag plating. The Pd plating time = 15 min and Ag plating time = 30 min was used in each sequence (for each plating, solution volume = 50 ml, sample surface area = 2 cm², bath temp. = 60 °C, pH = 11).

single metal deposition, the dendritic morphology of the Pd-Ag sequential deposits was not expected. The causes leading to the dendritic Pd-Ag sequential deposits is discussed in the later sections). The sequential deposits consisted of four alternate layers of Pd (~1 μm) and Ag (~0.5 μm) each (total 8 layers). Ayturk et al. [115] under the similar Pd and Ag plating condition observed the Pd-Ag sequential deposits morphology very similar to the morphology shown in Fig. 5.5.

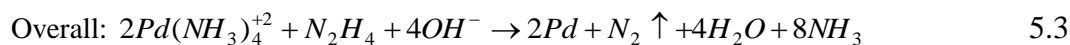
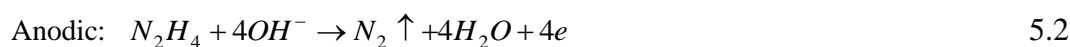
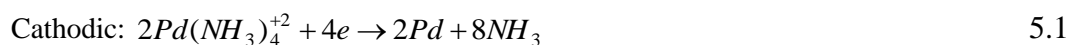
The Pd-Ag sequential deposits (Ag condition 1) showed highly non-uniform growth more in the perpendicular direction but little in the lateral direction to the substrate surface, therefore little substrate pore coverage was expected. Ma et al. [60] used the poor pore coverage property of the Pd-Ag sequential deposits obtained under Ag plating condition 1 to form the intermetallic diffusion barrier, referred to as the Pd/Ag intermetallic diffusion barrier, to separate the dense Pd or Pd alloy layer from the porous metal substrate. The Pd-Ag barrier was effective to avoid the contamination of the dense Pd layer from the porous stainless steel substrate components when the Pd membranes were exposed to temperature as high as 575 $^{\circ}\text{C}$ [115]. Also the deposition of several micrometers thick layer of Pd-Ag deposits (Ag condition 1) did not introduce significant resistance for the He flow through the porous metal substrate showing the difficulty of the Pd-Ag deposits to produce thin and H_2 selective membranes.

5.3.3. LSV polarization characteristics of Pd and Ag electroless baths

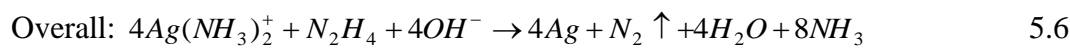
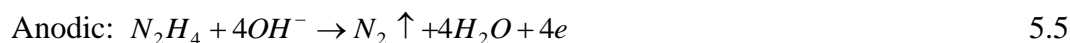
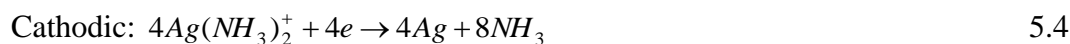
The electroless deposition occurs with the mechanism similar to the electro deposition with the difference that both oxidation and reduction reactions occur on the same electrode surface for the electroless plating [73]. Therefore, the effect of plating conditions on the morphology of electroless plating deposits could better be understood

by the polarization characteristics of the individual redox reactions involved in the electroless plating using electrochemical techniques such as linear sweep voltammetry (LSV). The overall reactions of the electroless Pd and Ag deposition based on N_2H_4 as the reducing agent used in this study is widely accepted with the following redox reactions [68].

Pd:



Ag:



According to the mixed potential theory [116], the rate of a redox reaction depends on the electrode potential and is independent of other redox reactions taking place on the same electrode. The polarization curve of individual redox reactions can be added to predict the overall polarization characteristics of the electrode (see Chapter 2, Section 2.32. for more details). In the case of electroless plating, the actual electrode potential at which the electroless plating occurs corresponds to the potential with net zero current and lies between the electrode potential of the metal ions and the reducing agent in the bath. For example, the standard hydrogen electrode (SHE) potentials for Pd and Ag are 0.98 and 0.79 respectively [67]. The presence of NH_3 and EDTA lowered the electrode potentials of the metals in the bath. The stability constants for the complexing reactions of NH_3 and EDTA with Pd were reported to be 10^{32} and 10^{18} respectively while the

corresponding values for Ag were $10^{7.2}$ and $10^{7.3}$ respectively [117]. Based on the values of the stability constants and the higher concentration of NH_3 than EDTA kept in the bath (Table 5.1), NH_3 acted as the main complexing agent for both metals. In the presence of NH_3 , the equilibrium electrode potentials for the Pd and Ag metal ions in the bath were estimated as -0.04 V (-0.23 V with respect to Ag/AgCl, 3M NaCl reference electrode) and 0.16 V (-0.03 V with respect to Ag/AgCl, 3M NaCl reference electrode) with respect to the standard hydrogen electrode (SHE) respectively using the Nernst equation (see Appendix A, Table A.4 for the calculations). The value of the standard electrode potential for the N_2H_4 oxidation is -1.12 V. Thus according to the mixed potential theory, the actual electrode potential (with respect to SHE) for the electroless plating at the standard conditions lied between -0.04 and -1.12 V and 0.16 and -1.12 V for the Pd and Ag deposition respectively. See Appendix C for using the mixed potential theory to the LSV data shown in the next Sections 5.3.3.1 and 5.3.3.2.

5.3.3.1. Ag and Pd polarization characteristics

The cathodic polarization curve for the Ag bath showed fast reduction kinetics for the metal. Fig. 5.6a shows the polarization curve of the solution. The solid line curve shows the scan obtained in the presence of Ag while the dotted line curve shows the scan obtained in the blank solution with no Ag present in the solution. The Ag deposition started approximately at the electrode potential of 15 mV and within the overpotential of 15 to 25 mV, the Ag deposition reached a point where the overall deposition process was limited by the mass transfer step of the Ag ions to the sample surface as indicated by no increase in the current on further increasing the overpotential for the Ag deposition (Fig. 5.6a). In the case of Pd bath, the polarization curve on the Pd

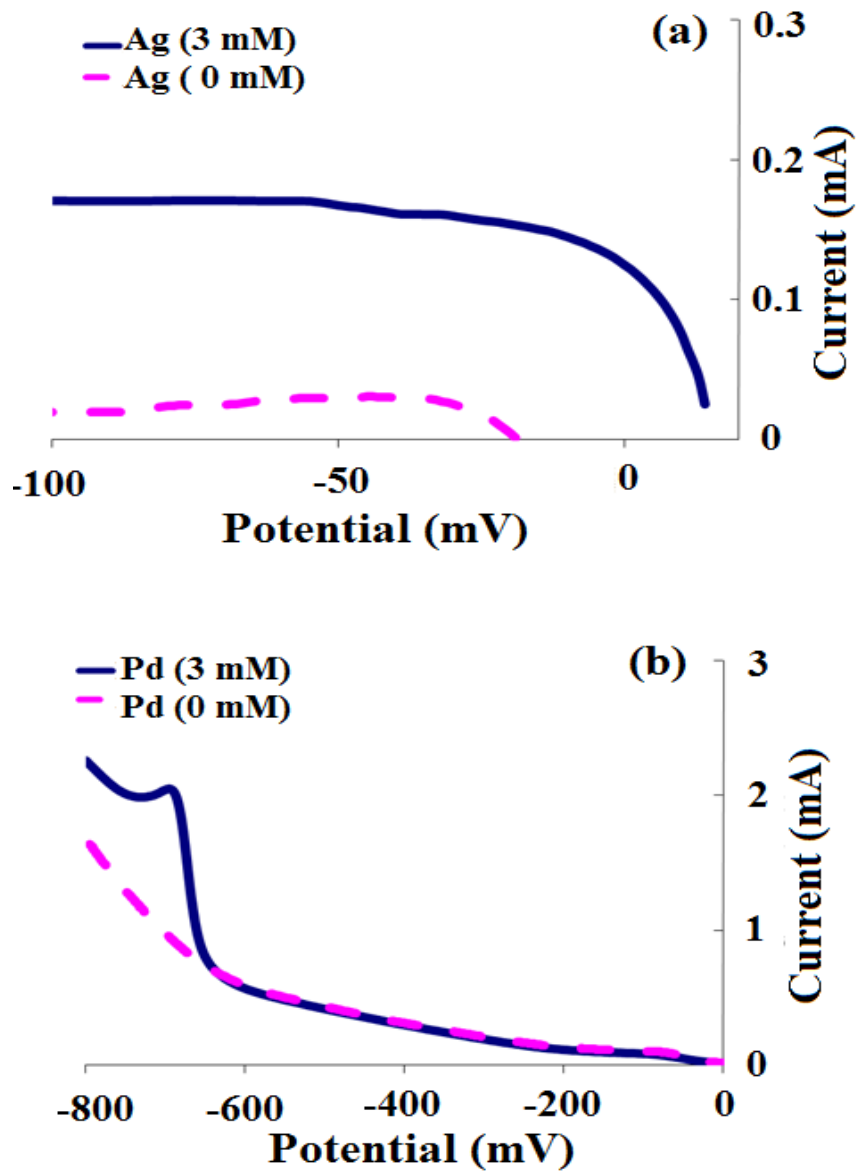


Fig. 5.6. Polarization curve obtained on the Pd or Ag coated stainless wires (plating solution volume = 50 ml, temp. = 60 °C, pH = 11 and sample surface area = 0.63 cm²) (a) Ag solution on the Ag surface, (b) Pd solution on the Pd surface.

surface as shown in Fig. 5.6b showed large overpotential associated with the reduction of Pd. The solid line curve and dotted line curve show the LSV scan obtained on solution with and without Pd ions respectively. It can be seen in Fig. 5.6b that the Pd deposition occurred at the electrode potential between -650 and -700 mV (Note: the equilibrium electrode potential for the Pd ions in the solution was -230 mV with respect Ag/AgCl, 3 M NaCl). The overpotential associated with the Pd deposition lied in the range 420-470 mV, an order of magnitude higher than that associated with the Ag deposition process. Similar polarization characteristics were obtained by Sturzenegger and Puipe [118] in their electrodeposition of Pd and Ag from ammonia based bath. In fact, the fast reduction kinetics for Ag and the slow reduction kinetics related to Pd appeared to be very common irrespective of the complexing agent used in the bath. The large overpotential associated with the Pd deposition was reported by Brenner [67] from the thiocyanate based bath. Hasler et al. [119] used glycine based bath for the Pd-Ag electrodeposition bath. In their polarization curves for the Pd and Ag bath, the Pd deposition occurred at potential of 750 mV more cathodic than the Ag deposition. The metals with univalent ions such as Ag show in general relatively fast reduction kinetics as compared to divalent or trivalent ions [120].

The reduction characteristics of both metals did not change much when the surface was altered. Fig. 5.7a shows the effect of the surface on the Ag reduction. The solid line shows the polarization curve of the Ag solution obtained on the Ag surface while the dotted line shows the similar curve obtained on the Pd surface. In both cases, the Ag reduction kinetics was fast and within 15-25 mV change of the electrode potential in the cathodic direction, the cathodic currents started decreasing and the line became flat signifying the overall deposition process limited by the mass transfer of the Ag ions to

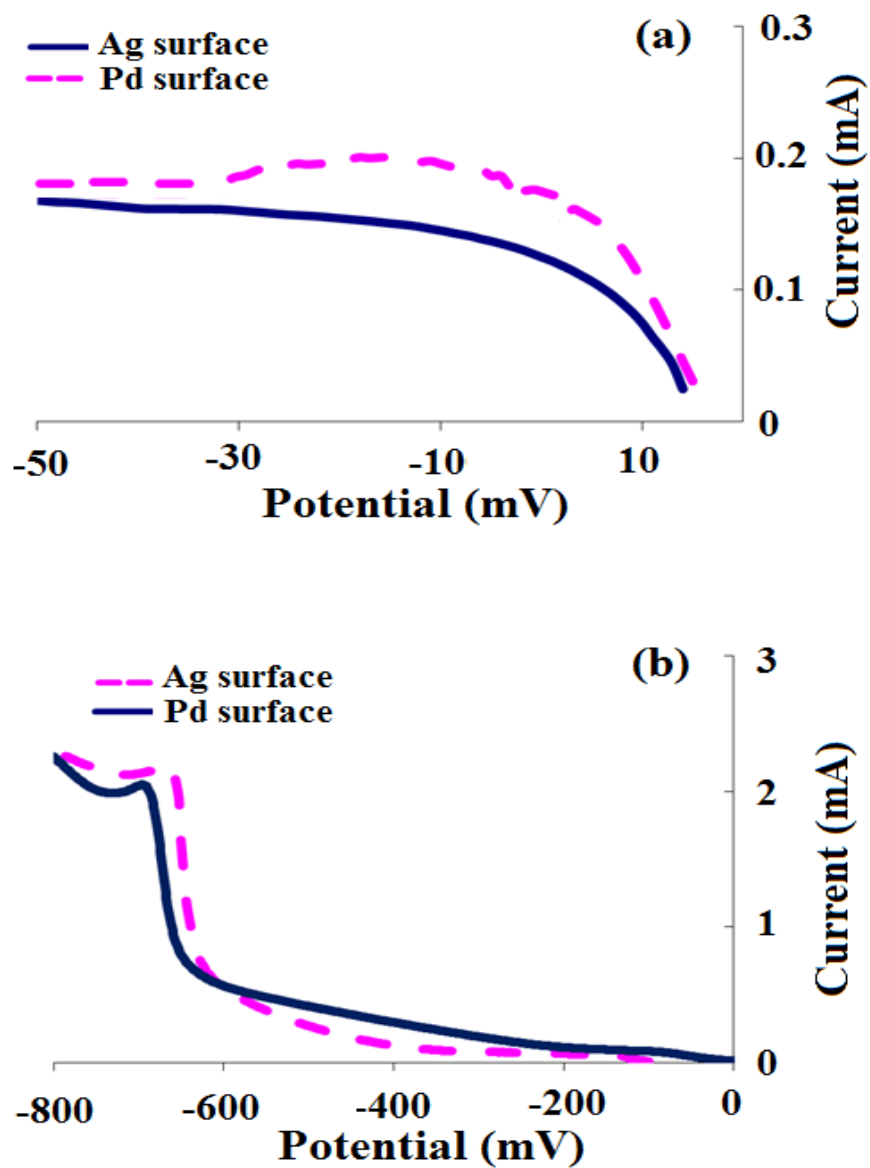


Fig. 5.7. Polarization curve obtained on Pd or Ag coated stainless steel wires (plating solution volume = 50 ml, temp. = 60 °C, pH = 11 and sample surface area = 0.63 cm²)
(a) Ag solution on the Ag and Pd surface, (b) Pd solution on the Ag and Pd surface.

the sample surface. Similarly, the polarization curve obtained for the Pd solution on the Ag surface did not show any significant difference from that obtained on the Pd surface. Again the large overpotential associated with the Pd deposition was also observed on the Ag surface (Fig. 5.7b). Therefore, the nature of the surface on which the deposition was initiated did not have any significant effect on the reduction characteristics of both metals.

5.3.3.2. *N₂H₄ polarization characteristics*

The anodic polarization curves obtained for the N₂H₄ solution on the Pd and Ag surface showed a large difference in the catalytic activity for the N₂H₄ oxidation. Fig. 5.8a and Fig. 5.8b show the polarization curves of the N₂H₄ solution obtained on the Ag and Pd surface respectively. The solid line and dotted line curves show the polarization characteristics of the solution with and without N₂H₄ presence respectively. The Pd surface showed more catalytic activity than the Ag surface for the N₂H₄ oxidation. At the electrode potential of 0 V, the anodic current associated with the oxidation of N₂H₄ was an order of magnitude higher for the Pd surface than that for the Ag surface. Ohno et al., [74] also observed higher N₂H₄ oxidation catalytic activity on the Pd surface in comparison to the Ag surface. In a bath containing 0.175 M Na₂EDTA (pH=12), the N₂H₄ oxidation current on the Pd surface started at potential 200 mV more cathodic than the oxidation potential on the Ag surface.

5.3.4. Morphology of the electroless Pd-Ag deposits

Based on the polarization characteristics of Pd, Ag and N₂H₄, the large overpotential

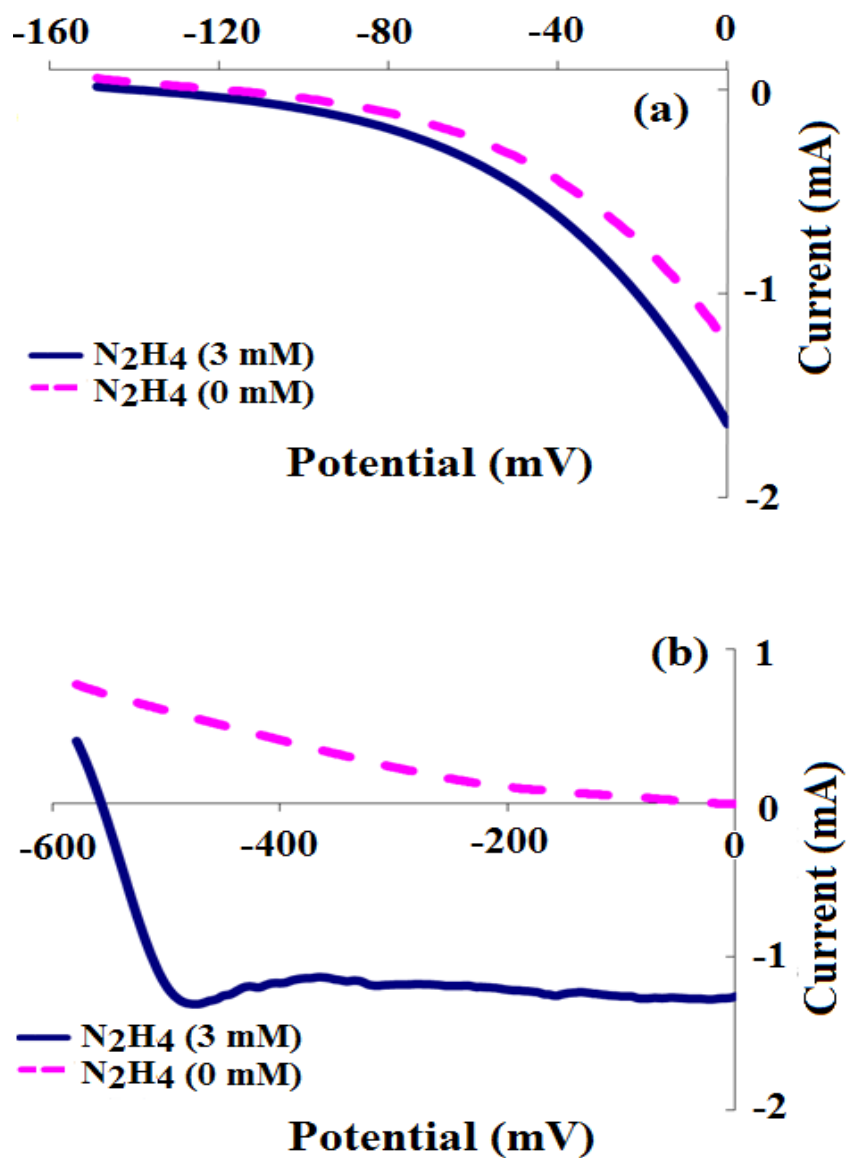


Fig. 5.8. LSV scan of the oxidation of N_2H_4 on the Pd or Ag coated stainless steel wires (plating solution volume = 50 ml, temp. = 60 °C, pH =11 and sample surface area = 0.63 cm²) (a) Ag surface, (b) Pd surface.

associated with the Pd reduction, the strong catalytic activity of the Pd surface for N_2H_4 oxidation and the fast reduction of Ag with relatively lower catalytic activity of the Ag surface for the N_2H_4 oxidation meant that the overall electroless deposition potential for Pd was more cathodic than that for the Ag deposition.

In general, the deposition potential is affected by the ratio of the reducing agent to metal ions in the bath. Increasing the ratio of the reducing agent to metal ions lowers the deposition potential. The condition 1 for the Ag deposition used the N_2H_4 concentration (5.6 mM) that was more than the stoichiometrically required for the Ag concentration of 3 mM (Eqn. 5.6). The low penetration of Ag into the substrate pores at plating condition 1 (Fig. 5.2b and Fig. 5.4b) could be explained on the basis of the deposition process taking place at the potential where the overall deposition process was significantly controlled by the mass transfer of the Ag ions to the sample surface. In the case of the Pd deposition, the N_2H_4 concentration (5.6 mM) was less than the stoichiometric requirement for the Pd ions concentration of 16 mM (Eqn. 5.3). The large overpotential associated with the Pd reduction and the low N_2H_4 to Pd ratio in the bath indicated less significance of the mass transfer of the Pd ions to the sample surface in the overall deposition process. Therefore, the Pd deposits showed better pore penetration than the Ag deposits (Fig. 5.2a and Fig. 5.4a). Based on the average Pd plating rate ($\sim 6 \mu\text{m}/\text{h}$ or $\sim 0.068 \text{ mM Pd}/\text{cm}^2\text{-h}$ based on the first 45 min of plating) and Ag plating rate ($\sim 1.2 \mu\text{m}/\text{h}$ or $\sim 0.012 \text{ mM Ag}/\text{cm}^2\text{-h}$ based on the first 45 min of plating), the N_2 gas evolved in the case of the Pd deposition ($\sim 0.034 \text{ mM N}_2/\text{cm}^2\text{-h}$ or $\sim 0.76 \text{ ml N}_2/\text{cm}^2\text{-h}$) was 12 times more than that evolved in the case of the Ag deposition ($0.003 \text{ mM N}_2/\text{cm}^2\text{-h}$ or $\sim 0.06 \text{ ml N}_2/\text{cm}^2\text{-h}$) (see Eqn. 5.3 and Eqn. 5.6). The relatively higher amount of gas evolved could provide better bath agitation [121-123] and further

reduce the effect of mass transfer step in the case of the Pd deposition. The amount of gas evolved was more in the case of Pd than Ag but did not hinder the penetration of Pd into the substrate pores (see Fig. 5.2a and Fig. 5.4b).

Though the Ag electroless deposits showed more deposition on the top than inside the pores of the substrate, the deposits were relatively uniform. In comparison to the electroless Pd or Ag deposits (Fig. 5.4a and Fig. 5.4b), the Pd-Ag electroless sequential deposits (Fig. 5.5) were highly non-uniform. The difference in the morphology of Pd-Ag sequential deposits was drastic from what could be expected from the projection based on the morphology of individual Pd and Ag electroless deposits (Fig. 5.4a and Fig. 5.4b) layered sequentially on each other. This unexpected morphology of the electroless Pd-Ag sequential deposits can be explained on the basis of the difference in the N_2H_4 oxidation catalytic activity of the Pd and Ag surface. An order of magnitude higher catalytic activity of the Pd surface meant that when Ag was deposited (at condition 1) on the Pd surface, the Ag deposition took place at a very high overpotential, i.e., more cathodic potential, under severe mass transfer limitation resulting in deposits showing highly non-uniform and dendritic growth with poor substrate pores penetration. Fig. 5.9 shows the schematic of the morphology evolution of Pd-Ag sequential deposits under the Ag plating condition 1. The first Pd deposit layer showed uniform growth all over the substrate surface and also showed good substrate pores penetration. The following Ag deposit layer deposited on top of the Pd deposit layer showed highly non-uniform and dendritic growth and covered the Pd deposits only at the top of the substrate without covering the Pd deposits inside the pores of the substrate because Ag deposited under severe mass transfer limitation on the Pd surface. The Pd deposits inside the substrate pore continued to provide the catalytic

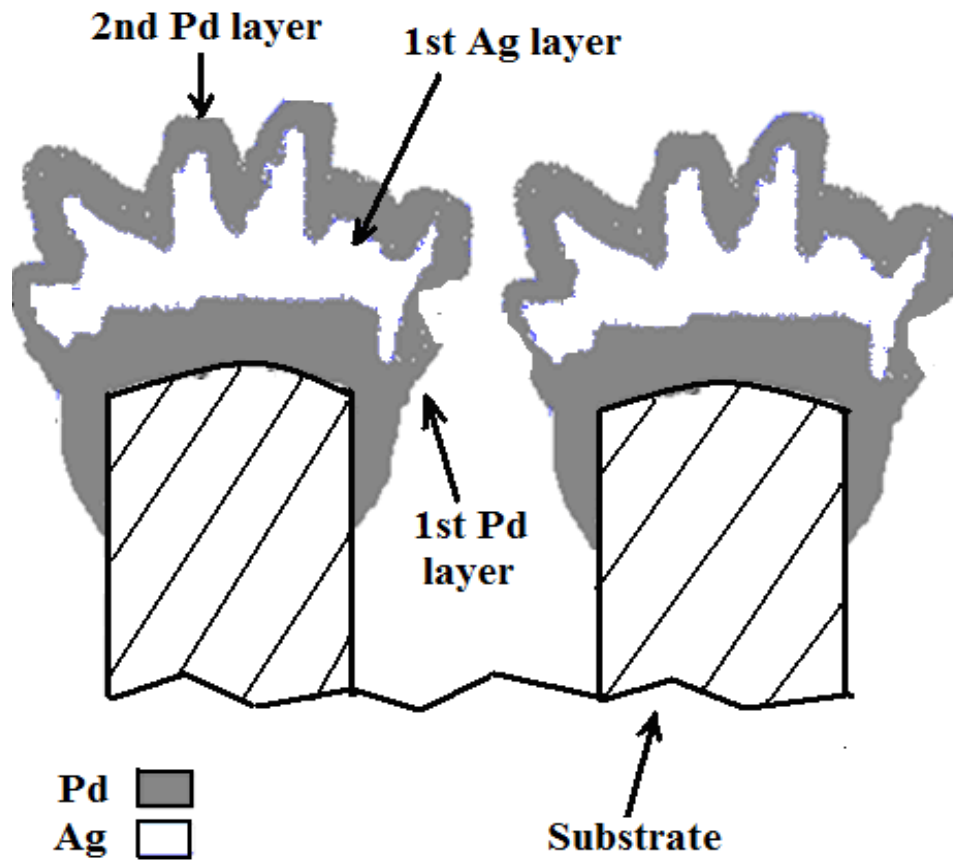


Fig. 5.9. Schematic of the Pd-Ag sequential deposits morphology evolution under Ag plating condition 1.

activity for the N_2H_4 oxidation and Ag continued to deposit under severe mass transfer limitation and at high overpotential with highly non-uniform morphology. The following second layer of Pd deposits on the first Ag deposit layer followed the contour of the Ag deposits beneath with overall morphology being non-uniform. Dimitirov et al. [124] also observed the non-uniform and dendritic growth in the case of Ag electrodeposits obtained from an $AgNO_3$ solution when the deposition overpotential exceeded a certain critical value. The critical value of the overpotential above which dendrites formed increased with increased Ag salt concentration in the solution.

The non-uniform growth of the Ag deposits was avoided by modifying the plating conditions to lower the deposition overpotential such as higher Ag to N_2H_4 ratio (condition 2 and 4) or stirring the substrate (condition 3). Fig. 5.10a, Fig. 5.10b and Fig. 5.10c show the effect of lower N_2H_4 to Ag ratio i.e., condition 2 (Fig. 5.10a) and condition 4 (Fig. 5.10b) and substrate rotation (condition 3) on the Ag deposition respectively. Compared to deposits shown in Fig. 5.2b, the Ag deposits shown in Fig. 5.10 demonstrated good pore penetration. The Ag plating condition 4 showed relatively lower deposition rate as compared to condition 2 and 3, therefore for the comparison of the deposits morphology obtained under condition 4 with the deposits morphology obtained under condition 2 and 3, the Ag plating for condition 4 was executed for relatively longer time to achieve the deposits in the similar thickness range as that of the deposits obtained under condition 2 and 3.

Ag deposited under the modified plating conditions on the Pd surface showed uniform growth as evident from the SEM images of the deposits shown in Fig. 5.11. Compared to Fig. 5.11a (condition 1), the deposits shown in Fig. 5.11b, Fig. 5.11c and Fig. 5.11d were compact and showed equal growth both in the perpendicular and the

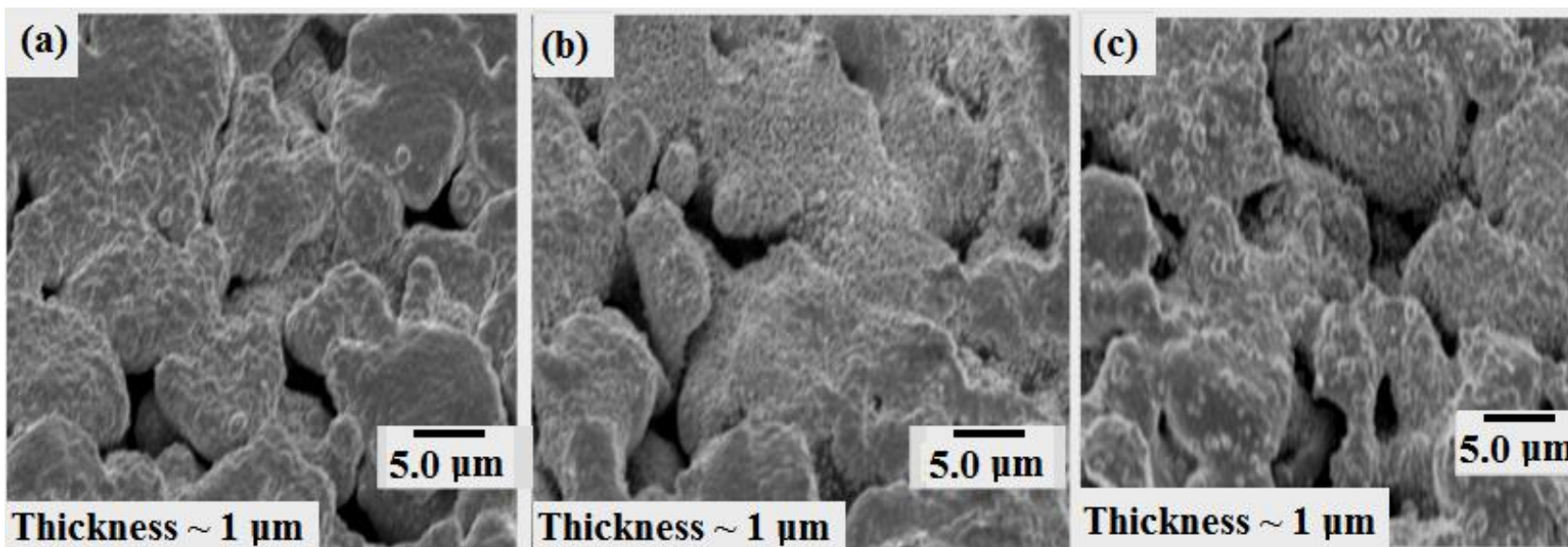


Fig. 5.10. Ag electroless deposition on PSS coupons surface (plating solution volume = 50 ml, sample surface area = 2 cm², bath temp. = 60 °C, pH = 11) (a) condition 2 and 45 min plating, (b) condition 3 and 45 min plating, (c) condition 4 and 150 min plating.

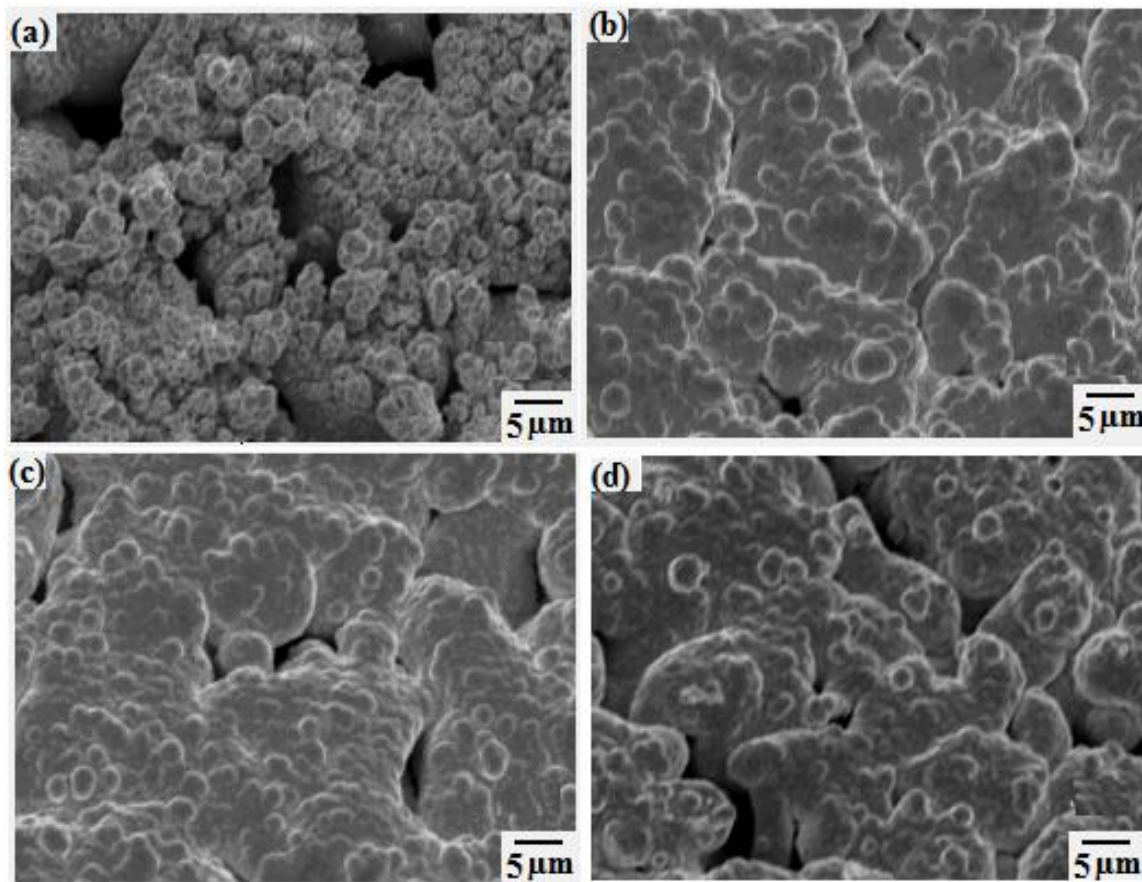


Fig. 5.11. Ag electroless plating on Pd (20 min plating) plated surface (plating solution volume = 50 ml, sample surface area = 2 cm², bath temp. = 60 °C, pH = 11)(a) condition 1, 90 min plating (b) condition 2, 90 min plating (c) condition 3, 90 min plating (d) condition 4, 270 min plating.

lateral direction to the substrate surface.

The X-ray diffraction patterns of the deposits are shown in Fig. 5.12. Compared to the sample shown in Fig. 5.11a, the X-ray diffraction patterns of samples of Fig. 5.11b, Fig. 5.11c and Fig. 5.11d (see Fig. 5.12b, Fig. 5.12c and Fig. 5.12d) showed a relatively higher fraction of Ag in the deposits. The Ag deposits obtained at condition 1 (Fig. 5.11a) showed poor coverage of the underneath layer of the Pd deposits, resulting in the lower ratio of Ag to Pd in the X-ray diffraction pattern.

The morphology of the Pd-Ag deposits continued to show the similar trend as shown in Fig. 5.11 with increase in the thickness of the sequentially obtained deposits. The SEM images of samples deposited with two alternate layers of Pd and Ag each are shown in Fig. 5.13. The deposits obtained at condition 1 (Fig. 5.13a) were highly non-uniform and dendritic, however, the deposits obtained at condition 2, 3 and 4 were relatively very compact and uniform (Fig. 5.13b, Fig. 5.13c and Fig. 5.13d). It was also observed during the sequential deposition that the Pd deposition after the Ag plating step showed an induction period of 80-90 minutes in the case of Ag plating conditions 2, 3 and 4. Conversely, in the case of the Ag plating condition 1, the Pd deposition started instantly without any induction period. This was due to the difference in morphology of the Ag deposits obtained at different plating conditions. In the case of plating conditions 2, 3 and 4, the Ag deposits covered the underneath Pd surface completely. The low catalytic activity of the Ag surface for the N_2H_4 oxidation and higher overpotential associated with the Pd reduction meant that the Pd deposition was controlled by the nucleation step in the beginning hence the long induction time. On the other hand, the Ag deposits in the case of condition 1 did not completely cover the underneath Pd surface. Therefore in the case of condition 1, the underneath Pd surface

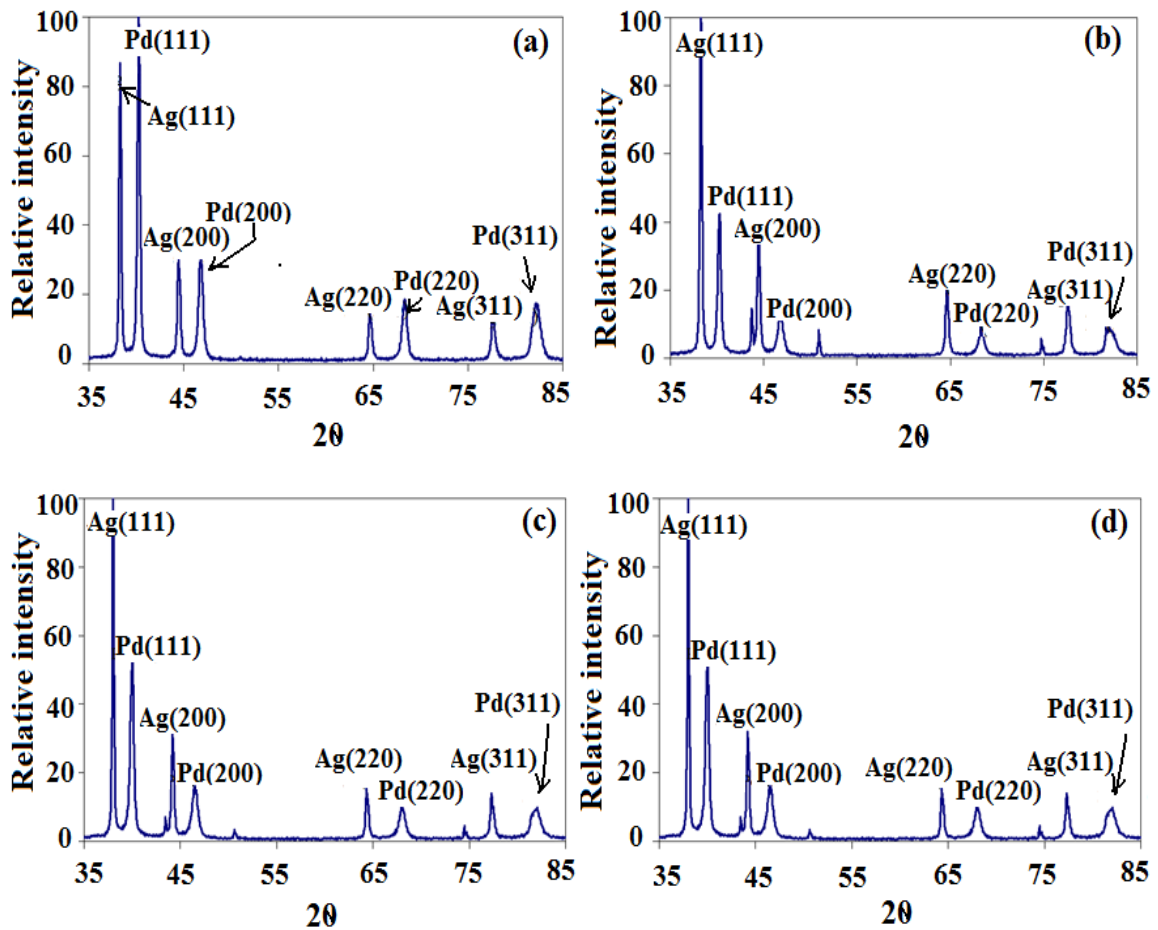


Fig. 5.12. X-ray diffraction pattern of samples with Ag plating on Pd (20 min) plated surface (a) condition 1 (90 min Ag plating) (b) condition 2 (90 min Ag plating) (c) condition 3 (90 min Ag plating) (d) condition 4 (270 min Ag plating).

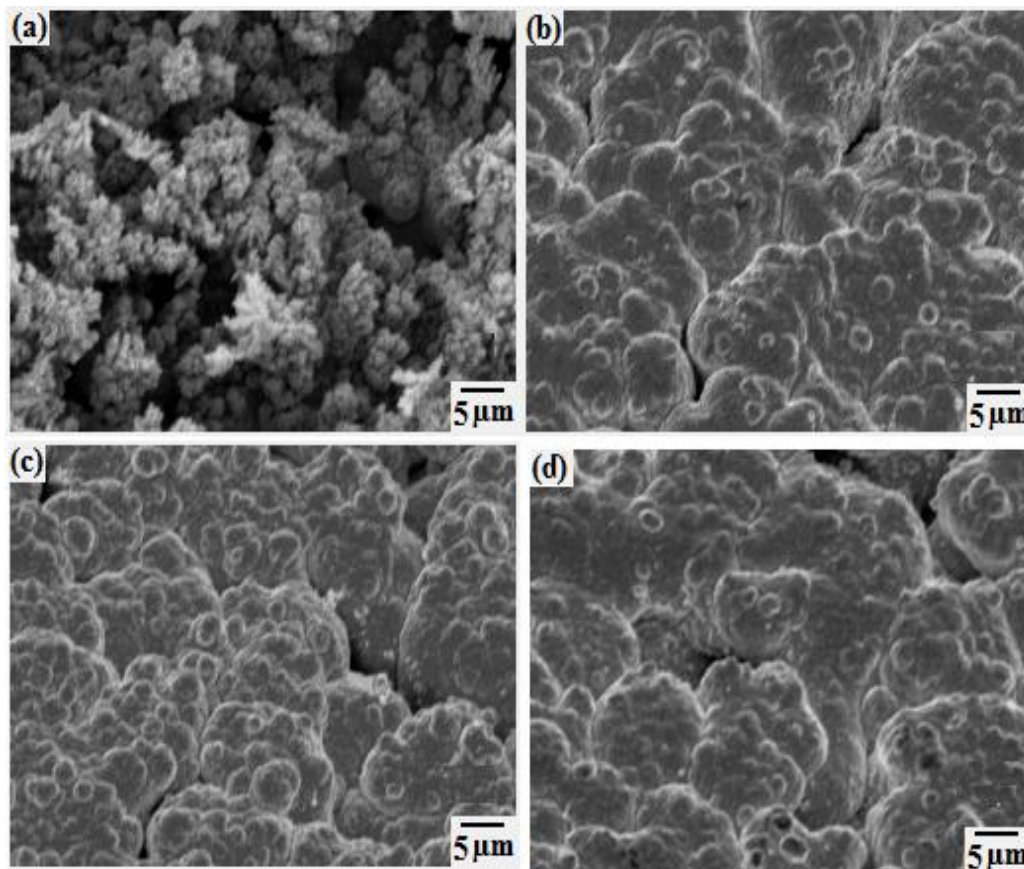


Fig. 5.13. Pd-Ag sequential deposits with two alternate layers of Pd (12 min) and Ag each a. Ag plating condition 1 (Ag plating time 45 min) b. Ag plating condition 2 (Ag plating time 45 min) c. plating condition 3 (Ag plating time 45 min) d. Ag plating condition 4 (Ag plating time 150 min)

also provided the catalytic activity for the oxidation of N_2H_4 causing Pd to deposit instantly. In the case of plating condition 1, Pd could be deposited instantly on the top of Ag without activating the Ag deposit layer with Pd nuclei, however, in order to keep the plating steps constant in all four cases (Ag plating conditions 1, 2, 3 and 4), all the samples shown in Fig. 5.13 were activated with the Pd nuclei after each plating step.

Fig. 5.14 shows the SEM image of the cross-section of the Pd-Ag sequential deposits (total thickness $\sim 9 \mu m$) obtained by plating four alternate layers of Pd ($\sim 1.5 \mu m$) and Ag ($\sim 0.7 \mu m$) each i.e., total 8 layers of Pd and Ag. Condition 2 was used for the Ag deposition. In comparison to the cross-section image of the sequential deposits obtained under Ag plating condition 1 (see Fig. 5.5), the sequential deposits obtained under condition 2 were uniform (see Fig. 5.14) and suitable to synthesize the H_2 selective Pd-Ag membrane.

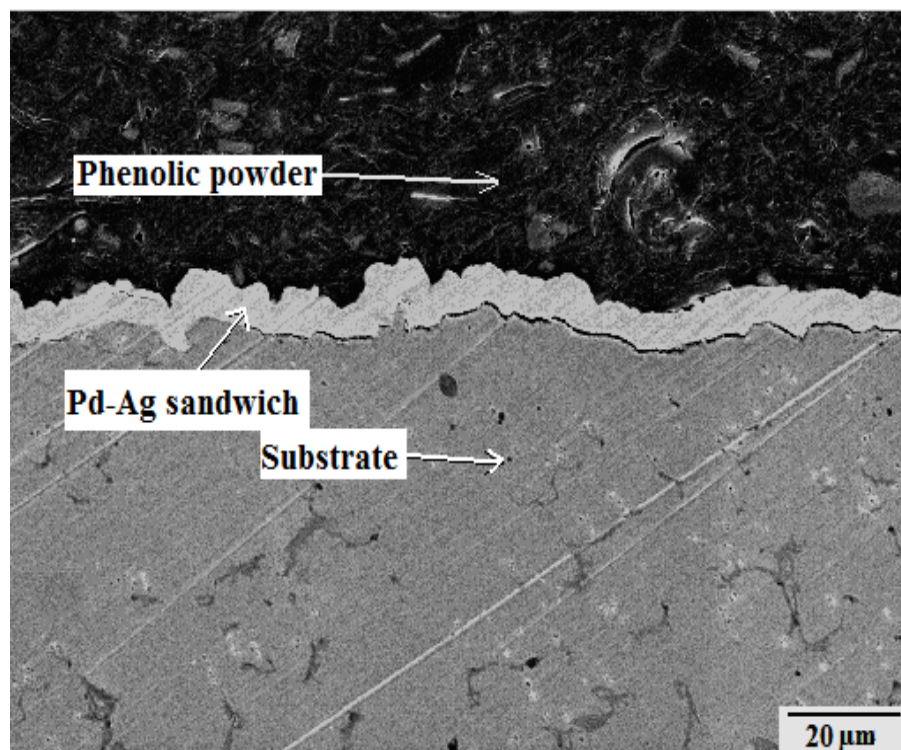


Fig. 5.14. The sequential Pd-Ag deposits obtained using the Ag plating condition 2 on the PSS surface. Total five sequences of Pd-Ag plating were used with Pd plating time = 15 min and Ag plating time = 20 min for each sequence. For each plating, the solution volume = 50 ml, bath temp. = 60 °C, and pH = 11 was maintained.

5.4. Conclusion

The effect of plating conditions on the Pd and Ag deposits morphology was demonstrated from the H₂ selective Pd-Ag membrane preparation point of view. It was shown by the LSV study that the overpotential at which the Ag deposition occurred had important effects on the deposits morphology. For the similar Ag plating conditions, the Ag deposition occurred at a higher overpotential on the Pd surface than on the Ag surface because of the higher catalytic activity of the Pd surface for the N₂H₄ oxidation than the Ag surface. The higher overpotential associated with the Pd deposition and higher Pd to N₂H₄ ratio (16 mM/5.6 mM) in the bath resulted in the overall Pd deposition not significantly affected by its diffusion in the solution and led to the uniform deposition on the substrate surface. However, the Ag plating conditions with lower Ag to N₂H₄ ratio (3 mM/5.6 mM) led to its deposition occurring at a high overpotential on the Pd surface. The Ag deposition at the higher overpotential on the Pd surface resulted in the overall Ag deposition severely controlled by its diffusion in the solution and leading to highly non-uniform Ag deposits. The non-uniform Ag deposits resulted in overall non-uniform and dendritic Pd-Ag sequential deposits unsuitable to synthesize thin and H₂ selective membrane. The Ag electroless bath conditions favoring the deposition at low overpotential such as substrate stirring or high Ag to N₂H₄ ratio (20/4, 3/1) ratio eliminated the dendritic morphology of the Ag deposits and produced uniform Pd-Ag sequential deposits, better suited for the synthesis of thin and H₂ selective membranes.

6. Pd-Ag co-deposition: Conventional NH₃ and EDTA based bath chemistry

6.1. Introduction

The NH₃+EDTA based bath described in Chapter 5 was further studied for the co-deposition or simultaneous deposition of Pd-Ag. The bath was used in all the studies reported in the literature for the synthesis of Pd-Ag membranes using the co-deposition method [8, 88-90], therefore is referred to as conventional co-deposition bath in this study. In all the literature studies for the co-deposition, the substrate used was non-metallic except by Shu et al. [88] who used porous stainless steel and the focus was on either investigating the effect of bath parameters on the plating rate or the overall composition of the deposits obtained. The other important deposit properties from the membrane synthesis point of view such as morphology and compositional homogeneity were not investigated and required further detailed study.

In Chapter 5, Section 5.3.3, it was shown that the deposition potentials of Pd and Ag, based on the calculation using the Nernst equation and the stability constants of the complexing reactions of Pd and Ag with NH₃, were approximately 200 mV apart and Ag acted as the noble metal. Due to the large overpotential associated with the Pd deposition, the actual deposition of Pd occurred at 650-700 mV lower potential than that of Ag. However, the simultaneous presence of the two metals in the case of the co-deposition bath could influence their deposition characteristics, thus, the results expected from the LSV study of the individual baths might not be directly applicable to the co-deposition case and a detailed investigation of the Pd-Ag co-deposition was

necessary. Also, other factors such as the bath components concentration, pH and temperature could significantly influence the deposition characteristics of Pd and Ag in the case of the co-deposition.

This chapter focused on studying the effect of the plating parameters using the conventional NH_3 +EDTA bath on the co-deposit properties such as the overall composition, compositional uniformity, crystalline structure, morphology and the overall plating rate. Furthermore, in order to better understand the relationship between the plating parameters and the deposit properties, the linear sweep voltammetry scans were also performed for the co-deposition bath on the stainless steel wire deposited with Pd or Ag layer as the substrate. The plating parameters investigated were bath components concentration (total metal, NH_3 and N_2H_4 concentration), pH, and temperature of the solution and bath agitation.

The complexing agents in the bath drastically influence the deposition potential of the metals [117, 125, 126]. Sillen and Martell [117] reported complexing reactions and stability constants for various complexing agents with several metals. For a particular metal, the stability constant value varied drastically from one complexing agent to another, therefore affected the deposition potential of the metal. According to Kiss [125] and Paunovic and Ohno [126], the complexing agents not only affected the deposition potentials by forming different metal-complexes but also affected the polarization characteristics of the metals by simply adsorbing on the metals surface. The effect of different complexing agents on the deposition potentials of Pd and Ag was therefore also investigated using the linear sweep voltammetry (LSV) technique. The combined NH_3 +EDTA complexing agents in the conventional co-deposition bath were separately investigated as the complexing agents. Other complexing agents studied were

glycine ($\text{H}_2\text{NCH}_2\text{COOH}$) and KCl . Other than the metal reduction, the important reaction was the oxidation of N_2H_4 (used in the conventional co-plating bath as the reducing agent) from the electroless deposition point of view. The presence of a complexing agent in the bath could also influence the oxidation characteristics [127] of N_2H_4 , therefore the suitability of N_2H_4 as the reducing agent in the presence of various complexing agents investigated was also studied using the LSV technique.

6.2. Experimental

6.2.1. Conventional NH_3 +EDTA bath and plating conditions

PSS coupons described in Chapter 3, Section 3.2.1 were used as the substrate. For the average plating rates, the deposition was performed for first 45 min and three coupons were used for each data point. In each case, the loading (the ratio of the plating solution volume to the plated area) of $25 \text{ cm}^3/\text{cm}^2$ ($50 \text{ cm}^3/2 \text{ cm}^2$) was maintained and no more than 15% of the metal in the bath was consumed. For the effect of the plating parameters on the morphology of the deposits, the deposition was carried out for 2 h and loading of $50 \text{ cm}^3/\text{cm}^2$ ($100 \text{ cm}^3/2 \text{ cm}^2$) was maintained in each case. The bath composition used is shown in Table 6.1 and the pH of the bath was adjusted by using HCl or NaOH . Prior to any plating experiment, the substrate was cleaned in the basic solution and sensitized and activated with the tin chloride and palladium chloride solution to initiate the deposition process as described in Chapter 3, Section 3.2.2.

6.2.2. Pd and Ag LSV polarization study

For the electrochemical study of the electroless co-plating baths, the linear sweep

Table 6.1. *NH₃ and EDTA based Pd-Ag co-deposition bath*

Bath component	Conc. range
Total metal conc.	1 - 13 mM
Pd(NH ₃) ₄ Cl ₂ .H ₂ O	0 - 10 mM
AgNO ₃	0 - 4 mM
NH ₃	1.5 - 9 M
Na ₂ EDTA	0.10 M
N ₂ H ₄	1.5 - 24 mM
pH	10 - 13
Temp. °C	40 - 80
Loading, cm ³ /cm ²	50 - 100

voltammetry (LSV) scans were obtained using the BAS electrochemical station described in Chapter 3, Section 3.5.2. The stainless steel wires (0.2 cm diameter and 1 cm length) covered with electroless plated Ag or Pd deposits (approximate thickness 2 μm) acted as the working electrode. For all the LSV scans in the case of the conventional bath ($\text{NH}_3 + \text{EDTA}$ bath) and co-plating baths with different complexing agents, the total metal concentration of 13 mM with the Ag concentration = 3 mM was maintained in the bath. The bath composition with different complexing agents is shown in Table 6.2. The LSV scans were obtained at the rate of 10 mV/s with sensitivity of 1 mA/V. All the scans for the Pd and Ag baths started from the potential near to the rest potential of the baths towards the cathodic direction. The solution volume of 50 ml and temperature of 60 $^\circ\text{C}$ was maintained for all the scans.

For the N_2H_4 polarization scans in the presence of different complexing agents, the N_2H_4 concentration of 3 mM was used in all the baths. In the case of the N_2H_4 polarization scans, the scans were again initiated from the potential near to the rest potential of the baths but towards the anodic direction.

6.2.3. Membrane synthesis

In order to compare the Pd-Ag co-deposits based on the conventional $\text{NH}_3 + \text{EDTA}$ bath with pure Pd deposits for the synthesis of a thin and H_2 selective membrane, two membranes, R-01 (pure Pd plated membrane) and R-05 (Pd-Ag co-deposited membrane) supported on PSS tubes, as described in Chapter 3 Section 3.2.1, were synthesized. Before the deposition step, the tubes were oxidized at 500 $^\circ\text{C}$ (10 h) in air.

R-01 was synthesized using the Pd plating conditions described in Chapter 5, Section

Table 6.2. Complexing agents and their bath composition

Bath components	NH₃ bath	EDTA bath	glycine bath	KCl bath
PdCl ₂ (mM)	0-10	0-10	0-10	0-10
AgNO ₃ (mM)	0-3	0-3	0-3	0-3
KCl (M)	-	-	1.5	4
NH ₄ OH (M)	3	-	-	-
Na ₂ EDTA (M)	-	0.18	-	-
H ₂ NCH ₂ COOH (M)	-	-	0.8	-
H ₃ BO ₃ (M)	-	-	-	0.04
pH	11	11	11	11
Temp. °C	60	60	60	60

5.2.1 i.e., Pd/N₂H₄ ratio = 16 mM/5.6 mM. For the synthesis of R-05, the co-deposition bath with a total metal concentration of 4 mM and 15 at% Ag was used. The co-deposits obtained using the conventional bath were dendritic and non-uniform (showing more growth in the perpendicular direction to the substrate surface). Therefore in the case of R-05, prior to each He flux data point taken during the synthesis, the membrane was dried (80 °C) overnight and polished (to remove the perpendicular portion of the deposits, making the deposits to grow more in the lateral direction) very gently with 800 grit size SiC paper. Note: The procedure of polishing with SiC paper during the plating was performed only for R-05 and R-12 (see Chapter-8, Section 8.3.3 for more details about R-12) in this study.

6.2.4. Deposit composition and crystalline structure

The composition and morphology of the deposits were studied using scanning electron microscope (SEM) equipped with EDX. The examination of the crystalline structure of the deposits was performed using Rikagu X-ray diffractometer.

6.3. Results and discussion

6.3.1. Pd and Ag polarization characteristics using conventional NH₃+EDTA bath

Fig. 6.1a shows the LSV polarization characteristics of the Pd-Ag co-deposition bath on the Pd surface. The solid line and dotted lines show the scans obtained with and without Pd and Ag presence in the bath respectively. As can be seen from the figure, the solid line showed two peaks, one at the potential of -40 to -50 mV and second at the

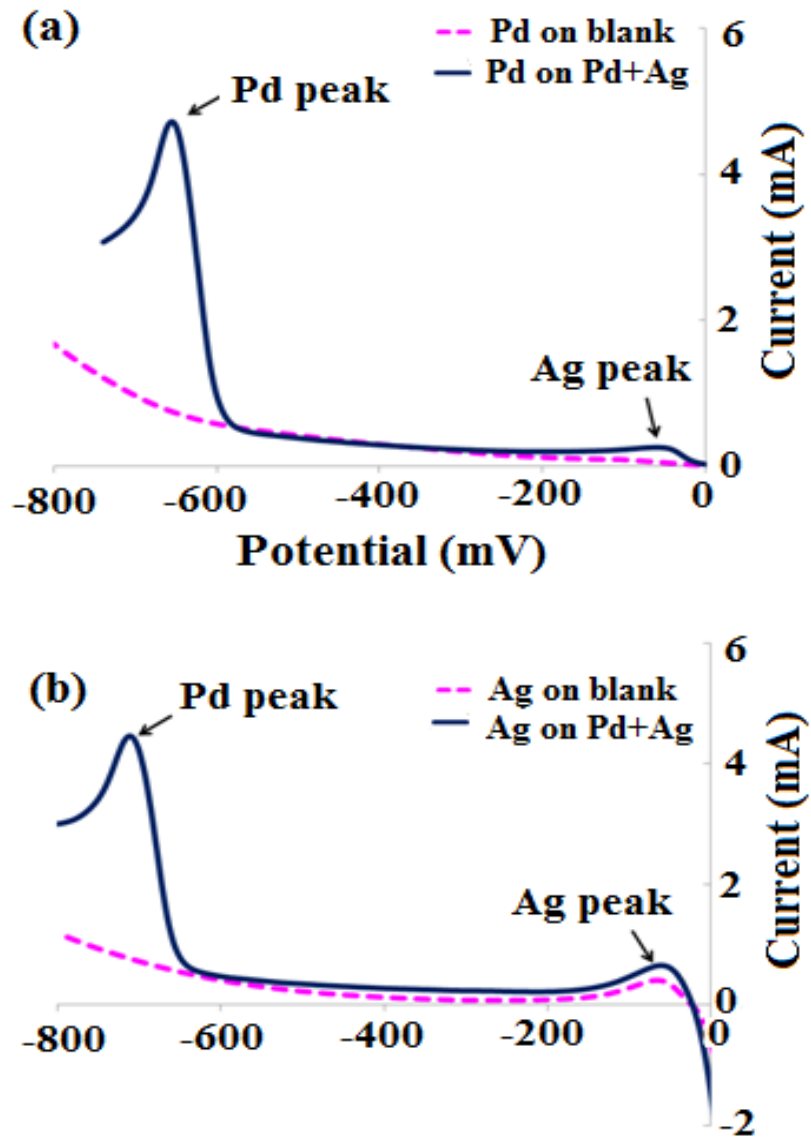


Fig. 6.1. Pd and Ag polarization characteristics of the co-deposition bath (a) on the Pd surface (b) on the Ag surface

potential of -650 to -700 mV. The first peak corresponded to the deposition of Ag and was very close to the deposition peak (-10 mV) of Ag obtained from the Ag bath on the Pd surface (see Chapter 5, Section 5.3.3). At the potential of the first peak, the color of the working electrode changed from metallic grey to white indicating the initiation of the Ag deposition. As the electrode potential continued to decrease, the color of the electrode changed gradually from white towards light dark until the appearance of second peak when the electrode color abruptly changed to dark black. The second peak corresponded to the deposition of Pd and the deposition potential was close to the deposition potential of the Pd deposition observed for the Pd bath (see Chapter 5, Section 5.3.3). At the potential of the second peak, the working electrode surface color changed from light black to dark black indicating the initiation of the Pd deposition. For the LSV scan obtained for the blank solution, i.e. in the absence of Pd and Ag in the solution, no such changes in the color of the working electrode were observed. The simultaneous presence of Pd and Ag in the co-deposition bath did not significantly alter their polarization characteristics on the Pd surface as compared to the single metal polarization characteristics (see Chapter 5, Section 5.3.3). Pd in the bath acted as less noble metal and its deposition occurred at the potential 600 to 650 mV more cathodic than the Ag deposition. The large difference in the deposition potential of Pd and Ag suggested that for the co-deposition of Pd and Ag, the electrode potential of -600 to -650 mV was required, Ag had to be deposited at very large overpotential with its (Ag) deposition severely controlled by its diffusion in the solution.

The polarization characteristics of Pd and Ag on the Ag surface (Fig. 6.1b) were very similar to the one obtained on the Pd surface (Fig. 6.1a). The dotted lines in Fig. 6.1b show scan obtained from the blank solution (i.e., without the Pd and Ag presence in the

bath) and the solid line shows the scan obtained with the Pd and Ag presence in the bath. Again, the solid line showed two peaks in comparison to the dotted line. The first peak at the potential of -40 to -50 mV corresponded to the Ag deposition and no color change was observed at this potential for the Ag surface. The second peak observed at potential of -650 to -700 mV corresponded to the Pd deposition and was very close to the deposition potential of Pd on Ag surface from Pd bath (see Chapter 5, section 5.3.3). At the starting of the second peak during the LSV scan, the light black surface of the working electrode changed to dark black indicating the Pd deposition. Therefore, the nature of the surface showed no significant differences for the simultaneous deposition of Pd and Ag and also the deposition characteristics of Pd and Ag for the co-deposition bath were very similar to the Pd and Ag deposition characteristics from the single metal baths.

6.3.2. Effect of the total metal concentration (conventional bath)

From the XRD pattern of the deposits shown in Fig. 6.2, it is clear that the Pd-Ag deposits obtained were bimetallic, i.e., the deposits were a mixture of individual particles of Pd and Ag metal. Therefore these deposits required further annealing step to make the Pd-Ag alloy. Under all the plating conditions used in this study, the deposits obtained were bimetallic.

Fig. 6.3 shows the effect of the total metal concentration on the average total metal plating rate and the concentration of Ag in the deposits. The average total metal plating rate showed the increasing trend with the increase in the total metal concentration in the bath. The increase in the plating rate could be explained simply on the basis of law of mass action. The metal ions were reactants in the overall deposition reaction (see

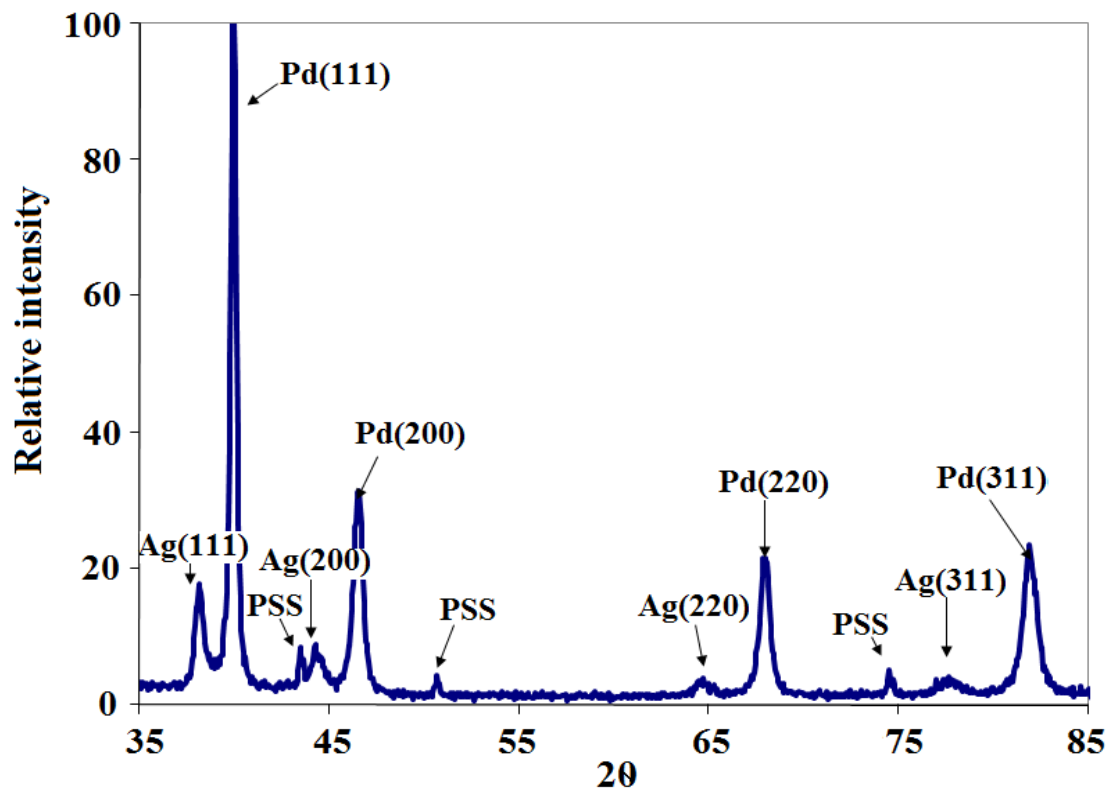


Fig. 6.2. XRD pattern of Pd-Ag co-deposits. Bath composition: total metal conc. = 4 mM, Ag (at%) = 10, N_2H_4 = 6 mM, NH_3 = 3 M, Na_2EDTA = 0.1 M, pH = 11 and Temp. = 60 °C.

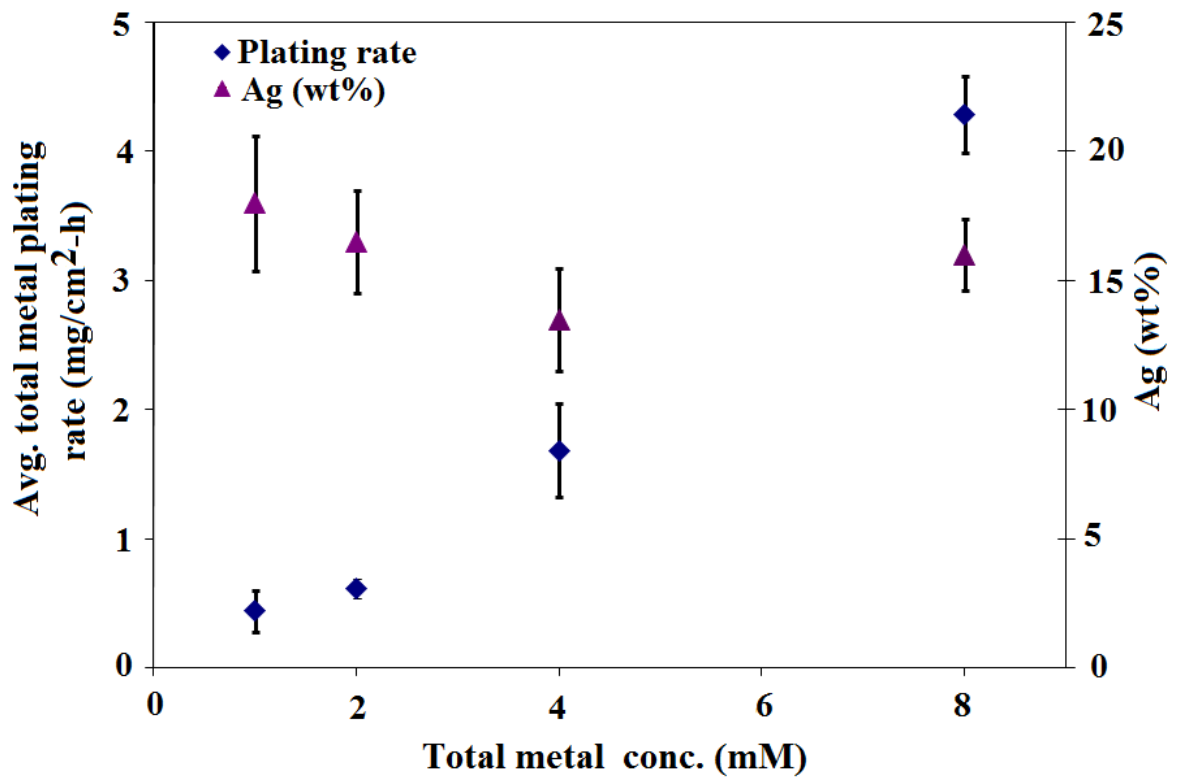


Fig. 6.3. Effect of the total metal concentration on the average total plating rate and the composition of the deposit. Bath composition: Ag (at%) = 10, N_2H_4 = 5.6 mM, NH_3 = 3 M, Na_2EDTA = 0.1 M, pH = 11 and Temp. = 60 °C.

Chapter 5, Section 5.3.3), therefore, the increase in the deposition rate was expected to be due to the increase in the total metal concentration. It can also be observed from Fig. 6.3 that the plating rate did not show linear increase with the increase in the concentration but at higher concentrations, the rate was higher than that expected from the linear extrapolation of the lower concentration. The possible reason for the non-linear increase in the deposition rate was that the overall deposition reaction involved formation of N_2 gas at the substrate surface. The increase in the plating rate due to the increased total metal concentration was accompanied by a larger N_2 gas formation, further enhancing the diffusion of reacting species (metal ions and N_2H_4) in the bath [122] thereby, resulting in the non-linear increase in the overall deposition rate.

The wt% of Ag in the deposits (see Fig. 6.3) did not show any notable trend with the increase in the total metal concentration. The average concentration of Ag in the deposits ranged between 13-18 wt%. The ratio between the Pd and Ag (10 at% Ag) in the bath was constant as the total metal concentration varied between 1-8 mM in the bath, therefore little variation in the deposits composition was expected as a result of total metal concentration change in the bath.

Fig. 6.4 shows the effect of the total metal concentration on the morphology of the deposits after 2 h of plating in each case. Due to the low deposition rate for the concentrations of 1 and 2 mM, the deposits obtained in 2 h were not thick enough to clearly indicate the characteristics of the deposits morphology (particularly for 1 mM concentration). However, for the concentration of 4 mM and 8 mM, it can be observed that the deposits were porous and dendritic showing preferential growth in the perpendicular direction to the substrate surface. For the concentration of 8 and 4 mM, the deposits morphology obtained for the first 45 min was very similar to that obtained

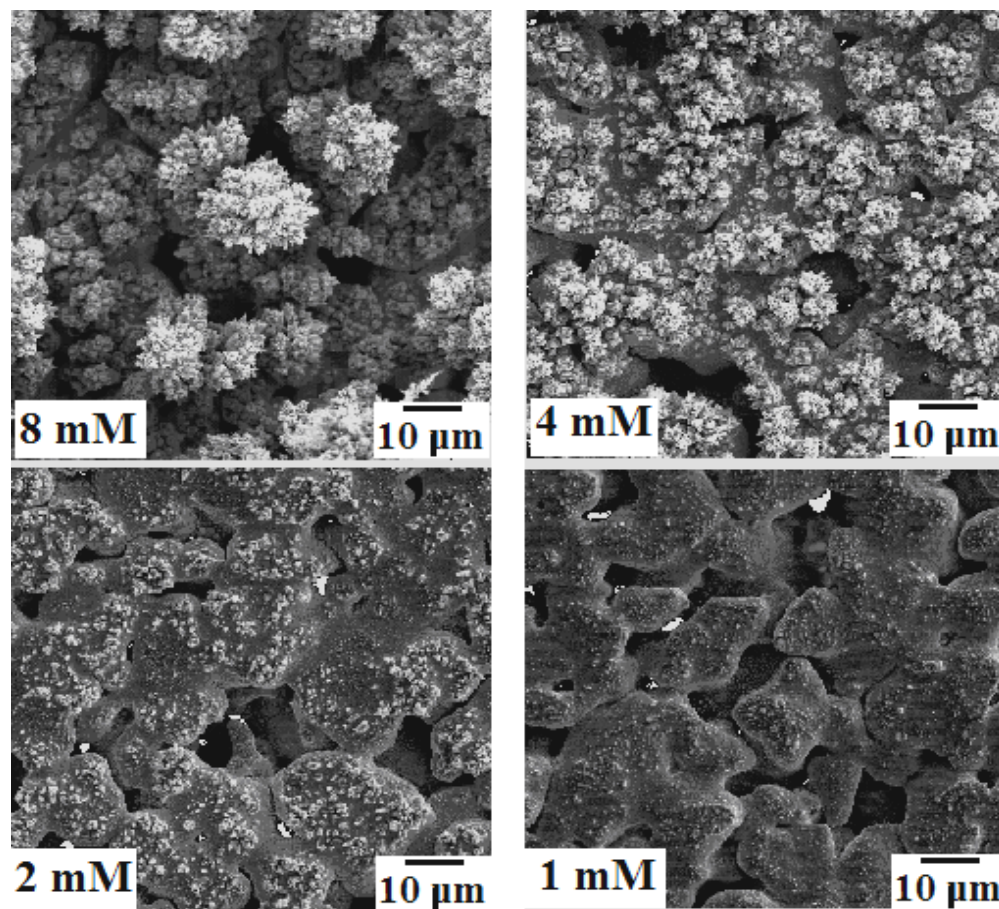
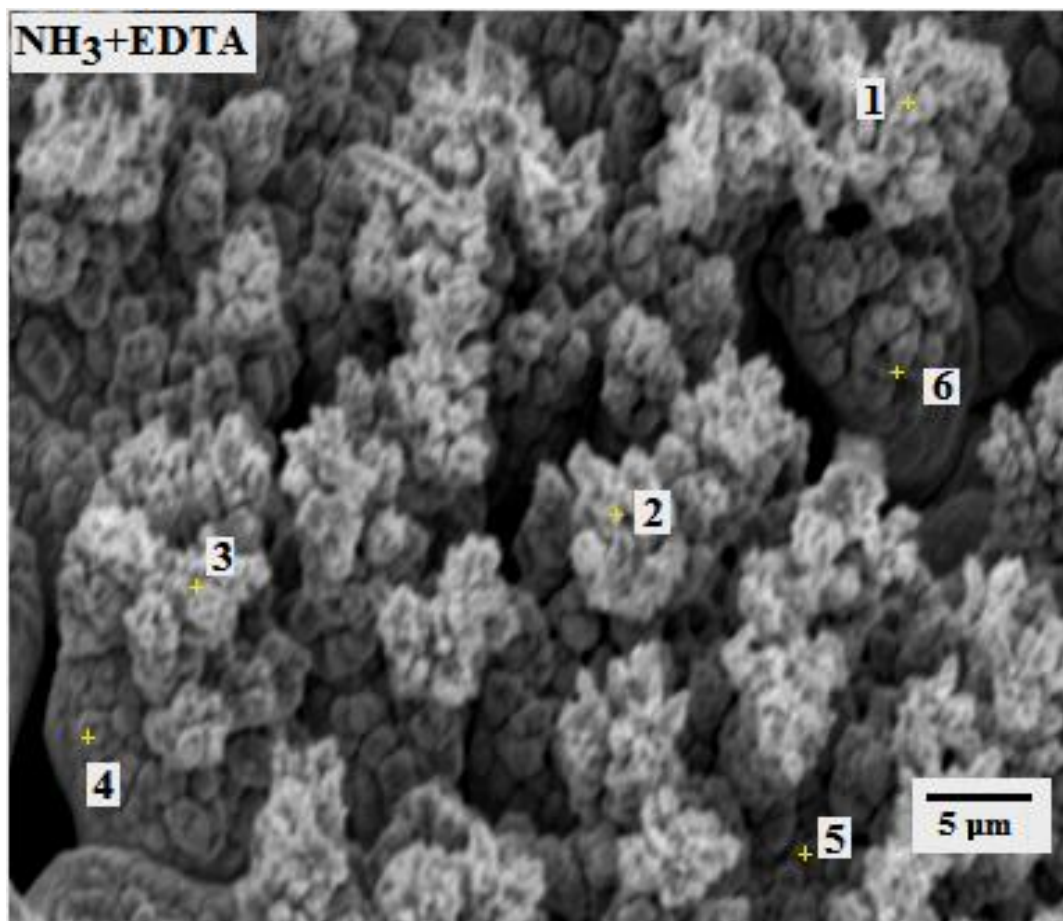


Fig. 6.4. Effect of the total metal concentration on the morphology of the Pd-Ag deposit. Bath composition: Ag (at%) = 10, N_2H_4 = 5.6 mM, NH_3 = 3 M, Na_2EDTA = 0.1 M, pH = 11 and Temp. = 60 °C.

for 2 and 1 mM respectively for the 2 h plating time, indicating that with further thickness increase, the morphology of deposits obtained at 2 and 1 mM concentration would appear similar to the morphology of the deposits obtained at 8 and 4 mM concentration. The deposits obtained at all concentrations appeared dark black and showed very poor adhesion, more for the deposits obtained at 4 and 8 mM (2 h plating time) concentration. The deposits obtained could easily be removed by gentle thumb rubbing even more in the case of 4 and 8 mM concentration. According to Calusaru [128], there are regions of overpotential for every metal in which compact, dendritic and powder deposits are obtained. When the overpotential exceeds a certain value called critical overpotential value [128], the deposits obtained are dendritic and powder in nature. As can be seen in the Fig. 6.1, there existed a large potential difference in the deposition of Pd and Ag. The Ag deposition occurred at large overpotential and severe mass transfer controlled conditions, leading to dendritic and powder deposits with low adhesion.

Fig. 6.5 shows the typical distribution of Pd and Ag in the deposits obtained by the EDX spot scan analysis. Top points (points 1, 2 and 3) in the figure represent deposits near to the solution side (farther away from the substrate) and bottom points (points 4, 5 and 6) represent deposits near the substrate and farther away from the solution side. The top points showed relatively higher concentration of Ag in comparison to the bottom points. The deposits obtained showing higher Ag concentration towards the solution side and lower Ag concentration farther away from the solution side was true for all the plating conditions investigated. The inhomogeneous distribution of Ag (concentrated more towards the solution side) was due to its deposition occurring at severely mass transfer controlled conditions from the co-plating bath (see Fig. 6.1).



Tag	Pd (wt%)	Ag (wt%)	Tag	Pd (wt%)	Ag (wt%)
1	58	42	4	95	5
2	80	20	5	90	10
3	63	37	6	98	2

Fig. 6.5. Typical Pd and Ag distribution obtained in the deposits. Bath composition: total metal conc. = 4 mM, Ag (at%) = 10, N_2H_4 = 5.6 mM, NH_3 = 3 M, Na_2EDTA = 0.1 M, pH = 11 and Temp. = 60 °C. ((Note: the points with high Ag wt% are the points in the deposits more closure to the solution side and the points with low Ag wt% are points away from the solution side and more near to the substrate side)

6.3.3. Effect of N_2H_4 concentration (conventional bath)

The increasing concentration of N_2H_4 in the solution increased the average total metal plating rate as shown in Fig. 6.6 until the concentration of N_2H_4 reached 6 mM. After 6 mM of N_2H_4 concentration, the plating rate reached a plateau. The increase in the concentration of N_2H_4 could lead to the decrease in the overall potential at which the Pd and Ag deposition occurred. After the concentration of N_2H_4 exceeded the amount required stoichiometrically (approximately 2 mM) for 4 mM concentration of metals in the solution, the overall deposition potential could reach a value where the overall Pd deposition was also limited more and more by the diffusion of its ions in the solution (note: during the co-deposition, the Ag deposition always occurred under the conditions where the diffusion of its ions in the solution was the rate limiting step). Therefore, after 6 mM, further increase in the N_2H_4 concentration could lead to a decrease in the electrode potential at which the electroless plating occurred but due to the diffusion of both Pd and Ag in the solution controlling the overall deposition process, no increase in the deposition rate occurred with the further increase in the N_2H_4 concentration in the solution. The increasing concentration of N_2H_4 in the solution decreased the wt% of Ag in the deposits (Fig. 6.6). The increase in the concentration of N_2H_4 up to 6 mM lowered the Ag wt% in the deposit. Again when the N_2H_4 concentration in the bath was less than the stoichiometric requirement (i.e. less than 2 mM), the Ag deposition was controlled by its diffusion in the solution more than the Pd deposition but with the increased concentration of N_2H_4 , the Pd deposition also started being controlled more and more by its diffusion in the solution. Therefore, the Pd deposition rate increased relatively more than the Ag deposition rate (which was already controlled by Ag diffusion in the solution), resulting in the increase in the Pd or decrease in the Ag

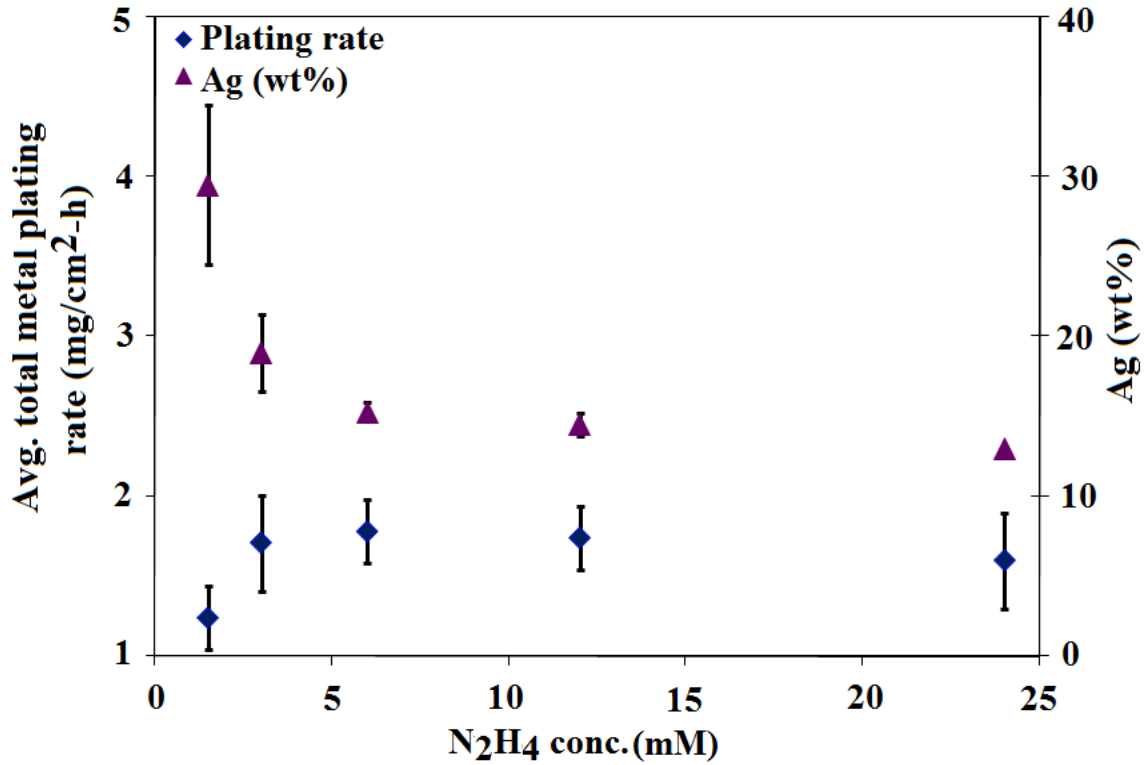


Fig. 6.6. Effect of the N_2H_4 concentration on the average plating rate and deposit composition. Bath composition: Total metal conc. = 4 mM (10 at% Ag), NH_3 = 3 M, Na_2EDTA = 0.1 M, pH = 11 and Temp. = 60 °C.

content in the deposits. Above 6 mM concentration of N_2H_4 in the bath, both Pd and Ag deposition process was limited by their respective mass transfer, therefore showing little change in their ratio in the deposits as well as the average total metal plating rate.

The morphology of the deposits (Fig. 6.7) obtained at different concentrations of N_2H_4 did not show any noticeable difference. The deposits were again porous, dendritic and dark with poor adhesion with the substrate surface.

6.3.4. Effect of NH_3 (conventional bath)

Fig. 6.8 shows the effect of the NH_3 concentration on the average plating rates and the deposits composition. It can be observed from the figure that the average total metal plating rates and the Ag wt% in the deposits showed increasing trend with the increase in the NH_3 concentration. The increase in the plating rates and Ag wt% could be due to the slight agitation of plating solution caused by the release of a large amount of NH_3 gas bubbles that occurred at higher concentration of NH_3 (6 and 9 M). Due to the limited solubility of NH_3 at 60 °C, at the concentration of 6 and 9 M, the NH_3 gas bubbles were observed to have formed over the entire solution and provided some agitation in the solution. The agitation in the solution increased the average total metal plating rate by enhancing the diffusion of metal ions in the solution. Since the deposition of Ag was relatively more limited by its mass transfer in the solution, any agitation in the bath would lead to its increased content in the deposits.

Fig. 6.9 shows the SEM images of the deposits obtained at different concentrations of NH_3 . The deposits showed a slight variation in morphology at various concentrations of NH_3 and the overall trend was more growth in the perpendicular direction to the

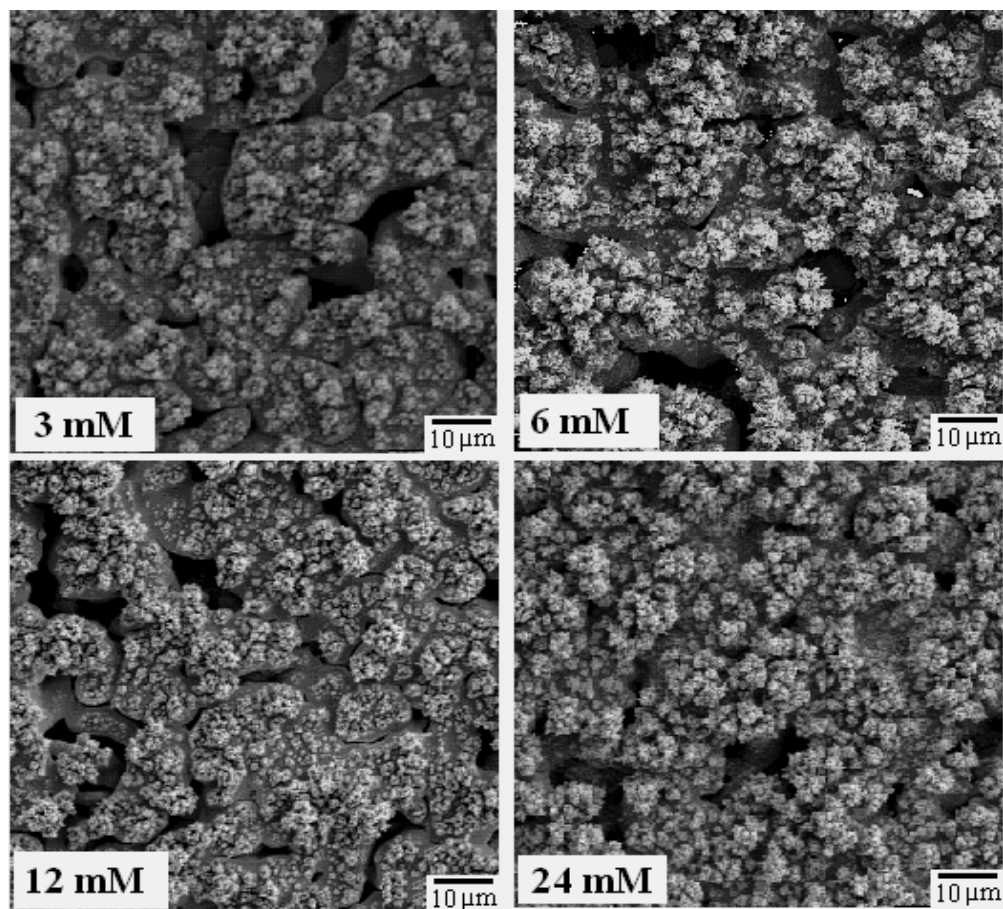


Fig. 6.7. Effect of the N_2H_4 concentration on the morphology of the deposit. Bath composition: Total metal conc. = 4 mM (10 at% Ag), $NH_3 = 3 M$, $Na_2EDTA = 0.1 M$, pH = 11 and Temp. = 60 °C.

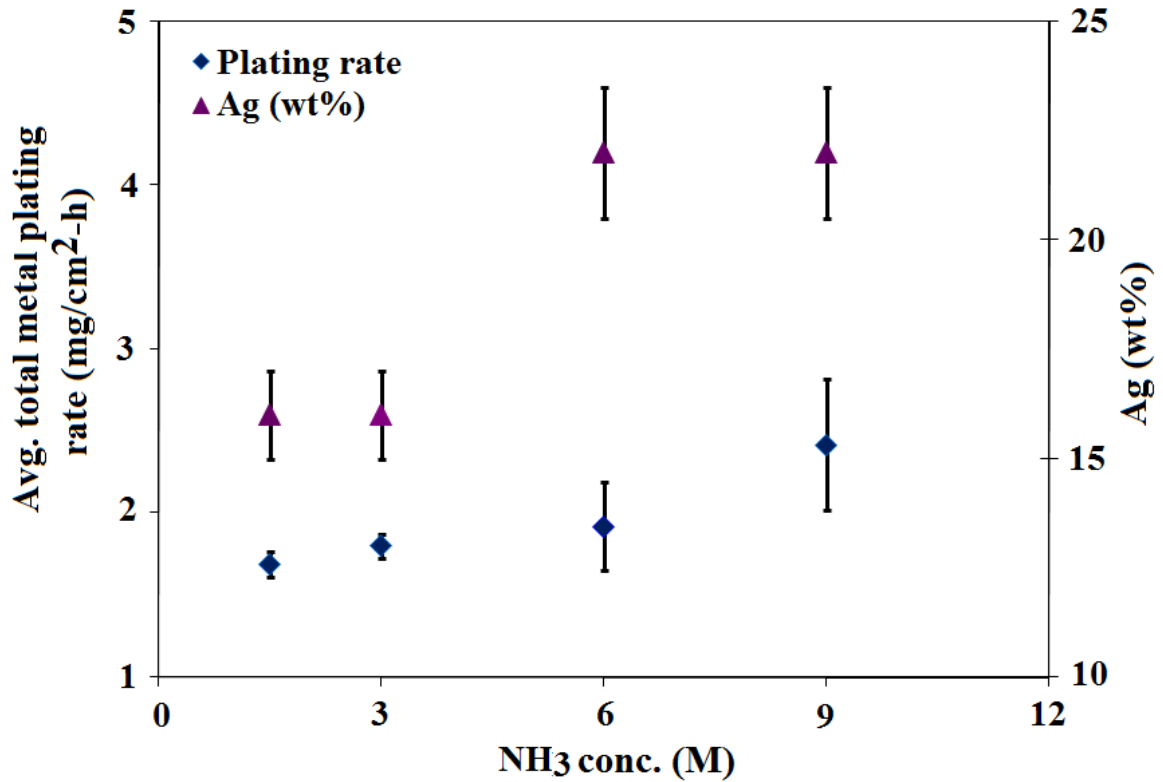


Fig. 6.8. Effect of the NH_3 concentration on the average plating rates and deposit composition. Bath composition: Total metal conc. = 4 mM (10 at% Ag), N_2H_4 = 5.6 mM, Na_2EDTA = 0.1 M, pH = 11 and Temp. = 60 °C.

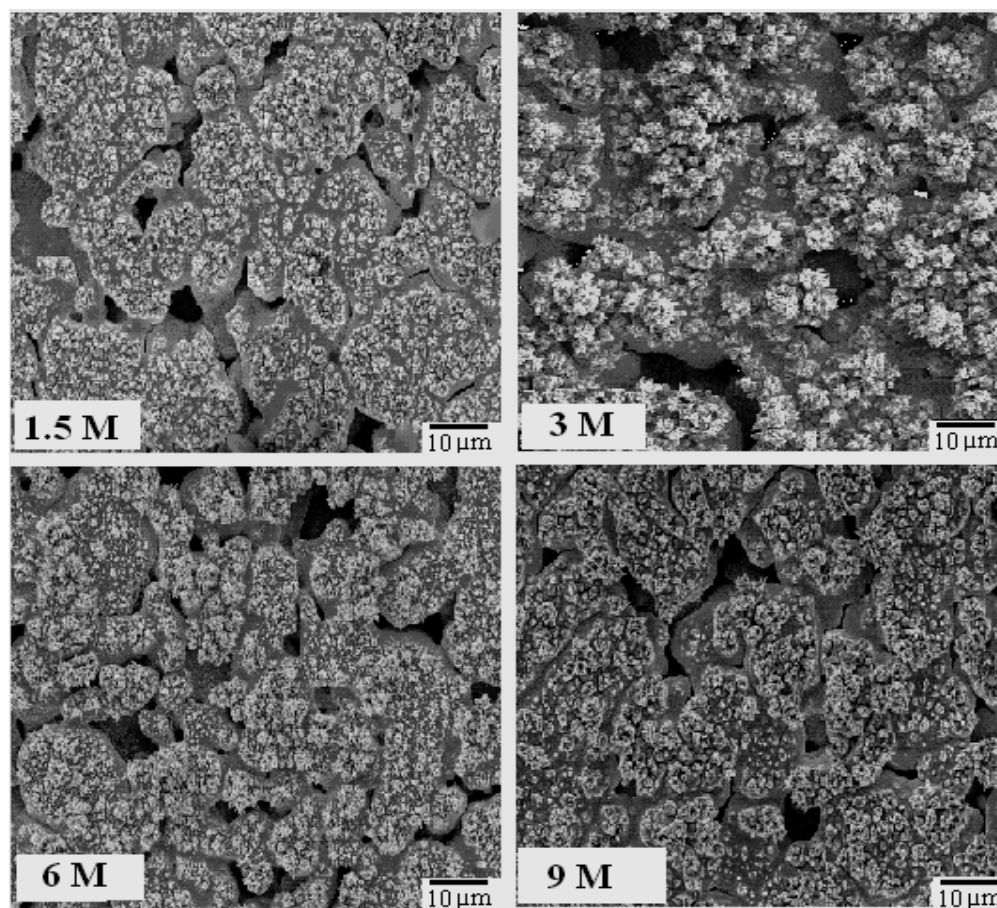


Fig. 6.9. Effect of the NH_3 concentration on morphology of the deposits. Bath composition: Total metal conc. = 4 mM (10 at% Ag), N_2H_4 = 5.6 mM, Na_2EDTA = 0.1 M, pH = 11 and Temp. = 60 °C.

substrate surface. Also the adhesion of the deposits was very poor (see Section 6.3.2 for the cause leading to the poor adhesion).

6.3.5. Effect of pH (conventional bath)

The overall oxidation reaction of N_2H_4 consisted of reacting with OH^- ions and the formation of N_2 and H_2O as products of the reaction (see Chapter 5, Section 5.3.3). Therefore, the increase in the pH resulted in the increase of concentration of the reacting species (OH^- in this case) and caused the overall oxidation rate of N_2H_4 to increase which could result in the lowering of the electrode potential at which the electroless deposition occurred. The decrease in the electroless deposition potential caused the observed increase in the average total metal plating rate (see Fig. 6.10). As can be observed from Fig. 6.10, the pH increase resulted in an increase in the plating rate until pH of 12 and then showed decline at pH of 13. The drop in the plating rate after pH of 12 was due to the bath instability. The bath after pH of 12 showed the precipitation of the metal ions in the bulk of the solution, resulting in the depletion of the metal ions in the solution and affecting the plating rates adversely.

The pH increase affected negatively the Ag wt% in the deposit (Fig. 6.10). The increase in the pH lowered the electroless deposition potential which favored the deposition of less noble metal Pd in the plating solution and the trend was clearly seen when pH increased from 10 to 13.

The increasing pH showed improvement in the morphology of the deposits (Fig. 6.11). The deposits became less porous and dendritic as the pH increased. The deposits obtained at pH of 12 and 13 were more homogeneous than obtained at pH of 10 and 11.

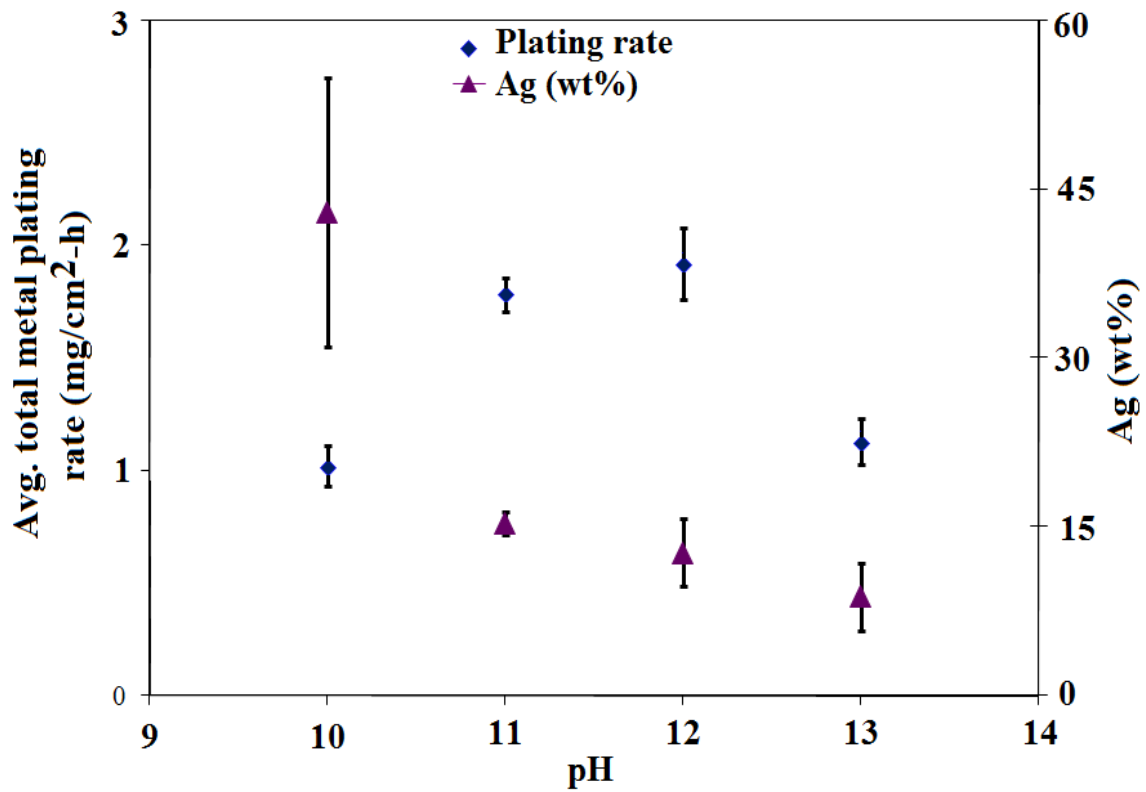


Fig. 6.10. Effect of pH on the average plating rate and deposit composition. Bath composition: Total metal conc. = 4 mM (10 at% Ag), $N_2H_4 = 5.6$ mM, $NH_3 = 3$ M, $Na_2EDTA = 0.1$ M and Temp. = 60 °C.

The plating conditions with pH of 13 were not suitable for the membrane synthesis because of the unstable nature of the bath. Therefore, the plating conditions with pH of 12 were optimum from the morphological point of view. However, the deposits at pH 12 still showed more tendencies to grow in the vertical direction to the substrate surface and the deposits adhesion with the substrate surface was poor (see Section 6.3.2 for the cause leading to the poor adhesion).

6.3.6. Temperature effect (conventional bath)

The increase in the temperature increased the plating rates (Fig. 6.12). The plating rate showed noticeable sensitivity towards temperature. The average total metal plating rate increased with the increase in the temperature between 40 and 80 °C. The increase in the temperature could enhance the diffusion of the reactants and the products of the deposition reaction. The N_2H_4 oxidation and metal ions reduction reactions were also expected to increase with the temperature increase, therefore the increase in the average total metal plating rate with the temperature increase was logical. The increase in the Pd content in the deposits was observed when the temperature changed from 40 to 80 °C. The increase in the Pd content could be explained on the basis of large overpotential associated with the Pd deposition, i.e., large energy barrier associated with the Pd reduction, showing high sensitivity towards the temperature. Also, the increase in the oxidation rate of N_2H_4 with the temperature increase [74] could lower the electroless plating potential which favored the deposition of less noble metal Pd in the bath. As can be seen from Fig. 6.12, the increasing temperature decreased the Ag wt% in the deposits with the value of approximately 20 (at 40 °C) to 12 wt% (at 80 °C).

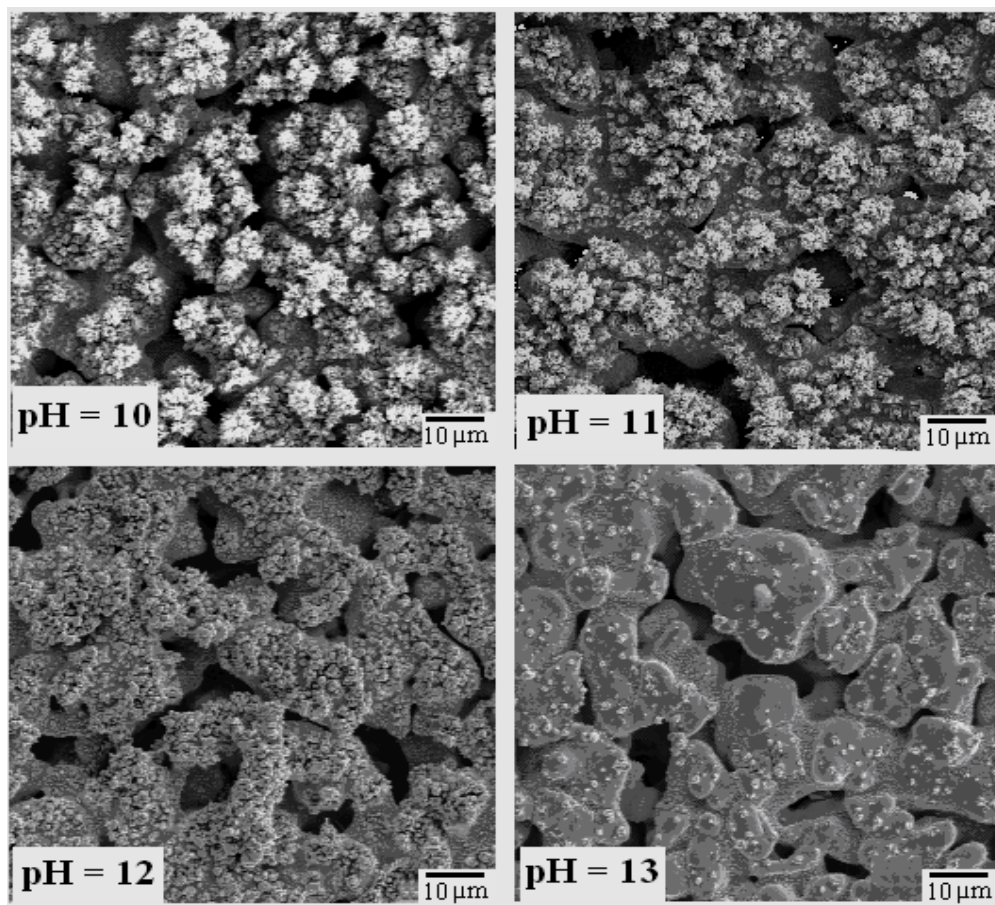


Fig. 6.11. Effect of pH on the morphology of the deposit. Bath composition; Total metal conc. = 4mM (10 at% Ag), N_2H_4 = 5.6 mM, NH_3 = 3 M, Na_2EDTA = 0.1 M and Temp. = 60°C.

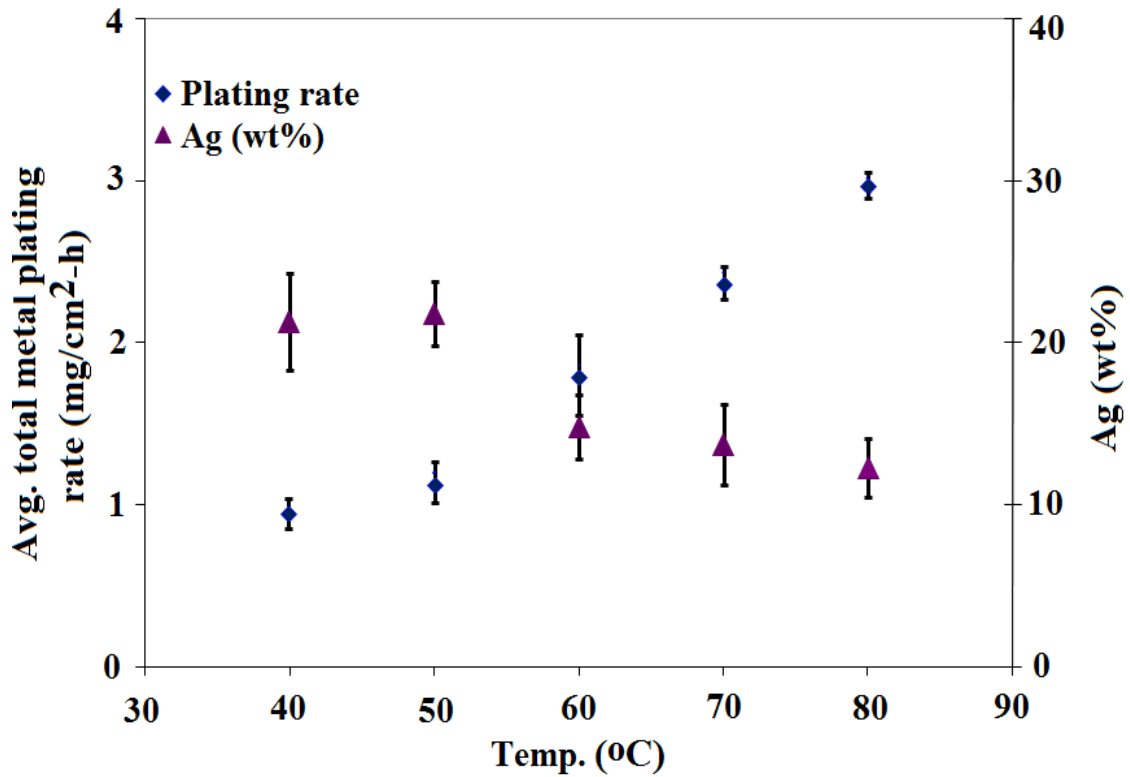


Fig. 6.12. Effect of temperature on the average plating rate and the deposit composition. Bath composition: Total metal conc. = 4 mM (10 at% Ag), N_2H_4 = 5.6 mM, NH_3 = 3 M, Na_2EDTA = 0.1 M and pH = 11.

The morphology of the deposits did not show any major change with variation in the bath temperature. The deposits became thicker and thicker with increasing temperature (as the plating time was the same for all the temperatures) but with little variation in the morphological characteristics (Fig. 6.13). The deposits obtained at 40 °C were not thick enough to show the clear characteristics of morphology, but were very similar to the deposits obtained at 60 °C and 2 mM total concentration (see Fig. 6.4) showing high tendency to grow in the vertical direction to the substrate surface with little pore coverage. The deposits obtained at 40, 50, 70 and 80 °C were very similar to one another in terms of the morphology. The deposits showed large tendency to grow in the perpendicular direction to the substrate surface. Also the deposits were porous and dendritic.

6.3.7. Effect of metal ratio (conventional bath)

Any desired ratio of Pd to Ag in the deposits (particularly 0 to 30 wt% Ag, which was the range of interest from the membrane synthesis point of view [7]) could be achieved by altering the ratio of the metal ions in the solution (see Fig. 6.14). The total metal concentration was kept constant at 4 mM. The change in the metal ratio did not show any considerable change in the average total metal plating rate, however, the change in the metal ratio in the bath had significant effect on the deposits concentration (see Fig. 6.14). The increase in the concentration of Ag in the solution resulted in the increase in the Ag concentration in the deposits. As can be observed from Fig. 6.14, Ag showed the preferential deposition to Pd when the Ag concentration in the bath was 75 at% or higher, i.e., only the Ag deposition occurred for 75 at% or higher concentration in the bath. The deposits obtained were bimetallic, therefore, the increase in the Ag

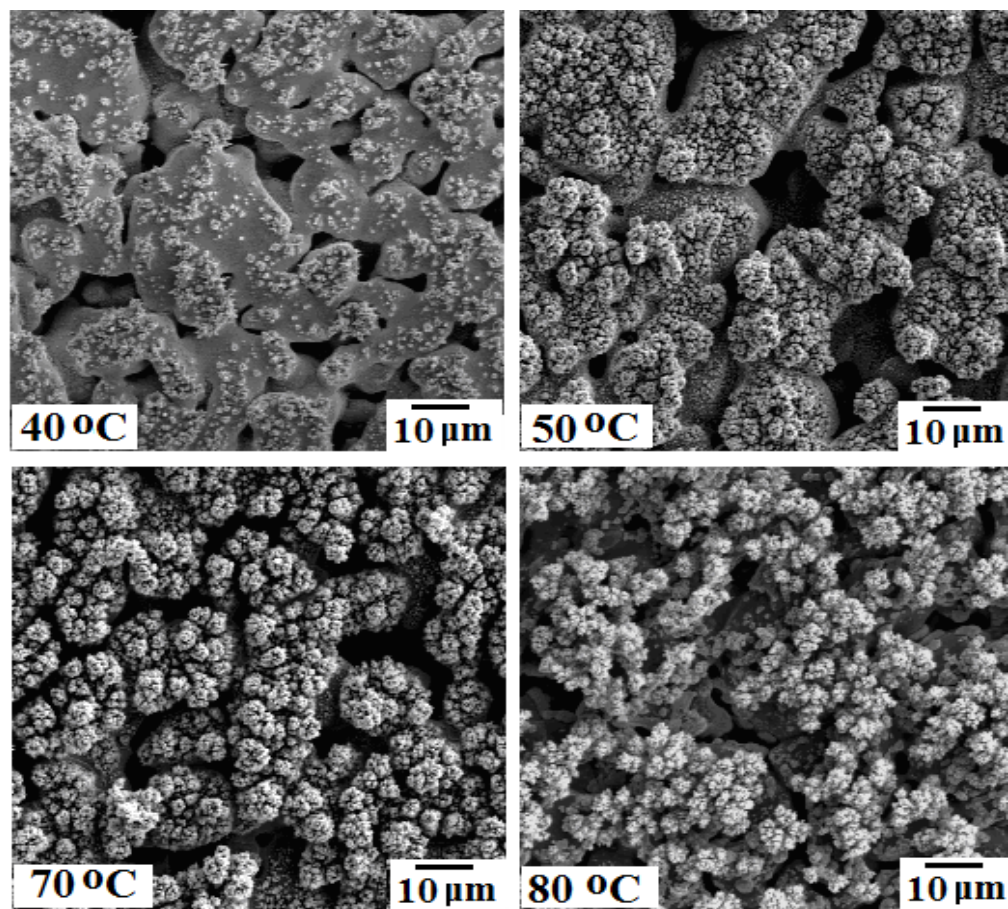


Fig. 6.13. Effect of temperature on the morphology of the deposits. Bath composition: Total metal conc. = 4 mM (10 at% Ag), N_2H_4 = 5.6 mM, NH_3 = 3 M, Na_2EDTA = 0.1 M and pH = 11.

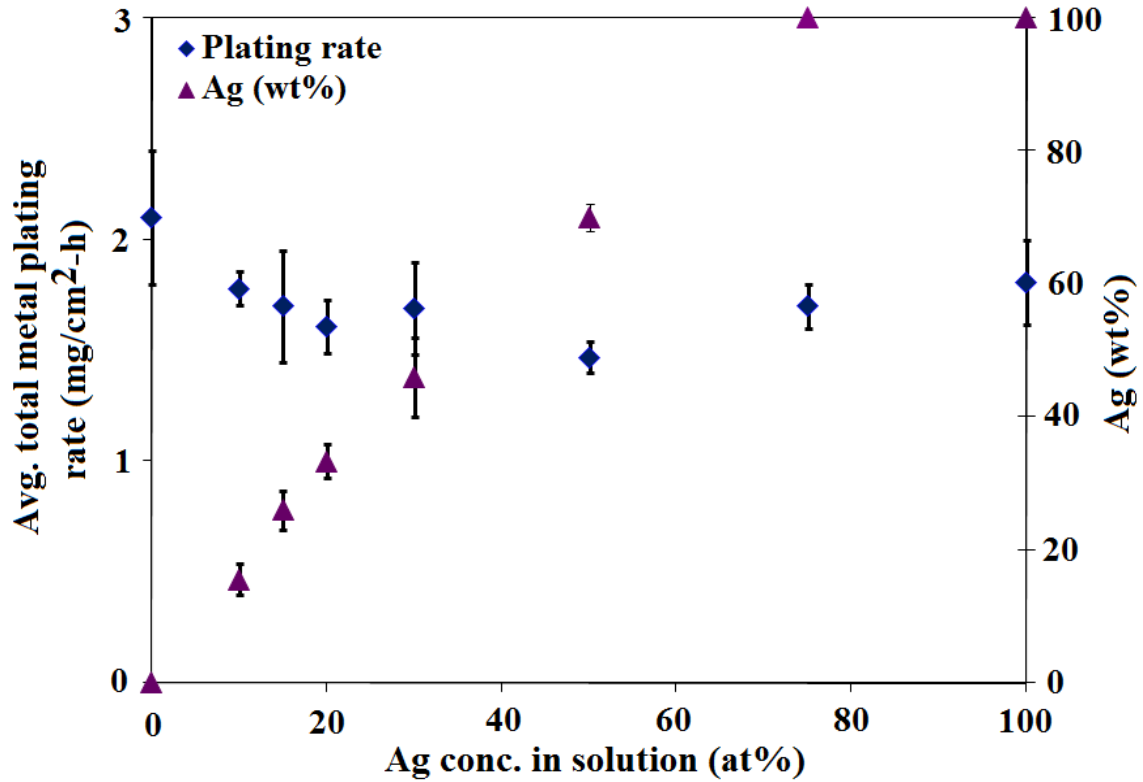


Fig. 6.14. Effect of at% Ag on the deposit composition and average total metal plating rate. Bath composition: Total metal conc. = 4 mM, N_2H_4 = 5.6 mM, NH_3 = 3 M, Na_2EDTA = 0.1 M and pH = 11.

concentration in the deposits meant relatively more surface coverage by Ag deposits than Pd deposits. The low catalytic activity of Ag for the N_2H_4 oxidation than Pd (see Chapter 5, Section 5.3.3.1) meant that as the Ag concentration in the deposits increased, the oxidation rate of N_2H_4 decreased causing the increase in the electroless deposition potential. The increase in the electroless deposition potential with increasing Ag concentration and the high overpotential associated with the Pd deposition meant that when the Ag concentration was 75 at% in the solution, the electroless deposition potential increase to an extent that the Pd deposition was not possible anymore and the pure Ag deposits were obtained. Cheng et al. [8] also observed the pure Ag deposition from their Pd-Ag co-deposition bath when the Ag content in their bath exceeded as low as 5 at%. The Ag to Pd ratio at which pure Ag deposition would occur depended strongly on the total metal to N_2H_4 ratio, pH, temperature and the substrate surface condition because all these factors decided the electroless deposition potential. Shu et al. [88] prevented the pure Ag deposition by first pre-plating the porous stainless steel surface with Pd for 5 min, i.e., making the substrate more active for the N_2H_4 oxidation so that the overall electroless deposition potential was cathodic enough for the Pd deposition, before dipping the substrate in the co-deposition bath.

6.3.8. Effect of substrate rotation (conventional bath)

The substrate rotation had drastic influence on the morphology and composition of the obtained deposits. Fig. 6.15 and Fig. 6.16 show the X-ray diffraction patterns and the SEM images of the samples deposited at different speeds of substrate rotations for a bath with a total metal concentration of 4 mM and 10 at% Ag in the solution. The samples deposited at 100 rpm did not show any significant difference in the deposits

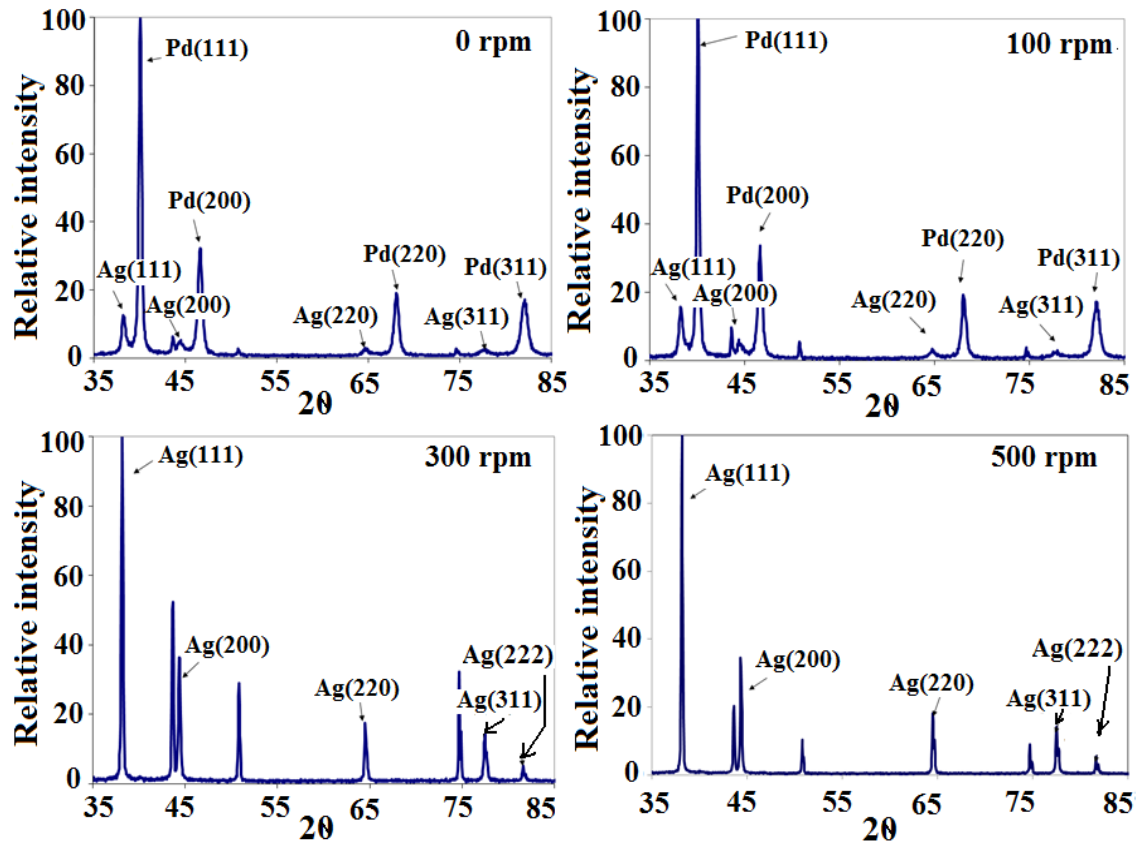


Fig. 6.15. Effect of the substrate rotation on the phase composition of the deposits; Bath composition: Total metal conc. = 4 mM (10 at% Ag), N_2H_4 = 5.6 mM, NH_3 = 3 M, Na_2EDTA = 0.1 M and pH = 11.

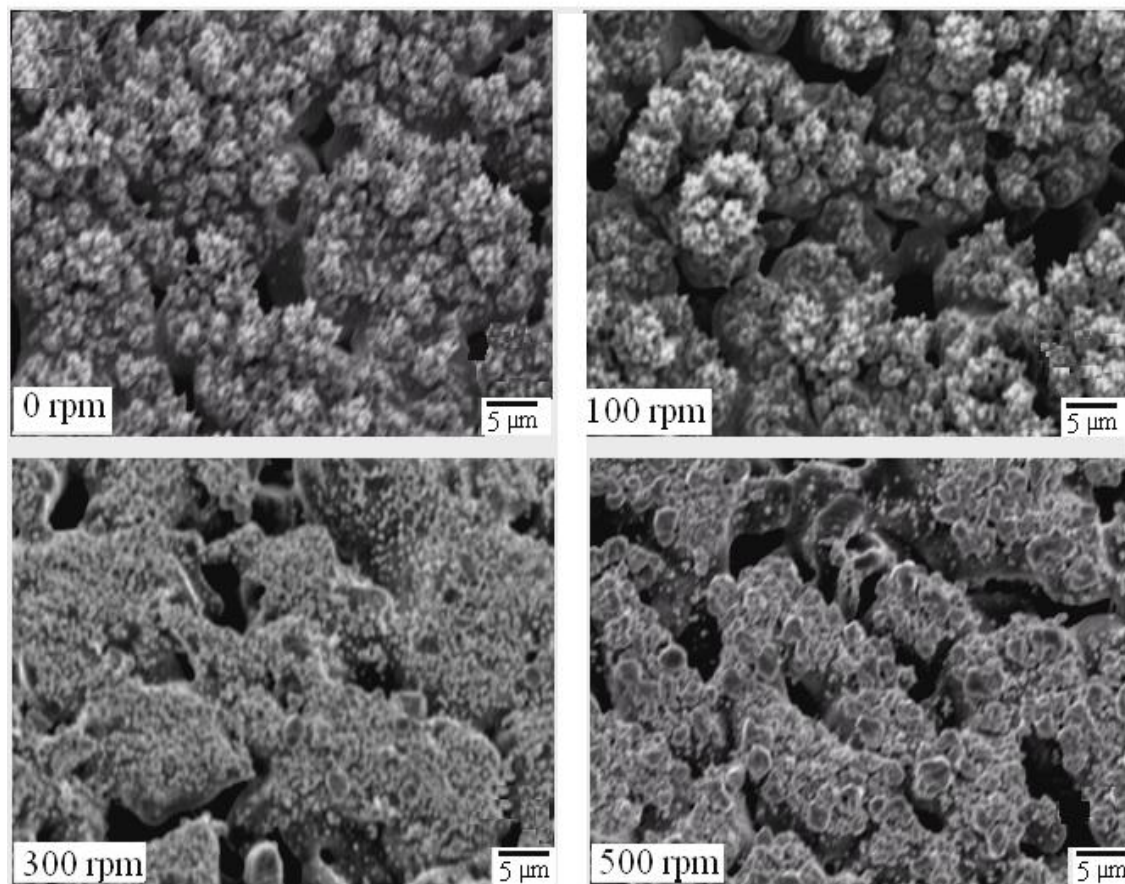


Fig. 6.16. Effect of the substrate rotation on the morphology of the deposits; Bath composition: Total metal conc. = 4 mM (10 at% Ag), N_2H_4 = 5.6 mM, NH_3 = 3 M, Na_2EDTA = 0.1 M and pH = 11.

morphology in comparison to the morphology of the deposits obtained at 0 rpm. The deposits obtained at 300 and 500 rpm had different morphology than that of the deposits obtained at 0 and 100 rpm. The deposits obtained at 0 and 100 rpm were co-deposits as indicated by the presence of both Pd and Ag peaks in the X-ray diffraction patterns of the samples (Fig. 6.15), however, only Ag peaks were observed for the samples deposited at 300 and 500 rpm. Also the ratio of Ag (111) to Pd (111) peaks showed increasing trend with increasing the substrate rotation. The average total metal deposition rate of 2.3, 4.2, 0.6 and 0.75 mg/cm²-h was observed for samples deposited at 0, 100, 300 and 500 rpm respectively. The average total metal deposition rate was based on total plating time of 2 h.

The difference in the deposit composition and morphology could be explained on the basis that the Ag deposition was controlled by its diffusion in the solution relative to the Pd deposition. The Ag content in the deposits therefore was expected to increase with the increased substrate rotation. Also, due to the enhanced mass transfer of all the reacting species in the bath due to the substrate rotation, the total average metal plating rate was expected to increase with the increase in the substrate rotation. However, the average total metal plating rate increased for the samples with 100 rpm rotation in comparison to the samples with 0 rpm rotation and then dropped for the samples with 300 and 500 rpm rotation. The increasing substrate rotation showed increase in the Ag concentration in the deposits and the samples with 300 and 500 rpm rotation showed only Ag deposition. Therefore, for the samples with 300 and 500 rpm rotation, once the Pd activated surface was covered with Ag deposits, the Pd deposition on the Ag surface was not possible (because of the low N₂H₄ oxidation activity of Ag, see Chapter 5, Section 5.3.4) and only Ag continued to deposit for the rest of the deposition time. The

Ag concentration in the solution was very low (0.4 mM) and therefore the drop in the average total metal plating rate was observed for 300 and 500 rpm samples. The deposits for 0 and 100 rpm cases were co-deposits and Ag under such conditions deposited at very high overpotential and under severe mass transfer controlled conditions leading to dendritic growth. On the other hand, for 300 and 500 rpm samples, due to the low activity of the Ag surface for the N_2H_4 oxidation, the overpotential for the Ag deposition was relatively low leading to relatively uniform and compact deposits.

6.3.9. Membrane synthesis-He flux decline (conventional bath)

Fig. 6.17 compares the He flux decline during the synthesis of pure Pd membrane (R-01) and co-deposited Pd-Ag membrane (R-05). It can be noticed from the figure that pure Pd membrane did not show any He leak after the deposition of approximate 21.5 μm thick layer of Pd, however for R-05, the He leak of 21 ml/min was observed after the deposition of approximate 33.5 μm thick layer of Pd-Ag co-deposits despite having gentle mechanical treatment at various steps during the synthesis. The difficulty of the Pd-Ag co-deposits for preparing a He gas tight membrane could be ascribed to their morphology. The morphology of the co-deposits obtained using the conventional NH_3 +EDTA based bath was non-uniform with the deposits showing dendritic structure and poor substrate pore coverage. In contrast to the Pd-Ag co-deposits, the Pd deposits were uniform (see Chapter 5, Section 5.3.1) and showed good pore coverage, therefore were suitable for preparing thin and He dense membrane.

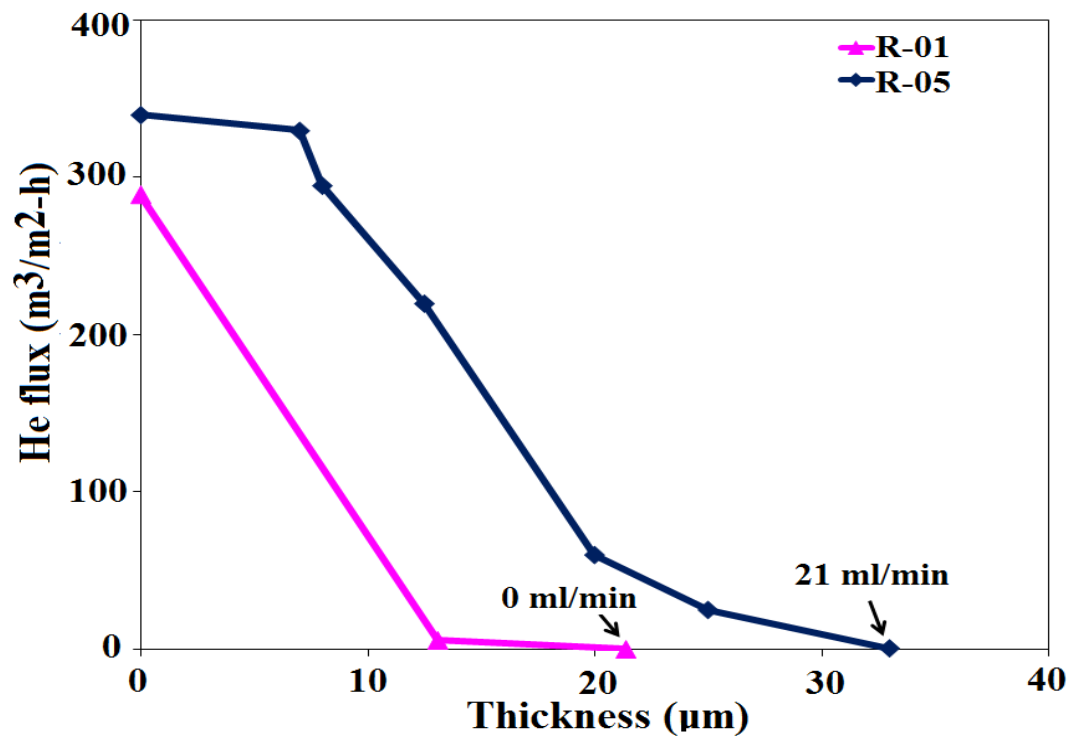


Fig. 6.17. He flux (at $\Delta P = 1$ atm) during synthesis of membranes a. Pure Pd membrane
b. Pd-Ag co-deposited membrane (Total metal conc. = 4 mM with 15 at% Ag)

6.3.10. Glycine influence on the Pd and Ag deposition

6.3.10.1. Individual Pd and Ag polarization from glycine bath

The individual polarization characteristics of Pd and Ag are shown in Fig. 6.18 and Fig. 6.19 respectively. The Pd deposition occurred in the potential range of -550 to -575 mV (Fig. 6.18a). The surface change in the case of the Pd deposition did not alter the Pd deposition characteristics. The Pd deposition on the Ag surface (Fig. 6.18b) occurred approximately in the same potential range, -550 to -575 mV, as that observed on the Pd surface.

Glycine at pH value of 11 existed in the form of gly^- ($\text{NH}_2\text{CH}_2\text{COO}^-$) which was the form taking part in the complexing reactions with metal ions in the solution [129-131] (see Appendix A for more details). The value of the stability constant for the complexing reaction of glycine with Pd was reported to be $10^{17.5}$ [132]. The equilibrium potential for 10 mM Pd concentration and 0.8 M glycine concentration in the bath was calculated to be 0.41 V (with respect to the standard hydrogen electrode (SHE), see Appendix A for the calculation). The electrode potential of Ag/AgCl, 3 M NaCl reference electrode with respect to the SHE was 0.19 V [133], therefore, the equilibrium potential for 10 mM Pd in the presence of 0.8 M glycine was 0.22 V or 220 mV with respect to Ag/AgCl, 3 M NaCl reference electrode used in this study. The actual Pd deposition in the presence of glycine started in the potential range of -550 to -575 mV, therefore the overpotential i.e., difference between the equilibrium potential of Pd (220 mV) and the observed deposition potential (-550 to -575 mV), associated with the Pd deposition in the presence of glycine was approximately in the range of 770 to 795 mV. The overpotential of 770 to 795 mV for the Pd deposition was based on the equilibrium potential of Pd calculated at 25 °C. The actual value (based on the

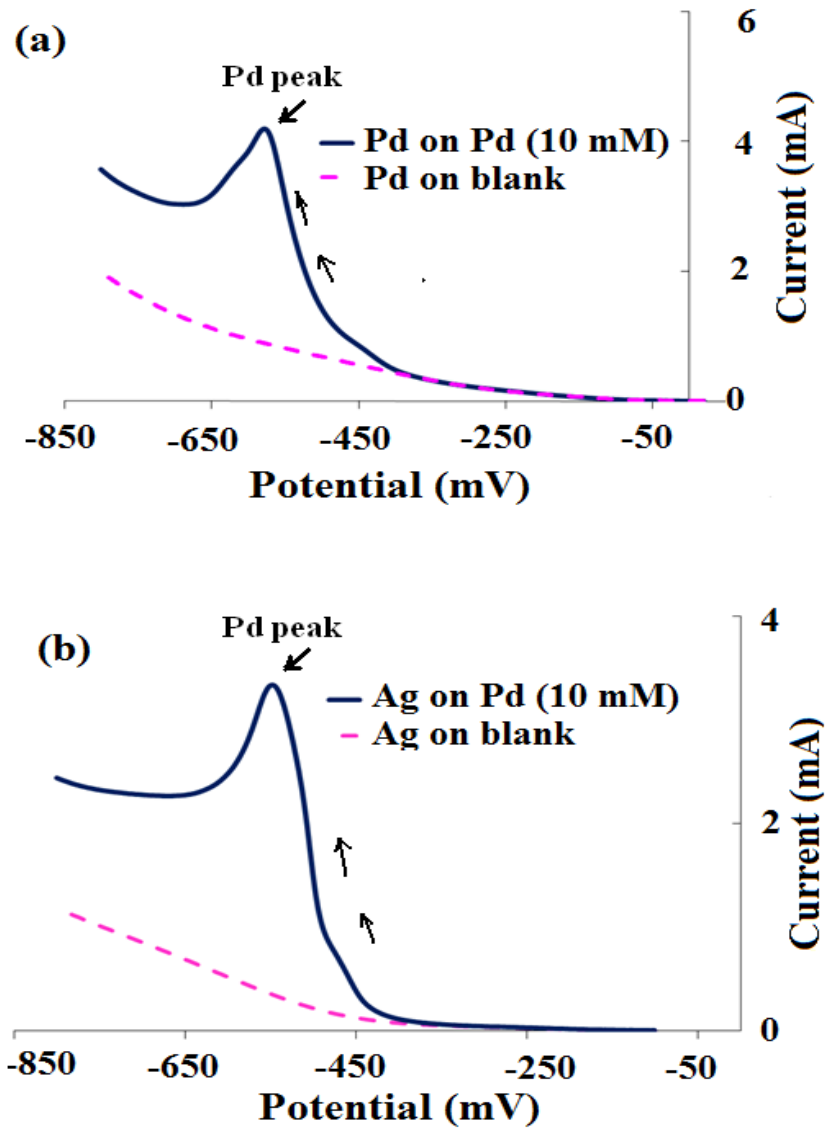


Fig. 6.18. Pd polarization characteristics in the presence of glycine at temp. = 60 °C and Pd concentration. = 10 mM in the bath (a) on the Pd surface (b) on the Ag surface

equilibrium potential at 60 °C) of the overpotential associated with the Pd deposition based on the equilibrium potential at 60 °C might be different from the calculated value because the value of the stability constant of Pd at 60 °C with glycine might be different from the value at 25 °C used in the calculation. The other reason for the difference could be the presence of KCl in the bath used in this study and the possibility of existence of combined complexing reactions of Pd with glycine and Cl⁻.

Fig. 6.19 shows the Ag polarization scans obtained in the presence of glycine. Fig. 6.19a shows the LSV scan obtained on the Ag surface. As can be seen in the figure, indicated by the Ag peak level, the Ag deposition started in the potential range of 10 to -15 mV. The Ag polarization characteristics on the Pd surface were very similar to the Ag surface (Fig. 6.19b). The Ag deposition on the Pd surface started in the same potential range i.e. 10 to -15 mV as on the Ag surface.

The value of stability constant for the complexing reaction of glycine with Ag was reported as $10^{7.20}$ [117]. Using the Nernst equation and the stability constant value, the equilibrium potential for Ag (3 mM) and glycine (0.8 M) was calculated to be 0.23 V (SHE) or 0.04 V (Ag/AgCl, 3 M NaCl, 25 °C) (see Appendix A for the calculation). The potential for the actual deposition of the Ag was observed to be approximately 10 mV. As compared to the Pd deposition, very little overpotential (~ 30 mV) was observed for the Ag deposition. The equilibrium deposition potential difference between Pd and Ag was (220 – 40 mV) 180 mV, however, the large overpotential associated with Pd deposition meant that the large difference (~ 565 mV) existed between the Pd and Ag deposition potentials in the presence of glycine.

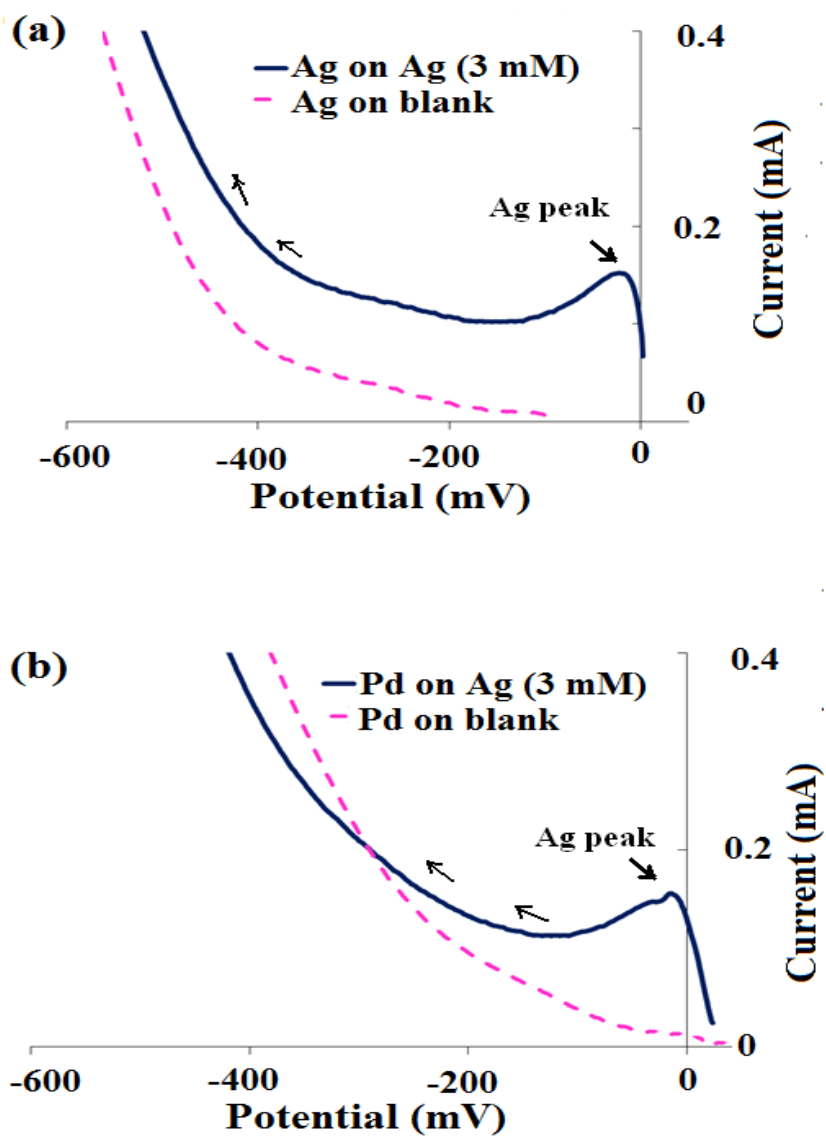


Fig. 6.19. Ag polarization characteristics in the presence of glycine at temp. = 60°C and Ag conc. = 3 mM (a). on the Ag surface (b). on the Pd surface

6.3.10.2. *Simultaneous Pd and Ag polarization characteristics from glycine bath*

Fig. 6.20 shows the polarization characteristics for Pd and Ag in their simultaneous presence in the glycine bath. The deposition potential in the mixed bath for both Pd and Ag were very close to the deposition potential from their individual plating baths. The Ag deposition peak occurred at potential of -15 to -25 mV on the Pd surface (Fig. 6.20a). The Pd deposition on the Pd surface occurred in the potential range of -550 mV to -600 mV. The Pd and Ag deposition on the Ag surface occurred approximately in the same range as on the Pd surface (Fig. 6.20b). The Ag peak relative to the Pd peak was very small and is not very clear from Fig. 6.20a and Fig. 6.20b. The Ag peak could be very clearly seen on the CV scans (see Appendix B) obtained on the Pd and Ag surface at the same potential as seen on the LSV scan here (Fig. 6.20)

Hasler [119] also observed the large difference between the Pd and Ag deposition potential (~ 700 mV) in the presence of glycine. The potential-current curve reported by the author [119] was obtained at 25 °C on the brass surface.

6.3.11. **Suitability of the complexing agents**

The LSV scans similar to the glycine scans (see Fig. 6.18, Fig. 6.19 and Fig. 6.20) shown in this chapter were obtained for other complexing agents, NH_3 , EDTA and KCl (see Appendix B for details). The summary of the deposition potential of Pd and Ag in the presence of various complexing agents is shown in Table 6.3. The deposition potential shown was the approximate potential where the Pd or Ag deposition was observed to be initiated. The potential difference between the Pd and Ag deposition

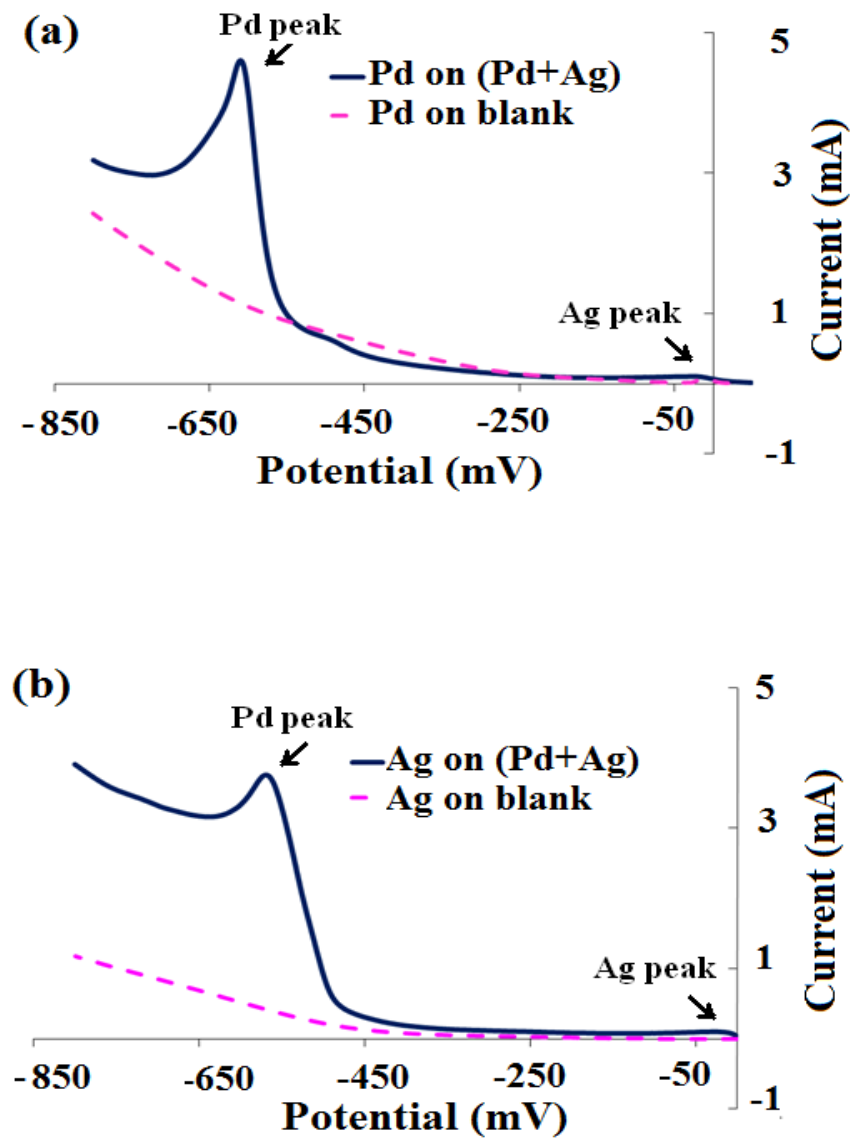


Fig. 6.20. Pd and Ag polarization characteristics in the presence of glycine at temp. = 60 °C, Pd concentration. = 10 mM and Ag conc. = 3mM (a) on the Pd surface (b) on the Ag surface

Table 6.3. Summary of the deposition potential in the presence of various complexing agents

	Complexing agent →		NH ₃	EDTA	Glycine	KCl	
Equilibrium Potential (mV) →	Calculated at 25 °C,	Pd	-240	220	220	190	
	Ag/AgCl, NaCl 3 M	Ag	-30	60	40	-10	
Deposition potential (~ mV) →	Single metal bath	Pd	-675	-450	-560	140	
		Ag	-85	75	5	-125	
	Co-deposition bath	Pd	-675	-475	-575	125	
		Ag	-85	100	-20	-125	
	Potential difference						
	Single metal bath	Pd-Ag	-590	-525	-565	265	
Co-deposition bath	Pd-Ag	-590	-550	-555	250		

based on the single metal and simultaneous deposition is also reported. Based on the difference between the deposition potential of Pd and Ag, the order of suitability of the complexing agents for the Pd-Ag co-deposition increased as $\text{NH}_3 < \text{Glycine} < \text{EDTA} < \text{KCl}$.

6.3.12. N_2H_4 Oxidation

N_2H_4 was found suitable for the Pd and Ag reduction (see Chapter 5, Section 5.3.3.2) in the case of the conventional bath ($\text{NH}_3 + \text{EDTA}$) and could reduce Pd and Ag both individually and simultaneously. We further investigated the suitability of N_2H_4 as the reducing agent for the plating baths with all the complexing agents studied in this chapter. Fig. 6.21 shows the polarization characteristics of N_2H_4 oxidation on the Pd and Ag surface. The Pd surface showed higher activity for the N_2H_4 oxidation characteristics (Fig. 6.21a) than the Ag surface (Fig. 6.21b) in the presence of all the complexing agents. N_2H_4 was found suitable for the Pd deposition in all the cases because the potential at which oxidation occurred was very close to the deposition potential observed for Pd. In the case of KCl, the oxidation current for N_2H_4 on the Pd surface started approximately at the potential of -400 mV. The large difference (550 mV) existed between the Pd deposition potential (150 mV) and the N_2H_4 oxidation potential (-400 mV) indicating that the addition of N_2H_4 could result in the homogeneous precipitation of Pd in the KCl bath.

N_2H_4 was considered to be suitable for the pure Ag deposition in the presence of all complexing agents other than KCl (Fig. 6.21b). The Ag surface showed least activity for the N_2H_4 oxidation in the presence of KCl (Fig. 6.21b). In fact, very little oxidation activity was observed in the presence of KCl as indicated by the polarization scans

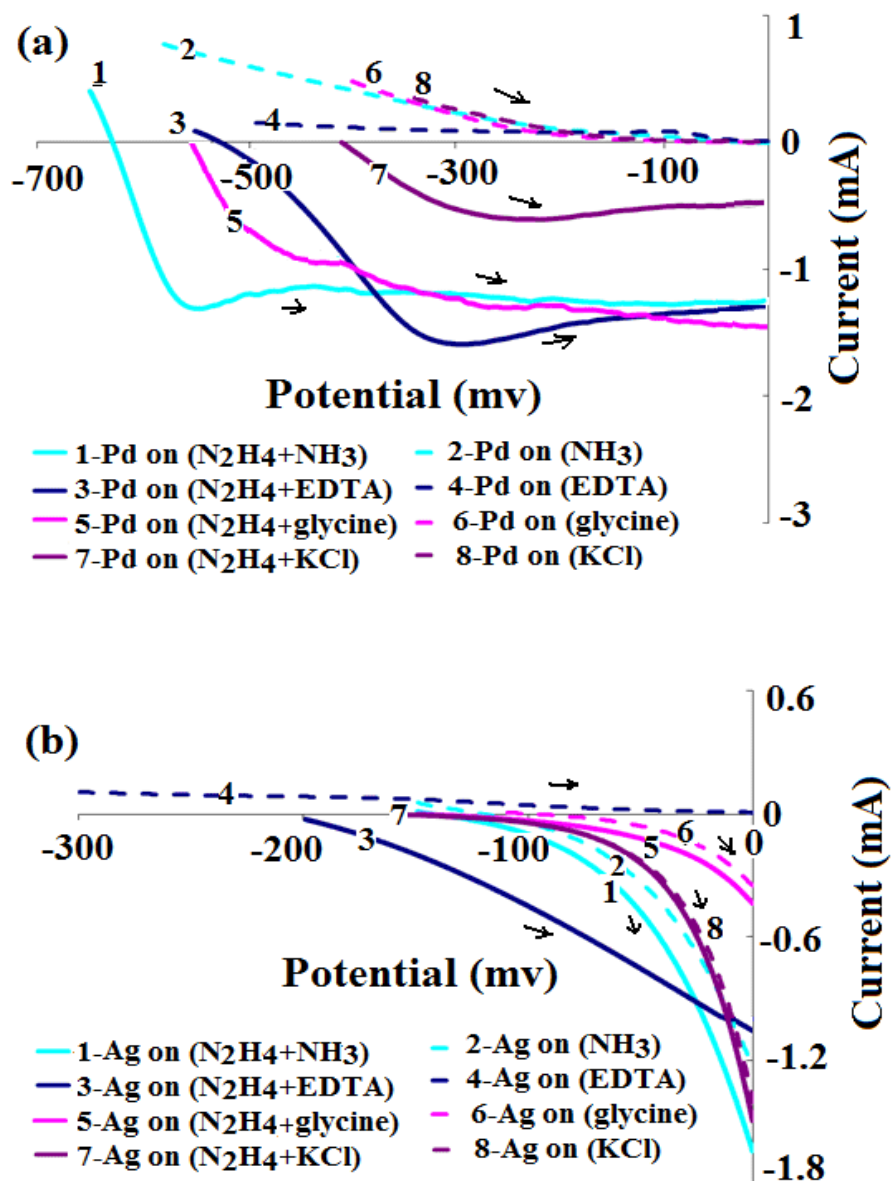


Fig. 6.21. N_2H_4 polarization characteristics in the presence of different complexing agents investigated in this study (a) on the Pd surface (b) on the Ag surface

obtained with and without N_2H_4 presence in the KCl bath. The Ag deposition in the presence of KCl occurred around the potential range of -100 to -150 mV. Almost no current was observed for the N_2H_4 oxidation in the potential range of the Ag deposition (-100 to -150 mV) indicating that N_2H_4 could not be suitable for the pure Ag deposition in the presence of KCl. However in the presence of Pd and Ag in the KCl bath, the Ag deposition was possible because the Pd deposits could provide the catalytic surface for the N_2H_4 oxidation leading to the deposition Ag along with Pd.

6.4. Conclusion

The simultaneous presence of Pd and Ag in the case of the conventional NH_3 +EDTA based co-deposition bath did not show any significant effect on their deposition characteristics compared to the deposits obtained from single metal baths. The Pd deposition occurred at electrode potential of 600 to 650 mV more cathodic than the Ag deposition. The deposition characteristics did not change with the nature of the surface and the co-deposition characteristics were very similar on both Pd and Ag covered surface. Under the co-deposition conditions, the Ag deposition was severely controlled by its diffusion in the solution resulting in non-uniform and dendritic deposits. The increasing pH, N_2H_4 concentration and temperature favored the Pd deposition but increasing the NH_3 concentration favored the Ag deposition. The overall Ag wt% in the deposits could easily be controlled by simply varying the Ag to Pd ratio in the bath particularly in the range of 0 to 30 wt%. The increase in the substrate rotation resulted in the increase of Ag concentration in the deposits and at the substrate rotation speed of 300 rpm or higher, only the Ag deposition occurred. Pd in the presence of NH_3 , EDTA and glycine showed large overpotential for the deposition, however, very little overpotential was associated with the Ag deposition under the similar conditions. The Pd acted as the less noble metal in the presence of NH_3 , EDTA and glycine and the large potential difference was observed between the Pd and Ag deposition (-550 to -590 mV). The Pd and Ag deposition potential difference (~250 mV) in the presence of KCl was relatively much lower than that for the other complexing agents, therefore, KCl was found to be the most suitable complexing agent for the co-deposition. Pd acted as the more noble metal than Ag in the presence of KCl and very little overpotential was observed for both Pd and Ag deposition. N_2H_4 was observed to be suitable for the pure

Pd deposition in all the baths. In the presence of KCl, nearly negligible N_2H_4 oxidation current was observed in the potential range of the Ag deposition showing non-suitability of N_2H_4 for the pure Ag deposition. However, N_2H_4 was suitable for the Pd and Ag co-deposition in the KCl bath where Pd present in the co-deposits could provide catalytic activity for the oxidation of N_2H_4 leading to the Ag deposition along with Pd.

7. Sequentially deposited Pd-Ag membranes and their annealing characteristics

7.1. Introduction

As discussed in the introduction section of Chapter 5, the plating conditions played an important role in the deposits properties. For the sequential plating, the important properties are the morphology and lateral growth of the deposits on the substrate surface. The good lateral growth of the deposits is necessary to cover the pores of the substrate to prepare He gas tight membrane. The Pd and Ag plating conditions found suitable for preparing the Pd-Ag membrane by the sequential method in Chapter 5, Section 5.3.4 were applied for the membrane synthesis. Based on the study described in Chapter 5, Section 5.3.4, it was concluded that Pd electroless deposits (Pd/N₂H₄ ratio = 16 mM/5.6 mM) and the plating conditions such as high Ag/N₂H₄ ratio (20 mM/4 mM) or Ag/N₂H₄ ratio (3 mM/5.6 mM) with substrate rotation (500 rpm) produced deposits with good pore penetration without any dendritic morphology and therefore suitable for the Pd-Ag composite membrane preparation. In this chapter, we used the plating conditions concluded suitable for the Pd-Ag deposition in Chapter 5 to synthesize the Pd-Ag membranes.

The objective of the work described in this chapter was to synthesize H₂ selective Pd-Ag membranes and investigate their annealing and subsequent H₂ permeation characteristics at different temperatures and pressures. The deposition method could influence the annealing and H₂ permeation of Pd-Ag membranes. The Ag deposition by electroplating method was also investigated in this chapter to prepare a Pd-Ag H₂ permeation characteristics. Four membranes were prepared in this study. The first

membrane was prepared using the Pd electroless and Ag electroplating sequential deposition while the rest of the membranes were prepared using the Pd and Ag electroless sequential deposition.

7.2. Experimental

7.2.1. Plating conditions and substrate

Four porous Inconel tubes were used as the substrates (see Chapter 3, Section 3.2.1) for the membranes synthesis. All the substrates were deposited with the γ -alumina layer by sole gel method used as the intermetallic diffusion barrier layer and the substrate pores were filled with γ -alumina powder (see Chapter 3, Section 3.2.2 for details).

For the first substrate, R-06, the Pd-Ag sequential deposition was performed by combining the electroless plating (for Pd) and electroplating method (for Ag). Only the electroless plating method was used for the Pd-Ag sequential deposition for the rest of the substrates i.e., R-10, R-11 and R-13a. For the morphology and pore penetration study of the Ag electrodeposits, the plating conditions ($[Ag] = 100$ mM and current density = 2 mA/cm²) described in Chapter 3, Section 3.3 and the PSS coupons were used.

Table 7.1 summarizes the plating conditions and corresponding morphological characteristics of the obtained deposits investigated in Chapter 5. The Pd plating condition with Pd/N₂H₄ ratio of 16 mM/5.6 mM produced deposits with good substrate pore penetration and therefore was selected to deposit Pd for all four membranes. The Ag deposition in the case of R-06 was performed using the electroplating conditions with Ag concentration = 100 mM and current density = 2 mA/cm², described in Chapter 3, Section 3.3. For R-10, R-11 and R-13a, the Ag was deposited using the

Table 7.1. Summary of Pd and Ag plating conditions and obtained deposit characteristics investigated in Chapter 5

Plating condition	Deposit characteristics (Substrate pore penetration)
Pd electroless: Pd/N ₂ H ₄ = 16 mM/5.6 mM	Good
Ag electroless 1: Ag/N ₂ H ₄ = 3 mM/5.6 mM	Poor
Ag electroless 2: Ag/N ₂ H ₄ = 20 mM/4 mM	Good
Ag electroless 3: Ag/N ₂ H ₄ = 3 mM/5.6 mM, substrate rotation = 500 rpm	Good
Ag electroless 4: Ag/N ₂ H ₄ = 3 mM/1 mM	Good

electroless plating condition 2 described in Chapter 5, Section 5.2.1 i.e., the Ag plating condition with Ag/N₂H₄ ratio of 20 mM/4 mM which produced deposits with good substrate pore penetration. R-13a was attempted to be pure Pd membrane with the only difference that for roughly the first 2.0-2.5 μm membrane thickness, both Pd and Ag depositions were performed and then only the Pd deposition was performed for the rest of the thickness. The first 2-2.5 μm membrane thickness for R-13a had two Pd layers (~0.8 μm each) and two Ag layers (~0.3 μm thickness each) alternately deposited on each other. The Ag layers for R-13a were to provide additional intermetallic diffusion barrier along with the γ-alumina layer by the sole gel method. Ag did not show any solubility towards the substrate components such as Ni, Fe and Cr [51]. Therefore, the presence of Ag in Pd could also provide resistance towards penetration of the substrate components into Pd. R-13a after annealing and characterization steps was further treated with multi plating, annealing and mechanical polishing sequences and their effect on the H₂/He selectivity of the membranes was investigated (see Chapter 9). The Pd-Ag deposition in all three membranes, R-06, R-10 and R-11, consisted of three layers of Pd and two layers of the Ag deposited sequentially (Pd-Ag-Pd-Ag-Pd) in all three cases. The thickness of each layer was intended to be between 1-3 μm.

7.2.2. Annealing and H₂ permeation measurement

For the H₂ permeation measurements of the membranes, the set up described in Chapter 3, Section 3.5.3 was used. The membranes were annealed at 550 °C for 24 h except R-13a which stayed at 550 °C for only 10 h. Before annealing, the membranes were heated from room temperature to 400 °C (1 °C/min) in the He atmosphere. At 400 °C, the system was switched to H₂ gas and then heated to 550 °C (1 °C/min). After the annealing step at 550 °C, R-06, R-10 and R-11 were further tested for H₂ permeation

characteristics at 300 °C (180 h), 400 °C (40 h) and 500 °C (60 h) with a total time of 280 h. After annealing at 550 °C, R-13a was further tested for H₂ permeation characteristics only for 50 h (250 °C = 25 h, 300 °C = 15 h, 400 °C = 5 h and 500 °C = 5 h). At various stages during the membrane characterization for the H₂ permeation, the system was also switched from H₂ to He gas for a short time in order to measure the H₂/He selectivity of the membranes.

7.2.3. SEM and EDX characterization

The membranes after the H₂ permeation characterization test were further characterized with SEM and EDX for the compositional homogeneity across the cross section.

7.3. Results and discussions

7.3.1. The morphology of the Ag electrodeposits on PSS coupons

The initial Ag electrodeposits with thickness less than 1 μm showed very similar growth characteristics to that of electroless plated Pd observed in Chapter 5, Section 5.3.1. Fig. 7.1a shows the SEM images of the initial deposits. The Ag deposits showed very uniform growth over the substrate surface and the deposits showed equal growth on the top and inside the pores of the substrate, which was a desired deposit characteristic for the synthesis of thin and hydrogen selective membrane. The Ag deposition characteristic continued with the trend similar to the initial deposits as the thickness increased (Fig. 7.1b). The Pd electroless and Ag electroplated sequential deposits showed very uniform morphology as is evident from the SEM image of the cross-section of the deposits shown in Fig. 7.1c. The deposits consisted of four alternate

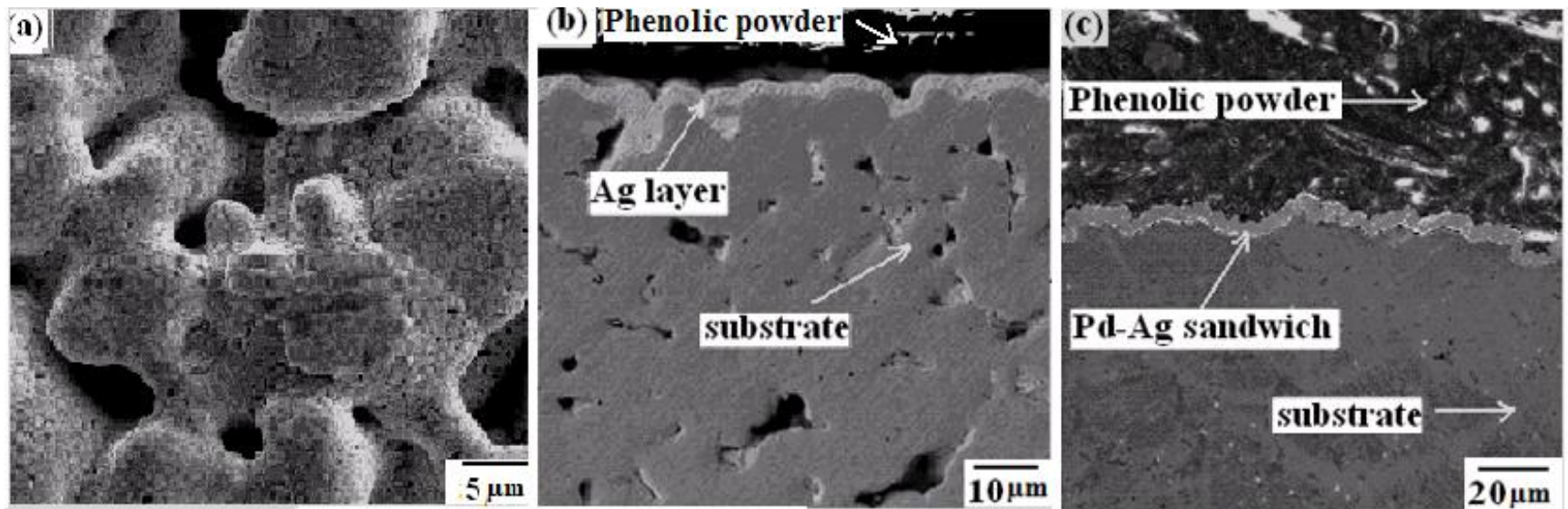


Fig. 7.1. The deposition characteristics of the Ag electrodeposits (a) initial 1 μm characteristics for thickness < (b) cross-section of the deposits, thickness > 3 μm (c) sequential Pd electroless and Ag electrodeposits

layers of Pd (~1 μm) and Ag (~0.5 μm) each (total 8 layers). The Ag concentration was 100 mM in the solution and the deposition was performed at 2 mA/cm². The Ag electrodeposition at 2 mA/cm² corresponded to approximately the average plating rate of 7.5 $\mu\text{m}/\text{h}$ based on the coupon plating performed for the first 45 minutes. It is believed that the high concentration of Ag in the electroplating bath and the low plating rate of Ag meant that the Ag electrodeposition occurred at low overpotential and without any significant mass transfer in the solution, similar to the electroless plating conditions 2, 3 and 4 of Chapter 5, leading to uniform Pd-Ag sequential deposits.

7.3.2. Synthesis of Pd-Ag membranes

The pre-treatment of the substrates before the Pd and Ag layers deposition resulted in the increase in the resistance for the He flow through the substrates. Fig. 7.2 shows the He permeance of the substrates after cleaning in the basic solution and after filling the pores with the alumina powder. The He permeance data were plotted against the average pressure (P_{avg}), the average of the pressures on the two sides of the substrate. The data were fitted to the straight line using the following equation.

$$\frac{\text{He}(\text{flux})}{\Delta P} = \alpha + \beta \times P_{\text{avg}} \quad 7.1$$

The intercept (α , m³/m²-atm-h) of the line indicated the contribution of the Knudsen flow and the slope of the line (β , m³/m²-atm²-h) signified the contribution of viscous flow to the overall He flow through the substrate [134]. After the alumina powder step, the He flux was 165, 206, 183 and 304 m³/m²-h ($\Delta P = 1$ atm) for R-06, R-10, R-11 and R-13a respectively. The pre-treatment steps resulted in approximately 40-60 % decline in the He flux of the substrates indicating that the γ -alumina powder did fill the

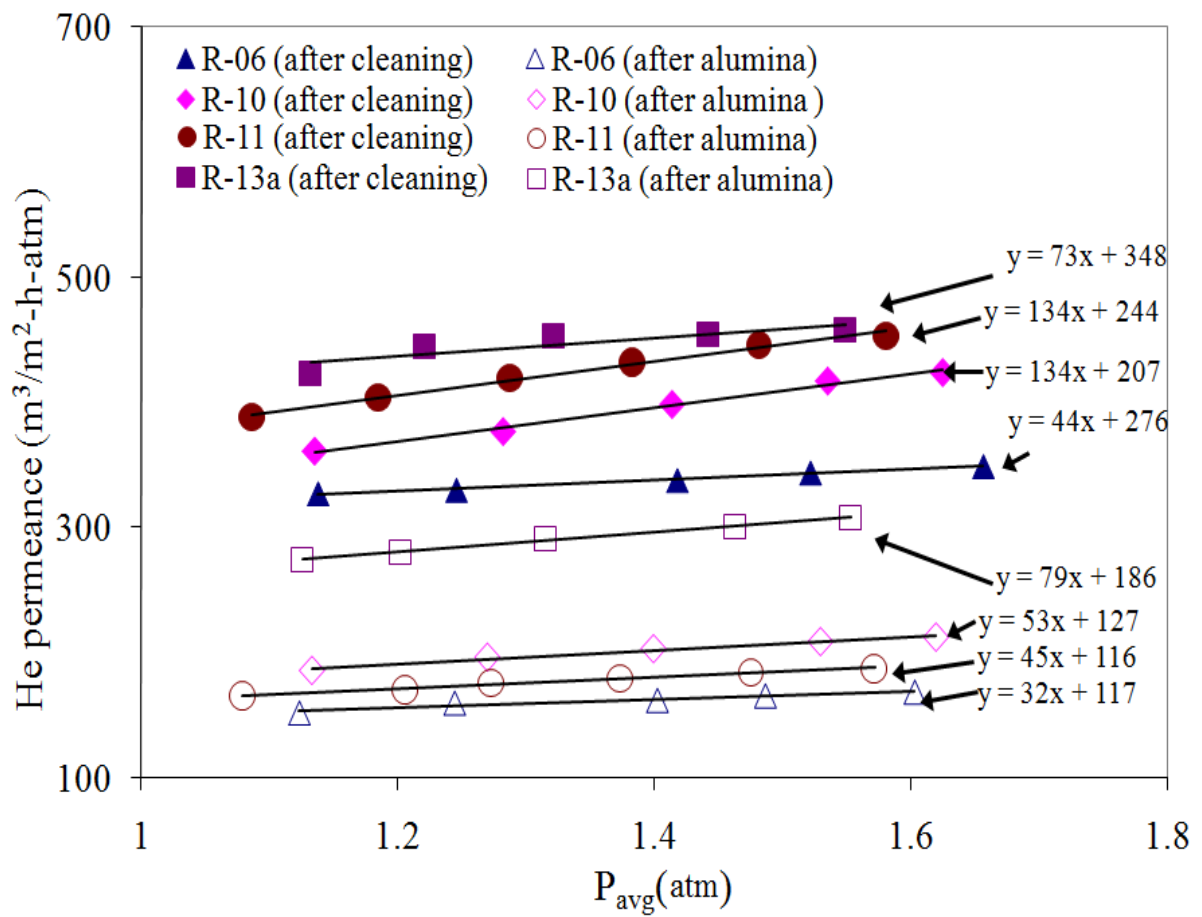


Fig. 7.2. He permeance of the substrates during the pre-treatment steps of cleaning and filling the substrate pores with alumina powder.

substrate pores but at the expense of significant increase in the substrate resistance for the gas flow. The He permeance data of the substrates after the pre-treatment step shown in Fig. 7.2 was used to calculate the H₂ flow resistance in the substrate later in this chapter.

Table 7.2 shows the thickness of each layer obtained during the synthesis step measured by the gravimetric method along with their sequence of the deposition. The deposition sequence consisted of the Pd deposition (Pd-1 layer) followed by the Ag layer deposition (Ag-1 layer) and so on. The actual thickness of each layer given in the table had uncertainty of $\pm 0.3\text{-}0.4 \mu\text{m}$. In R-06, R-10 and R-11, the overall Ag content was between 15 and 30 wt% estimated gravimetrically. In the case of R-13a, the overall Ag content ranged between 4-8 wt% and concentrated only in the first 2.0-2.5 μm thickness of the membrane. During the synthesis, after the deposition of the final layer of Pd-Ag or Pd in the case of R-13a, no He flow was detected for all the membranes at $\Delta P = 1 \text{ bar}$, i.e., Pd and Ag sequential deposits obtained showed complete pore coverage.

7.3.3. Annealing characteristics

All the membranes showed a sharp increase in the H₂ permeance when temperature was raised from 400 to 550 °C. The increase in the permeance could be attributed to: 1. the temperature increase and 2. change in the phase composition of the membranes, i.e., formation of the alloy phase due to the annealing of Pd-Ag layers. Fig. 7.3 shows the H₂ permeance of the membranes during the temperature rise from 400 to 550 °C and during annealing at 550 °C. Considerable increase in the H₂ permeance was observed for the first few hours at 550 °C and approximately after 15 h at 550 °C, no significant increase

Table 7.2. Gravimetric thicknesses of the sequentially deposited Pd-Ag layers

Layer type	Thickness, μm (R-06)	Thickness, μm (R-10)	Thickness, μm (R-11)	Thickness, μm (R-13a)
Pd-1	2.2	2.6	1.8	0.8
Ag-1	1.0	1.3	1.0	~0.3
Pd-2	3.0	3.2	2.1	0.8
Ag-2	1.0	1.0	1.8	~0.3
Pd-3	1.4	1.3	2.0	4.8
Total thickness	8.6	9.4	8.7	7.0
Overall wt% Ag	19	23	29	7

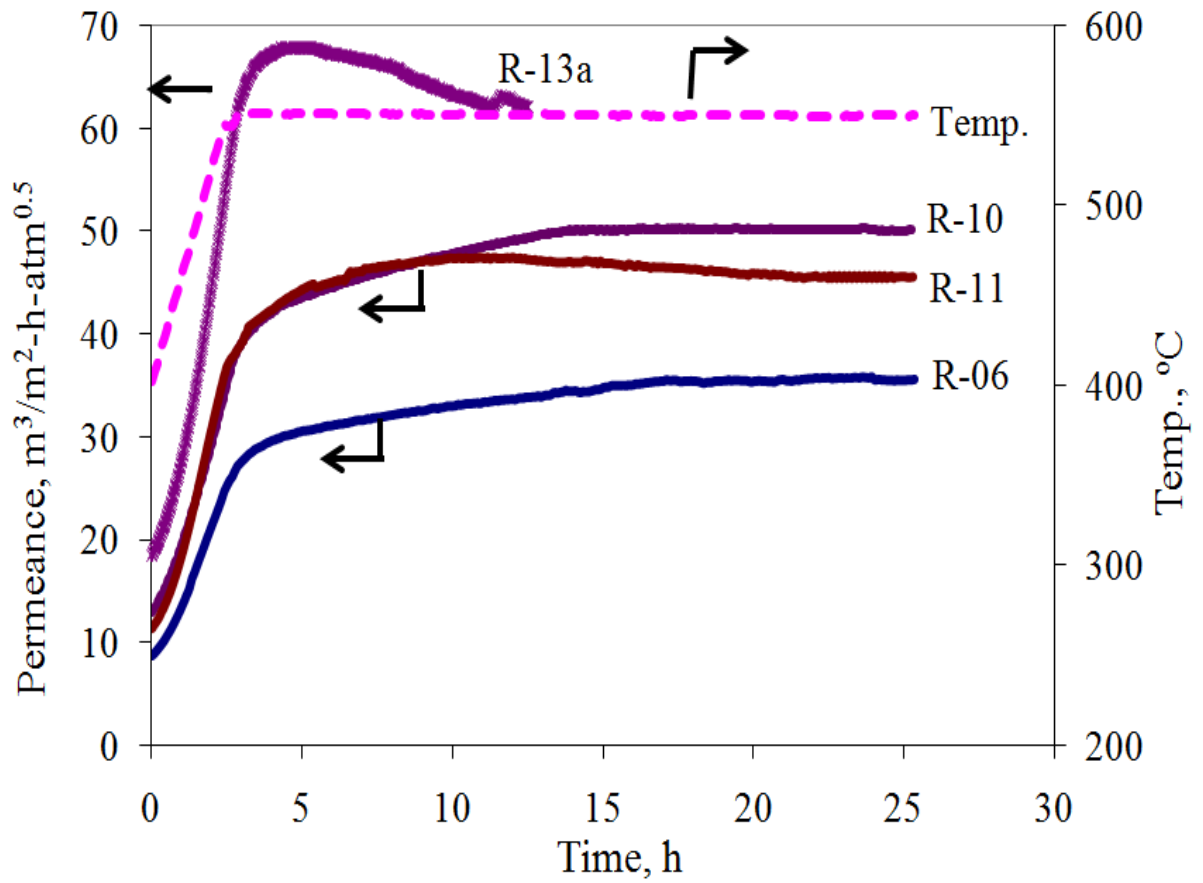


Fig. 7.3. H₂ permeance of the membranes during the temperature ramp from 400 to 550 °C and annealing step at 550 °C.

in the permeance was measured for R-06, R-10 and R-11 indicating that the annealing process was either near to completion or occurring at a very slow rate. R-13a at 550 °C showed an increase in H₂ for the first 1.5 h and then it became steady or in fact declined slightly. The shorter annealing time required for R-13a could be attributed to relatively thinner Ag layers deposited.

The membranes showed very large differences in the H₂ permeation before and after the annealing step at 550 °C. Fig. 7.4 shows the H₂ permeation of the membranes plotted in the Arrhenius form (i.e., $\ln(\text{H}_2 \text{ permeance})$ vs. $1/T$) based on the H₂ permeation data obtained during the temperature ramp between 400 and 550 °C. In comparison to the H₂ permeance at 400 °C before the annealing step, the H₂ permeance at 400 °C after the annealing step at 550 °C was significantly higher (see Fig. 7.4). The difference in the H₂ permeance of the membranes before and after the annealing step at 550 °C could be attributed to structural changes in the membranes. Before the annealing step at 550 °C, the membranes were in the form of Pd and Ag layers sequentially laying on top of each other, therefore H₂ had to permeate through the pure Ag layers which provided large resistance for the permeation. After the annealing step, the Ag layers disappeared due to the mixing with Pd layers forming the Pd-Ag alloy and subsequently the resistance for the H₂ permeation decreased resulting in the increase in the H₂ permeance of the membranes. The structural changes in the membranes during the annealing step also became evident from the difference in the slopes of the Arrhenius plots of the H₂ permeance of the membranes measured before and after the annealing step (see Fig. 7.4).

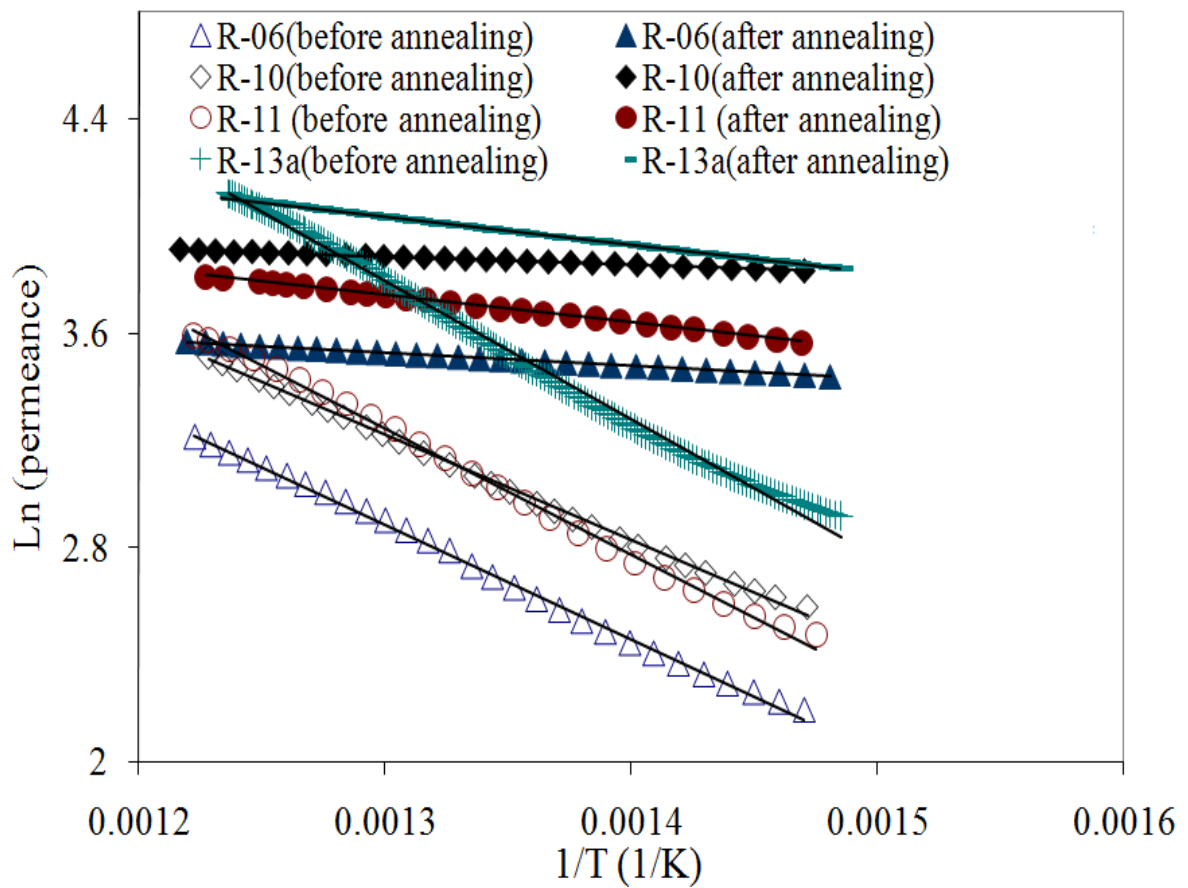


Fig. 7.4. H_2 permeance of the membranes measured during the temperature ramp between 400 and 550 °C before and after the annealing step at 550 °C.

7.3.4. Post annealing H₂ permeation characteristics

Fig. 7.5 shows the Sieverts' plot for the H₂ permeation for all membranes at 500, 400, 300 and 250 °C after the annealing step. The membrane showed differences in their H₂ permeance. The difference could be due to the factors such as differences in the substrate resistance for the H₂ flow (discussed later in this section) and the concentration of Ag (discussed in Section 7.3.5), in addition to the differences in the thickness of the membranes.

The H₂ permeation through the composite membranes consisted of diffusion through the Pd-Ag layer followed by the diffusion through the substrate. In order to estimate the actual Sieverts' driving force across the Pd-Ag layer, the unknown value of pressure at the interface between the Pd-Ag layer and the substrate was calculated by eliminating the pressure drop through the substrate. Fig. 7.6 shows the schematic of the H₂ permeation through the composite membrane. P₂ and P₁ in Fig. 7.6 refer to measured pressures on both sides of the membrane and P_i (unknown value) refers to the pressure at the substrate and Pd-Ag layer interface. For a particular H₂ flux measurement, the pressure drop through the substrate was calculated using Eq. 7.1. The unknown value of P_i was then calculated by adding the pressure drop through the substrate to the measured pressure P₁.

The values of α and β for H₂ at different temperatures required in Eq. 7.1 were obtained from the value of α and β for the He flow measured at room temperature (Fig. 7.2) using the following relations [48].

$$\frac{\alpha_{H_2}(T)}{\alpha_{He}(298)} = \frac{\sqrt{M_{He}}}{\sqrt{M_{H_2}}} \times \frac{\sqrt{298}}{\sqrt{T}} \quad 7.2$$

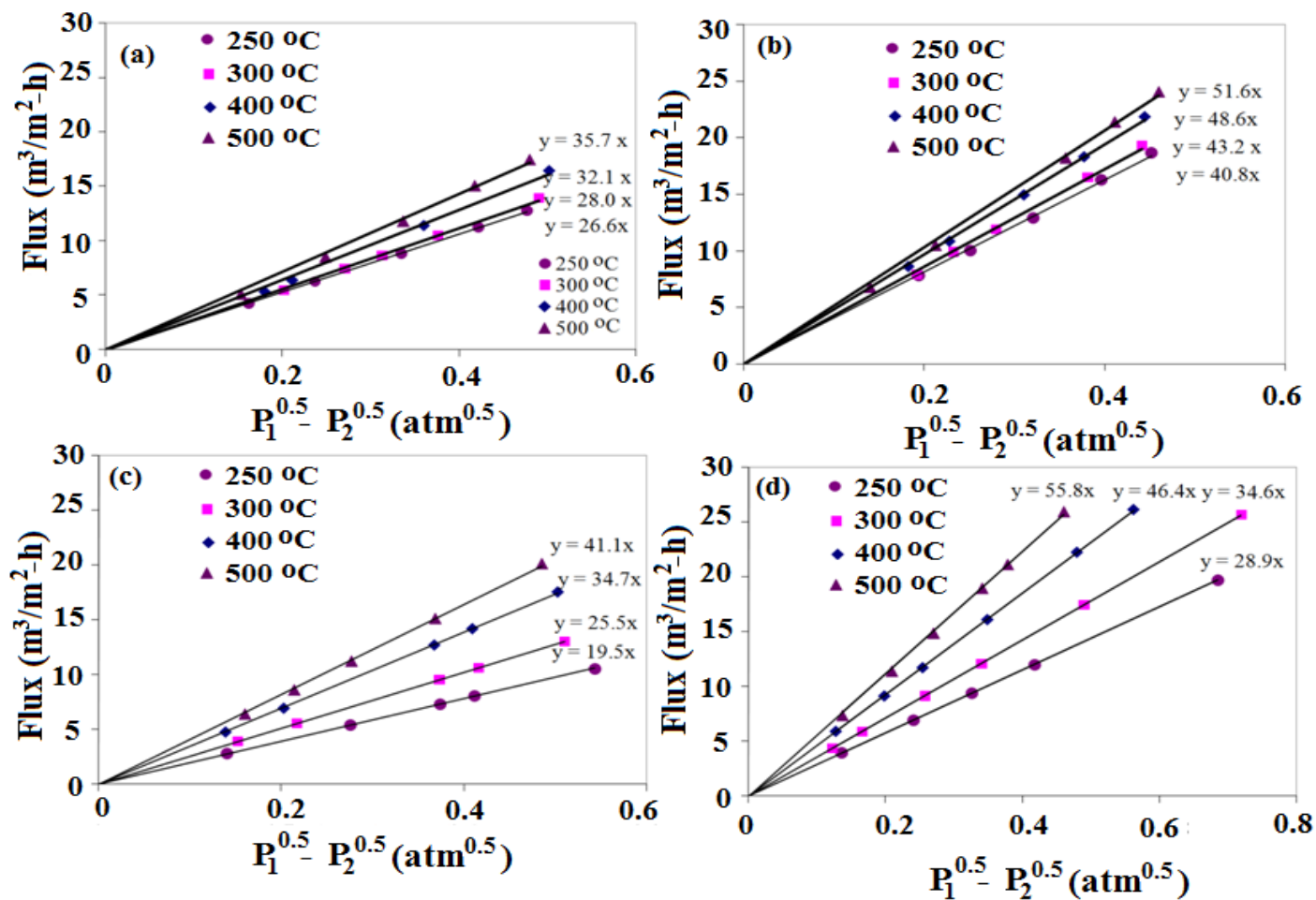


Fig. 7.5. Sieverts' plot for the H_2 permeation between 250 and 500 °C without accounting the pressure drop through the substrate (a) R-06 (b) R-10 (c) R-11 (d) R-13a.

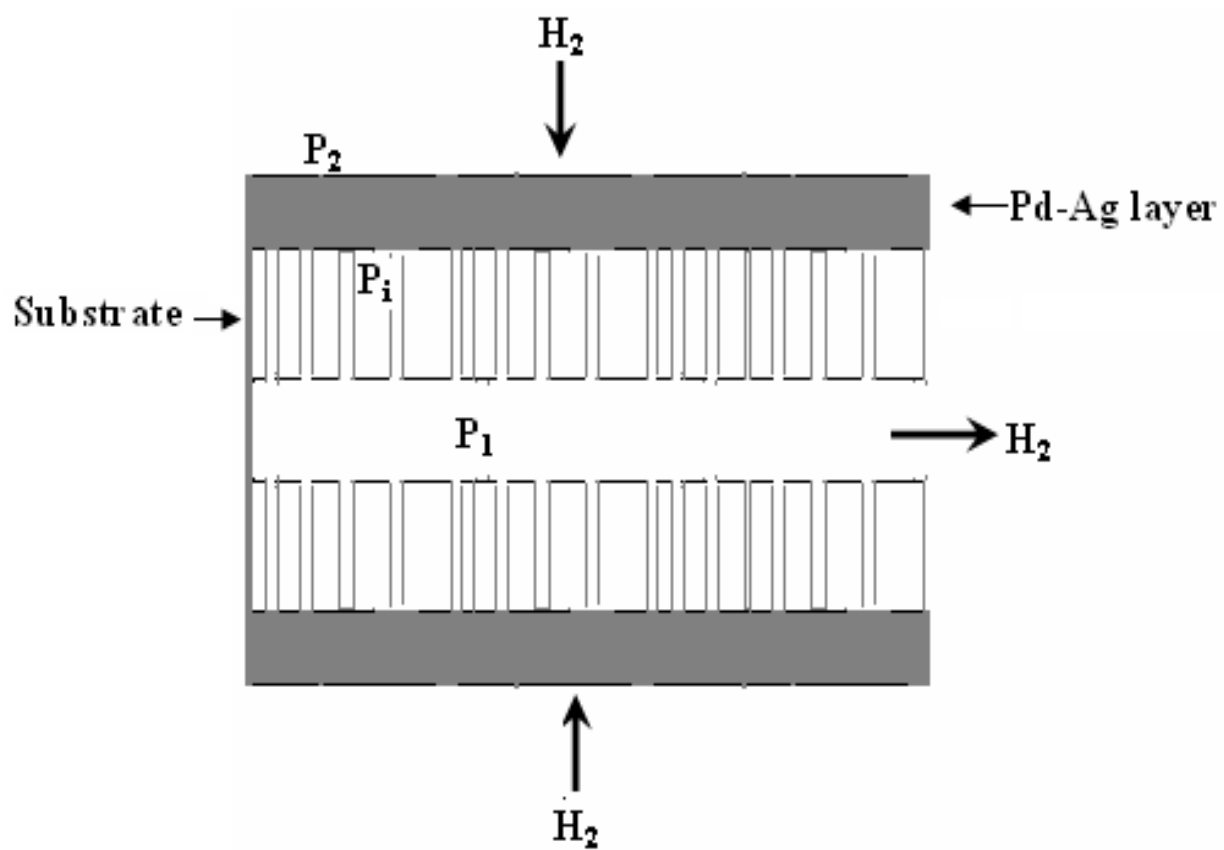


Fig. 7.6. Schematic of H_2 permeation through the composite membrane.

$$\frac{\beta_{H_2}(T)}{\beta_{He}(298)} = \frac{\mu_{He}(298)}{\mu_{H_2}(298)} \times \frac{\mu_{H_2}(298)}{\mu_{H_2}(T)} \times \frac{298}{T} \quad 7.3$$

The symbols μ , M , T , α and β in Eqn. 7.2 and Eqn. 7.3 stand for viscosity of the gas (kg/m-sec), molecular weight of the gas (g/mole), temperature (K), Knudsen contribution to the gas flow (m³/m²-h-bar) and viscous contribution to the gas flow (m³/m²-h-bar²) through the substrate respectively.

Fig. 7.7 shows the Sieverts' plot using P_2 and P_1 to calculate the Sieverts' driving force for the H₂ permeation. After accounting for the substrate resistance, the H₂ permeability (i.e. membrane thickness multiplied by its H₂ permeance) for R-06, R-10, R-11 and R-13 at 300 °C was 266, 464, 241 and 254 m³- μ m/m²-h-atm^{0.5} respectively. The differences in the H₂ permeability could be attributed to the difference in the Ag concentration of the membranes (see section 7.3.5 for the SEM and EDX compositional analysis of the membranes). The membranes showed H₂ permeability trends consistent with the literature report [7] with respect to the trends in the Ag wt% of the membranes (see Table 7.3 for the Ag wt% in the membranes by EDX analysis). The higher permeability of R-10 could be attributed to its near the optimum Ag (23 wt%) concentration (see Table 7.3 for the membranes Ag wt%).

Fig. 7.8 shows the Arrhenius plot of the H₂ permeance of the membranes based on the data shown in Fig. 7.7. The activation energy for H₂ permeation through R-06, R-10, R-11 and R-13a was estimated to be 4.9, 4.2, 11.5 and 10.0 kJ/mole respectively. The calculated activation energy was lower than that for the pure Pd membrane (12-16.4 kJ/mole) [10, 102, 135]. The lower activation energies of the membranes than the pure Pd membranes could be attributed to the effect of the addition of Ag into Pd [101]. The permeability of H₂ in the Pd-Ag alloy membrane can be written as directly

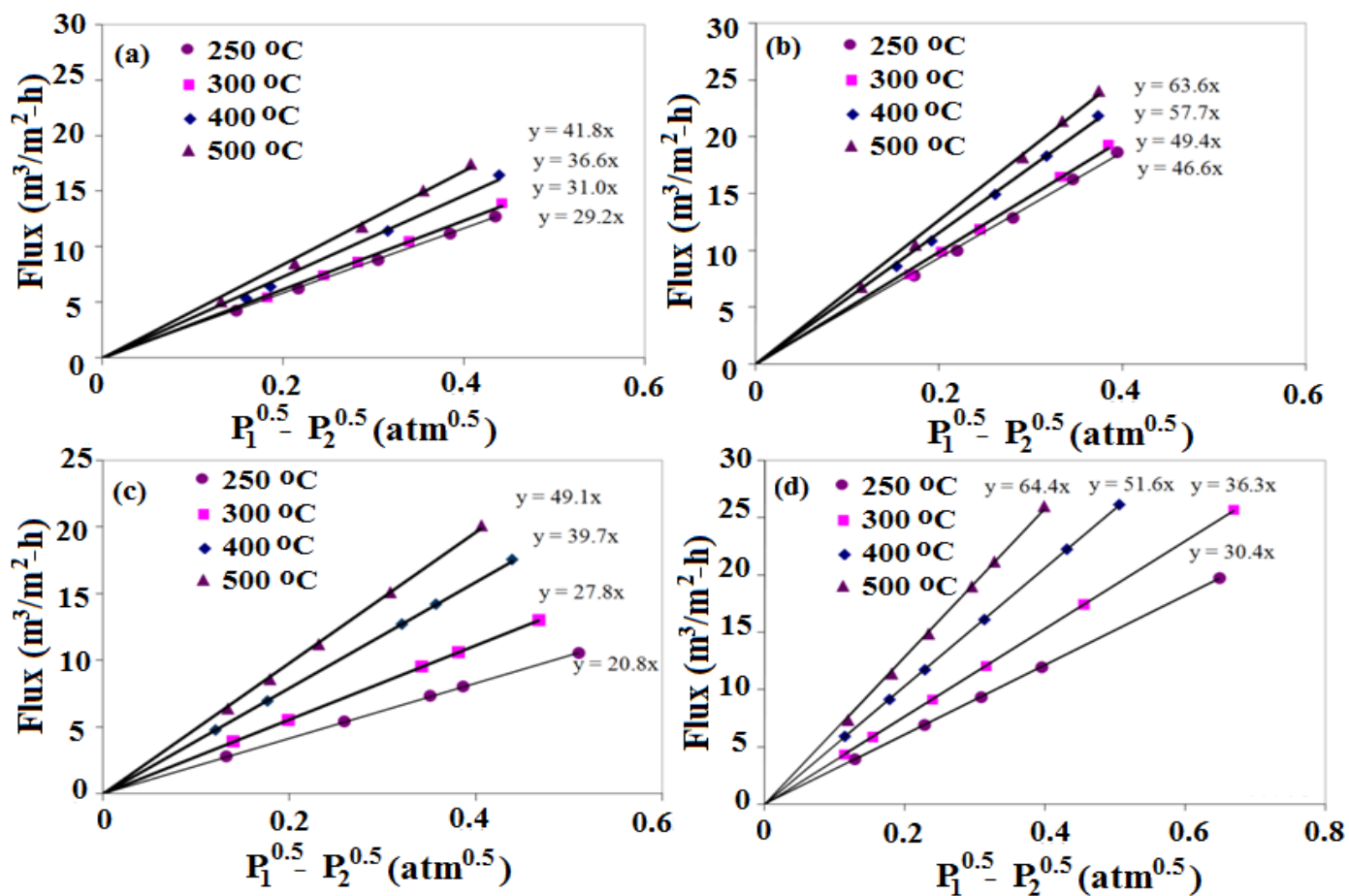


Fig. 7.7. Sieverts' plot for the H_2 permeation between 250 and 500 °C with accounting the pressure drop through the substrate (a) R-06 (b) R-10 (c) R-11 (d) R-13a.

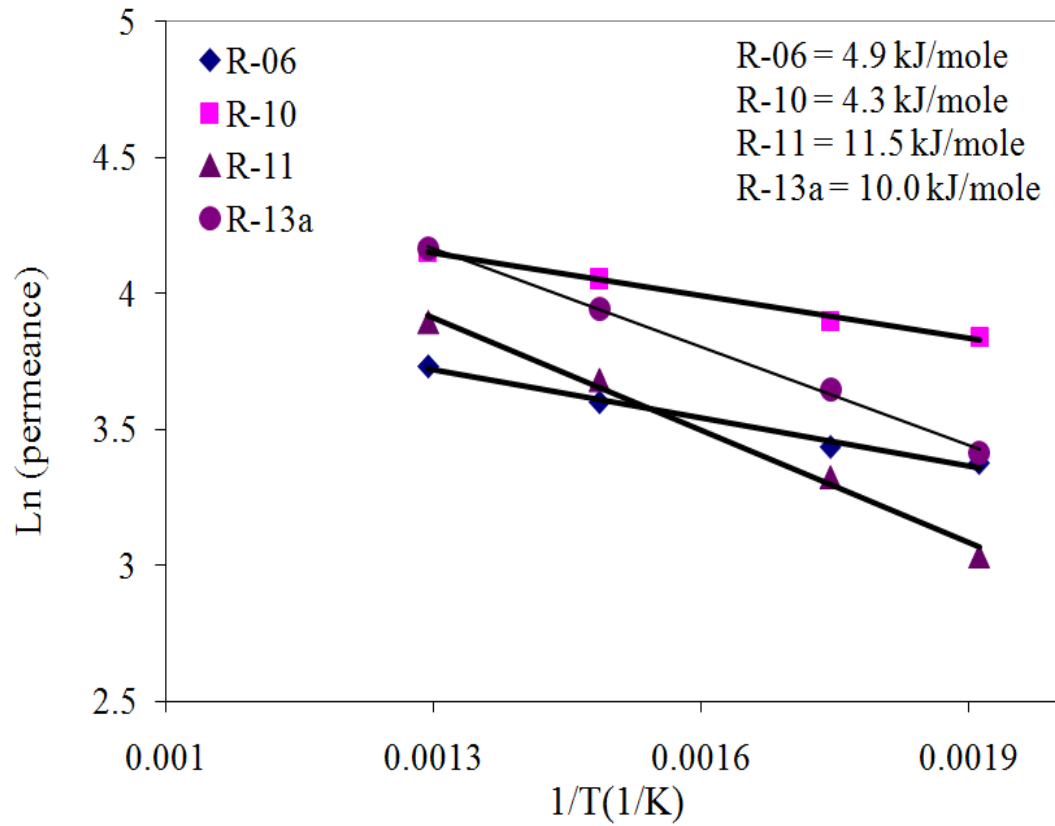


Fig. 7.8. Arrhenius plot for the H_2 permeance (250-500 °C) of the membranes after annealing at 550 °C.

proportional to the product of hydrogen diffusivity and solubility (see Chapter 4, Section 4.2) as shown in Eq. 7.4 [101].

$$P \propto DS \propto D_0 \exp\left[-\frac{E_D}{RT}\right] S_0 \exp\left[\frac{-\Delta H}{RT}\right] \propto D_0 S_0 \exp\left[-\frac{E_D + \Delta H}{RT}\right] \quad 7.4$$

Where the symbols P, D, S, E_D and ΔH in Eqn. 7.4 stand for the H₂ permeability (m³-m/m²-h-atm^{0.5}), H-atom diffusivity (m²/h), H-atom solubility (m³/m³-atm^{0.5}), activation energy for the H-atom diffusion (kJ/mole) and the enthalpy change for the hydrogen solubility (kJ/mole of H-atoms) respectively in the Pd-Ag alloy. Eqn. 7.4 shows that the activation energy for the H₂ permeability is the sum of the activation energy for the H-atoms diffusion and the change in the enthalpy for the hydrogen solubility in the Pd-Ag alloy. The alloying of Pd with Ag increased the activation energy for the H-atoms diffusion in Pd [102] and decreased the change in the enthalpy for H-atoms solubility in Pd with the minimum in the range of 20-40 wt% Ag in Pd [102, 95]. Therefore, the net effect was that the sum of E_D and ΔH decreased up to 20-30 wt% Ag in Pd and then increased with further addition of Ag into Pd [102]. For example, the value of activation energy (E_D) for the H-atoms diffusivity changed from 22.0 to 24.7 kJ/mole [102] and the change in the enthalpy (ΔH) decreased from -8.4 to -15.3 kJ/mole when Ag wt% in the Pd increased from 0 to 30 [102]. Therefore, the net effect was the decrease in the activation energy for H₂ permeability from 13.6 (Pd with 0 wt% Ag) to 8.2 kJ/mole (Pd with 20 wt% Ag) [102].

The activation energy for the H₂ permeation in Pd-Ag alloy foils reported in the literature is shown in Fig. 7.9 [17, 99, 101-103, 112]. Based on the data shown in Fig. 7.9, the average activation energy for the Pd-Ag (25 wt%) alloy was 7.3 kJ/mole. It can be also observed from Fig. 7.9 that the activation energy decreases with the increase in the Ag content up to 20-30 wt% and then start increasing with further increase in the Ag

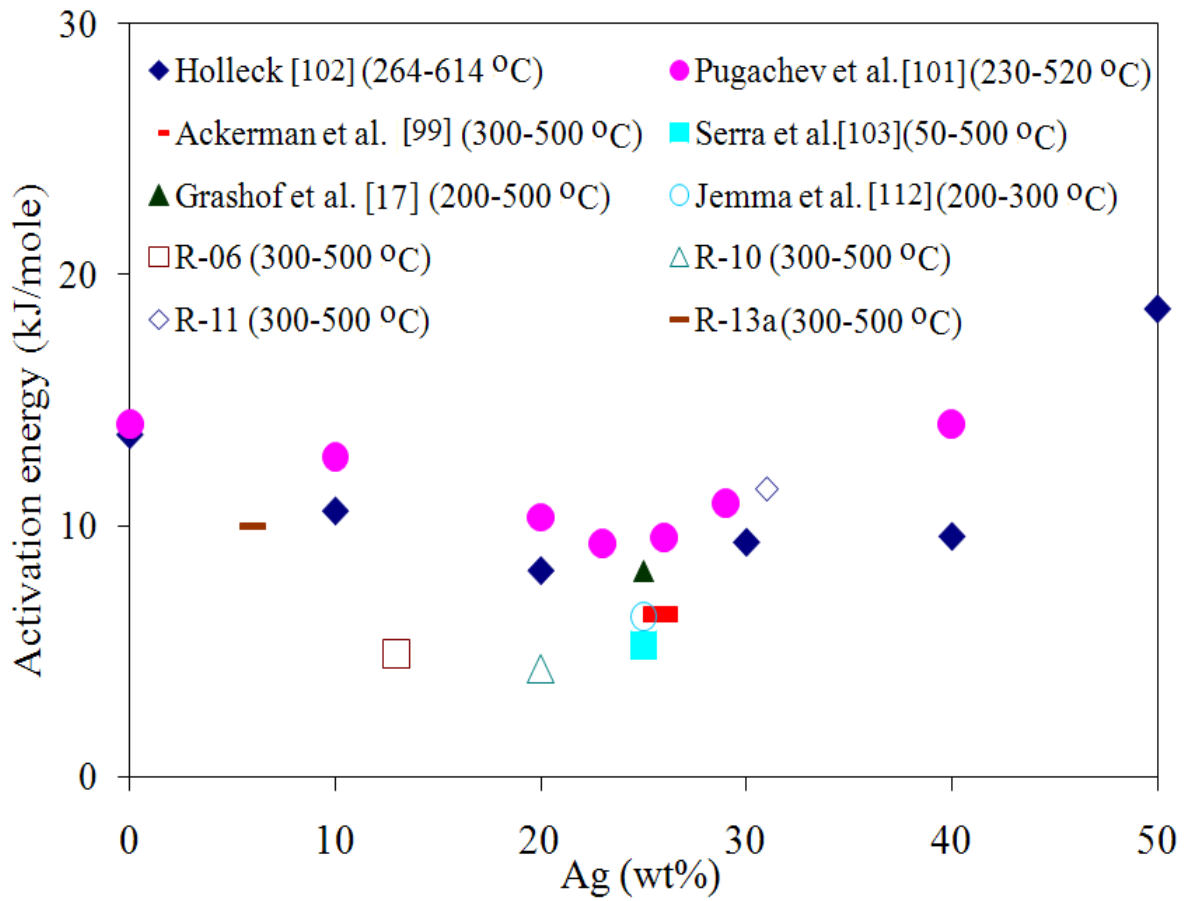


Fig. 7.9. Activation energy for the H_2 permeation in Pd-Ag alloy with different wt% Ag

wt% in the Pd-Ag alloy. The lower activation energy of Pd-Ag alloy for the H₂ permeation than that of pure Pd indicated that the H₂ permeability in Pd-Ag alloy would decrease at a lesser rate than that of Pd on temperature decrease, making Pd-Ag alloy membranes more effective for the H₂ separation at lower temperatures. The trend of more effectiveness of Pd-Ag membranes for H₂ separation at lower temperatures became clear in Fig. 7.10, which shows the relative H₂ permeance of the membranes with respect to the permeance of the Pd foil. The relative permeance was calculated by dividing the H₂ permeance of the membrane (obtained from Fig. 7.7) with the H₂ permeance of the Pd foil of the same thickness as that of the membrane. The Pd foil permeance was taken from Guazzone [19], who compiled the permeance data from several literature reports. According to Guazzone [19], the H₂ permeance of Pd foil could be written as the following equation (Eqn. 7.5)

$$Q = \frac{525}{z} \exp\left(\left(\frac{-14.6 \times 1000}{8.314}\right)\left(\frac{1}{T} - \frac{1}{773}\right)\right) \quad 7.5$$

Where Q , z and T stands for the H₂ permeance of the Pd foil (m³/m²-h-atm^{0.5}), thickness of the foil (μm) and temperature (K) respectively.

7.3.5. SEM and EDX analysis

Several SEM images of the cross-section of the membranes were taken at random locations and the thickness of Pd-Ag layer was measured. Typical images of the cross-section are shown in Fig. 7.11. The Pd-Ag layer thickness of R-06 ranged between 6.0 and 11 μm with an average value of 8.4 μm. For R-10 and R-11, the thickness ranged between 5.3 and 12.0 μm (average value = 8.5 μm) and 5.6 and 11.5 μm (average value = 8.8 μm) respectively. The average thickness of the Pd-Ag layer measured by the SEM

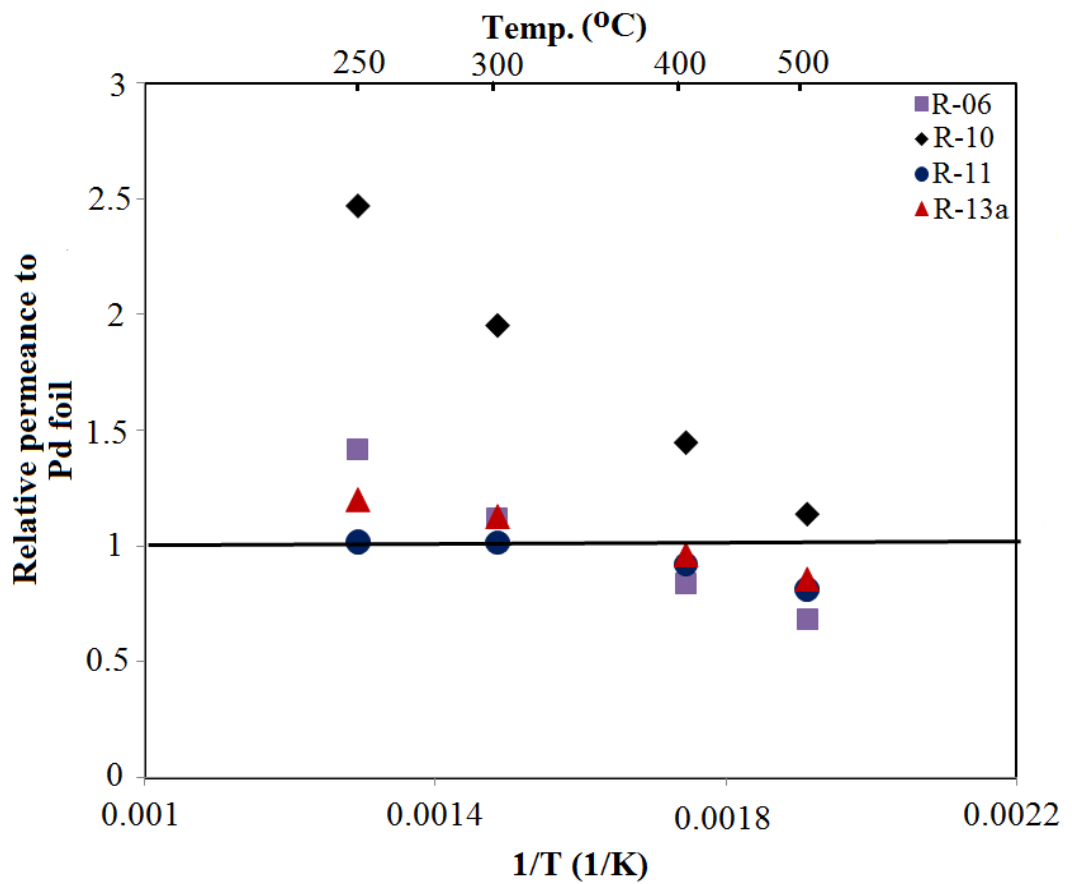


Fig. 7.10. H₂ permeance of the membranes relative to the pure Pd foils with the thickness same as that of the membranes

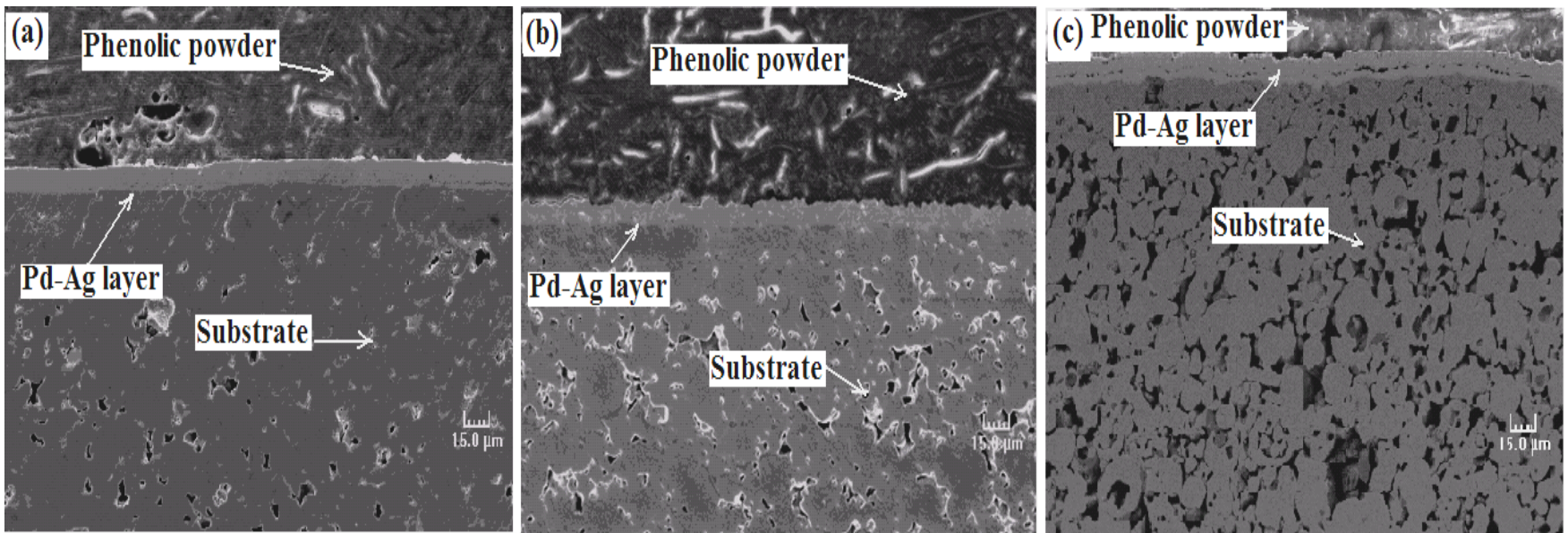


Fig. 7.11. SEM image of the membrane cross- section after annealing and H_2 permeation characteristics study (a) R-06 (b) R-10 (c) R-11

and gravimetric method in all the membranes agreed fairly well and the difference was less than $1\ \mu\text{m}$ in all three membranes.

The EDX line scans of the cross-sections showed fairly uniform distribution of Pd and Ag in the membranes. Fig. 7.12 shows the EDX line scans of the cross sections of the membranes. As can be seen in the line scans, the small amount Pd was also observed on the substrate side. The presence of Pd on the substrate side was due to the thin layer of Pd sputtered on the samples before the line scan acquisition.

Several authors have reported Pd-Ag annealing results in the context of synthesizing Pd-Ag membranes very similar to the present study. According to Shu et al. [43], Ag showed penetration depth of $1.2\ \mu\text{m}$ into Pd when a $2.4\ \mu\text{m}$ thick Pd layer with a very thin layer of Ag on the top was annealed at $600\ ^\circ\text{C}$ for 5 h in H_2 . In other similar study, Ma et al. [86] deposited a $2.4\ \mu\text{m}$ Pd layer followed by a $0.75\ \mu\text{m}$ thick Ag layer on the top of an oxidized stainless steel substrate. The layers were then annealed at $600\ ^\circ\text{C}$ for 10 h but in the He atmosphere. The Ag concentration gradient existed in the annealed Pd-Ag layer with more Ag concentration on the tip of the substrate pore than inside the pore. This was due to the deposition morphology of Ag layer itself. Ag deposited more on the tip of the substrate pore than inside the pore, resulting in the incomplete annealing of the Pd-Ag layer. Keuler et al. [136] annealed $4.0\ \mu\text{m}$ thick sequentially deposited Pd and Ag layers (24 wt% Ag) at $650\ ^\circ\text{C}$ (5 h, in the H_2 atmosphere). Their concentration profile analysis showed fairly complete annealing of the Pd-Ag layers.

The EDX spot scans obtained at random locations across several cross-sections of R-06 and R-10 revealed that at no point in the membranes, Ag wt% exceeded the value of 30, however, in the case of R-11, few spots with Ag wt% as high as 40 were also observed. The overall wt% of Ag in the membranes based on the EDX area scans of

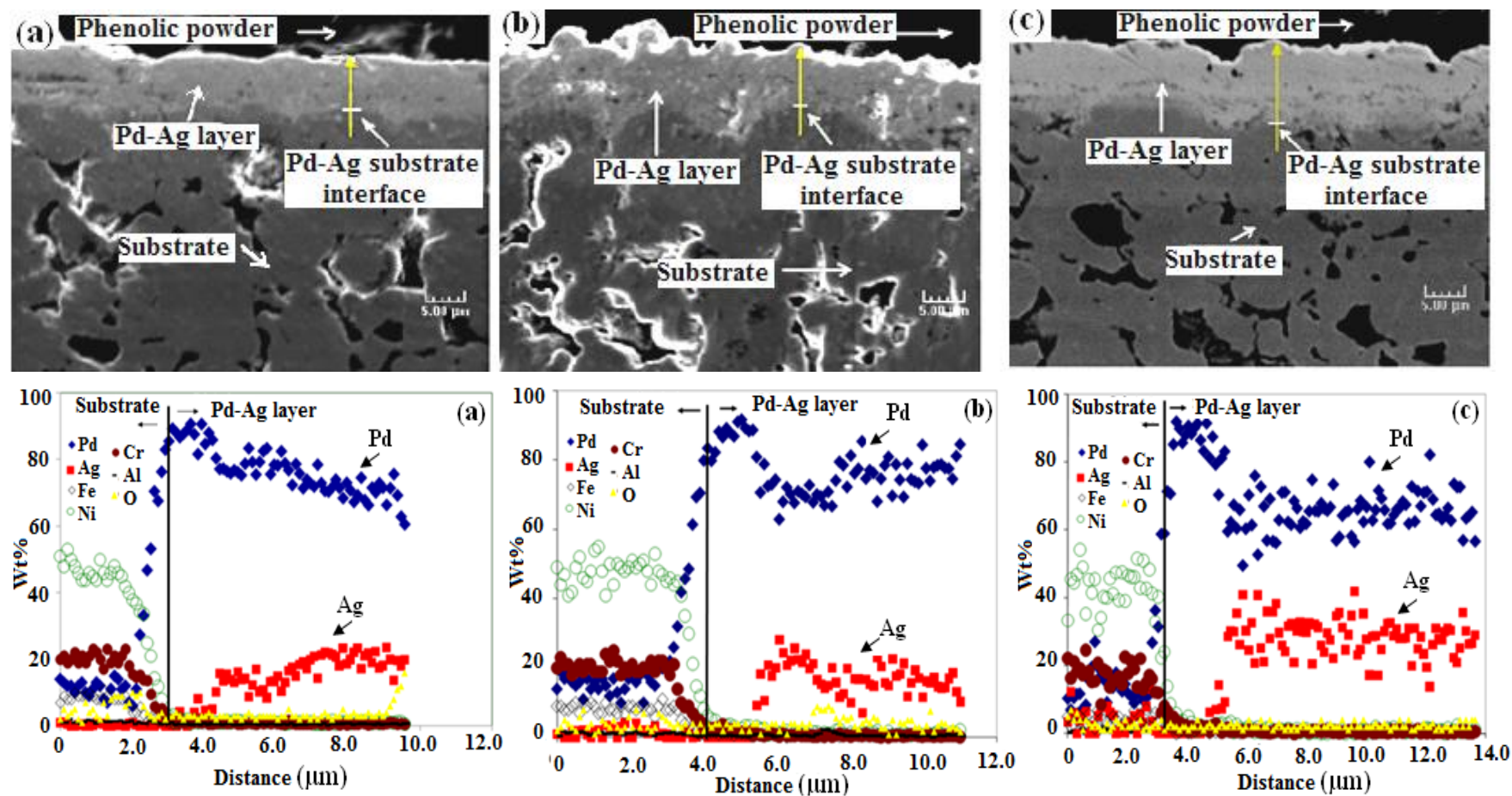


Fig. 7.12. EDX line scans of the membranes cross-section after annealing and H_2 permeation characteristics study (a) R-06 (b) R-10 (c) R-

Pd-Ag layer cross section varied from regions to regions measured by the EDX cross-section area scan for the membrane at several locations. The average Ag wt% for R-06, R-10 and R-11 was 13, 20, 31 respectively (Table 7.3). The higher permeability of R-10 could be attributed to its near the optimum Ag (23 wt%) concentration [7].

7.3.6. H₂/He selectivity ($\Delta P = 1 \text{ atm}$)

The membranes showed decline in H₂/He selectivity after annealing at 550 °C. No He leak was detected ($\Delta P = 1 \text{ atm}$) in R-06, R-10 and R-13a prior to the annealing step at 400 °C, however R-11 showed He leak of 0.2 ml/min before annealing at 400 °C ($\Delta P = 1 \text{ atm}$). The He leak after the annealing step increased to 6, 2, 3 and 2.6 ml/min ($\Delta P = 1 \text{ atm}$) with corresponding H₂/He selectivity of 85, 380, 184 and 280 for R-06, R-10, R-11 and R-13a respectively. For all the membranes, no decline in the selectivity was measured on further characterization at 300 and 400 °C. However at 500 °C, the selectivity declined from 95 to 60 for R-06, 436 to 335 for R-10 and 215 to 150 for R-11 after 60 h. R-13a was exposed to 500 °C for only 5 h and no significant increase in the He flux was observed. The decline in the membrane selectivity on exposure at 550 °C was also reported by Paglieri et al. [137] for their alumina supported pure Pd membranes. The authors [137] postulated the incorporation of bath components into the deposits, crystalline defects in the deposits as the possible causes for the decline in the membrane selectivity. Guazzone [11] and Guazzone and Ma [138] also observed the decline in the selectivity of Pd membranes on exposure in the temperature range of 400-500 °C. According to the authors, due to the small grain size of the Pd deposits, the deposits contained extra energy and on heating, the deposits released the excess energy through grain growth by incoherent sintering mechanism resulting in the pore formation

Table 7.3. *The Ag wt% measured by EDX area scan*

Location	R-06	R-10	R-11
	(Ag wt%)	(Ag wt%)	(Ag wt%)
1	19	26	27
2	12	23	26
3	12	18	35
4	10	18	36
5	17	18	29
6	10	19	31
average	13	20	31

in the deposits. Similar factors could be responsible (as mentioned by Paglieri et al. [137], Guazzone [11] and Guazzone and Ma [138]) for the decline in the selectivity observed for the membranes in this study. The other factors such as the entrapment of the formed N_2 gas could create porosity in the deposits and lead to the decline in the membrane on heating (see Chapter 9 for details)

7.4. Conclusion

Thin and He dense Pd-Ag membranes were successfully synthesized by the electroless and electroplating conditions used in this study. The membranes on annealing showed significant increase in the H₂ permeance due to the Pd-Ag alloy formation. After the annealing step, the membranes showed low activation energy for the H₂ permeability in agreement with lower activation energy reported for Pd-Ag alloy membranes in the literature. The annealing conditions used were suitable for the alloying of Pd-Ag layers in the thickness range of 2-3.0 μm or less. Also significant decline in the membrane selectivity was observed due to the He leak formation under the investigated annealing conditions.

8. Pd-Ag co-deposits: characterization and membrane synthesis

8.1. Introduction

This chapter focused on the characterization of the Pd-Ag co-deposits obtained under the plating conditions with different complexing agents investigated in Chapter 6. The Pd-Ag simultaneous deposition method has advantages over the sequential deposition method in terms of less number of steps involved in the membrane synthesis and possibly easier annealing of the Pd-Ag deposits. The advantage of easy annealing of the Pd-Ag deposits in the case of simultaneously deposition could only be achieved if the deposits obtained were either the alloy phase or the particles size of the obtained Pd-Ag deposits (if the co-deposits were individual particles of Pd and Ag) is in the range of few micrometers with homogeneous distribution of the two metals throughout the deposits. Therefore, the objective of the study in this chapter was to characterize the Pd-Ag co-deposits obtained under the plating conditions with different complexing agents. The important deposits characteristics investigated from the membrane synthesis point of view were morphology (important for preparing thin and H₂ selective membrane), Pd and Ag particle size (important from Pd-Ag alloying point of view), Pd-Ag distribution in the deposits (important from alloying point of view) and crystalline structure (important from the alloy formation point of view).

8.2. Experimental

8.2.1. Plating conditions and substrate

The bath compositions used for the Pd-Ag co-deposition in the case of NH_3 and glycine based baths were the same as shown in Chapter 6, Section 6.2 with the difference that the total metal concentration was lowered to 4 mM. The EDTA based bath at $\text{pH} = 11$ (used for the LSV study, see Chapter 6, Section 6.2) showed instant homogeneous precipitation of Pd and Ag ions in the bath. The stability of EDTA based bath was improved by lowering the bath pH by simply adjusting the amount of NaOH added into the solution. The EDTA based bath at $\text{pH} = 9.5$ (total metal concentration = 4 mM) was observed to be stable (no homogeneous precipitation of Pd and Ag) for a minimum of 2 h at $60\text{ }^\circ\text{C}$ after the addition of N_2H_4 and was used for the deposition. In all the experiments involving the Pd-Ag deposition and investigating the bath stability (for NH_3 , EDTA and glycine based baths), the N_2H_4 concentration of 5 mM was maintained. All the deposition experiments were performed on the PSS coupons (see Chapter 3, Section 3.2).

In contrast to NH_3 , EDTA and glycine baths, the KCl bath used in Chapter 6 (see Section 6.2) showed precipitation of Pd and Ag ions in the solution on the addition of N_2H_4 in all the basic pH range ($\text{pH} > 7.0$). Therefore, the combination of several reducing agents and different pH conditions were investigated to find the stable bath conditions (see Table 8.1 for the bath compositions). For the Pd-Ag deposition on the PSS coupons from KCl bath, the coupons were activated with Pd nuclei (see Chapter 3, Section 3.2.2) and pre-plated Pd for 3 min to have a very activated surface before dipping in the KCl solution. The KCl bath in acidic conditions showed severe dissolution (oxidation) of the PSS components and lead to Pd-Ag deposition even

Table 8.1. KCl bath composition

Bath component	Conc. range
Total metal conc.	2 - 10 mM
PdCl ₂	1.6 - 8 mM
AgNO ₃	0.4 - 2 mM
KCl	4 M
H ₃ BO ₃	0.04 M
N ₂ H ₄	2 - 50 mM
HCHO	2 mM - 2 M
TMAB	1-2 mM
(Triethylamine borane)	
pH	1.5 - 11
Temp. °C	20-60

without the presence of a reducing agent in the solution. To avoid the dissolution (oxidation) of the PSS coupons in the acidic KCl bath and clearly see the effect of N_2H_4 and HCHO as the reducing agents, Pd foils (2 cm^2 and $\sim 20\text{ }\mu\text{m}$ thick) were used as the substrate in place of the PSS coupons. Before dipping the Pd foils in the KCl solution, the foils were plated with Pd for 3 min to achieve the very activated surface. All the depositions in the KCl bath were performed for 2 h.

For all the stability conditions investigated in the KCl bath, the solution volume of 20 ml was used and was examined for 10 minutes in order to observe the precipitation of Pd and Ag ions in the solution. In all the deposition cases, the loading (the ratio of the plating solution volume to the plated area) of $25\text{ cm}^3/\text{cm}^2$ ($50\text{ cm}^3/2\text{ cm}^2$) was maintained.

8.2.2. Coupon annealing

For the annealing characteristics of the Pd-Ag co-deposits, the substrate (PSS coupons) with Pd-Ag co-deposits was annealed at 400 and 500 °C in the H_2 atmosphere for 10 h. The substrate was heated to 250 °C (5 °C/min) in the He atmosphere and then switched to H_2 atmosphere. The temperature was then ramped up to 400 or 500 °C (5 °C/min) in the H_2 atmosphere and remained in the H_2 atmosphere for 10 h at 400 or 500 °C. All the coupons used for the annealing experiments were oxidized at 700 °C (10 h) in air before performing the Pd-Ag co-deposition.

8.2.3. Membrane synthesis and characterization

For the membrane preparation using the glycine based bath, two inconel tubes (~ 23

cm² each) designated as R-09 and R-12 were used. The inconel tubes were oxidized in air at 700 °C for 10 h before the Pd-Ag deposition. Since, the membranes prepared in this study were not exposed to temperature higher than 400 °C, therefore the oxidation of the inconel tubes was used as the intermetallic diffusion barrier step (see Chapter 3, Section 3.2.2). The oxidation layer formed at 700 °C was expected to be an effective intermetallic diffusion barrier without causing significant mass transfer resistance for the H₂ gas diffusion through the substrate (see Chapter 3, Section 3.2.2). The tubes were graded with alumina powder (0.3 μm) followed by activation with Pd nuclei (see Chapter 3, Section 3.2.2) before the plating step. The total metal concentration in the plating bath was kept at 4 mM with 10 at% Ag.

R-09 was plated for 9.5 h. The solution was replaced after every 60 minutes. After 6 h of plating, the membrane surface was gently rubbed with thumb to remove any loose deposits obtained. The synthesis procedure for R-12 was slightly different from that adopted for R-09. In the case of R-12, the membrane surface was polished with SiC paper (1200 grit size) after every 1 h of plating to remove any loose deposits obtained. The plating solution, similar to the R-09 plating procedure, was replaced after every 60 minutes of plating. R-12 after 9 h of plating was almost He gas tight (He flow at ΔP = 1 atm was 0.1ml/min), therefore, for the next 3 h of plating, the polishing with SiC paper was not performed.

R-09 and R-12 after the synthesis step were heated in order to study their annealing and H₂ permeance characteristics in the temperature range of 250-400 °C. The membranes were heated from room temperature to 250 °C (1 °C/min) in the He atmosphere and switched to the H₂ atmosphere. The temperature was then successively increased by a step of 50 °C between 250 and 400 °C. The membranes at each

temperature were exposed to H₂ for as long as the H₂ permeance was stabilized and Sieverts' data for the H₂ permeation were obtained. After reaching 400 °C, R-12 was cooled by a step of 50 °C to 250 °C. At each temperature on cooling, again Sieverts' data for the H₂ permeation were obtained

8.2.4. Deposits morphology, compositional homogeneity and phase characterization

The morphology and homogeneity of the deposits were characterized with scanning electron microscope (SEM) equipped with EDX. For the Pd and Ag particles size analysis, the EDX spot scans were obtained at several locations throughout the deposits and the EDX penetration depth calculation was performed to obtain the particles size.

The examination of the crystalline structure of the deposits was performed using the X-ray diffractometer.

8.3. Results and discussions

8.3.1. Baths stability in the presence of N₂H₄

Before performing the actual Pd-Ag deposition, all the baths (NH₃, glycine, EDTA and KCl) were studied for their stability. NH₃ and glycine based baths (pH = 11) were stable (i.e. no homogeneous precipitation of Pd and Ag) with the presence of N₂H₄ in the bath. In contrast to the NH₃ and glycine based baths, the KCl and EDTA based baths (pH = 11) showed immediate precipitation of Pd and Ag upon the addition of N₂H₄. The EDTA based bath was made stable (no precipitation of Pd and Ag was observed for 2 h) by lowering the bath pH to 9.5 (by adjusting the amount of NaOH) which was used for

the deposition. In the case of KCl as the complexing agent, the bath showed instant homogeneous precipitation of Pd and Ag in the basic pH range (> 7) on addition of N_2H_4 . The KCl bath with the total metal concentration as low as 1 mM and N_2H_4 concentration of 1 mM showed instant homogeneous Pd and Ag precipitation between room temperature and 60 °C in the basic pH range.

The homogeneous precipitation occurred on the addition of N_2H_4 for the KCl bath in the basic conditions, therefore, other conditions (different reducing agents and acidic pH conditions) were explored for the stability of the KCl bath. Table 8.2 shows the stability results obtained for the different conditions. TMAB (trimethylamine borane) was not suitable as the reducing agent in all the pH conditions. TMAB concentration as low as 1 mM produced immediate precipitation of the metal ions in the bath. N_2H_4 and HCHO in the acidic conditions (pH ~ 1.5) did not show homogeneous precipitation of Pd and Ag and the bath was stable for the N_2H_4 and HCHO concentrations as high as 50 mM and 2 M respectively. N_2H_4 and HCHO in the acidic KCl bath were tested as the reducing agents for the Pd-Ag deposition on the PSS coupons and Pd foils.

8.3.2. Deposits morphology, crystalline structure and compositional homogeneity

Fig. 8.1 shows the morphology of the Pd-Ag co-deposits with the thickness between 3 and 4 μm obtained from NH_3 , glycine and EDTA based baths. The deposits obtained from the NH_3 bath (Fig. 8.1a) were dendritic in morphology with poor adhesion. The deposits could be removed by gentle thumb rubbing. The morphological characteristics of the deposits were very similar to those obtained from conventional NH_3 +EDTA bath (see Chapter 6, Section 6.3.2). The large difference existed between the Pd and Ag

Table 8.2. Stability checking for the KCl bath with 20 wt% Ag and 2 mM concentration of reducing agent.

Reducing agent → Conditions ↓	N ₂ H ₄	HCHO	TMAB	N ₂ H ₄	HCHO	TMAB
60 °C						
	TMC* = 2 mM			TMC* = 10 mM		
Basic (pH ~ 10)	IP	IP	IP	IP	IP	IP
Neutral (pH~6.4)	IP	NS	IP	IP	NS	IP
Acidic (pH ~1.5)	S	S	IP	S	S	IP
20 °C						
	TMC* = 2 mM			TMC* = 10 mM		
Basic (pH ~ 10)	IP	IP	IP	IP	NS	IP
Neutral (pH~6.4)	IP	NS	IP	IP	NS	IP
Acidic (pH ~1.5)	S	S	IP	S	S	IP

Symbols used:

*TMC** = total metal concentration, *IP* = immediate precipitation, *S* = stable for 10 minutes, *NS* = not stable for 10 minutes, *TMAB* = trimethylamine borane

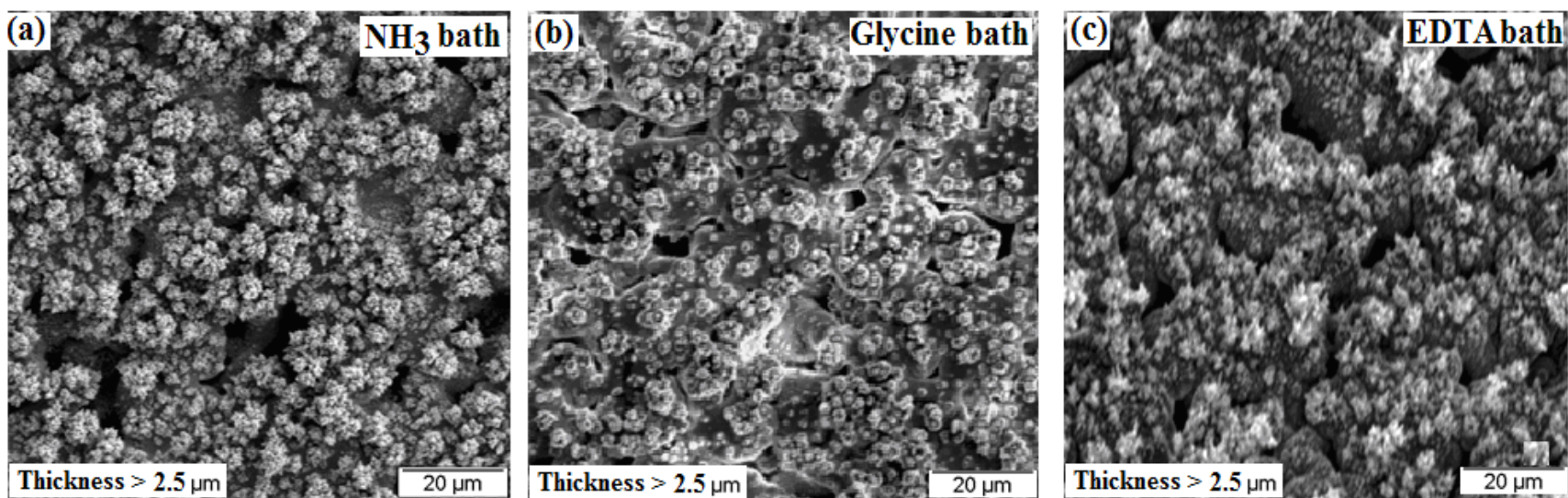


Fig. 8.1. SEM images of the Pd-Ag co-deposits obtained at total metal concentration = 4 mM (10 at% Ag), temp. = 60 °C and N₂H₄ = 5 mM in the bath (a) NH₃ bath, pH = 11 (b) Glycine bath, pH = 11 (c) EDTA bath, pH = 9.5

deposition potentials in the presence of NH_3 (see Chapter 6, Section 6.3.10) and was similar to that observed in the presence of conventional NH_3 +EDTA bath (Chapter 6, Section 6.3.1). The deposits obtained from the EDTA bath (Fig. 8.1c) were not considerably different from the deposits obtained from the NH_3 bath. The deposits obtained from the EDTA bath showed the dendritic morphology and poor adhesion similar to the deposits from the NH_3 bath. The reason for the dendritic morphology and poor adhesion could be attributed again to the large deposition potential difference of Pd and Ag in the presence of EDTA (see Chapter 6, Section 6.3.10) similar to the NH_3 bath. The difference in the deposition potentials of Pd and Ag in the presence of glycine was similar to that observed in the presence of EDTA (see Chapter 6, Section 6.3.10), however the deposits obtained from the glycine bath (Fig. 8.1b) were relatively compact in morphology in comparison to the deposits obtained from the EDTA and NH_3 bath (Fig. 8.1a and Fig. 8.1c). The deposits (glycine based) showed more growth in the perpendicular direction than the lateral direction to the substrate surface. The adhesion of the deposits from the glycine bath was better than the deposits obtained from the NH_3 and EDTA baths, however, the deposits could still be removed by the mild thumb rubbing.

According to Calusaru [128], there were regions of the overpotential for the deposition of every metal where compact, rough and dendritic deposits are obtained. The overpotential above which the metal deposits show dendritic morphology is called critical overpotential. For the same metal, the critical overpotential above which the deposits started showing dendritic morphology was dependent on the plating bath conditions and components such as the complexing agent in the bath [139]. For the glycine bath in this study, in addition to the lower difference between the deposition

potential of Pd and Ag in comparison to the NH_3 bath, the additional reason for the relatively compact deposits could be attributed to the increased critical overpotential for the Ag deposits in the presence of glycine.

Fig. 8.2 shows the X-ray diffraction patterns of the deposits shown in Fig. 8.1 obtained from the NH_3 , glycine and EDTA bath. Fig. 8.2 also shows the standard XRD patterns of Pd and Ag metal. As can be seen from Fig. 8.2, the patterns obtained for the deposits from all three baths matched with the individual standard patterns of Pd and Ag and the deposits obtained were bimetallic in structure, i.e., the deposits were mixture of individual Pd and Ag particles and required further annealing treatment to form Pd-Ag alloy.

In contrast to the NH_3 , glycine and EDTA baths, the acidic KCl bath (pH \sim 1.5) was very corrosive towards the PSS coupons. A PSS coupon when immersed in the KCl solution without HCHO, PdCl_2 and AgNO_3 for 20 min, lost its weight from 0.7532 g (before dipping in the solution) to 0.7290 g (after 20 min). A large amount of gas H_2 evolved at the coupons surface indicating the dissolution (oxidation) of coupon components (Fe, Ni, Cr). Fig. 8.3 shows the SEM images of the deposits obtained from the KCl bath (pH \sim 1.5) using HCHO (50 mM) as the reducing agent. Fig. 8.3a shows the deposits obtained in the presence of HCHO and Fig. 8.3b shows the deposits obtained in the absence of HCHO. The presence of Pd-Ag deposits from the KCl bath without HCHO indicated that the substrate itself acted as the reducing agent (i.e. the oxidation of the PSS components resulted in the reduction of Pd and Ag ions in the solution). The gas bubbles similar to that observed for the PSS coupon immersed in the KCl bath without the metal ions appeared at the substrate surface indicating the substrate oxidation. During the 2 h deposition, the substrate corresponding to Fig. 8.3a lost its

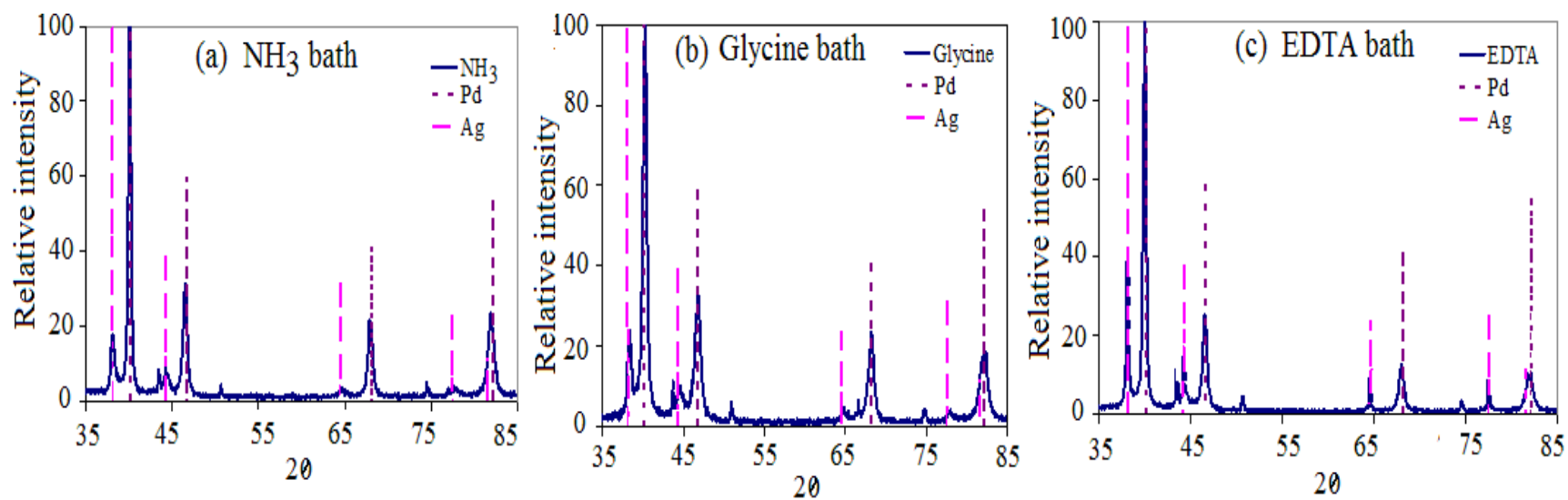


Fig. 8.2. XRD pattern of the Pd-Ag co-deposits obtained at total metal concentration = 4 mM (10 at% Ag), temp. = 60 °C and N_2H_4 = 5 mM in the bath (a) NH_3 bath, pH = 11 (b) Glycine bath, pH = 11 (c) EDTA bath, pH = 9.5

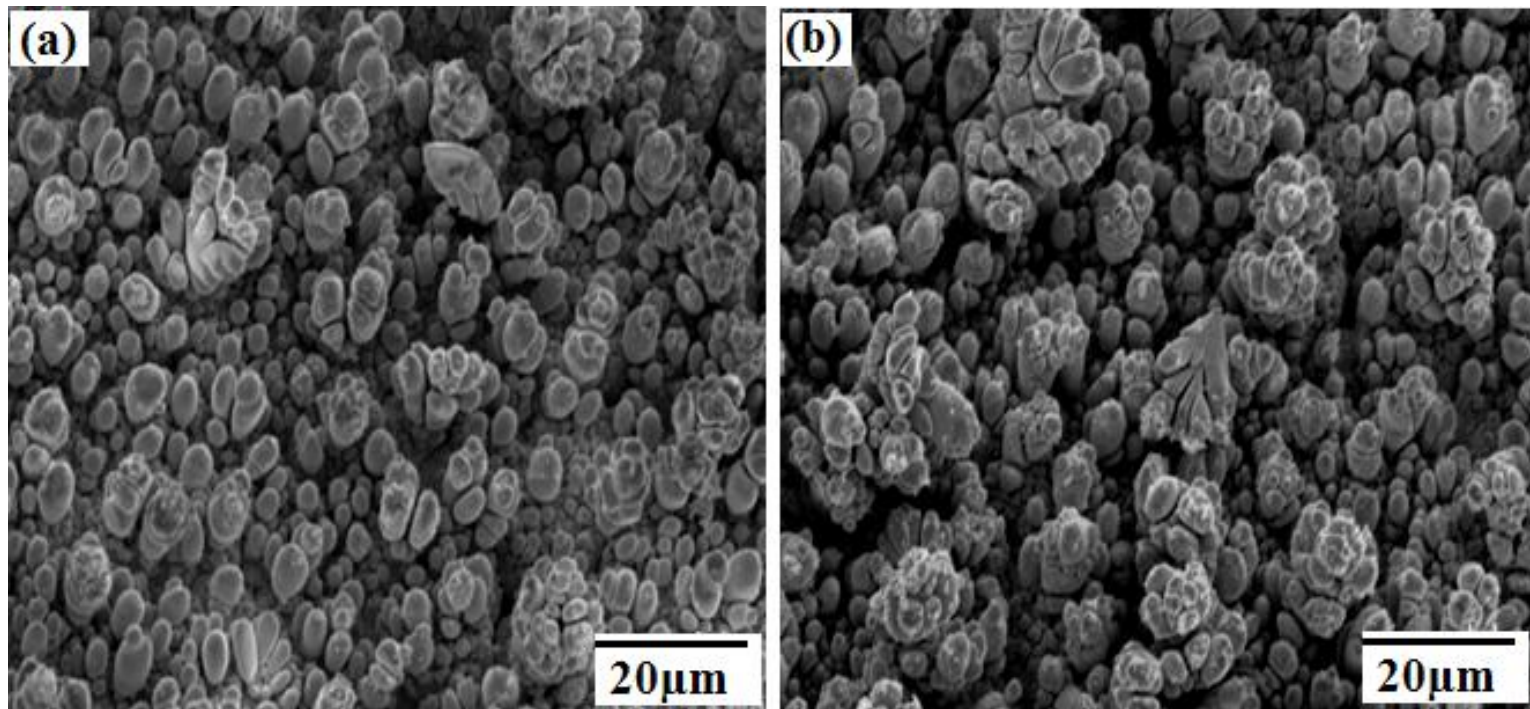


Fig. 8.3. SEM images of the deposits obtained from KCl bath ($\text{pH}\sim 1.5$) with HCHO (50 mM) as the reducing agent and bath temperature = 60°C . Total metal concentration was 10 mM with 20 at% Ag in the bath (a) with HCHO in solution (b) without HCHO in solution

weight from 0.7640 g to 0.6773 g and the substrate corresponding to Fig. 8.3b lost its weight from 0.6188 g to 0.5712 g. The weight loss indicated a large amount of dissolution (oxidation) of the substrates. From the EDX area scan analysis, the overall Ag wt% in the deposits was 18 (for the deposits corresponding to Fig. 8.3a) and 16 (for the deposits corresponding to Fig. 8.3b).

The XRD pattern of the deposits corresponding to Fig. 8.3 is shown in Fig. 8.4. The patterns show only single phase present which was in contrast to the bimetallic deposits obtained from the NH_3 , EDTA and glycine baths. The presence of single phase meant that the as obtained deposits from the KCl bath were Pd-Ag alloy and did not require further annealing step to form the alloy phase.

The deposits obtained from the NH_3 , glycine and EDTA baths, all showed large lack of composition homogeneity from region to region on the substrate surface. Fig. 8.5 shows the typical EDX spot scans of the deposits shown in Fig. 8.1. The overall Ag wt% obtained by the EDX area scan in the deposits shown in Fig. 8.5 was 14, 17 and 40 for NH_3 , glycine and EDTA bath respectively. The tag points in Fig. 8.5 with higher Ag wt% overall represented the regions in the deposits which were closer to the plating solution (away from the substrate surface) and the points with lower Ag wt% represented overall the regions closer to the substrate surface (farther away from the plating solution). The inhomogeneous Pd and Ag concentration in the co-deposits was not favorable from obtaining a homogeneous Pd-Ag alloy membrane. For example, the deposits obtained from NH_3 based bath (Fig. 8.5a) showed concentration of Ag as high as 42 wt% at the regions closure to the solution side in the deposits and as low as 2 wt% at the regions closure to the substrate side. In order to form the alloy with uniform Pd-Ag concentration across the thickness of the deposits, Ag from the high concentration

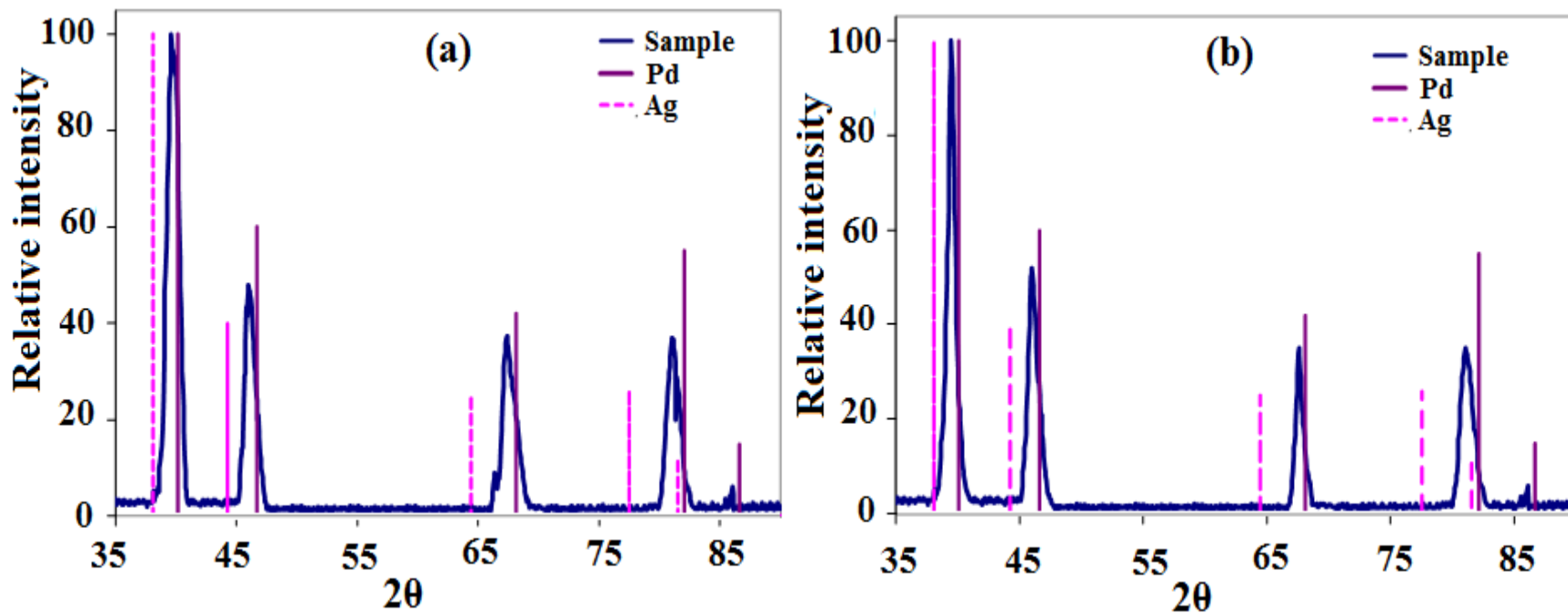


Fig. 8.4. The X-ray diffraction patterns of the deposits obtained from KCl bath (pH~1.5) with HCHO (50 mM) as the reducing agent and bath temperature = 60 °C. The total metal concentration was 10 mM with 20 at% Ag in the bath (a) with HCHO in solution (b) without HCHO in solution

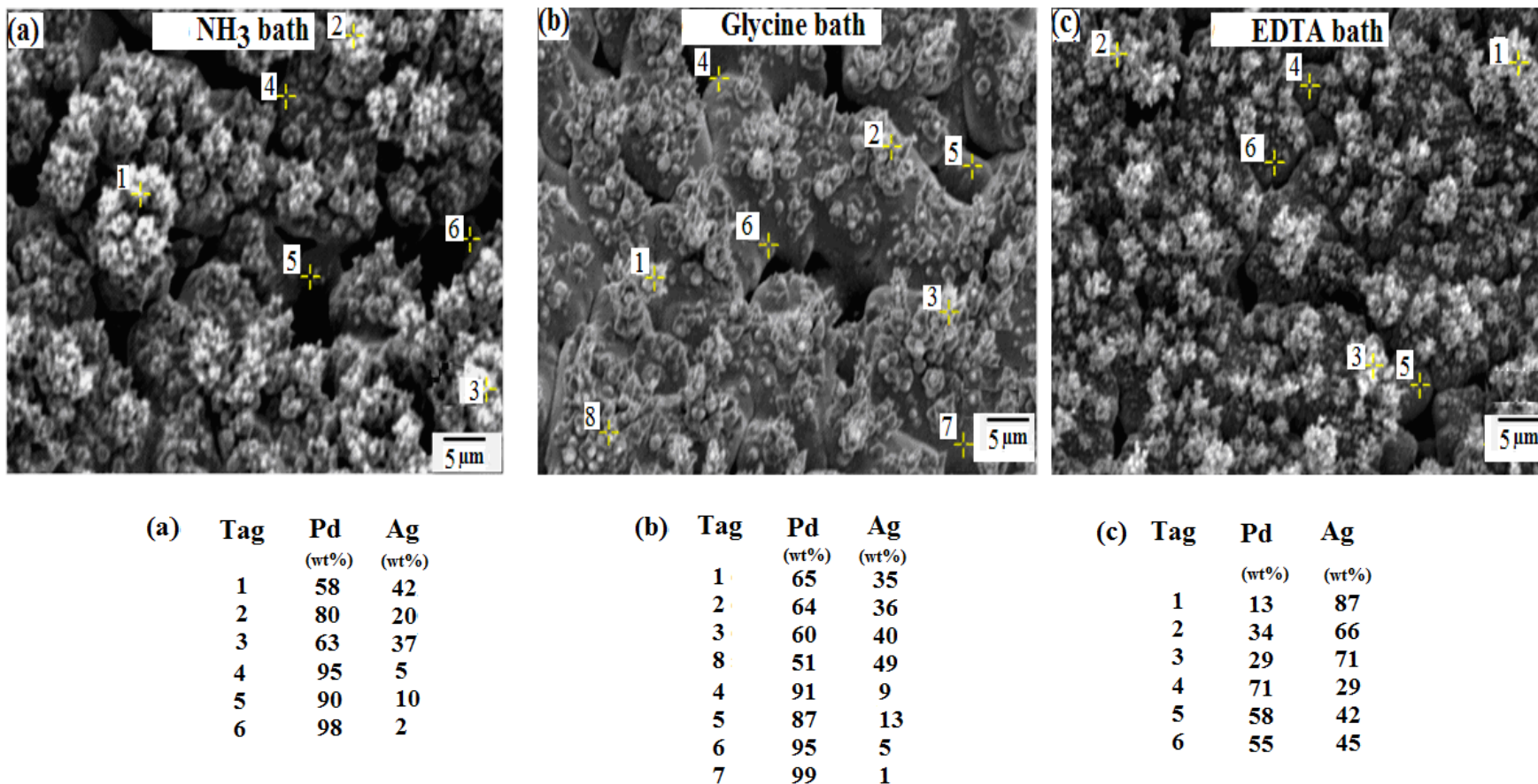
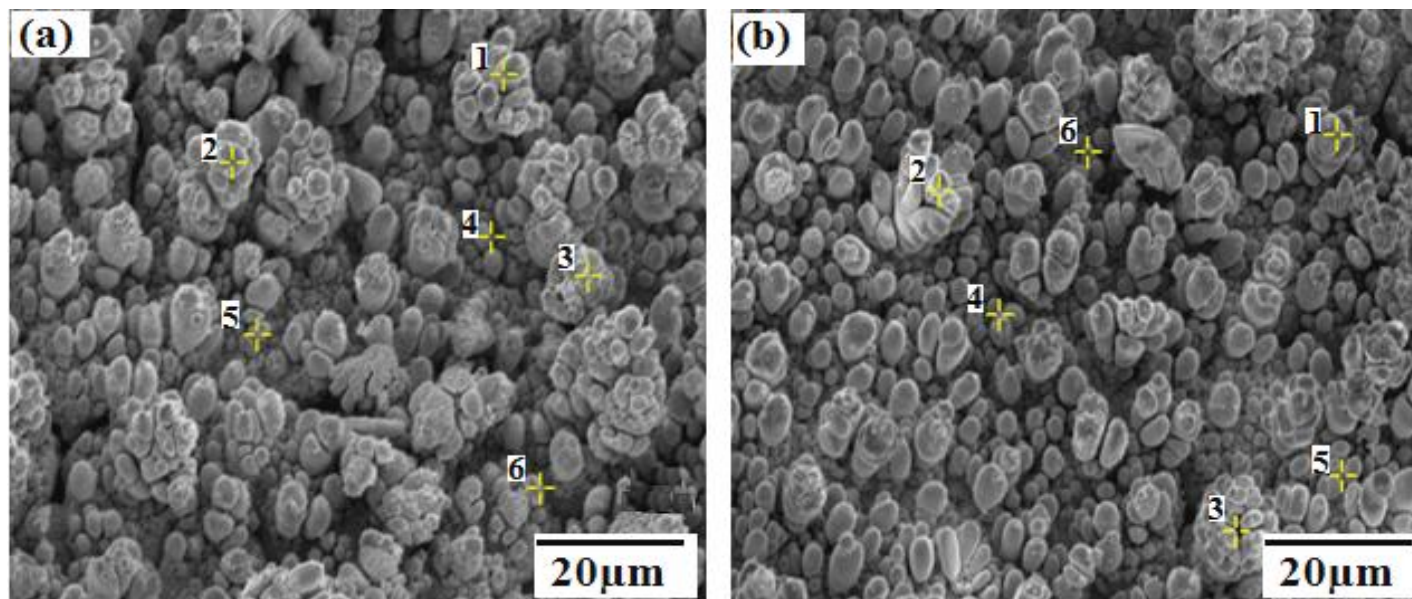


Fig. 8.5. EDX spot scans of the Pd-Ag co-deposits obtained at total metal concentration = 4 mM (10 at% Ag), temp. = 60 °C and N_2H_4 = 5 mM in the bath (a) NH_3 bath, pH = 11 (b) Glycine bath, pH = 11 (c) EDTA bath, pH = 9.5. (Note: the points with high Ag wt% are the points in the deposits more closure to the solution side and the low Ag wt% points are points away from the solution side and more near to the substrate side)

regions has to diffuse through 3 to 4 μm thickness (the approximate thickness of the deposits shown in Fig. 8.5a) which was from annealing viewpoint equivalent to the sequentially deposited layer of Ag on the top of 3 to 4 μm thick Pd layer. The Ag in all the three baths deposited under severe mass transfer limitation due to the large deposition potential difference between Pd and Ag leading to the inhomogeneous distribution of Pd and Ag in the deposits. It can also be noted from Fig. 8.5 that the glycine deposits showed relatively compact morphology, nonetheless the deposits obtained from the glycine bath showed Pd and Ag compositional inhomogeneity across the deposits similar to the deposits from NH_3 and EDTA baths

The deposits obtained from the KCl bath were very homogeneous in Pd and Ag composition than the deposits obtained from NH_3 , glycine and EDTA baths. Fig. 8.6a and Fig. 8.6b show the EDX spot scans at several locations corresponding to the deposits shown in Fig. 8.3a and Fig. 8.3b respectively. The variation in the Pd and Ag concentrations in the deposits was much less than in those deposits obtained from NH_3 , EDTA and glycine baths. The difference was due to the differences in the deposition potential of Pd and Ag in different baths. Pd and Ag showed the least difference in their deposition potential in the case of KCl bath (see Chapter 6, Section 6.3.10), therefore, providing conditions for more homogeneous Pd and Ag deposits. The deposits obtained from the KCl bath (see Fig. 8.3) showed more tendencies to deposit in the perpendicular direction to the substrate surface. The more growth in the perpendicular direction could be due to the fast dissolution (oxidation) of the substrate components. The fast oxidation of the substrate could lead to the reduction of Pd and Ag to such a high rate that both Pd and Ag start depositing under the conditions when their diffusion in the solution significantly controlling the overall deposition process and leading to the non-uniform



Tag	Pd (wt%)	Ag (wt%)	Tag	Pd (wt%)	Ag (wt%)
1	83	17	1	82	18
2	85	15	2	83	17
3	80	20	3	82	18
4	86	14	4	76	24
5	82	18	5	84	16
6	79	21	6	79	20

Fig. 8.6. EDX spot scans of the deposits obtained from KCl bath (pH~1.5) with HCHO (50 mM) as the reducing agent at bath temperature = 60 °C. Total metal concentration was 10 mM with 20 at% Ag in the bath (a) with HCHO in the solution (b) without HCHO in the solution. (Note: the points with high Ag wt% are the points in the deposits more closure to the solution side and the points with low Ag wt% are points away from the solution side and more near to the substrate side)

growth (as discussed in Chapter 5, Section 5.3.4.).

The PSS substrate itself acted as the reducing agent for Pd and Ag in the KCl bath, therefore, the reducing ability of HCHO for the Pd and Ag ions was not clear from the Pd and Ag deposition on the PSS coupons (Note: The dissolution of PSS components itself led to the Pd and Ag deposition in the absence of HCHO). In order to clearly observe the reducing ability of HCHO in the KCl bath, the Pd-Ag deposition from the KCl bath (same conditions as that used in Fig. 8.3) was performed on the Pd foils (~20 μm). Both N_2H_4 (50 mM) and HCHO (50 mM) were tested as the reducing agents. No Pd-Ag deposition was obtained from KCl bath involving N_2H_4 as the reducing agent. The foil weight remained the same before and after the deposition (2 h). In the case of HCHO after 2 h of plating, the Pd-Ag deposits with approximate thickness of 4 μm were achieved indicating that HCHO could reduce Pd and Ag from the KCl bath. Fig. 8.7a shows the SEM image of the Pd foil surface dipped in KCl bath without HCHO presence. No deposition occurred in the absence of HCHO. The Pd foil weight remained the same before and after the deposition. In the absence of the Pd-Ag deposition, Fig. 8.7a shows basically the surface of a Pd foil. Fig. 8.8b shows the SEM image of the Pd-Ag deposits (approximately 4 μm thick layer) obtained using the HCHO as the reducing agent on the Pd foil. The deposits were smooth and the EDX spot scan analysis (see Fig. 8.7c and Fig. 8.7d) showed very uniform distribution of Pd and Ag. The EDX area scan showed overall 21 wt% Ag in the deposits. The x-ray diffraction pattern of the deposits showed single crystalline phase (Fig. 8.8) indicating the deposits as Pd-Ag alloy similar to the coupon study (Fig. 8.4).

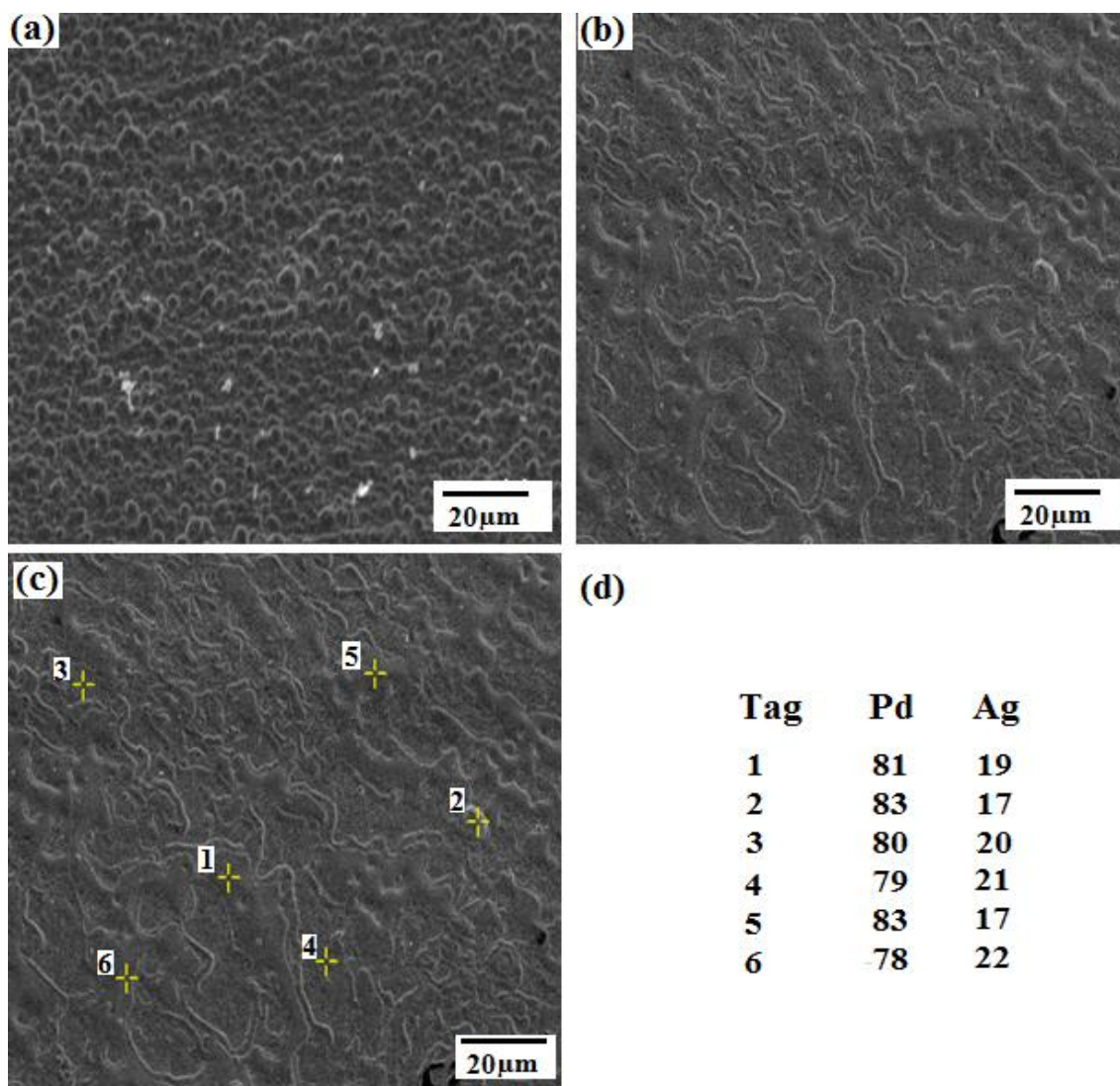


Fig. 8.7. SEM and EDX analysis of the Pd-Ag deposits obtained on the Pd foil from the KCl bath (pH~1.5) with HCHO (50 mM) as the reducing agent and bath temperature = 60 °C. Total metal concentration was 10 mM with 20 at% Ag in the bath (a) SEM image of the foil immersed in the KCl bath without HCHO presence (b) SEM image of the deposits obtained in the presence of HCHO (c) EDX spot scans of the deposits obtained in the presence of HCHO corresponding to image (b) and (d) corresponding Pd and Ag spot composition

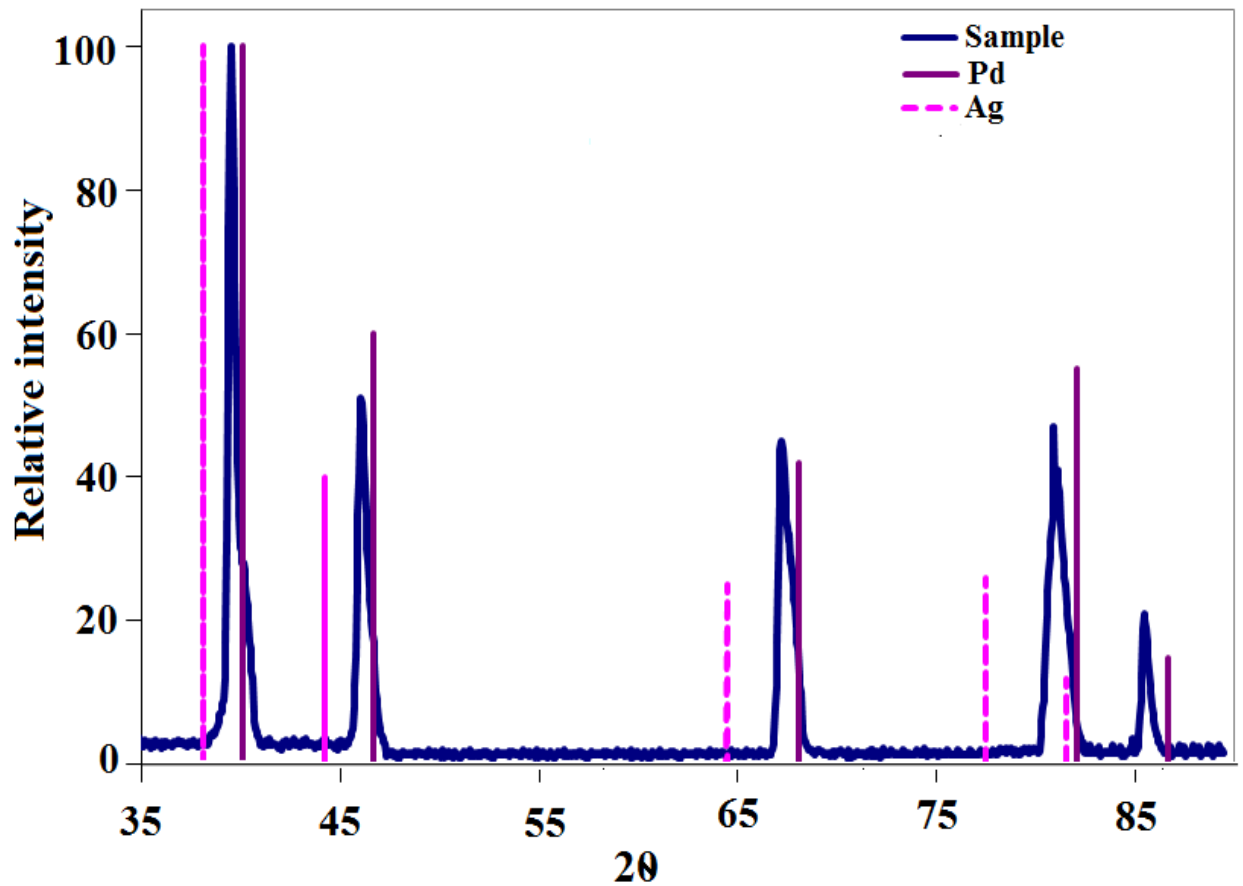


Fig. 8.8. XRD patterns of the deposits (corresponding to Fig. 8.7b) obtained on the Pd foil from the KCl bath (pH~1.5) with HCHO (50 mM) as the reducing agent and bath temperature = 60 °C. Total metal concentration was 10 mM with 20 at% Ag in the bath

8.3.3. Annealing characteristics of the glycine based deposits

8.3.3.1. Annealing time estimation and characteristics

The Pd-Ag co-deposits obtained from NH_3 , glycine and EDTA based baths were bi-metallic in structure and required further annealing step to form the alloy. Since the glycine based deposits were relatively compact in morphology, therefore more suitable for the synthesis of H_2 selective Pd-Ag membranes than the NH_3 and EDTA based deposits. The glycine based deposits were further studied for the estimation of the Pd and Ag particles size (important from annealing point of view) and the annealing conditions required to form the Pd-Ag alloy.

Fig. 8.9 shows the XRD patterns of the glycine based deposits with approximate thickness of $3.5 \mu\text{m}$ and overall 10 wt% Ag. The pattern (a) shows as plated deposits without any treatment after the deposition and the deposits were bimetallic in the phase composition. The pattern (b) shows the deposits after heating treatment at 400°C in H_2 for 10 h. After annealing at 400°C , the deposits still showed incomplete alloying as can be observed from the pattern (b) showing the presence of the two phases (pure Pd and Pd-Ag alloy) in the deposits. The deposits showed single phase after treatment at 500°C for 10 h in H_2 (Fig. 8.9, pattern (c)) indicating that 10 h at 500°C were roughly sufficient for annealing of the deposits. It can be noted from Fig. 8.9, pattern c, that after annealing at 500°C the presence of a single peak showed Pd-Ag alloy phase but the peak was relatively broader than that observed for other single phase shown in the figure, e.g., pure Pd phase (Fig. 8.9, pattern a). The broader nature of the alloy phase peak could be attributed to the presence of Pd-Ag alloy phase with varying composition across the thickness of the deposits. As discussed in the previous section (also see Fig. 8.5), the deposits obtained from glycine bath showed compositional inhomogeneity

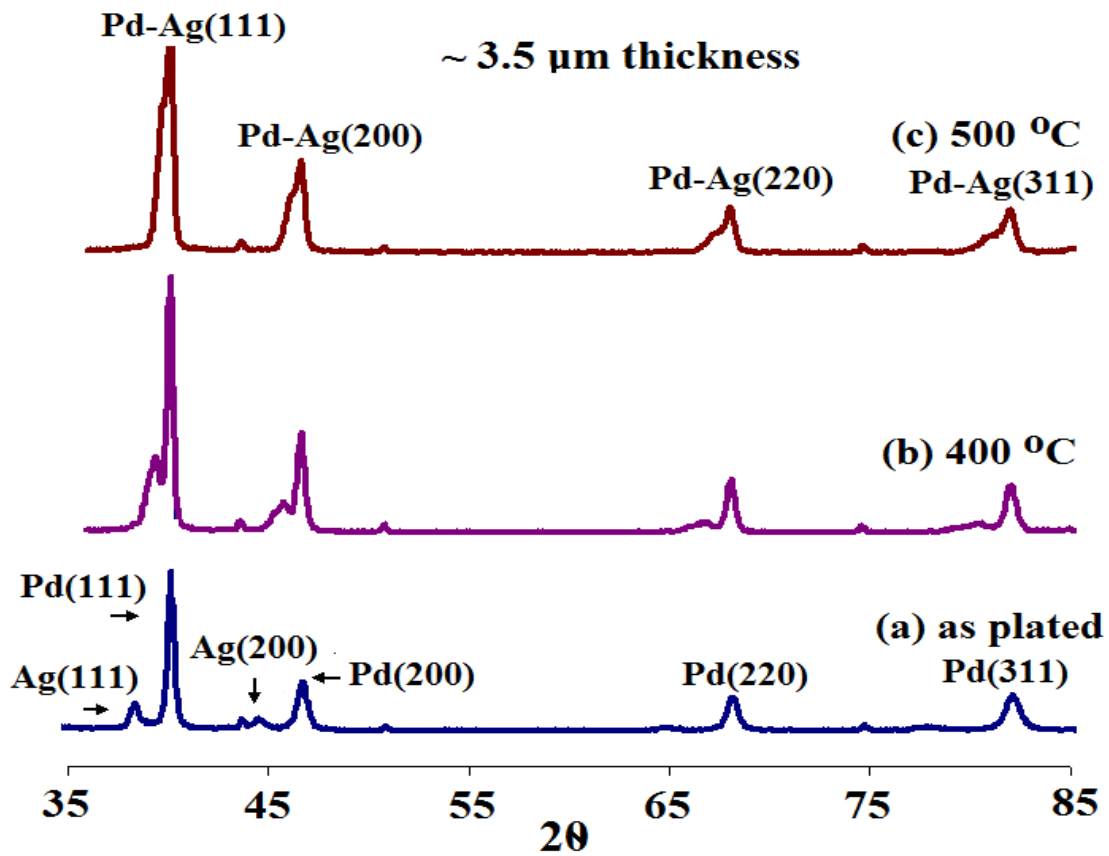


Fig. 8.9. XRD patterns of the glycine based Pd-Ag deposits with approximate 10 Ag wt% in the deposits (a) as deposited (b) after the heating treatment at 400 °C for 10 h in H₂ (c) after the heating treatment at 500 °C for 10 h in H₂

across the thickness (more concentration of Ag towards the solution side), therefore could result in the alloy phase with different composition across the thickness and broader alloy phase peak observed in Fig. 8.9, pattern c.

Fig. 8.10 shows the H₂ permeance plots of the membranes, R-09 and R-12, (prepared using the glycine based bath) during annealing between 250 and 400 °C. R-09 was plated for the total time of 9.5 h and no He flux (at $\Delta P = 2$ atm) was observed after the plating step. Since the deposits were the mixture of Pd and Ag particles, the total thickness, assuming that all the deposits were Pd, was 7.1 μm (by gravimetric method) and 8.1 μm (by gravimetric method) assuming that the total deposits were Ag. The coupon study for the glycine bath with the same composition (10 at% Ag in the bath) as that used for the membrane preparation, produced deposits with overall 17 wt% Ag. It can be safely said that the thickness of the membrane ranged between 7.1-8.1 μm and more towards 7.1 μm because the majority of the deposits were Pd. R-12, after total plating time of 12 h, also did not show any He flux ($\Delta P = 2$ atm). The thickness of the membrane ranged between 8.3 (assuming all the deposits as Pd) and 9.5 μm (assuming all the deposits as Ag). Based on the EDX area scan analysis of the membrane cross-section after the annealing step, R-12 had overall 6 wt% Ag, indicating the membrane thickness more towards 8.3 μm .

R-09 showed an increase in the H₂ permeance both at 250 °C and 300 °C (Fig. 8.10a). The He leak growth and H₂/He selectivity of the membranes (R-09 and R-12) during annealing are shown in Fig. 8.11. When the membrane was at 250 °C, the He leak increased from 0.05 to 0.2 ml/min (see Fig. 8.11a) and the H₂ permeance increased from 7 to 15 $\text{m}^3/\text{m}^2\text{-h-atm}^{0.5}$. The increase in the H₂ permeance could be attributed to the annealing of Pd and Ag deposits. At 300 °C, R-09 developed large He leak

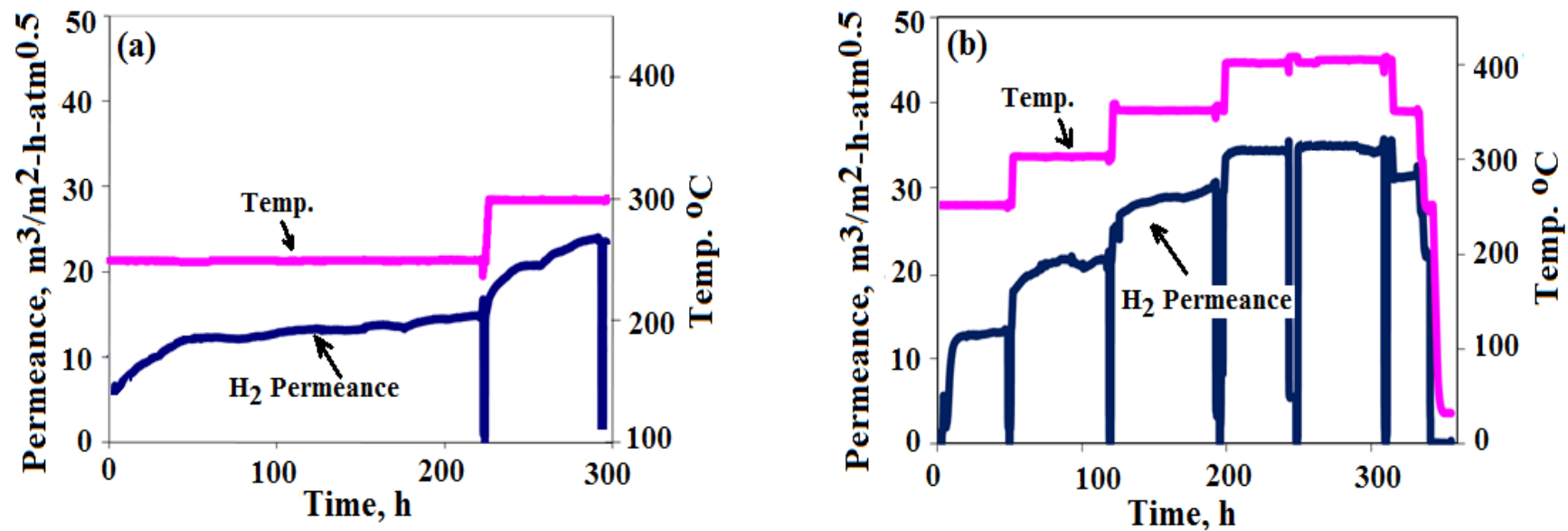


Fig. 8.10. H₂ permeation and annealing characteristics membranes synthesized using the glycine based bath (a) R-09 (b) R-12

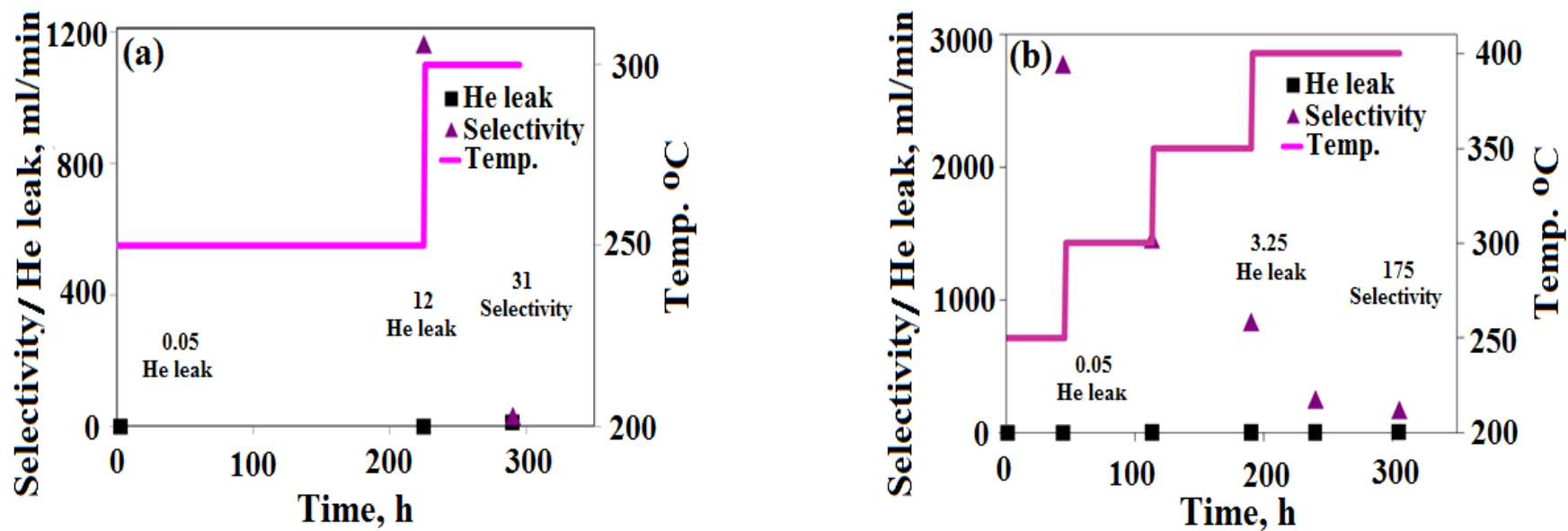


Fig. 8.11. He leak and selectivity decline of the membranes during annealing and H_2 permeation characterization (a) R-09 (b) R-12

and the H₂ permeance increase could be due to the annealing effect as well as the He leak increase. Due to the large leak developed, the annealing study was terminated. The water bubble test after the annealing step showed the presence of the defects all over the membrane surface. The development of the large He leak in the membrane could be due to the non-uniform growth of the Pd-Ag deposits obtained. Since the deposits (based on the coupons study, Fig. 8.1b) showed non-uniform growth, more growth in the perpendicular direction to the substrate surface and lesser tendency for the lateral growth, therefore it was difficult to form the dense and H₂ selective membrane.

Fig. 8.10b shows the H₂ permeance of R-12 during the annealing performed in the 250-400 °C range. The membrane showed significant increase in the H₂ permeance at each temperature between 250-350 °C and the increase could be attributed to the annealing of the Pd-Ag deposits. However, at 400 °C for over 100 h, no significant increase was observed, indicating that the annealing of the deposits was complete or occurring at a very slow rate. The increase in the H₂ permeance became more evident from the Sieverts' plot of the H₂ permeance of the membrane (see Fig. 8.12). Fig. 8.12a shows the Sieverts' data measured when going up in the temperature from 250-400 °C and Fig. 8.12b shows the Sieverts' data obtained when cooling down the membrane from 400-250 °C. The total exposure time between 250-350 °C was 200 h. The coupon annealing study (Fig. 8.9) indicated significant Pd-Ag alloy formation at 400 °C within the short period of 10 h indicating that annealing was possible even at temperatures lower than 400 °C provided the annealing time was significantly higher than 10 h.

In comparison to R-09, the He leak growth was slower in R-12 (Fig. 8.11b). R-12 after a total exposure time of approximately 300 h between 250-400 °C showed H₂/He selectivity ($\Delta P = 1\text{atm}$) of 175 at 400 °C. The higher selectivity of R-12 could be

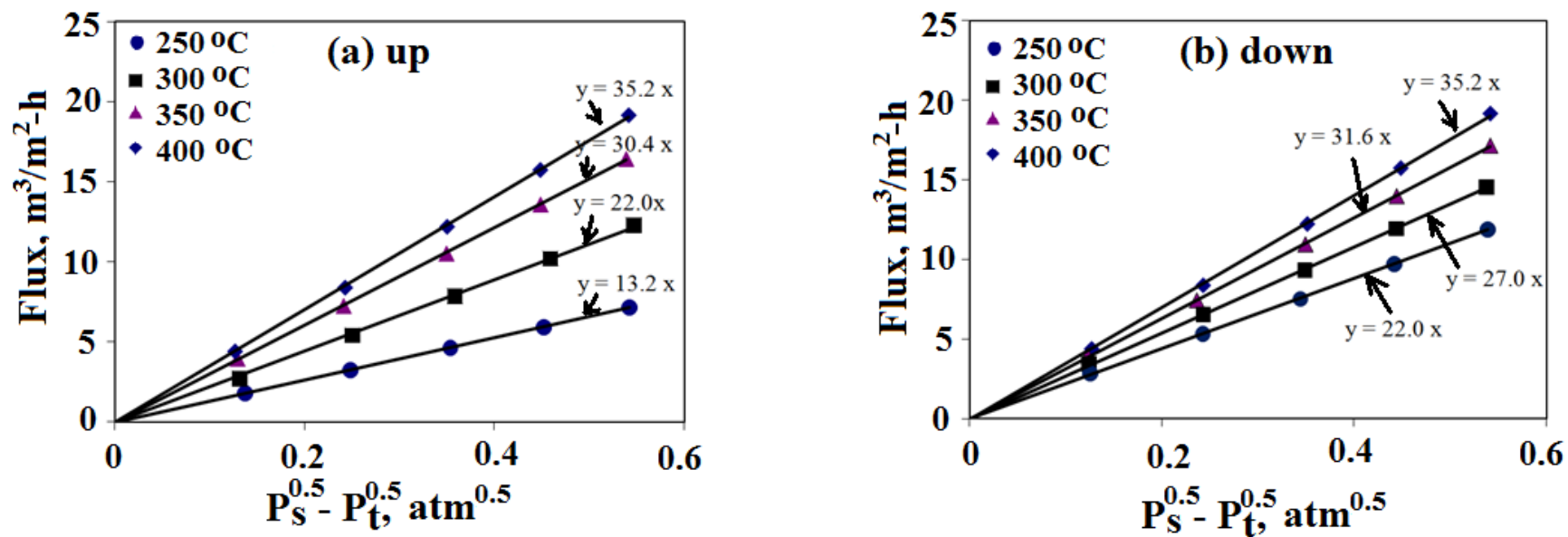


Fig. 8.12. Sieverts' plot for the H_2 permeance of R-12 between 250-400 °C (a) during heating up membrane from 250 to 400 °C, the data were taken after the H_2 permeance reached steady state at each temperature (b) during cooling the membrane from 400 to 250 °C.

attributed to its synthesis procedure. As mentioned earlier in this chapter, the deposits obtained from the glycine bath showed more tendencies to grow in the perpendicular direction to the substrate surface. The synthesis procedure for R-12 included the SiC paper polishing in between the plating sequences. The polishing step could remove the perpendicular portions of the deposits, therefore making the deposits grow relatively more in the lateral direction. The good lateral growth was desired for preparing H₂ selective membranes (see introduction section in Chapter 5).

The typical EDX line scans of the cross-sections of R-12 after the annealing step is shown in Fig. 8.13. Ag was present only in the 2-3 μm membrane thickness opposite from the substrate side. The SiC paper polishing of the membrane surface removed the perpendicularly growing parts of the deposits. As shown in the EDX spot scan analysis of the glycine deposits (Fig. 8.5b), Ag was concentrated more at the higher points (more towards the solution side). Therefore during the polishing steps, the peaks of the deposits rich in Ag were removed leading to the absence of Ag in the EDX line. Since, the polishing was not executed for the last 3 h of membrane plating, Ag was not removed for that portion of the membrane. The increase in the H₂ permeance of the membrane (Fig. 8.10 and Fig. 8.12) was due to the annealing of the Pd-Ag deposits present within 2-3 μm thickness opposite from the substrate side. As mentioned earlier, the compositional homogeneity of as plated Pd-Ag deposits across the entire cross-section was necessary for obtaining alloy membrane with uniform Pd and Ag distribution across the entire thickness of the membrane. If the distribution of the Pd and Ag in as plated deposits across the thickness was not uniform, Pd and Ag were required to diffuse across the entire thickness of the deposits in order to obtain alloy membrane with uniform Pd-Ag composition and required very high annealing

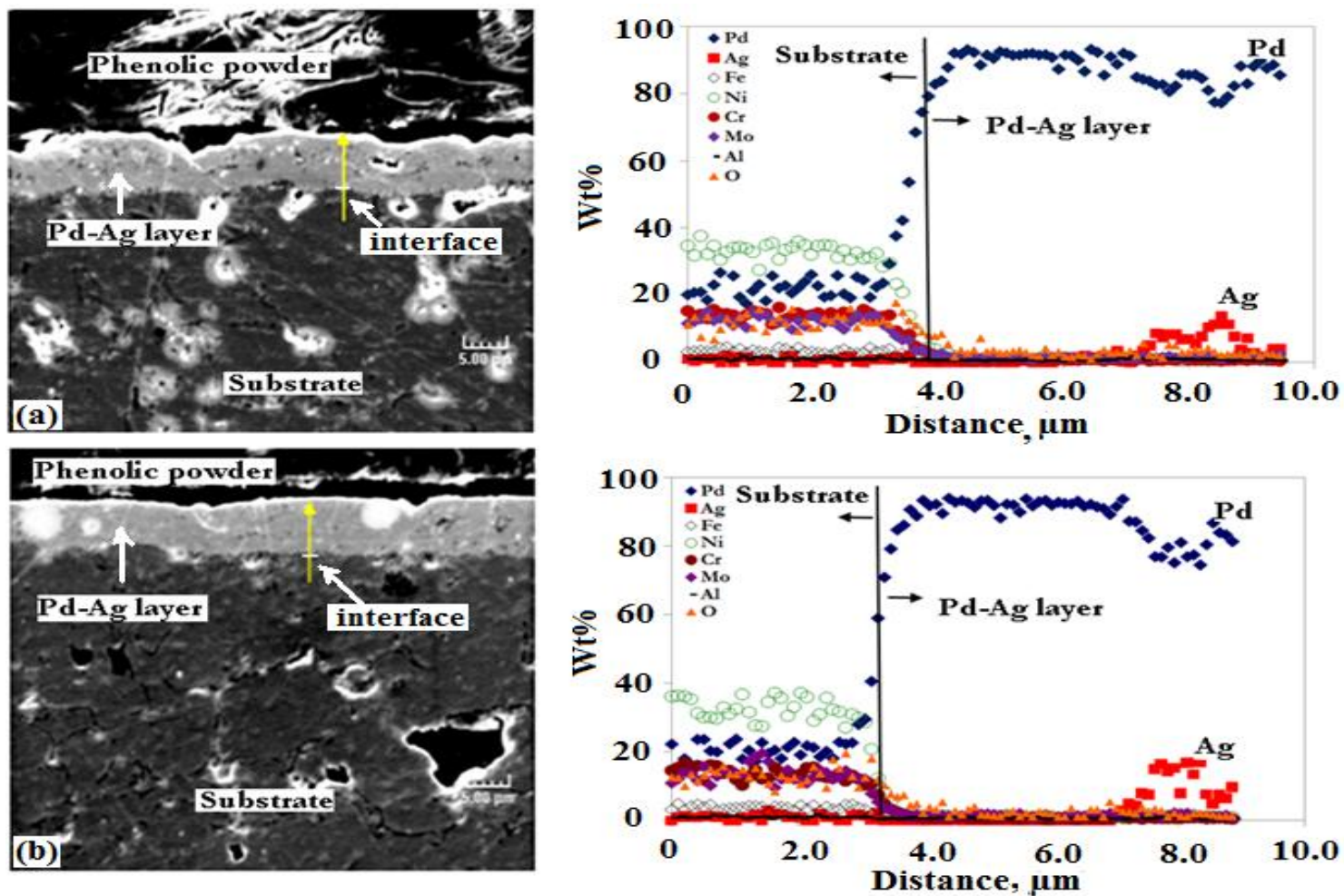


Fig. 8.13. The EDX analysis of the cross sections of R-12(overall Ag wt% ~ 8) after annealing between 250 and 400 °C for more than 300 h.

temperatures ($> 550\text{ }^{\circ}\text{C}$, see Chapter 7, Section 7.3.5) . In the case of R-12, Pd-Ag deposits were present only within 2-3 μm thickness due to the plating process itself (the rest of the thickness was only pure Pd deposits) and the annealing conditions used (250-400 $^{\circ}\text{C}$) resulted in only mixing of Pd and Ag within the 2-3 μm thickness itself, emphasizing the importance of uniform distribution of Pd and Ag in the as plated deposits for obtaining homogeneous Pd-Ag alloy membrane under the mild annealing conditions (400 $^{\circ}\text{C}$ or less).

8.3.3.2. Pd-Ag particle size based on EDX penetration depth

The penetration depth information of EDX could be used to estimate the particles size in a given EDX sample [140, 141]. Fig. 8.5b shows the EDX spot scans at different locations in the glycine based deposits. The EDX spot scan showed both the presence of Pd and Ag at each location. The depth in the deposits from which x-rays originated for the spot scans could be given by the following equation [141].

$$d_{edx} = \frac{0.064}{\rho} (E_o^{1.68} - E_c^{1.68}) \quad 8.1$$

Where

d_{edx} = x-rays penetration depth, μm

ρ = density of deposits (Pd or Ag), g/cm^3

E_o = electron beam energy used for the EDX spot scans, KV (15 kV was used for all the EDX spot scans)

E_c = critical excitation energy of the characteristics lines used for the identification of Pd or Ag, kV (The L_a line used for the identification of Pd had energy of 2.84 kV and 2.98 kV for Ag)

The solution of Eqn. 8.3 provided the value of penetration depth of 0.48 and 0.55 μm for Pd and Ag respectively. As all the spots for glycine deposits indicated presence of both Pd and Ag, therefore the size of Pd and Ag particles was in the range of penetration depth of EDX ($\sim 0.5 \mu\text{m}$). The EDX spot scans obtained for the deposits from NH_3 and EDTA baths also showed presence of both Pd and Ag at each spot, indicating the size range of particles equal to the penetration depth of EDX. The Pd and Ag particles size ($\sim 0.5 \mu\text{m}$) was less than the thickness ($\sim 1-3 \mu\text{m}$) of the sequentially deposited Pd and Ag layers (see Chapter 7, Section 7.3.2). The low particles size indicating that the annealing conditions required for the co-deposits were milder than that required for the Pd-Ag sequential deposits ($550 \text{ }^\circ\text{C}$, 24 h) provided that the Pd-Ag distribution of as plated deposits were uniform across the thickness.

8.4. Conclusion

The Pd-Ag deposits obtained from NH_3 , EDTA and glycine bath showed non-homogeneous distribution of Pd and Ag. The Ag was more concentrated towards the solution away from the substrate side. In comparison to the NH_3 and EDTA baths, the deposits obtained from the glycine bath were relatively uniform in morphology, therefore more suitable for membrane synthesis. The Pd and Ag particles size of the glycine based deposits were approximately in the 0.5 μm range and the deposits could be annealed in the 300-400 $^\circ\text{C}$ temperature range which was lower than the annealing temperature (550 $^\circ\text{C}$) used for annealing the Pd and Ag sequential deposits. The membrane prepared using the glycine bath without any polishing during the plating sequence showed large drop in the membrane selectivity on heating. Based on the SEM coupons study of the morphology of the deposits, the decline in the membrane selectivity was believed to be due to the non-uniform morphology of the deposits showing tendencies to grow more in the perpendicular direction to the substrate surface. The polishing steps during the membrane plating reduced the non-uniform growth by selectively removing the perpendicularly growing deposits but also removed the majority of the Ag deposited. Coupon studies showed that the KCl bath in the acidic conditions with HCHO as reducing agent produced very uniform composition Pd and Ag deposits. The Pd-Ag deposits obtained from KCl bath were alloy phase, therefore requiring no annealing step for the membrane synthesis. The KCl bath needs to be further studied for the membrane synthesis. The substrate for the membrane could be protected from corrosion (due to the acidic KCl bath) using a thin layer of Pd ($\sim 0.5 \mu\text{m}$ thick) before dipping the substrate in the KCl bath.

9. He Leak mitigation in membranes

9.1. Introduction

The membranes synthesized in this study so far (see Chapter 7, Section 7.3.1) showed decline in the H₂/He selectivity when exposed to temperatures in the range 300-550 °C. There exists a large amount of literature on Pd based composite membranes, however, there are only few studies mentioning the effect of long term temperature exposure on the selectivity of Pd based composite membranes [50, 51, 137, 138, 142]. In all the reports [50, 51, 137, 138, 142] mentioning the selectivity of Pd based membranes, the electroless method was used to prepare the membranes and the decline in membrane's selectivity appears to be not affected by the composition of the membrane. Pd [137, 138, 140], Pd-Ag [51] and Pd-Cu [50] membranes all showed decline in the selectivity. According to Guazzone and Ma [138], the Pd membranes showed H₂/He selectivity decline when exposed to temperature greater than 400 °C. The He leak growth in the Pd membranes was very sensitive to the temperature. The rate of the He leak growth at 550 °C was two orders of magnitude higher than that at 450 °C [138]. The He leak growth was due to the pinhole formation in the supported Pd film, clearly visible in the SEM images for the supported Pd films heated at 600 and 650 °C for 48 h [11, 138]. The Pd membranes at 500 and 550 °C also showed the He leak growth, but the pinholes could not be seen in the SEM images of the supported Pd films heated at 500 and 550 °C [11]. The lack of the visibility of pinholes was due to the small size of pinholes (~0.25 μm), less than the SEM resolution (~1 μm). According to Paglieri et al. [137], the decline in the membrane selectivity depended on the membrane

thickness and was inversely proportional to the supported Pd film thickness [137].

The Pd or Ag layer in the case of composite membranes is deposited on a substrate with different chemical composition and structure. The lattice mismatch between Pd or Ag and the substrate could introduce stresses [143] in the as deposited Pd or Ag layer. The stresses present on heating the membranes to high temperatures (temperature > 400 °C) could lead to pinhole formation in the Pd or Ag layer and therefore observed decline in the membranes selectivity (see Chapter 7, Section 7.3.6). The other source of introduction of stresses at high temperature (temperature >400 °C) could be the difference in the co-efficient of thermal expansion of the substrate and the deposited Pd or Ag layer, which could lead to the pinhole formation. The unsupported Pd or Ag film is free of the above mentioned stresses, caused by the contact with the substrate. Therefore if the free standing Pd or Ag film was heated (>400 °C) and the pinholes were observed similar to the pinholes observed by Guazzone [11] in the supported Pd film, the factors other than stresses could be the cause of the pinhole formation.

The objective of the study in this chapter was to synthesize Pd and Pd-Ag membranes by multi step plating, annealing and mechanical polishing method with improved H₂/He selectivity in the temperature range between 300-550 °C. The synthesis procedure adopted was similar to the one used by Saini [144] using multi plating and annealing steps for the Pd membrane preparation. The procedure adopted in this study involved additional mechanical polishing steps between the plating and annealing steps in comparison to the procedure of Saini [144]. The theory behind the effect of the used synthesis method on the H₂/He selectivity is also discussed. In order to see the possible effect of the stresses on pinhole formation in the Pd and Ag films, the free Pd and Ag films were also prepared by the electroless method and heated at high temperature (700

°C) and further characterized by SEM.

9.2. Experimental

The two porous inconel tubes (see Chapter 3, Section 3.2.1) were used as the substrate for the membrane synthesis and were designated as R-13b and R-14. R-13b was the continuation of R-13a discussed in Chapter 7, Section 7.2.1. The γ -alumina layer by the sole gel method was used as the intermetallic diffusion barrier layer and the substrate pores were filled with γ -alumina powder (0.3 μm size powder) by simply hand rubbing the powder slurry on the substrate surface to narrow the pore size distribution of the substrate (see Chapter 3, Section 3.2.2 for details).

After the annealing and H_2 permeation characteristics study (see Chapter 7, Section 7.3.3 and Section 7.3.4), R-13a was subjected to multi plating, annealing and polishing steps (designated R-13b after this point). R-13b was plated with Pd deposits only. The total thickness of R-13b was 17.1 μm . R-14 was Pd-Ag membrane prepared by the sequential plating method (each Pd layer ~ 1.5 -2.5 μm and each Ag layer 0.7-1.0 μm) with total thickness of 14.7 μm . The plating conditions used for the deposition of Pd (in the case of R-13b and R-14) and Ag (in the case of R-14) in this study were the same as that used for R-10 and R-11 (see Chapter 7, Section 7.3.2).

The plating, annealing and mechanical polishing steps were executed in the following way. The membranes were plated till no or very little He leak was measured ($\Delta P = 2.5$ atm) and then annealed at 550 °C for 10 h in H_2 . For the annealing step, the membranes after plating step were heated up to 400 °C (1 °C/min) in the He atmosphere and then switched to the H_2 atmosphere. The temperature was then ramped to 550 °C at the rate of 1 °C/min. After 10 h at 550 °C, the membranes were cooled to 400 °C in the

H₂ atmosphere and Sieverts' law data for the H₂ permeance were measured. The membranes were next cooled down to room temperature, the membranes surface was polished (see Chapter 3, Section 3.4). After the polishing step, the membrane surface was cleaned with HCl (0.1 M) and ethanol to remove any dirt and grease or oil incorporated on the membrane surface followed by the plating step. The entire sequence of plating, annealing and polishing was repeated until the membrane after the polishing step did not show any He leak or very small He leak, measured at $\Delta P = 2.5$ atm. The plating, annealing and polishing sequence was repeated four times for R-13b and two times for R-14. After the final plating, annealing and polishing sequence, the membranes were plated with the final layer of Pd (R-13b ~ 2.4 μm and R-14 ~ 2 μm) before characterizing the membranes for the H₂/He selectivity in the temperature range of 300-450 °C for more than 550 h (approximately 21 days). The membranes were kept in H₂ atmosphere. To measure the He leak, membranes were switched to He atmosphere and the He leak was measured at $\Delta P = 2$ atm, using the bubble flow meter (see Chapter 3, Section 3.5.1).

The free standing Pd and Ag films were prepared by depositing 8-10 μm thick layer on a very smooth non-porous stainless steel plate and detached afterward. The pinholes formed at 500 and 550 °C were not detected by SEM [11], therefore the Pd and Ag films were heated at 700 °C in H₂ atmosphere for 48 h in order to clearly see the pinholes by SEM.

The Pd plating conditions for the preparation of R-13b and R-14 used were the same as described in Chapter 5, Section 5.2 and Chapter 7, Section 7.2.1. The Ag deposition was performed using the plating conditions with the Ag/N₂H₄ ratio of 20 mM/4 mM as described in Chapter 5, Section 5.2.

SEM and EDX were used for the composition analysis of the cross-section of the membranes after the H₂/He selectivity characterization and for imaging the pinholes formed in the Pd and Ag films after heating in the H₂ atmosphere

9.3. Results and discussions

9.3.1. Possible leak mechanism

The free standing Pd and Ag films when heated at 700 °C showed presence of a large number of pinholes (Fig. 9.1). The pinholes in free standing films suggested that the factors other than the stresses associated with the substrate interaction could be causing the pinholes formation. Guazzone [11] also concluded in the case of Pd film supported on porous Hastelloy substrate that tensile stresses present in the as deposited Pd film were released within 1 h at 400 °C. The Pd membrane tested at 400 °C by Guazzone [11] showed no decline in the H₂/He selectivity for the first 1 h, indicating little possibility of the stresses in the Pd film causing the pinhole formation [11]. The possible reason for the pinholes formation in the electroless plated Pd and Ag films could be due to the large defects present in the as deposited Pd film. The defects could be in the form of voids due to the trapped solution, the gas bubbles trapped inside the deposits (note - The N₂H₄ oxidation during the Pd and Ag plating resulted in the formation of N₂ gas) and large number of grain boundaries present. The as deposited Pd deposits had grain size ranging 40-60 nm [114, 144]. The low Pd grain size indicated the presence of a large number of grain boundaries and grain boundary defects present in the Pd deposits. According to Nakahara and Okinaka [145], a large number of voids were observed in the TEM (Transmission electron microscopy) study of the Cu deposits

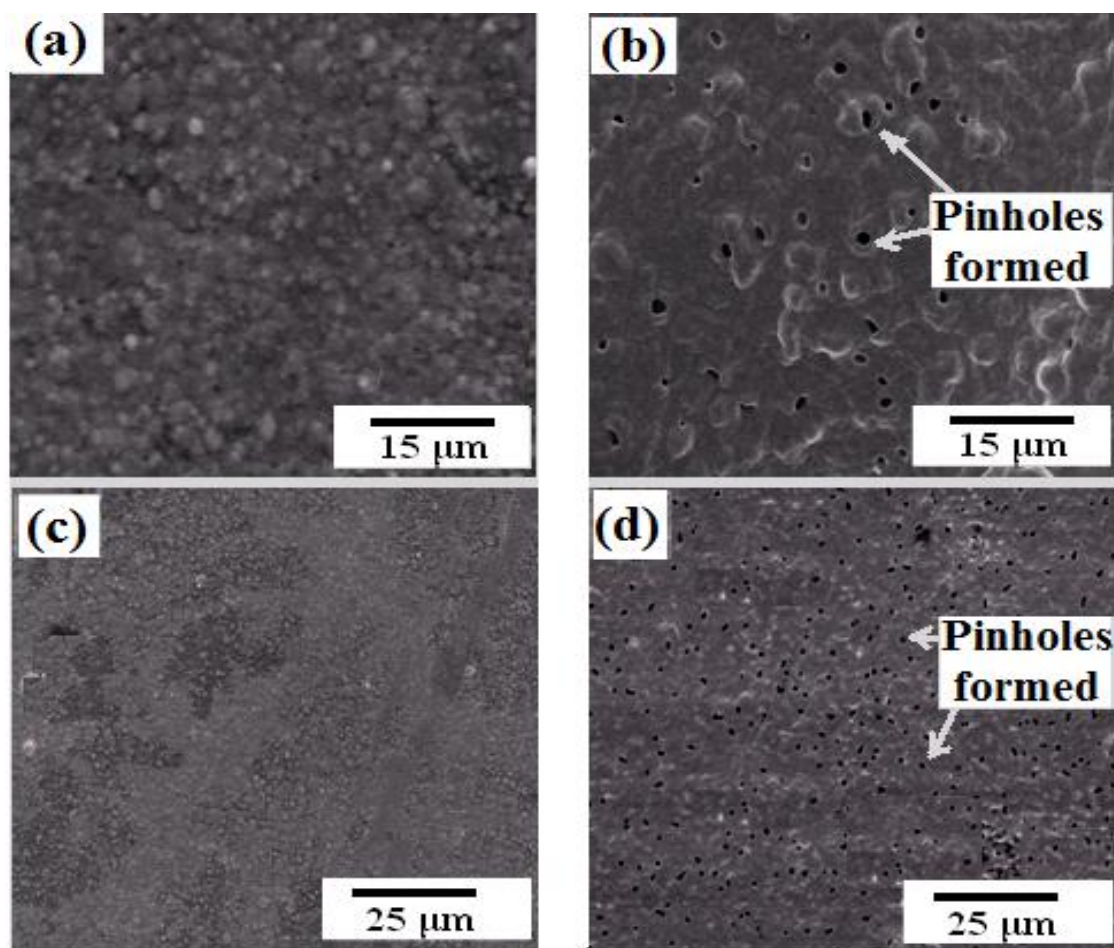


Fig. 9.1. SEM images of Pd and Ag films (a) fresh plated Pd film (b) Pd film heated at 700 °C for 48 h in H₂ (c) fresh plated Ag film (d) Ag film heated at 700 °C for 48 h in H₂.

obtained by the electroless method. Formaldehyde was used as the reducing agent and its oxidation involved evolution of H₂ gas. The TEM images of the Cu deposits showed the existence of a large number of voids, due to the trapped H₂ gas, in the size range of 200-300 nm [145]. On heating the deposits, the voids showed agglomeration and formed a continuous crack across the deposits thickness and subsequently mechanical failure of the Cu film. The presence of voids in the deposited Cu was also verified by the density measurement of the deposits. The density of Cu metal is 8.92 g/cm³, the density measured for the obtained Cu deposits was 8.86 g/cm³. The defects also appear to be present in the deposits obtained from the electroplating method [146]. The Au electro-deposits obtained from cyanide bath showed the presence of voids from 5 to 200 nm size and average size of the voids increased on heating [146]. The plating bath used for the Pd deposition in this study was adapted from the bath developed by Rhoda [80]. The density of the obtained Pd deposits was measured at 11.96 g/cm³ by Rhoda [80] whereas the density of Pd metal is 12.03 gm/cm³ indicating 0.5% void volume present in the Pd deposits. The Pd plating conditions used in this study were similar to those by Rhoda [80] and the presence of a similar amount of defects in the deposits could be expected.

Based on the presence of the defects in Pd deposits as mentioned in the previous paragraph, the possible mechanism of the leak formation could be agglomeration of these defects on heating and forming the through-through pinholes in the Pd film allowing He gas to pass through the Pd film and causing the decline in the membrane selectivity on heating (see Appendix F for a case study involving a pure Pd membrane supported on porous metal substrate on the possibility of formation of pinholes due to the defects present in the Pd deposits). Fig. 9.2 shows the schematic of a Pd film describing the effect of multistep plating, annealing and polishing on preventing the

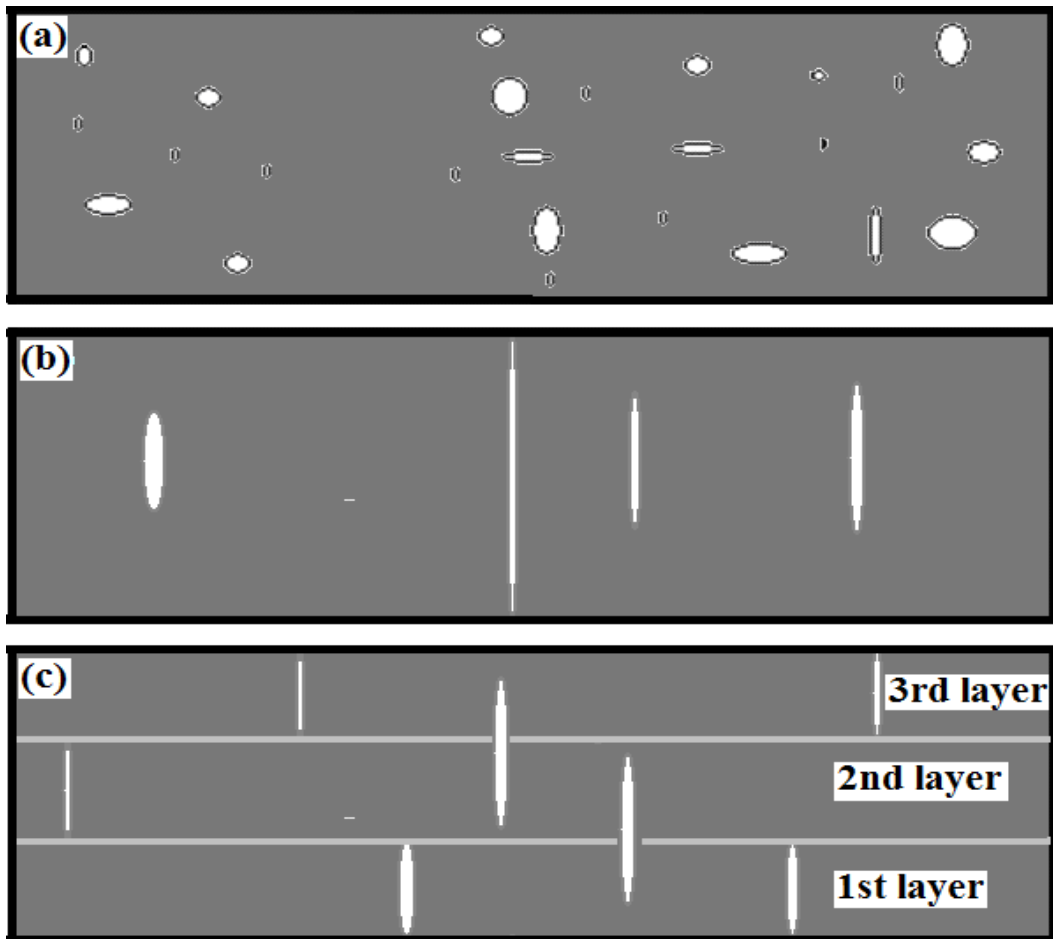


Fig. 9.2. Schematic of voids present in the film (a) as deposited Pd film (b) Pd film heated at high temperature (c) Pd films subjected to repeated sequence of plating and heating

formation of through-through pinholes due to the defects present in as deposited Pd film and avoiding the decline in the membrane selectivity (H_2/He) on heating. Fig. 9.2a shows the voids present in the as deposited Pd film and Fig. 9.2b shows agglomeration of the small voids present in the film into large voids on heating and forming through-through pinholes. The effect of multi step plating, annealing and mechanical polishing in preventing the decline in the membrane selectivity is shown in Fig. 9.2c. When the He gas tight Pd layer deposited on the substrate was annealed at high temperature (550 °C in this study), the voids in the Pd film agglomerated (see Fig. 9.2a and Fig. 9.2b) and formed few through-through pinholes. The Pd membrane with pinholes after annealing was mechanically polished and the 2nd Pd layer was deposited and annealed again. The second annealing caused again formation of pinholes in the second layer deposited. In the second annealing, in order to make the membrane to show He leak, the pinholes formed in the second Pd layer should align with the pinholes in the first layer to make through-through pinholes all through the combined first and second layer. Only very few pinholes formed in the second Pd layer would align with the pinholes in the first layer and the chances of forming through-through pinholes in the combined first and second layer would drastically reduced. Fig. 9.2c shows the schematic of the Pd film consisting of three layers of Pd prepared by the plating and annealing sequence. It can be seen in Fig. 9.2c that there are pinholes which go through first and second layer and pinholes which go through the second and third layer but no pinhole which goes through all the three Pd layers representing that the multi step plating, annealing and mechanical polishing could drastically reduce the presence of through-through pinholes.

9.3.2. Effect of multi step plating, annealing and polishing on He leak

Fig. 9.3a and Fig. 9.3b show the effect of the sequence of plating, annealing and mechanical polishing on the He leak formation ($\Delta P = 1$ atm, room temperature) in R-13b and R-14 respectively. The He leak in the membranes reduced as the plating, annealing and polishing sequences increased which could be attributed to the lack of connection of pinholes in each different deposited layer with each other to form through-through pinholes. In each case, the He leak remained same or decreased during the polishing step in comparison to the preceding annealing step except for the first polishing step for R-13. The sharp increase in the He leak after the first polishing step for R-13 could be attributed to excessive removal of Pd ($\sim 3 \mu\text{m}$) layer such that the total membrane thickness was reduced below the minimum Pd layer thickness required for the substrate pores coverage (Note- there is a certain Pd layer thickness required to cover the pores of substrate and to achieve a He gas tight membrane).

Guazzone [11] studied the He leak development in several Pd membranes (supported on porous hastelloy and stainless steel tubes with $0.1 \mu\text{m}$ media grade) in the temperature range of $300\text{-}550$ °C. The membranes were graded with alumina powder before the deposition of the Pd layer and the membrane thickness ranged between 5.6 and $19 \mu\text{m}$. The procedure for the preparation of membranes consisted of simply depositing a He gas tight Pd layer without any annealing and polishing steps. The He leak growth rate data of the membranes in the temperature range of $300\text{-}550$ °C was fitted to the following equation.

$$\ln(Y) = -28486 \frac{1}{T} + 27.616 \quad 9.1$$

Where Y and T in Eqn. 9.1 represent the rate of the growth of He flux

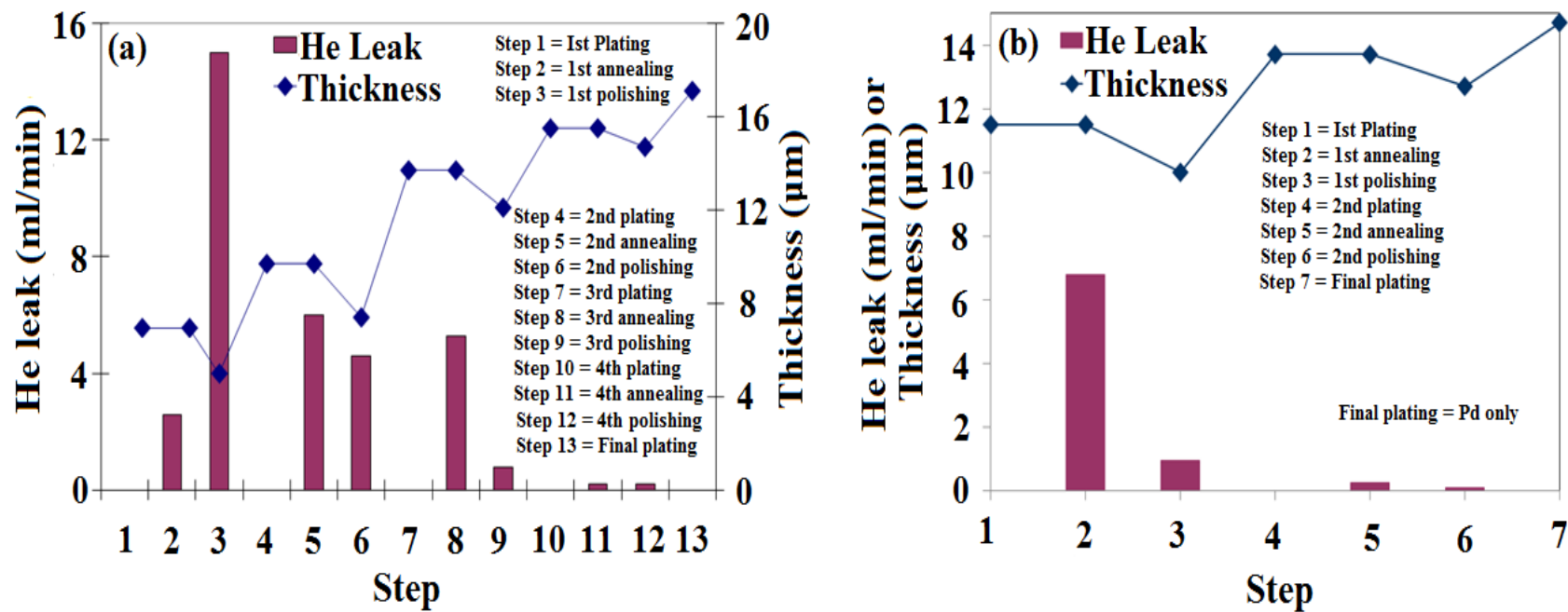


Fig. 9.3. He leak progression on multi step plating, annealing and mechanical polishing steps (a) for R-13b (b) for R-14

$(\text{m}^3/\text{m}^2\text{-h-atm})/\text{h}$ and temperature (K) respectively. R-13b after four sequences of annealing (i.e. total time of 40 h at 550 °C) prepared by using the plating, annealing and polishing procedure showed He leak of 0.2 ml/min (at $\Delta P = 1$ atm, room temperature) (see Fig. 9.3a). According to Eqn. 9.1, the He leak of the membrane (R-13b with membrane area = 23 cm²) after 40 h exposure at 550 °C should be equal to 1.4 ml/min (at $\Delta P = 1$ atm and 550 °C). The lower value of the He leak shown by R-13b than that predicted by Eqn. 9.1 after 40 h at 550 °C could be attributed to the plating, annealing and polishing procedure. As discussed in the next section, R-13b after final plating step (thickness = 17.1 μm) did not show any He leak (at $\Delta P = 2$ atm) on exposure at 450 °C for >200 h, however significant He leak (0.06 ml/min at $\Delta P = 1$ atm and between 0.12 and 0.16 ml/min depending on the contribution of Knudson and viscous flow to the total He leak at $\Delta P = 2$ atm) was predicted by Eqn 9.1 for the membranes prepared without annealing and polishing steps. R-14 after 20 h at 550 °C (after two sequences of annealing, 10 h each, and prepared by plating, annealing and polishing procedure) showed He leak of 0.20 ml/min ($\Delta P = 1$ atm, room temperature), however Eqn. 9.1 estimated higher He leak (0.70 ml/min, $\Delta P = 1$ atm). As discussed in the next section, after the final plating (thickness = 14.7 μm) step, R-14 was tested for the He leak growth for more than 200 h at 450 °C and no He leak was detected ($\Delta P = 2$ atm). Based on Eqn. 9.1, the He leak of 0.06 ml/min at $\Delta P = 1$ atm (and between 0.12 and 0.16 ml/min depending on the contribution of Knudson and viscous flow to the total He leak at $\Delta P = 2$ atm) was expected of a pure Pd membrane prepared by simple plating (without annealing and polishing steps). It is to be noted here that R-14 was a Pd-Ag membrane, therefore difference in the He leak growth of the membrane in comparison to that projected by Eqn. 9.1 could be attributed to the presence of Ag and the difference in the preparation procedure.

The H_2 permeance of the membranes decreased with each sequence of plating, annealing and polishing. Fig. 9.4 shows the H_2 permeance of the membranes after each annealing step. The permeance was measured at 400 °C after the completion of the annealing step at 550 °C. The decrease in the permeance was mainly due to the increase in the total thickness of the membranes with progression of each plating, annealing and polishing step.

9.3.3. H_2/He selectivity characterization

Both membranes did not show any He leak through the testing period of more than 550 h between 300-450 °C (> 200 h at 450 °C), indicating that the plating, annealing and polishing approach was effective in reducing the formation of through-through pinholes in the membranes (Fig. 9.5). In addition, the membranes were also exposed to 550 °C in H_2 atmosphere (R-13b = 40 h and R-14 = 20 h) during the plating, annealing and polishing sequences. Fig. 9.5a and Fig. 9.5b show the H_2 permeance of R-13b and R-14 respectively. It can be seen from the figures that R-14 showed higher H_2 permeance than R-13b. R-14 showed the H_2 permeance of 22.5, 30.1 and 34.5 $m^3/m^2\text{-h-atm}^{0.5}$ at 300, 400 and 450 °C respectively and was higher than that of pure Pd membrane (estimated by Eqn. 7.5) by factor of 1.4 at 300 °C, 1.2 at 400 °C and 1.15 at 450 °C. The higher H_2 permeance of R-14 could be attributed to the presence of Ag in the membrane. Based on the EDX area scan analysis of the membranes cross-section at several locations, the overall wt% Ag was 9 in R-14. The H_2 permeance of R-13b was lower than that expected for pure a Pd membrane using Eqn. 7.5 in Chapter 7. For example, at 450 °C, R-13b showed H_2 permeance of 12.6 $m^3/m^2\text{-h-atm}^{0.5}$, however, the permeance of 26.2 $m^3/m^2\text{-h-atm}^{0.5}$ was expected based on Eqn. 7.5 (Chapter 7) for a

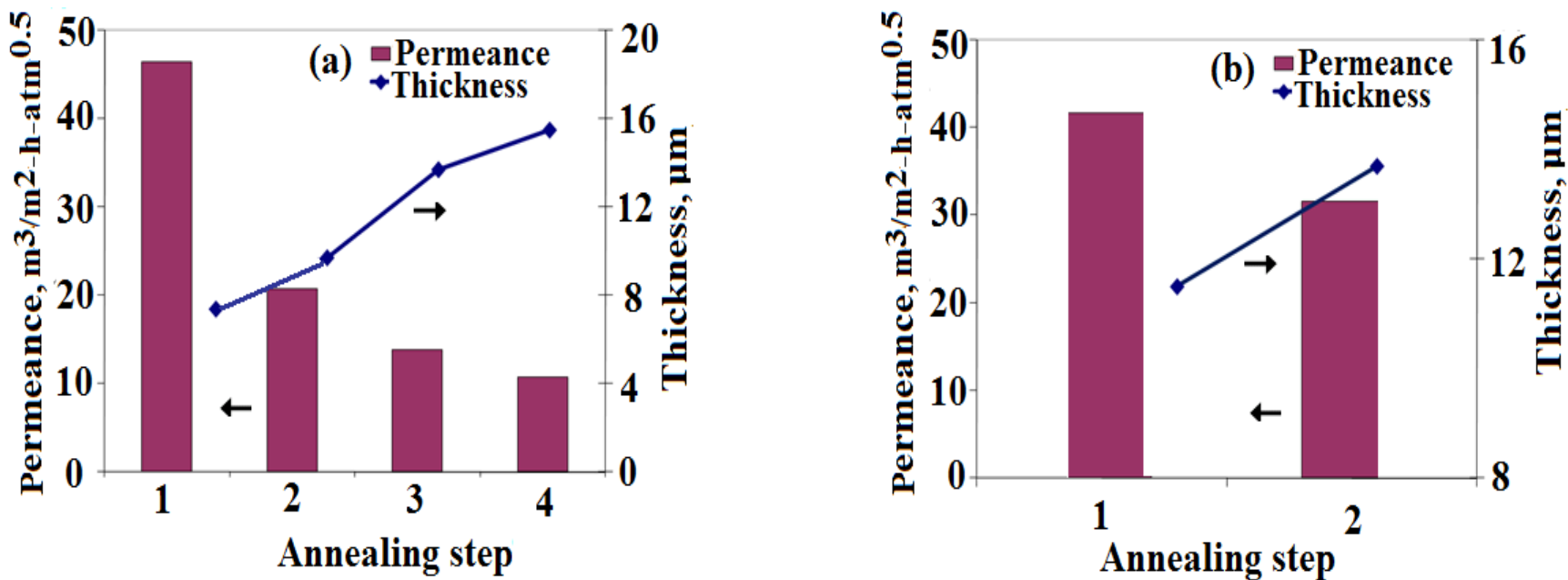


Fig. 9.4. Effect of repeated steps of plating, annealing and polishing on the H_2 permeance of membranes measured at $400^\circ C$ after the annealing step at $550^\circ C$ (a) R-13b (b) R-14

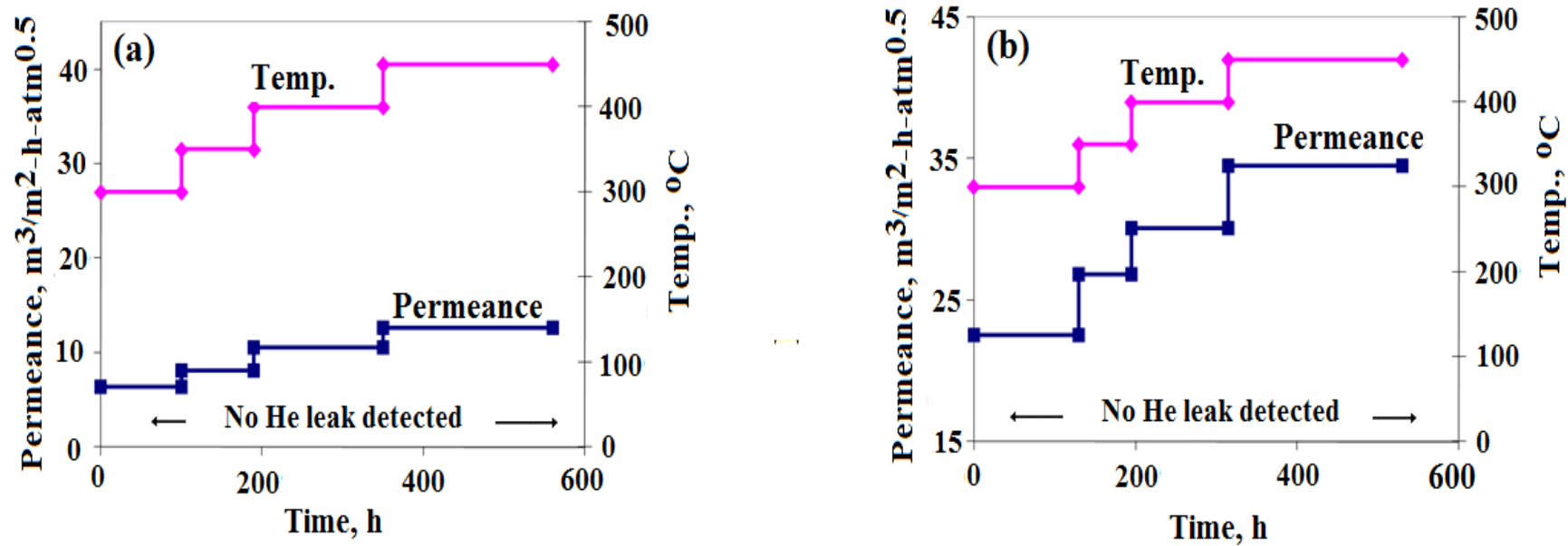


Fig. 9.5. H_2 permeance and H_2/He selectivity of membranes (after synthesis by multi plating, annealing at $550^{\circ}C$ and polishing step) in the temperature range $300-450^{\circ}C$ for more than 550 h (a) R-13b (b) R-14

membrane with thickness equal to 17.1 μm . The polishing step during the membrane synthesis was performed using the lathe machine. The jaw of the lathe machine holding the membrane was lubricated with grease and oil. Therefore accidental incorporation of the grease and oil on the membrane surface and incomplete cleaning afterward before the next plating step could introduce impurities (e.g. carbon) in the membrane, resulting in the lower H_2 permeance of the membrane.

The typical EDX line scans of the cross-section of the membranes is shown in Fig. 9.6. The scans were taken in the direction of the arrow of the line. The line scan for R-13b showed the presence of Ag very near to the substrate (2.5-3.5 μm), very similar to the plating sequence of the membrane. In the case of R-14, Ag was present throughout the cross-section of the membrane. Although the final layer ($\sim 2 \mu\text{m}$) deposited in the case of R-14 was pure Pd, Ag was present in the 2 μm region opposite to the substrate side. The Ag presence could be due to the diffusion occurring during the membrane exposure for more than 550 h between 300-450 $^\circ\text{C}$. Based on the EDX area scan of the membrane cross section at several locations, R-13b had 3 wt% overall Ag and was almost a pure Pd membrane.

Based on Sieverts' data obtained in the temperature range of 300-450 $^\circ\text{C}$, R-13b showed higher activation energy for the H_2 permeation than that for R-14 (Fig. 9.7). The lower activation energy of R-14 could be explained on the basis of its relatively higher Ag content (Note- the activation energy of Pd for the hydrogen permeation decreased on addition of Ag up to 20-25 wt%, see Chapter 7, Section 7.3.4). R-13b had relatively lower Ag content and was limited to 2.5-3.5 μm thick region near the substrate. Due to its low content of Ag, R-13b was closer to the pure Pd membrane. The lower activation energy of R-14 in comparison to R-13b, again indicated (see Chapter 7,

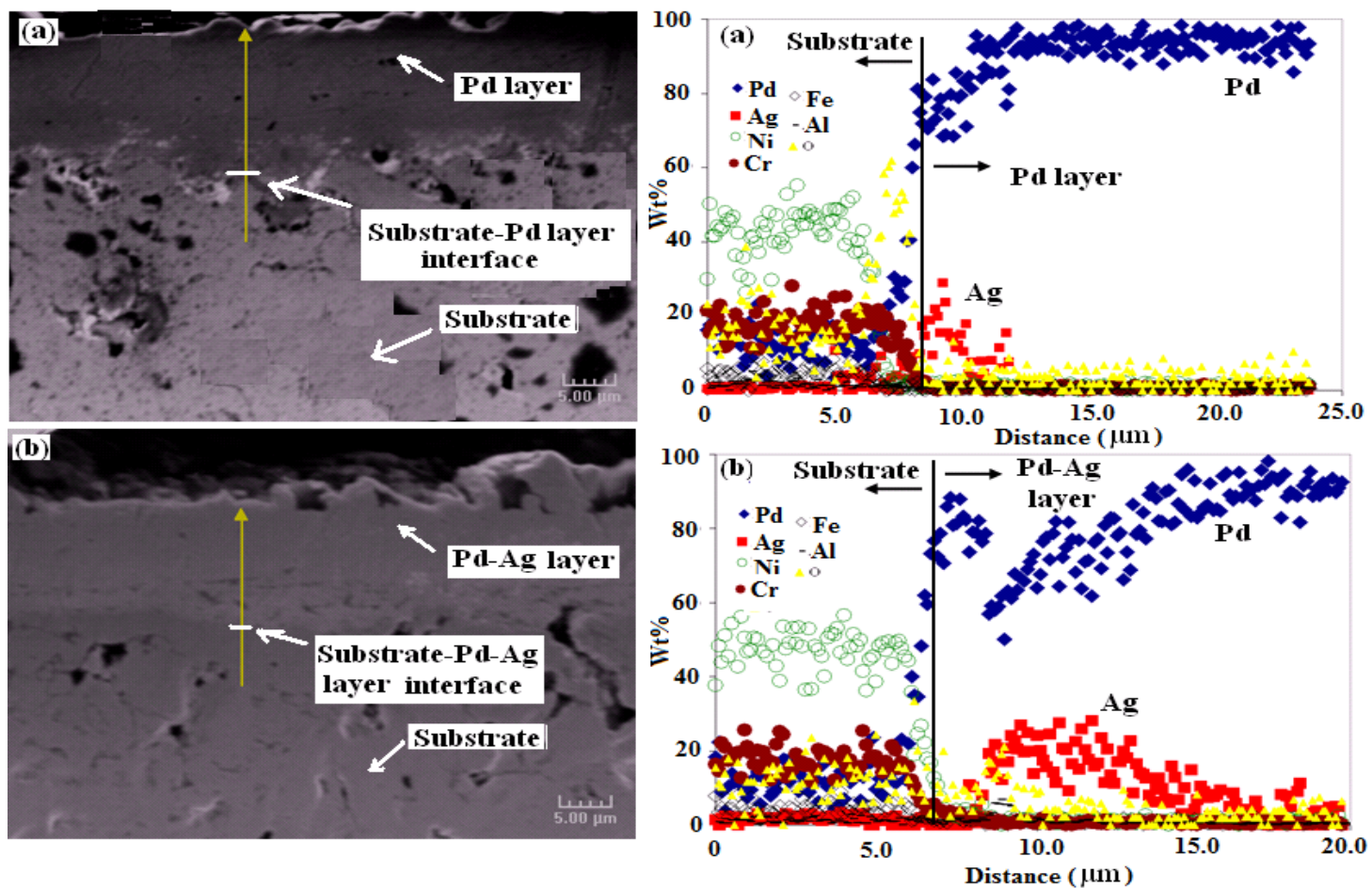


Fig. 9.6. The typical EDX line scans of the membrane cross-sections after the H_2 permeance and selectivity characteristics study in the temperature range of 300-450 °C for more than 550 h (a) R-13b (b) R-14

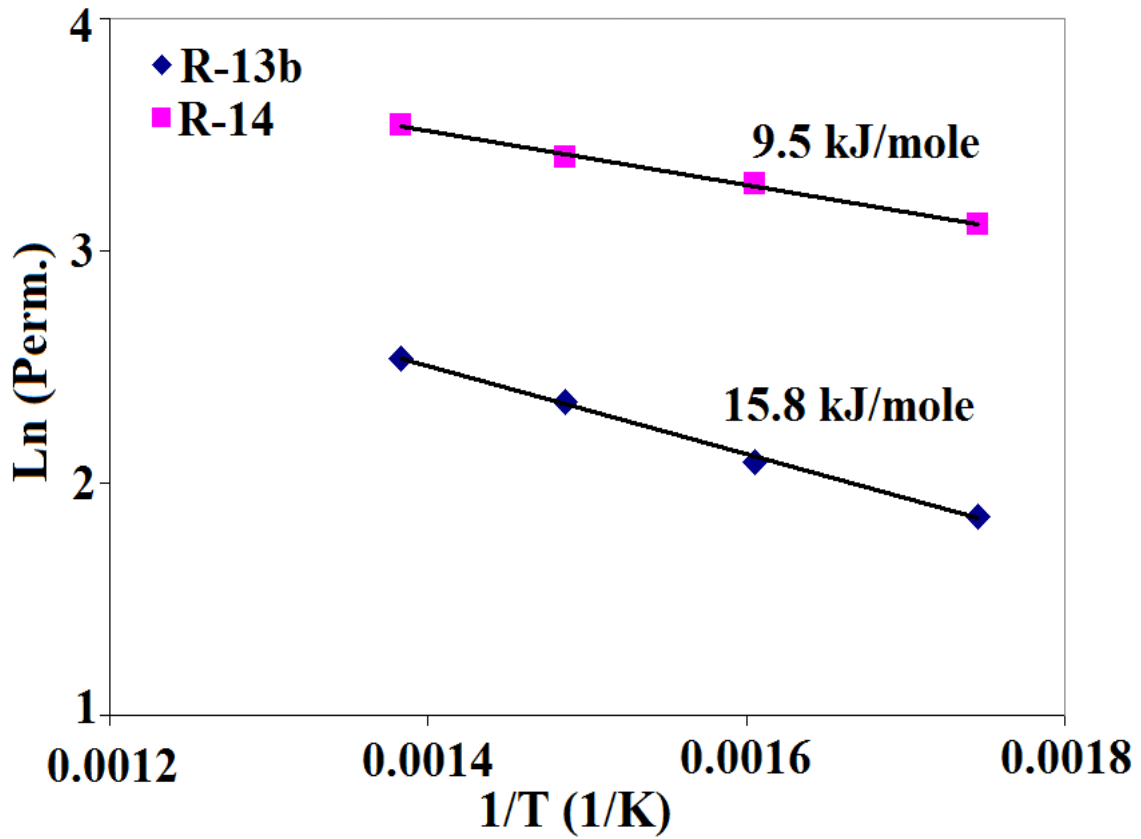


Fig. 9.7. Arrhenius plot of the H_2 permeance of the membranes (synthesized by multi plating, annealing (550 °C) and polishing steps) between 300-450 °C for R-13b and R-14

Section 7.3.4) that the Pd-Ag membranes were more effective for the H₂ permeation at lower temperatures than the pure Pd membrane.

9.4. Conclusion

The pinholes formation in the Pd and Pd-Ag membranes could be due to the voids or porosity present in the Pd and Pd-Ag deposits. The voids present in the deposits agglomerated on heating and in a few cases, the voids agglomeration causing the through-through pinholes in the membrane. The resulting through-through pinholes caused the He leak and the decline in the selectivity of the membranes. The multi step plating, annealing and polishing approach avoided alignment of the pinholes in each deposited layer from forming through-through pinholes in the membrane. The membranes prepared by multi step plating, annealing and polishing approach were selectivity stable between 300-450 °C for more than 550 h. The membranes were at 450 °C for more than 200 h (> 8 days) out of 550 h. The Ag content in R-14 was more than that of R-13b. The higher Ag content in R-14 resulted in the lower activation energy for the H₂ permeation in comparison to R-13b. The lower activation energy of R-14 implied that R-14 was more effective for H₂ separation at lower temperatures than R-13b.

10. Conclusions

- ❖ The multi layer sequential Pd-Ag plating method was successfully utilized for the first time to synthesize thin ($< 10 \mu\text{m}$ thickness) and H_2 selective Pd-Ag membranes.
- ❖ The conventional Ag ($[\text{Ag}]/[\text{N}_2\text{H}_4] = 3 \text{ mM}/5.6 \text{ mM}$) and Pd ($[\text{Pd}]/[\text{N}_2\text{H}_4] = 16 \text{ mM}/5.6 \text{ mM}$) plating conditions, used for the Pd-Ag membrane synthesis using the bi layer method, lead to the dendritic and non-uniform multi layer Pd-Ag sequential deposits, not suitable for the membrane synthesis. Ag under the conventional plating conditions ($[\text{Ag}]/[\text{N}_2\text{H}_4] = 3 \text{ mM}/5.6 \text{ mM}$) was deposited at high overpotential and under the severe mass transfer controlled conditions on the Pd surface resulting in the dendritic and non-uniform Pd-Ag deposits.
- ❖ The modification to the conventional Ag plating conditions ($[\text{Ag}]/[\text{N}_2\text{H}_4] = 3 \text{ mM}/5.6 \text{ mM}$) such as higher Ag to N_2H_4 ratio ($[\text{Ag}]/[\text{N}_2\text{H}_4] = 20 \text{ mM}/4 \text{ mM}$ or $[\text{Ag}]/[\text{N}_2\text{H}_4] = 3 \text{ mM}/1 \text{ mM}$) or substrate stirring (500 rpm) prevented the Ag deposition at high overpotential and under the severe mass transfer controlled conditions on the Pd surface. The Pd-Ag multi layer sequential deposits obtained under the modified Ag plating conditions were compact and uniform suitable for the synthesis of thin and H_2 selective Pd-Ag membranes.
- ❖ The Ag electroplating conditions ($[\text{Ag}] = 100 \text{ mM}$ and current = $2 \text{ mA}/\text{cm}^2$) also

led to the Ag deposition at low overpotential on the Pd surface and the resulting Pd (by electroless method, $[\text{Pd}]/[\text{N}_2\text{H}_4] = 16 \text{ mM}/5.6 \text{ mM}$) and Ag (by electroplating method) multi layer sequential deposits were compact and uniform.

- ❖ The Pd-Ag membranes synthesized by the multi layer sequential method with Pd and Ag layers each in the thickness range of 2.0-3.0 μm or less were successfully annealed at 550 $^\circ\text{C}$ for 24 h.
- ❖ The Pd-Ag sequentially prepared membranes after annealing at 550 $^\circ\text{C}$, 24 h showed lower activation for the H_2 permeation (4.3–11.5 kJ/mole) than that of the pure Pd membranes (12-16.4 kJ/mole). The low activation energy for the Pd-Ag membranes was in agreement with the lower activation energy reported for the Pd-Ag alloy membranes in the literature.
- ❖ The low activation energy for the H_2 permeation of Pd-Ag membranes meant that on decreasing the temperature, the H_2 permeation of the Pd-Ag membranes decreased at a lesser rate than that of the pure Pd membranes making Pd-Ag membranes more effective at lower temperatures. A Pd-Ag (20 wt%) membrane prepared by multi layer sequential method showed H_2 permeance higher by the factor of 1.44 at 400 $^\circ\text{C}$, 1.95 at 300 $^\circ\text{C}$ and 2.47 at 250 $^\circ\text{C}$ in comparison to the H_2 permeance of the Pd foil with the thickness same as that of the Pd-Ag (20 wt%) membrane.
- ❖ The sequentially prepared Pd-Ag membranes showed decline in the H_2/He

selectivity under the annealing (550 °C) and H₂ permeation characteristics (550 °C) study conditions.

- ❖ The sequentially prepared Pd-Ag membranes showed decline in the H₂/He selectivity under the annealing (550 °C) and H₂ permeation characteristics (500 °C) study conditions.
- ❖ The Pd-Ag co-deposits obtained using the conventional NH₃+EDTA bath were dendritic, inhomogeneous in composition and non-uniform and showed poor adhesion with the porous stainless steel substrate. The co-deposits were bi-metallic, therefore required the annealing step to form the Pd-Ag alloy.
- ❖ There existed a large difference in the deposition potentials of Pd and Ag in the presence of NH₃+EDTA in the conventional bath. The Pd deposition occurred at an electrode potential 600 to 650 mV more cathodic than the Ag deposition. Under the co-deposition conditions, the Ag deposition was severely controlled by its mass transfer in the solution resulting in the dendritic and inhomogeneous deposits with non-uniform morphology.
- ❖ The non-uniform morphology of the Pd-Ag co-deposits obtained using the conventional NH₃+EDTA bath meant that the co-deposits were not suitable for synthesizing a thin and H₂ selective Pd-Ag membrane. A 33.5 thick layer of co-deposits on the PSS tube (0.1 μm media grade) did not produce He dense membrane whereas the Pd (Pd deposits showed uniform morphology) layer of thickness 21.5

μm produced a He tight membrane on the PSS tube (0.1 μm media grade).

- ❖ The variation in the bath parameters (total metal concentration, N_2H_4 concentration, NH_3 concentration, pH and temperature) in the case of conventional NH_3 +EDTA bath affected the average Pd-Ag plating rates and the overall composition of the deposits but showed little improvement on the homogeneity, morphology and the adhesion of the deposits with the PSS substrate. The increasing pH, N_2H_4 concentration and temperature favored the Pd deposition while increasing NH_3 concentration in the bath favored the Ag deposition.
- ❖ Among the complexing agents investigated (NH_3 , EDTA, glycine and KCl), the order of the suitability of the complexing agents (based on the difference between the Pd and Ag deposition potentials) increased as $\text{NH}_3 < \text{glycine} < \text{EDTA} < \text{KCl}$. NH_3 , EDTA and glycine showed the large difference (550 mV or higher) similar to the conventional NH_3 +EDTA bath between the Pd and Ag deposition potentials whereas KCl showed the least difference (~ 250 mV) and was the best suited for the Pd-Ag co-deposition.
- ❖ N_2H_4 as the reducing agent was observed suitable for the Pd-Ag co-deposition in the basic conditions in the NH_3 , EDTA and glycine baths as the addition of N_2H_4 did not result in homogenous precipitation of Pd and Ag in the baths. The addition of N_2H_4 in the KCl bath (pH = 6.4-11) showed instant homogeneous precipitation of Pd and Ag in the bath. The use of HCHO as the reducing agent in the KCl bath under the acidic conditions (pH=1.5) resulted in a stable co-plating bath without the

homogeneous precipitation of Pd and Ag.

- ❖ The Pd-Ag deposits obtained from NH_3 , EDTA and glycine bath showed non-homogeneous distribution of Pd and Ag. The Ag was more concentrated towards the solution side (away from the substrate side). The co-deposits obtained were bi-metallic and required annealing step to form the Pd-Ag alloy. The co-deposits obtained showed poor adhesion with the PSS substrate.
- ❖ In comparison to the NH_3 and EDTA baths, the deposits obtained from the glycine bath were relatively uniform in morphology, therefore were relatively more suitable for the Pd-Ag membrane synthesis.
- ❖ The Pd-Ag co-deposits obtained from the glycine bath could be annealed at $500\text{ }^\circ\text{C}$ (10 h) which was less than the temperature used for annealing the sequentially obtained Pd-Ag deposits ($550\text{ }^\circ\text{C}$, 24 h). The EDX penetration depth analysis showed that the Pd and Ag particles size ($\sim 0.5\text{ }\mu\text{m}$) was less than the thickness of the sequentially deposited Pd and Ag layers ($1.0\text{-}3.0\text{ }\mu\text{m}$). Therefore the co-deposits required milder annealing conditions than that used for the sequentially obtained Pd-Ag deposits.
- ❖ The Pd-Ag membrane prepared using the glycine based co-deposition bath without any polishing during the plating sequence showed large drop in the membrane selectivity on heating. The decline in the selectivity was believed to be due to the non-uniform morphology of the deposits showing tendencies to grow more in the

perpendicular direction to the substrate surface. The polishing steps during the membrane plating reduced the non-uniform growth by selectively removing the perpendicularly growing deposits but also removed the majority of the Ag deposited.

- ❖ KCl bath in the acidic conditions with HCHO as the reducing agent produced very uniform composition of the Pd and Ag deposits. The Pd-Ag deposits obtained from KCl bath were alloy phase, therefore requiring no annealing step for the membrane synthesis.

- ❖ The free standing or unsupported Pd and Ag foils on heating (700 °C, 48 h) developed large number of pinholes. The pinholes in the unsupported free standing foils were believed to be formed due to the voids or porosity present in the Pd and Ag deposits. The voids present in the deposits (in the form of free standing foil and the deposits layer supported on the substrate) was believed to agglomerate on heating and in a few of the cases, the voids agglomeration caused formation of the through through pinholes in the membrane. The resulting through through pinholes caused the He leak and decline in the selectivity of the membranes. The multi step plating, annealing and polishing approach avoided alignment of the pinholes in each deposited layer and prevented the formation of through through pinholes in the membrane

- ❖ The multi step plating, annealing and polishing approach resulted in the Pd and Pd-Ag membranes showing stable selectivity between 300-450 °C for more than 550 h

(approximately 23 days). The membranes were at 450 °C in H₂ atmosphere for more than 200 h (> 8 days) out of 550 h.

11. Recommendations

- ❖ The KCl bath should further be used for the Pd-Ag membrane synthesis. The acidic KCl bath dissolved the porous metal substrate. The dissolution of the porous metal substrate could be avoided by plating a thin layer ($\sim 0.5 \mu\text{m}$) of pure Pd before dipping the substrate in the KCl bath.

- ❖ The porous metal substrate used in this study were oxidized or deposited with thin γ -alumina layer to form the intermetallic diffusion barrier to prevent the diffusion of substrate components into the Pd-Ag layer deposited on the top of the substrate. According to Ayrtuk [51], the PSS or inconel substrate components, Fe and Ni, showed complete miscibility with Pd but complete immiscibility with Ag. Ayrtuk [51] concluded Ag as a very good intermetallic diffusion barrier. However no study was done regarding the interaction of the porous metal components (Fe, Ni) with the Pd-Ag alloy and required further investigation. Tong et al. [56] also covered the PSS tube with the Ag layer ($\sim 0.3 \mu\text{m}$ thick) before depositing a Pd layer ($3 \mu\text{m}$) to prevent the intermetallic diffusion of the substrate components into the Pd layer. The membrane was exposed to $500 \text{ }^\circ\text{C}$ for more than 70 h and the Ag layer showed mixing with the Pd layer however no decline in the H_2 flux was observed indicating that Pd-Ag alloy itself could be resistant to the intermetallic diffusion and the intermetallic diffusion barrier step could be prevented in the case of composite Pd-Ag membrane synthesis.

-
- ❖ The relation between the porosity or voids present in the as plated Pd and Pd-Ag deposits and the formation of pinholes in the deposits on heating needs to be investigated in details. According to Nakahara [145], the Cu electroless deposits showed large number of voids present in the deposits due to the H₂ gas trapped in the deposits. The H₂ gas formed during the plating due to the oxidation of formaldehyde as the reducing agent in the plating bath and was trapped along the grain boundaries of the Cu deposits. The voids present in the Cu deposits on heating agglomerated and formed larger voids. In addition to the gas formed in the plating reaction, the solution could also be entrapped in the deposits between the grain boundaries [146] and resulted in the presence of voids in the deposits. The plating conditions affect the grain size [112] and grain boundaries in the deposits and therefore could affect the amount of porosity present in the deposits. Therefore, the effect of different plating conditions resulting in different grain sizes of Pd or Pd-Ag deposits and their subsequent effect on the pinholes formation should be thoroughly investigated.

 - ❖ In addition to Ag, alloying Pd with several other elements (Y, In, Ru, Au, Rh etc.) has been reported to increase the H₂ permeance and resistance to the H₂ embrittlement of Pd membranes. The plating baths and conditions to deposit the above mentioned alloying elements should be developed to synthesize the Pd-alloy membranes by sequential or co-deposition approach on the lines similar to the Pd and Ag deposition used in Chapters 5, 6 and 8 in this work

 - ❖ The Pd-Ag alloy membranes synthesized in this work could be further studied for

their performance under the steam reforming and water gas shift reactions for the H₂ production.

References

- [1] J.T.S. Irvine, The Bourne lecture-Power sources and the new energy economy, *J. Power Sources* 136 (2004) 203.
- [2] R. Agrawal, M. Offutt, M.P. Ramage, Hydrogen economy-an opportunity for chemical engineers?, *AIChE. J.* 51(6) (2005) 1582.
- [3] B.D. Solomon, A. Banerjee, A global survey of hydrogen energy research, development and policy, *Energy Policy* 34(2006) 781.
- [4] A.H. Tullo, Praxair plans big, *Chem. and Eng. News* September 16 (2002) 12.
- [5] E. Kikuchi, Membrane reactor application hydrogen production, *Catal. Today* 56 (2000) 97.
- [6] E. Wicke, G. Nernst, Phase diagram and thermodynamic behavior of the systems Pd/H₂ and Pd/D₂ at normal temperatures; H/D separation effects, *Ber. Bunsenges. Physik. Chem* 68 (1964) 224.
- [7] A. G. Knapton, Palladium alloys for hydrogen diffusion membranes-A review of high permeability materials, *Plat. Met. Rev.* 21 (1977) 44.
- [8] Y.S. Cheng, K.L. Yeung, Palladium-silver composite membranes by electroless plating, *J. Memb. Sci* 158 (1999) 127.
- [9] S. Uemiya, T. Matsuda, E. Kikuchi, Hydrogen permeable palladium-silver alloy membrane supported on porous ceramics, *J. Memb. Sci.* 56 (1991) 315.
- [10] P.P. Mardilovich, Y. She, Y.H. Ma, Defect-free palladium membranes on porous stainless-steel support, *AIChE J.*, 44(2) (1998) 310.
- [11] F. Guazzone, Engineering of substrate surface for the synthesis of ultra-thin composite Pd and Pd-Cu membranes for H₂ separation, *Ph.D. thesis, Worcester Polytechnic Institute, Worcester*, 2005.
- [12] J. Shu, B. P. A. Grandjean, A. V. Neste, S. Kaliaguine, Catalytic palladium-based reactors: a review, *Can. J. Chem. Eng.* 69 (1991) 1036.
- [13] T. Graham, on the absorption and dialytic separation of gases by colloid septa, *Phil. Trans. Roy. Soc. (London)*, 156 (1866), 399.

-
- [14] T. L. Ward, T. Dao, Model of hydrogen permeation behavior in palladium membranes, *J. Membr. Sci.* 153 (1999) 211.
- [15] M. Lagos, G. Martinez, I. K. Schuller, Kinetics of hydrogen absorption in transition metal and subsurface bonding, *Phys. Rev. B.* 29(10) (1984) 5979.
- [16] M. A. Pick, K. Sonnenberg, A model for atomic hydrogen-metal interactions-application to recycling, recombination and permeation, *J. Nucl. Mater.* 131 (1985) 208.
- [17] G. J. Grashoff, C. E. Pilkington, C.W. Corti, A review of the technology emphasizing the current status of palladium membrane diffusion, *Plat. Met. Rev.* 27(4) (1983) 157.
- [18] Fort, J. P. G. Farr, I. R. Harris, Comparison of palladium-silver and palladium-yttrium alloys as hydrogen separation membranes, *J. Less-Common Met.* 39 (1975) 293.
- [19] H. Kurokawa, T. Nakayama, Y. Kobayashi, K. Suzuki, M. Takahashi, S. Takami, M. Kubo, N. Itoh, P. Selvam, A. Miyamoto, Monte Carlo simulation of hydrogen absorption in palladium and palladium alloys, *Catal. Today* 82 (2003) 233.
- [20] H. Bruning, A. Sieverts, *Z. Phys. Chem.* 163A (1933) 409.
- [21] L. J. Gillespie, L. S. Galstaun, The palladium-hydrogen equilibrium and new palladium hydrides, *J. Am. Chem. Soc.* 58 (1936) 2565.
- [22] J. C. Barton, F. A. Lewis, Determination of the hydrogen content in palladium and palladium alloys from measurements of electrode potential and electrical resistance, A review, *Talanta* 10 (1963) 237.
- [23] L. W. Makceehan, The crystal structures of the system palladium-hydrogen, *Phys. Rev.* 21 (1923) 334.
- [24] F. Kruger, G. Gehm, *Annl. Phys.* 16 (174) (1933) 190.
- [25] A.K.M Fazle Kibria, Y. sakamoto, The effect of alloying of palladium with silver and rhodium on the hydrogen solubility, miscibility gap and hysteresis, *Int. J. Hydrogen Energy* 25 (2000) 853.
- [26] R.A. Karpova, I.P. Tverdovskii, Sorption of Hydrogen by Disperse Pd-Cu Alloys, *Zhur. Fiz. Khim.* 33 (1959) 1393.
- [27] A.A. Rodina, M.A. Gurevich, N.I. Doronicheva, The interaction of hydrogen with certain palladium-gold and palladium-silver-gold alloys, *Russ. J. Phys. Chem.* 45 (1971) 621.

-
- [28] A.W. Carson, T.B. Flanagan, F.A. Lewis, Absorption of hydrogen by Pd/Pt alloys- Electrical resistance as function of hydrogen, and one-atmospheric isobars, *Trans. Faraday Soc.* 56 (1960) 363
- [29] J.C. Barton, J.A.S. Green, F.A. Lewis, Changes of electrode potential and electrical resistance as a function of the hydrogen content of some Pd+Ni and Pd+Rh alloys, *Trans. Faraday Soc.* 62 (1966) 960.
- [30] H. Brodowsky, E. Poeschel, Hydrogen in palladium-silver alloys, *Z. Phys. Chem.* 44 (1965) 143.
- [31] E. Kikuchi, S. Uemiya, Preparation of supported thin palladium-silver alloy membranes and their characteristics for hydrogen separation, *Gas Sep. Purif.* 5 (4) (1991) 261.
- [32] R. Gryaznov, Metal containing membranes for the production of ultrapure hydrogen and the recovery of hydrogen isotopes” *Sep. Purif. Methods* 29(2) (2000) 171.
- [33] D.L. McKinley, Metal Alloy for Hydrogen Separation and Purification, *US patent*, 3,350,845; 1967
- [34] W. A. Swansiger, J. H. Swisher, J. P. Darginis, C. W. Schoenfelder, H₂ permeation in palladium-chromium alloys, *J. Phys. Chem.* 80 (3) (1976) 308.
- [35] Y. Sakamoto, T. Ohishi, E. Kumashiro, K Takao, Diffusivity and solubility of hydrogen in Pd-Fe and Pd-V alloys, *J. Less-Common Met.* 88 (1982) 379.
- [36] M. Kajiwara, S. Uemiya, T. Kojima, E. Kikuchi, Rhodium- and iridium-dispersed porous alumina membranes and their hydrogen permeation properties, *Catal. Today* 56 (2000) 83.
- [37] T.S. Moss. N.M. Peachey, R.C. Snow, R.C. Dye, Multilayer metal membranes for hydrogen separation, *Int. J. Hydrogen Energy* 23 (2) (1998) 99.
- [38] N.M. Peachey, R.C. Snow, R.C. Dye, Composite Pd/Ta metal membranes for hydrogen production, *J. Memb. Sci.* 111 (1996) 123.
- [39] D.J. Edlund, J. McCarthy, The relationship between intermetallic diffusion and flux decline in composite-metal membranes: implications for achieving long membrane lifetime, *J. Memb. Sci.* 107 (1995) 147.
- [40] J. R. Hufton, S. Mayorga, S. Sircar, Sorption-enhanced reaction process for hydrogen production, *AIChE. J.* 45 (1999) 248.
- [41] J. Shu, B.P.A. Grandjean, S. Kaliaguine, Asymmetric Pd-Ag/stainless steel catalytic membranes for methane steam reforming, *Catal. Today* 25 (1995) 327.

-
- [42] A. Li, W. Liang, R. Hughes, Characterization and permeation of palladium/stainless composite membranes, *J. Memb. Sci.* 149 (1998) 259.
- [43] J. Shu, A. Adnot, B.P.A. Grandjean, S. Kaliaguine, Structurally stable composite Pd-Ag membranes: introduction of a diffusion barrier”, *Thin Solid Films*, 286, (1996) 72.
- [44] S. Uemiya, Y. Kude, K. Sugino, N. Sato, T. Matsuda, E. Kikuchi E., A palladium/porous-glass composite membrane for hydrogen separation”, *Chem. Lett.* (1988) 1687.
- [45] S. Uemiya, Y. Kude, H. Ando, N. Sato, T. Matsuda, E. Kikuchi., Separation of hydrogen through palladium thin film supported on a porous glass tube, *J. Memb. Sci.* 56 (1991)303.
- [46] K.L. Yeung, S.C. Christiansen, A. Verma, Palladium composite membranes by electroless plating technique Relationships between plating kinetics, film microstructure and membrane performance, *J. Memb. Sci.* 159 (1999) 107.
- [47] Y.S. Cheng, K.L. Yeung, Effects of electroless plating chemistry on the synthesis of palladium membranes, *J. Memb. Sci.* 182 (2001) 195.
- [48] V. Jayraman, Y.S. Lin, Synthesis and hydrogen permeation properties of ultrathin palladium-silver alloy membranes, *J. Memb. Sci.* 104 (1995) 251.
- [49] K. Hou, R. Hughes, Preparation of thin and highly stable Pd/Ag composite membranes and simulative analysis of transfer resistance for hydrogen separation, *J. Memb. Sci.* 214 (2003) 43.
- [50] F. Rao, J.D. Way, R.L. McCormick, S.N. Paglieri, Preparation and characterization of Pd-Cu composite membranes for hydrogen separation, *Chem. Eng. J.* 93 (2003) 11.
- [51] M.E. Ayrtuk, Synthesis, annealing strategies and in situ-characterization of thermally stable composite thin Pd/Ag alloy membranes for H₂ purification, *Ph.D. thesis, Worcester Polytechnic Institute, Worcester*, 2007.
- [52] S. Ryi, J. Park, S. Kim, S. Cho, D. Kim, K. Um, Characterization of Pd-Cu-Ni ternary alloy membrane prepared by magnetron sputtering and Cu-reflow on porous nickel support for hydrogen production, *Sep. Purif. Technol.* 50 (2006) 82.
- [53] V.M. Gryaznov, O.S. Serebryannikova, Y.M. Serov, Preparation and catalysis over palladium composite membranes, *Appl. Catal., A* 96 (1993) 15.
- [54] Y.H. Ma, P.P. Mardilovich, Y. She, Hydrogen gas-extraction module and method of fabrication, *US patent* 6152987, 2000.
- [55] S. Nam, K. Lee, Hydrogen separation by Pd alloy composite membranes: introduction of diffusion barrier, *J. Memb. Sci.* 192 (2001) 177.

- [56] J. Tong, R. Shirai, Y. Kashima, Y. Matsumura, Preparation of a pinhole-free Pd-Ag membrane on a porous metal support for pure hydrogen separation, *J. Memb. Sci.* 260 (2005) 84.
- [57] I.P. Mardilovich, E. Engwall, Y.H. Ma, Dependence of hydrogen flux on the pore size and plating surface morphology of asymmetric Pd-porous stainless steel membranes, *Desalin.* 144 (2002) 85.
- [58] Y.H. Ma, I.P. Madilovich, P.P. Mardilovich, Effect of porosity and pore size distribution of the stainless steel on the thickness and hydrogen flux of palladium membranes. *J. Amer. Chem. Soc.* 46 (2) (2001).
- [59] N. Jemma, J. Shu, S. Kaliaguine, B.P.A. Grandjean, Thin palladium film formation on shot peening modified porous stainless steel substrate, *Ind. Eng. Chem. Res.* 35 (1996) 973.
- [60] Y.H. Ma, F. Guazzone, Composite gas separation modules having a layer of particles with uniform binder metal distribution, *US patent application*, 2006016332, 2006.
- [61] Y. H. Ma, I.P. Mardilovich, E.E. Engwall, Composite gas separation modules having high Tamman temperature intermediate layers, *US patent*, 7255726, 2007
- [62] J. Tong, H. Suda, K. Haraya , Y. matsumara, A novel method of for the preparation of thin dense Pd membrane on macro porous stainless steel filter, *J. Memb. Sci.* 260 (2005) 10.
- [63] G. Xomeritakis, Y.S. Lin, Fabrication of thin metallic membranes by MOCVD and sputtering, *J. Memb. Sci.* 133 (1997) 217.
- [64] C.F. Powell, J.H. Oxley, J.M. Blocher, Vapor deposition, *John Wiley & sons, New York*, 1966.
- [65] S. Ilias, R. Govind, Development of high temperature membranes for membrane reactor: an overview, *AIChE Symp. Ser.* 268 (1989) 18-25.
- [66] D.R. Biswas, Review: Deposition processes for films and coatings, *J Mater. Sci.* 21, 2217-2223 (1986).
- [67] A. Brenner, Electrodeposition of alloys: Principles and Practice, *Academic press*, V-1, 1963.
- [68] J.B. Hajdu, G.O. Mallory, Electroless plating: fundamentals and application, *The American Electroplaters and Surface Finishers Society, Orlando*, 1990.
- [69] R. Checchetto, N. Bazzanella, B. Patton, A. Miotello, Palladium membranes prepared by r.f. magnetron sputtering for hydrogen purification, *Surf. Coat. Technol.* 177-178 (2004) 73.

-
- [70] A. K. Sinha, Physical metallurgy handbook, *McGraw-Hill Inc.*, New York, 2003.
- [71] S. Yan, M. Hideaki, K. Katsuki and M. Shigeharu, Thin palladium membrane formed in support pores by metal-organic vapor deposition method and application to hydrogen, *Ind. Eng. Chem. Res.* 33 (1994) 616.
- [72] S. Nam, S. Lee, K. Lee., Preparation of a palladium alloy composite membrane supported in a porous stainless steel by vacuum electrodeposition, *J. Memb. Sci.* 153 (1999) 163.
- [73] I. Ohno, Electrochemistry of electroless plating, *Mat. Sci. Eng.*A146 (1991) 33.
- [74] I. Ohno, O. Wakabayashi, S. Haruyama, Anodic oxidation of reductants in electroless plating, *J. Electrochem. Soc.: Electrochem. Sci. and Technol.* . 132 (10) (1985) 2323.
- [75] I. Ohno, Measurement of the instantaneous rate of electroless plating by an electrochemical method, *Surf. Technol.* 13 (1981) 1.
- [76] T.C. Franklin, Some mechanisms of action of additives in electrodeposition processes, *Surf. Coat. Technol.* 30 (1987) 415.
- [77] A.M. Sullivan, P.A. Kohl, The autocatalytic deposition of gold in nonalkaline, gold thiosulfate electroless bath, *J. Electrochem. Soc.*142 (7) (1995) 2250.
- [78] J. O'M. Bockris, A.K.N. Reddy, Modern electrochemistry – an introduction to an interdisciplinary area, *Plenum Press*, New York, 1970.
- [79] K.I. Popov, N.V. Krstajić, Z.Dj. Jerotijević, Electrocrystallization of silver from silver nitrate solutions at low overpotentials, *Surf. Technol.* 26 (1985) 185.
- [80] R.N. Rhoda, Electroless palladium plating, *Trans. Inst. Metal Finish*, 36 (1959) 82.
- [81] J. Kim, Y.S. Lin, Palladium-modified yttria-stabilized zirconia membranes, *Ind. Eng. Chem. Res.* 39 (2000) 616.
- [82] R.C. Hurlbert, J.O. Konency, Diffusion of Hydrogen through Palladium, *J. Chem. Phys.* 34 (1961) 655.
- [83] F. Pearlstein, R.F. Weightman, Palladium electroless plating, *Plating*, 56(10) (1969)1158.
- [84] J.N. Keuler, L. Lorenzen, R.D. Sanderson, V. Prozesky, W.J. Przybyłowicz, Characterization of electroless plated palladium-silver alloy membranes, *Thin Solid Films* 347 (1999) 91.

-
- [85] B.K.R. Nair, J. Choi, M.P. Harold, Electroless plating and permeation features of Pd and Pd/Ag hollow fiber composite membranes, *J. Memb. Sci.* 288 (2007) 67.
- [86] Y.H. Ma, B.C. Akis, M.E. Ayturk, F. Guazzone, E.E. Engwall, I.P. Mardilovich, Characterization of intermetallic diffusion barrier and alloy formation for Pd/Cu and Pd/Ag porous stainless steel composite membranes, *Ind. Eng. Chem. Res.* 43 (2004) 2936.
- [87] J.N. Keuler, L. Lorenzen, Developing a heating procedure to optimize hydrogen permeance through Pd-Ag membranes of thickness less than 2.2 μ m, *J. Memb. Sci.* 195 (2002) 202.
- [88] J. Shu, B.P.A. Grandjean, E. Ghali, S. Kaliaguine, Simultaneous deposition of Pd and Ag on porous stainless steel by electroless plating, *J. Memb. Sci.* 77 (1993)181.
- [89] T. Huang, M. Wei, H. Chen, Preparation of hydrogen-permselective palladium-silver alloy composite membranes by electroless co-deposition, *Sep. Purif. Technol.* 32 (2003) 239.
- [90] D.A.P. Tanaka, M.A.L. Tanco, M.T. Suzuki, Preparation of palladium and silver alloy membrane on a porous α -alumina tube via simultaneous electroless plating, *J. Memb. Sci.* 247 (2005) 21.
- [91] N. Lbl, K. Schadeegg, Surface roughness effects in the electrodeposition of copper in the limiting current range, *J. Electrochem. Soc.* 114 (1967) 54.
- [92] Y. H. Ma, B. C. Akis, M. E. Ayturk, F. Guazzone, E. E. Engwall, I. P. Mardilovich, Characterization of intermetallic diffusion barrier and alloy formation for Pd/Cu and Pd/Ag Porous stainless steel composite membranes, *Ind. Eng. Chem. Res.* 43 (2004) 2936.
- [93] E.E. Engwall, I.P. Mardilovich, Y.H. Ma, Transport resistance for oxide diffusion barriers on porous metal supports used in composite Pd and Pd-alloy membranes, *ACS Fuel Chem. Div. Preprints* 48 (1) (2003) 390.
- [94] F. Guazzone, E.E. Engwall, Y.H. Ma, Effect of surface activity, defects and mass transfer on hydrogen permeance and n-value in composite palladium-porous stainless steel membranes, *Catal. Today* 118 (2006) 24.
- [95] F.A. Lewis, The palladium hydrogen system, *Academic Press, London, New york*, 1967.
- [96] A. Sieverts, E. Jurisch, A. Metz, *Z Anorg. Allg. Chem* 92 (1915) 329.
- [97] B.D. Morreale, M.V. Ciocco, R.M. Enick, B.I. Morsi, B.H. Howard, A.V. Cugini, K.S. Rothenberger, The permeability of hydrogen in bulk palladium at elevated temperatures and pressures, *J. Membr. Sci.* 87 (2003) 212.

-
- [98] J.F. Lynch, T.B. Flanagan, An investigation of the dynamic equilibrium between chemisorbed and absorbed hydrogen in the palladium/hydrogen system, *J. Phys. Chem.* 77 (22) (1973) 2628
- [99] F.J. Ackerman, G.J. Koskinas, Permeation of hydrogen and deuterium through palladium-silver alloys, *J. Chem. Eng. Data* 17(1) (1972) 51.
- [100] C. Picard, O.J. Kleppa, G. Boureau, High temperature thermodynamics of the solutions of hydrogen in palladium-silver alloys, *J. Phys. Chem.* 70 (6) (1979) 2710.
- [101] V.A. Pugachev, F.I. Busol, E.I. Nikolaev, B.P. Nam, Penetration and diffusion of hydrogen in palladium-silver alloys, *Russ. J. Phys. Chem.* 49(7) (1975) 1045.
- [102] G.L. Holleck, Diffusion and solubility of hydrogen in palladium and palladium-silver alloys, *J. Phys. Chem.* 74(3) (1970) 503.
- [103] E. Serra, M. Kemali, A. Perujo, D.K. Ross, Hydrogen and deuterium in Pd-25 pct Ag alloy: permeation, diffusion, solubilization, and surface reaction, *Metall. Mater. Trans. A* 29A (1998) 1023.
- [104] B.H. Howard, R.P. Killmeyer, K.S. Rothenberger, A.V. Cugini, B.D. Morreale, R.M. Enick, F. Bustamante, Hydrogen permeance of palladium-copper alloy membranes over a wide range of temperatures and pressures, *J. Membr. Sci.* 241 (2) (2004) 207.
- [105] W. Davis, USAEC report KAPL-1227, *U.S. Atomic Energy Commission*, 1954.
- [106] M.A. Pick, J.W. Davenport, M. Strongin, G.J. Dienes, Enhancement of hydrogen uptake rates for Nb and Ta by thin surface overlayers, *Phys. Rev. Lett.* 43 (1979) 286.
- [107] J.B. Taylor, I. Langmuir, The Evaporation of Atoms, Ions and Electrons from Caesium Films on Tungsten, *Phys. Rev.* 44 (1933) 423.
- [108] J.K. Roberts, The Adsorption of Hydrogen on Tungsten, *Proc. Roy. Soc.* A152 (1935) 445.
- [109] R.J. Behm, K. Christmann, G. Ertl, Adsorption of hydrogen on Pd (100), *Surf. Sci.* 99 (1980) 320.
- [110] J.K. Norskov, S. Holloway, N.D. Lang, Microscopic model for the poisoning and promotion of adsorption rates by electronegative and electropositive atoms, *Surf. Sci.* 137 (1984) 65.
- [111] A.B. Antoniazzi, A.A. Haasz, P.C. Stangeby, The effect of adsorbed carbon and sulfur on hydrogen permeation through palladium, *J. Nucl. Mater.* 162-164 (1989) 1065.

-
- [112] N. Jemaa, B.P.A. Grandjean, S. Kaliaguine, Diffusion coefficient of hydrogen in a Pd-Ag membrane: effect of hydrogen solubility, *Can. J. Chem. Eng.* 73 (1995) 405.
- [113] N. R. Roshan, A. P. Mishchenko, V. P. Polyakova, N. I. Parfenova, E. M. Savitsky, E. A. Voitekhova, V. M. Gryaznov, M. E. Sarylova, The effect of the surface state on the hydrogen permeability and the catalytic activity of palladium alloy membranes, *J. Less-Common Met.* 89 (1983) 423.
- [114] J. Shu, B.P.A. Grandjean, S. Kaliaguine, Morphological study of hydrogen permeable membranes, *Thin Solid Films* 252(1994) 26.
- [115] M.E. Ayrtuk, I.P. Mardilovich, E.E. Engwall, Y.H. Ma, Synthesis of composite Pd-porous stainless steel (PSS) membranes with a Pd/Ag intermetallic diffusion barrier, *J. Membr. Sci.* 285(2006) 385.
- [116] C. Wagner, W.Z. Traud, The interpretation of corrosion phenomena by superimposition of electrochemical partial reactions and the formation of potentials of mixed electrodes, *Z. Electrochim.* 44 (1938) 391.
- [117] L.G. Sillen, A.E. Martell, Stability constants for metal-ion complexes, *The Chemical Society, London*, 1964.
- [118] B. Sturzenegger, J.Cl. Puipe, Electrodeposition of palladium-silver alloys from ammoniacal electrolytes, *Plat. Met. Rev.* 28(3) (1984) 117.
- [119] Ph. Hasler, Th. Allmendiger, Electrodeposition of thin Pd-Ag films, *Surf. Coat. Technol.* 58 (1993) 179.
- [120] B.E. Conway, J.O'M. Bockris, E. Yeager, S.U.M. Khan, R.E. White, Kinetics and mechanisms of electrode processes, *Plenum Press, New York*, 1983.
- [121] W.S. Wu, G.P. Rangaiah, M. Fleischmann, Effect of gas evolution on dispersion in electrochemical reactor, *J. Appl. Electrochem.* 23 (1993) 113.
- [122] W.S. Wu, G.P. Rangaiah, Effect of gas evolution on mass transfer in an electrochemical reactor, *J. Appl. Electrochem.* 23 (1993) 1139.
- [123] E. Yeager, J.O'M. Bockris, B.E. Conway, S. Sarangapani, Comprehensive treatise of electrochemistry-Gas evolving electrode, *Plenum Press, New York*, 1983.
- [124] A.T. Dimitrov, S.H. Jordanov, K.I. Popov, M.G. Pavlovic, V. Radmilovic, electrodeposition of Ag from nitrate solutions: Part I. Effect of phosphate ions on morphology, *J. Appl. Electrochem.* 28 (1998) 791.

-
- [125] L. Kiss, Kinetics of electrochemical metal dissolution, *Elsevier, Amsterdam*, 1988.
- [126] M. Paunovic, I. Ohno, Proceedings of the symposium on “electroless deposition of metals and alloys”, *The Electrochemical Society, New Jersey*, V-88-12, 1988.
- [127] A.M. Sullivan, P.A. Kohl, The autocatalytic deposition of gold in nonalkaline, gold thiosulfate electroless bath, *J. Electrochem. Soc.* 142 (7) (1995) 2250.
- [128] A. Calusaru, Electrodeposition of metal powders, *Material Science Micrographs, New York*, 1979.
- [129] J. McDougall, M. El-sharif, S. Ma, Chromium electrodeposition using a chromium (III) glycine complex, *J. Appl. Electrochem.* 28 (1998) 929.
- [130] V. Cuculić, I. Pižeta, M. Branica, Voltammetric determination of stability constants of iron(III)-glycine complexes in water solution, *J. Electroanal. Chem* 583 (2005) 140.
- [131] J.L. Ortiz-Aparicio, Y. Meas, G. Trejo, R. Ortega, T.W. Chapman, E. Chainet, P. Ozil, Electrodeposition of zinc-cobalt alloy from a complexing alkaline glycinate bath, *Electrochim. Acta* 52 (2007) 4742.
- [132] J.A. Dean, Lange’s handbook of chemistry, *McGraw-Hill Inc., New York*, Fifteenth edition, 1999.
- [133] M.S. Antelman, The encyclopedia of chemical electrode potential, *Plenum press, New York*, 1982.
- [134] R.J.R. Uhlhorn, K. Keizer, A.J. Burggraaf, Gas and surface diffusion in modified γ -alumina systems, *J. Membr. Sci.* 46 (1989) 225.
- [135] I.B. Elkina, J.H. Meldon, Hydrogen transport in palladium membranes, *Desalination* 147 (2002) 445.
- [136] J.N. Keuler, L. Lorenzen, R.D. Sanderson, V. Prozesky, W.J. Przybylowicz, Characterizing palladium-silver and palladium-nickel alloy membranes using SEM, XRD and PIXE, *Nucl. Instrum. Methods Phys. Res., Sect. B* 158 (1999) 678.
- [137] S.N. Paglieri, K.Y. Foo, J.D. Way, A new preparation technique for Pd/alumina membranes with enhanced high temperature selectivity, *Ind. Eng. Chem. Res.* 38 (1999) 1925.
- [138] F. Guazzone, Y.H. Ma, Leak growth mechanism in composite Pd membranes prepared by electroless method, *AIChE J.* 54 (2) (2008) 487.

-
- [139] K.I. Popov, M.G. Pavlovic, M.D. Maksimovic, Comparison of the critical conditions for initiation of dendritic growth and powder formation in potentiostatic and galvanostatic copper electrodeposition, *J. Appl. Electrochem.* 12 (1982) 525.
- [140] D.E. Newbury, R.L. Myklebust, K.F.J. Heinrich, J.A. Small, Characterization of particles - monte carlo electron trajectory simulation, an aid for particle analysis, *National Bureau of Standards, Washington*, 1980.
- [141] J. Goldstein, Scanning electron microscopy and x-ray microanalysis: A text for biologists, material scientists, and geologists, *Plenum Press, New York*, 1981.
- [142] A. Li, W. Liang, R. Hughes, Fabrication of dense palladium composite membranes for hydrogen separation, *Catal. Today* 56 (2000) 45.
- [143] R. Koch, The intrinsic stress of polycrystalline and epitaxial thin films, *J. Phys. Condes. Matter.* 6 (1994) 9519.
- [144] A. Saini, An investigation of the cause of leak formation in palladium composite membranes, *MS thesis, Worcester Polytechnic Institute, Worcester*, 2006.
- [145] S. Nakahara, Y. Okinaka, Microstructure and mechanical properties of electroless copper deposits, *Annu. Rev. Mater. Sci.* 21 (1991) 93.
- [146] D.L. Rehrig, Effect of deposition method on porosity in gold thin films, *Plating* (1974) 43.
- [147] L. Nikolva, K. Ignatova, S. Stefanova, Effect of pulsating electrolysis parameters on the morphology and structure of Pd-Ag powder, *J Appl. Electrochem.* 26 (10) (1996) 1059.
- [148] Y.S. Lin, A.J. Burggraaf, Experimental studies on pore size change of porous ceramic membranes after modification, *J. Memb. Sci.* 79 (1993) 65.
- [149] R.H. Perry, D.W. Green, J.O. Maloney, Perry's chemical engineers' handbook, *McGraw-Hill, New York* 1997 (7th edition).

Nomenclature

A	= Electrode (cathode or anode) surface area, cm^2
Ag_{aq}^+	= free Ag (not bonding with any complexing agent other than water) in water, mole/ m^3
Pd_{aq}^{+2}	= free Pd (not bonding with any complexing agent other than water) in water, mole/ m^3
C	= density of Pd metal (mole/ m^3)
D	= diffusivity of H atom in Pd, m^2/s or m^2/h
D_o	= pre-exponential factor for diffusivity of H atom in Pd, m^2/s or m^2/h
D_{pore}	= average size of the pore of the substrate, m
E_{absol}	= activation energy for the H atom movement from Pd bulk to the Pd surface, kJ/mole
E_{des}	= activation energy barrier for the H atom desorption from the Pd surface, kJ/mole
E_{diff} or E_D	= activation energy for H atom diffusion in Pd, kJ/mole
E_{Ag}^o	= standard (in reference to standard H_2 electrode) electrode potential of Ag in water without the presence of any complexing agent, V
E_{Ag/Ag_{aq}^+}	= standard (in reference to standard H_2 electrode) electrode potential of Ag in water in the presence of a complexing agent, V
E_{Pd}^o	= standard (in reference to standard H_2 electrode) electrode potential of Pd in water without the presence of any complexing agent, V
$E_{Pd/Pd_{aq}^{+2}}$	= standard (in reference to standard H_2 electrode) electrode potential of Pd in water in the presence of a complexing agent, V
E_{sol}	= activation energy barrier for step involving the H atom transfer from the Pd surface into Pd bulk just beneath the Pd surface, kJ/mole
F	= Faraday constant, C/mole

$He(flux)$	= He flux through the substrate (m^3/m^2-h or m^3/m^2-s)
ΔH	= enthalpy change associated with H-atom dissolution from H_2 gas phase into Pd, kJ/mole H-atom
i	= Current measured at the electrode surface, A
i_o	= Equilibrium exchange current density for the redox reaction associated with metal ion or reducing agent in the bath, A/cm^2
j_{absol}	= H atom flux from the Pd bulk to the Pd surface, $mole/m^2-s$
j_{ad}	= the flux of H atoms dissociating at the Pd surface, $mole/m^2-s$
j_{des}	= dissociative desorption flux of H atoms from the Pd foil surface, $mole/m^2-s$
j_{diff}	= diffusion rate of H atoms or H_2 in Pd, $mole/m^2-s$
j_{sol}	= H atom flux from the Pd surface into the Pd bulk, $mole/m^2-s$
K_{absol}	= rate constant for the step involving H atom movement from the Pd bulk to the Pd surface, $mole/m^2-s$
K_{absol}^o	= pre-exponential factor for the rate constant for the step involving H atom movement from the Pd bulk to the Pd surface, $mole/m^2-s$
K_{des}	= H atom desorption rate constant, $mole/m^2-s$
K_{des}^o	= H atom desorption rate constant pre-exponential factor, $mole/m^2-s$
$K_{Siverts}$	= Sieverts' constant, $atm^{-0.5}$
K_{sol}	= rate constant for the H atom movement from the Pd surface into the Pd bulk, $mole/m^2-s$
K_{sol}^o	= pre-exponential factor for the rate constant for the H atom movement from the Pd surface into the Pd bulk, $mole/m^2-s$
L	= complexant in the solution
M	= molecular weight of H_2 or He gas, g/mole or kg/mole or metal ions in the Solution
n	= ratio of H atom to Pd atom in the Pd bulk
OX	= oxidation product of the reducing agent in the plating solution
p	= pressure of the H_2 or He gas phase, atm

P_{avg}	= Average of the pressures on the higher and lower side of the substrate, atm
ΔP	= pressure drop across the substrate, atm
RA	= reducing agent in the plating solution
s	= fraction of H_2 molecules striking the Pd surface and getting dissociatively adsorbed
S	= solubility of H_2 in Pd, mole /m ³ or m ³ /m ³ or mole/m ³ -atm ^{0.5} or m ³ /m ³ -atm ^{0.5}
S_1	= solubility of H atom on higher pressure side, mole/m ³
S_2	= solubility of H atom on lower pressure side, mole/m ³
T	= temperature of Pd foil, K
Y	= He flux growth rate, (m ³ /m ² -h-atm)/h
z	= distance along the thickness of Pd film from the higher H_2 pressure side or thickness of membrane, m or μ m
α	= Knudson contribution to the total H_2 or He flow, m ³ /m ² -h-atm or m ³ /m ² -s-Atm or the transfer co-efficient for the Pd reduction or the N_2H_4 oxidation
β	= viscous contribution to the total H_2 or He flow, m ³ /m ² -h-atm ² or m ³ /m ² -s-atm ² or symmetry factor for the Ag reduction reaction
η	= Electrode (cathode or anode) surface overpotential, V
τ	= the flux of H_2 molecules impinging on the Pd surface, mole/m ² -s
θ	= surface coverage of H atoms i.e. ratio of H atoms/Pd atoms on the Pd surface
μ	= viscosity of gas (H_2 or He), kg/m-s

A. Appendix: Pd and Ag equilibrium potential calculation

A.1. NH₃ as complexing agent

A.1.1. NH₃ speciation in water

NH₃ undergoes through following speciation reaction in water



$$K_{NH_3} = \frac{[NH_3][H_3O^+]}{[NH_4^+]} = 5.5 \times 10^{-10} \Rightarrow P_{KNH_3} = 9.25 \quad A.2$$

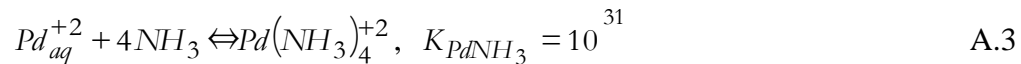
The Eqn. A.2 can be used to find the fraction of total NH₃ added existing in NH₃ and NH₄⁺ form at different pH in water (see Table A.1).

Table A.1. Fraction of NH₃ at different pH in water

pH	NH ₃ fraction
9	0.35
10	0.85
11	0.95
12	0.99

A.1.2. Complexing reaction of Pd and Ag with NH₃

Pd complexes with NH₃ as given in Eqn. A.3.



The total Pd present in the aqueous solution in the presence of NH₃ can be summed up

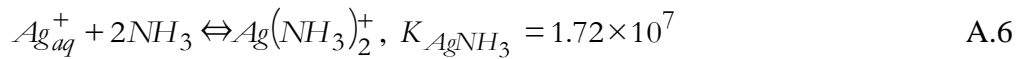
as is shown in Eqn. A.4

$$Pd(total) = Pd_{aq}^{+2} + Pd(NH_3)_4^{+2} \quad A.4$$

Eqns. A.3 and A.4 can be solved to find the fraction of the total Pd added in the form of Pd_{aq}^{+2} and the equilibrium potential of Pd in the presence of NH_3 can be calculated using the Nernst equation (see Eqn. A.5).

$$E_{Pd/Pd_{aq}^{+2}} = E_{Pd}^0 + \frac{RT}{2F} \ln(Pd_{aq}^{+2}) \quad A.5$$

Where E_{Pd}^0 is the standard electrode potential of the metal Pd in water without the presence of any complexing agent. R, T and F in Eqn. A.5 stand for the gas constant, temperature and Faraday constant respectively. Ag complexes with NH_3 as given in Eqn. A.6.



The total Ag in the aqueous solution in the presence of NH_3 can be summed up as

$$Ag(total) = Ag_{aq}^+ + Ag(NH_3)_2^+ \quad A.7$$

Using Eqns. A.6 and A.7, the equilibrium potential of Ag in the presence of NH_3 can be calculated using the Nernst equation (see Eqn. A.8)

$$E_{Ag/Ag_{aq}^+} = E_{Ag}^0 + \frac{RT}{F} \ln(Ag_{aq}^+) \quad A.8$$

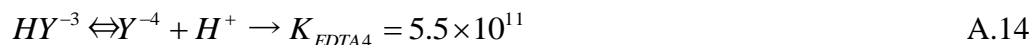
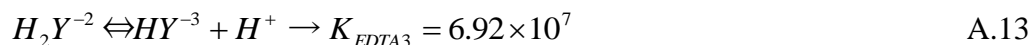
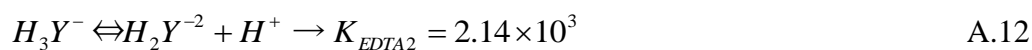
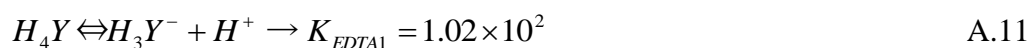
Where E_{Ag}^0 is the standard electrode potential of the metal Ag in water without the presence of any complexing agent.

A.2. EDTA as complexing agent

A.2.1. EDTA speciation in water

Na_2EDTA on addition into water dissociates into Na^+ and $EDTA^{-2}$. $EDTA$ can exist in $EDTA^{-1}$, $EDTA^{-2}$, $EDTA^{-3}$ and $EDTA^{-4}$ forms depending on the pH of water. The following equations (Eqn. A.9-A.15) give reactions involved among the different forms of $EDTA$. H^+ in Eqns A.9-A.15 stands for the hydronium ion in water.

$$\text{Assumption: } EDTA = Y \quad A.9$$



Y^{-4} is the form which acts as the complexing agent for several metals. Using Eqns. A.10-A.15, the fraction of Y (EDTA) in the form of Y^{-4} (EDTA⁻⁴) at different pH in water is shown in Table A.2.

A.2.2. Complexing reactions of EDTA with Pd and Ag

Pd complexes with $EDTA^{-4}$ as given in Eqn. A.16.



Total Pd in the aqueous solution in the presence of $EDTA^{-4}$ can be summed up as

$$Pd(total) = Pd_{aq}^{+2} + [Pd(EDTA)]^{-2} \quad A.17$$

Table A.2. Fraction of $EDTA^{-4}$ (Y^4) as function of pH in water

pH	$EDTA^{-4}$ fraction
9	0.02
10	0.10
11	0.90
12	~1.0

Eqns. A.16 and A.17 can be solved to find the fraction of the total Pd added in the form of Pd_{aq}^{+2} and the equilibrium potential of Pd in presence of $EDTA^{-4}$ can be calculated using the Nernst equation (see Eqn. A.18).

$$E_{Pd/Pd_{aq}^{+2}} = E_{Pd}^o + \frac{RT}{2F} \ln(Pd_{aq}^{+2}) \quad A.18$$

Ag complexes with $EDTA^{-4}$ as given in Eqn. A.19.



Total Ag in the aqueous solution in the presence of $EDTA^{-4}$ can be summed up as

$$Ag(total) = Ag_{aq}^{+} + (AgEDTA)^{-3} \quad A.20$$

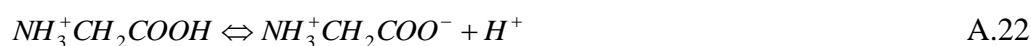
Eqns. A.19 and A.20 can be solved to find the fraction of the total Pd added in the form of Ag_{aq}^{+} and the equilibrium potential of Pd in presence of $EDTA^{-4}$ can be calculated using the Nernst equation (see Eqn. A.18).

$$E_{Ag/Ag^+_{aq}} = E_{Ag}^0 + \frac{RT}{F} \ln(Ag^+_{aq}) \quad A.21$$

A.3. Glycine as complexing agent

A.3.1. Glycine speciation in water

Glycine (NH_2CH_2COOH) in water goes through following speciation reactions (Eqns. A.22 and A.24).



$$K_{gly1} = \frac{[NH_3^+CH_2COO^-][H^+]}{[NH_3^+CH_2COOH]} = 4.57 \times 10^{-3} \Rightarrow P_{K_{gly1}} = 2.34 \quad A.23$$



$$K_{gly2} = \frac{[NH_2CH_2COO^-][H^+]}{[NH_3^+CH_2COO^-]} = 2.5 \times 10^{-10} \Rightarrow P_{K_{gly2}} = 9.6 \quad A.25$$

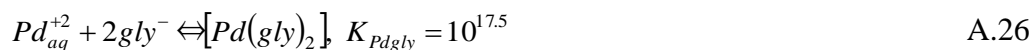
Glycine (gly) in the form of $NH_2CH_2COO^-$ (gly^-) is reported to be the complexing agent for Pd and Ag. [129] and forms the complexing reactions with Pd and Ag. Table A.3 shows fraction of gly in the form of gly^- at different pH.

Table A.3. Fraction of the total glycine added in the form of gly^- at different pH in water

pH	gly^- fraction
9	0.2
10	0.71
11	0.96
12	~1.0

A.3.2. Complexing reaction of Pd and Ag with glycine (gly)

Pd complexes with gly^- as given in Eqn. A.26.



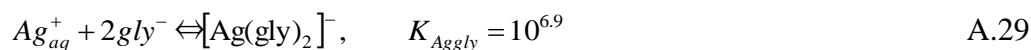
Total Pd in the aqueous solution in the presence of gly^- can be summed up as

$$Pd(total) = Pd_{aq}^{+2} + [Pd(gly)_2] \quad A.27$$

Eqns. A.26 and A.27 can be solved to find the fraction of the total Pd added in the form of Pd_{aq}^{+2} and the equilibrium potential of Pd in presence of gly^- can be calculated using the Nernst equation (see Eqn. A.28).

$$E_{Pd/Pd_{aq}^{+2}} = E_{Pd}^0 + \frac{RT}{2F} \ln(Pd_{aq}^{+2}) \quad A.28$$

Ag complexes with gly^- as given in Eqn. A.29.



Total Ag in the aqueous solution in the presence of gly^- can be summed up as

$$Ag(total) = Ag_{aq}^+ + [Ag(gly)_2]^- \quad A.30$$

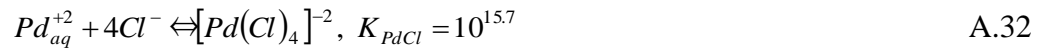
Eqns. A.29 and A.30 can be solved to find the fraction of the total Ag added in the form of Ag_{aq}^+ and the equilibrium potential of Ag in presence of gly^- can be calculated using the Nernst equation (see Eqn. A.31).

$$E_{Ag/Ag_{aq}^+} = E_{Ag}^0 + \frac{RT}{F} \ln(Ag_{aq}^+) \quad A.31$$

A.4. KCl as complexing agent

A.4.1. Complexing reactions of Pd and Ag with Cl⁻

KCl when added into water dissociates into K^+ and Cl^- ions. Cl^- is the in water which acts as complexing agent for Pd and Ag. Pd complexes with Cl^- as given in Eqn. A.32.



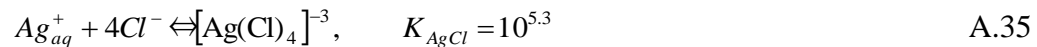
Total Pd in the aqueous solution in the presence of Cl^- can be summed up as

$$Pd(total) = Pd_{aq}^{+2} + [Pd(Cl)_4]^{-2} \quad A.33$$

Eqns. A.26 and A.27 can be solved to find the fraction of the total Pd added in the form of Pd_{aq}^{+2} and the equilibrium potential of Pd in presence of Cl^- can be calculated using the Nernst equation (see Eqn. A.34).

$$E_{Pd/Pd_{aq}^{+2}} = E_{Pd}^0 + \frac{RT}{2F} \ln(Pd_{aq}^{+2}) \quad A.34$$

Ag complexes with Cl^- as given in Eqn. A.35.



Total Ag in the aqueous solution in the presence of Cl^- can be summed up as

$$Ag(total) = Ag_{aq}^+ + [Ag(Cl)_4]^{-3} \quad B.36$$

Eqns. A.35 and A.36 can be solved to find the fraction of the total Ag added in the form of Ag_{aq}^+ and the equilibrium potential of Ag in presence of Cl^- can be calculated using the Nernst equation (see Eqn. A.37).

$$E_{Ag/Ag^+_{aq}} = E_{Ag}^0 + \frac{RT}{F} \ln(Ag^+_{aq}) \quad A.37$$

Table A.4 shows the calculation of the equilibrium potentials of Pd and Ag in the presence of different complexing agents using the Nernst equation along with the concentration of actual complexing species present in the bath.

Table A.4. The calculation of the equilibrium potentials of Pd and Ag in the presence of different complexing agents for $[Pd] = 10 \text{ mM}$ and $[Ag] = 3 \text{ mM}$ in the bath.

Complexing agent →	NH ₄ OH	Na ₂ EDTA	Glycine	KCl
Total conc. added (M)	3.0	0.18	0.8	4.0
Complexing species /conc. (M)	NH ₃ /2.85	EDTA ⁻⁴ /0.16	Gly ⁻ /0.77	Cl ⁻ /4.0
Pd_{aq}^{+2} (M)	1.5×10^{-35}	1.9×10^{-20}	5.3×10^{-20}	7.8×10^{-21}
Ag_{aq}^{+} (M)	2.1×10^{-11}	9.3×10^{-10}	6.4×10^{-10}	5.9×10^{-11}
Equilibrium potential (SHE) (V) Pd, Ag	-0.05, 0.16	0.40, 0.26	0.41, 0.25	0.38, 0.18
*Equilibrium potential (Ag/AgCl, 3 M NaCl) (V) Pd, Ag	-0.24, -0.03	0.21, 0.07	0.22, 0.06	0.19, -0.01

* The potential of Ag/AgCl, 3 M NaCl electrode with respect to standard hydrogen (SHE) electrode was 0.19 V [133].

B. Appendix: LSV and CV scans of effect of different complexing agents on the Pd and Ag deposition

B.1. NH₃ influence on the Pd and Ag deposition

B.1.1. Individual Pd and Ag polarization from NH₃ bath

The polarization characteristics of Pd from NH₃ based bath were very similar to that observed for the mixed NH₃ and EDTA bath (see Chapter 6) indicating that NH₃ was the principle complexing agent for Pd between NH₃ and EDTA used in Chapter 5 and Chapter 6. The large influence of NH₃ on the Pd deposition in the presence of both NH₃ and EDTA was expected because of the strong complexing reaction of NH₃ with Pd than that of EDTA [117]. Fig. B.1a shows the LSV scan obtained on the Pd surface. The Pd deposition started at potential about -650 to -700 mV. The CV scan obtained on the Pd surface (Fig. B.1b) indicated the Pd deposition potential range similar to the pointed out by the LSV scan. The Pd deposition characteristics were not altered when the surface changed from Pd to Ag (Fig. B.1c and Fig. B.1d). The peak obtained for the blank solutions i.e. without Pd in the solution in Fig. B.1c and Fig. B.1d at approximate potential of -75 to -100 mV was associated with the Ag deposition. The electrode potential exceeded beyond the oxidation potential of Ag and caused the dissolution of Ag and when the electrode potential moved towards cathodic direction, the dissolved Ag started to deposit resulting in the observed Ag peak (Fig. B.1c and Fig. B.1d).

The Ag deposition in the presence of NH₃ started at slightly different cathodic potential (at potential of approximate -75 to -100 mV, see Fig. B.2a and Fig. B.2b) than that observed from the mixed NH₃ and EDTA bath (see Chapter 5, Section 5.3.3.)

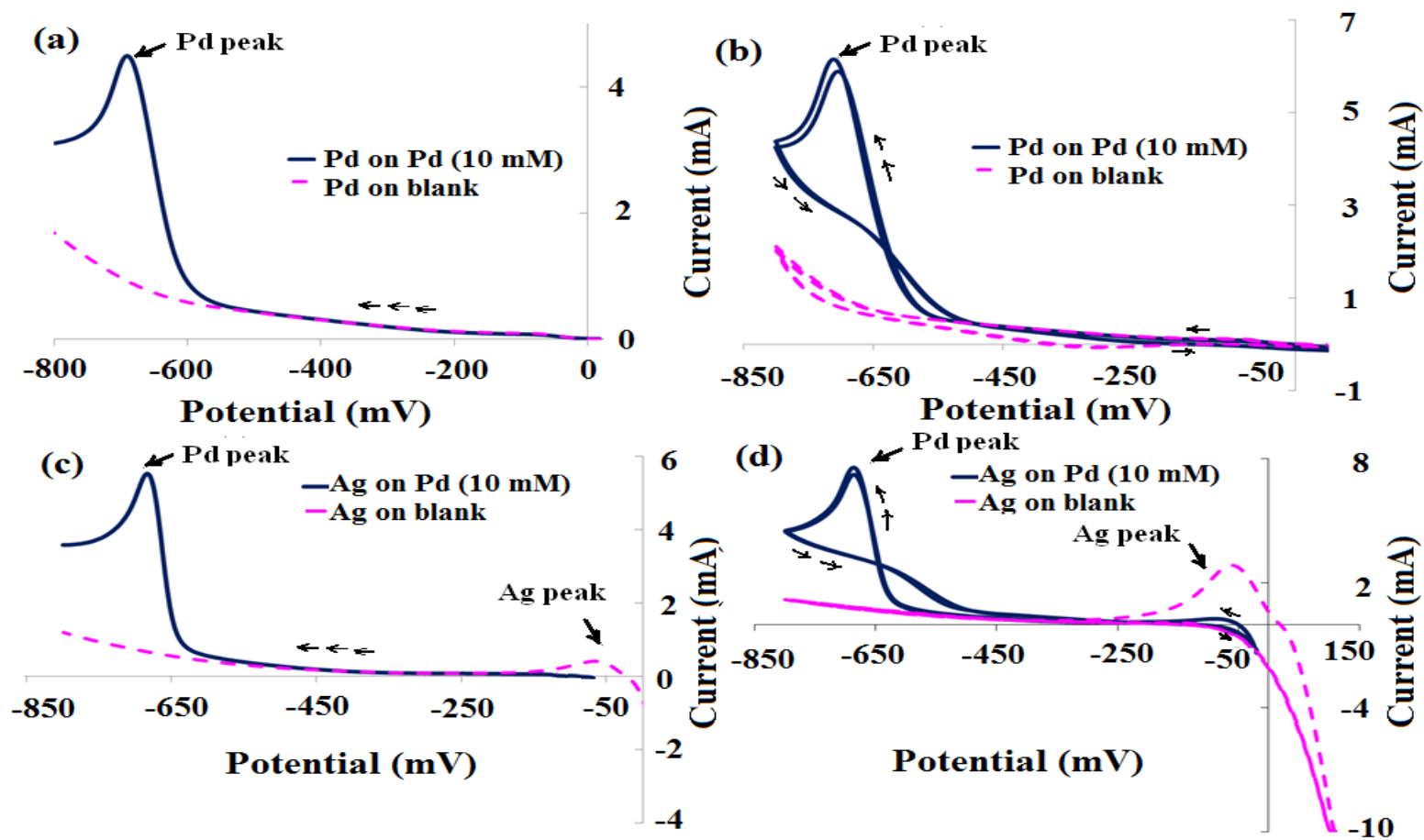


Fig. B.1. Pd polarization characteristics in the presence of NH_3 (for bath composition see Chapter 6, Section 6.2) (a). LSV scan on the Pd surface (b). CV scan on the Pd surface (c). LSV scan on the Ag surface (d). CV scan on the Ag surface

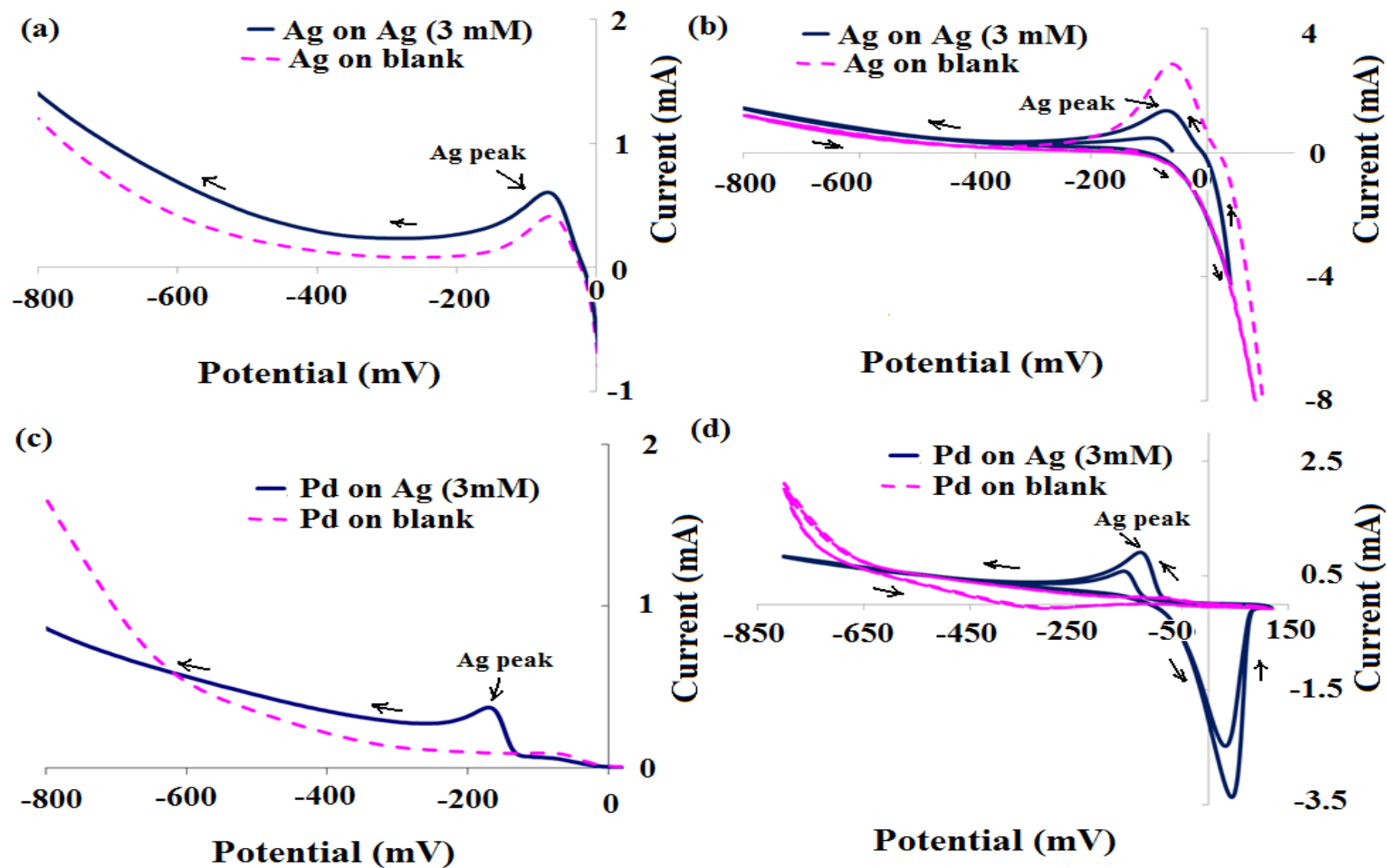


Fig. B.2. Ag polarization characteristics in the presence of NH_3 (for bath composition see Chapter 6, Section 6.2) (a). LSV scan on the Ag surface (b). CV scan on the Ag surface (c). LSV scan on the Pd surface (d). CV scan on the Pd surface

indicating that in the case of Ag, both EDTA and NH_3 influenced the Ag deposition. Both EDTA and NH_3 shows very similar stability constant for the complexing reaction with Ag [117], therefore could both have influence on the Ag deposition. The Ag deposition on the Pd surface (Fig. B.2c and Fig. B.2d) started at slightly more cathodic potential i.e., at potential -125 to -150 mV than the Ag surface, meaning that the surface had slight effect on the Ag deposition.

B.1.2. Simultaneous Pd and Ag polarization characteristics from NH_3 bath

Both LSV and CV scans showed two peaks for the Pd and Ag co-deposition bath in the presence of NH_3 (Fig. B.3). The first peak was associated with the Ag deposition and was observed at electrode potential value of -75 to -100 mV (Fig. B.3c and Fig. B.3d) for the Ag surface and at electrode potential of -100 to -125 mV (Fig. B.3a and Fig. B.3b) for the Pd surface. The second peak was associated with the Pd deposition observed at potential of -650 to -700 mV on both Pd and Ag surface. Based on the stability constants value of complexing reaction of Pd and Ag with NH_3 and the Nernst equation, the calculated Ag (3 mM) equilibrium potential in the presence of NH_3 (3 M) was 0.16 V (with reference to SHE) or -0.03 V (with reference to Ag/AgCl, 3 M NaCl, 25 °C). The calculated equilibrium potential for Pd (10 mM) in the presence of NH_3 (3 M) was -0.05 V (with respect to SHE) or - 0.240 V (with reference to Ag/AgCl, 3 M NaCl, 25 °C). The difference in the equilibrium potential of two metals was 200 mV but the actual deposition potential difference based on the LSV and CV scans (Fig. B.1, Fig. B.2 and Fig. B.3) was in the range of 550 to 600 mV. The difference was mainly due to the large overpotential associated with the Pd deposition. The calculated

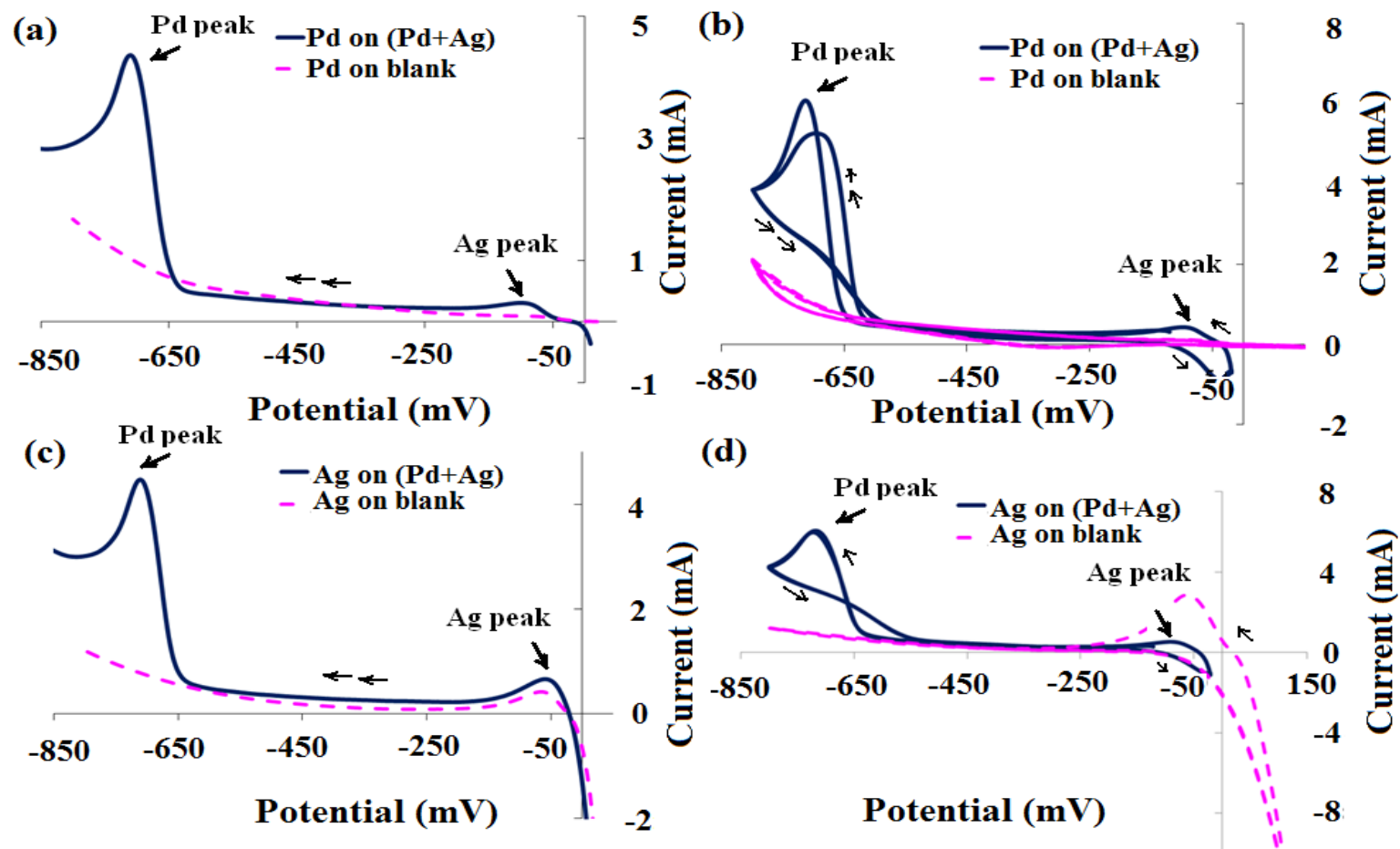


Fig. B.3. Pd and Ag polarization characteristics in the presence of NH_3 (for bath composition see Chapter 6, Section 6.2) (a). LSV scan on the Pd surface (b). CV scan on the Pd surface (c). LSV scan on the Ag surface (d). CV scan on the Ag surface

equilibrium potential for Pd was -240 mV (with reference to Ag/AgCl, 3 M NaCl, 25 °C) but the actual deposition was observed at potential of -650 to -700 mV (60 °C) i.e. at potential of 410 to 460 mV more cathodic than the calculated equilibrium potential (Note: The equilibrium potential calculation was based on 25 °C, however the value could be very different at 60 °C and therefore, the value of overpotential could be different than that based on 25 °C calculation). The large overpotential (~500 mV) for the Pd deposition in the presence of NH_4NO_3 (pH = 9.0) was also observed by Nikolova et al. [147].

Based on the Nernst equation, the equilibrium potential for the Ag concentration of 3 mM and NH_3 concentration of 3 M in the bath was calculated to be 0.16 V (SHE) or -0.03 V or -30 mV (Ag/AgCl, 3 m NaCl, 25 °C). The actual Ag deposition occurred at the electrode potential of -75 to -100 mV, therefore very little overpotential was associated with Ag deposition and the difference observed between the calculated equilibrium potential and measured deposition potential could be due to the temperature difference (Note: the equilibrium potential calculation was based on 25 °C however the temperature for the actual deposition was 60 °C). The Ag deposition with very little overpotential is very common irrespective of the complexing agent used in the bath [120, 124].

The large difference in the Pd and Ag deposition potential was also observed by Sturzenegger et al. [118] in their Pd and Ag bath in the presence of NH_3 . Based on their Pd and Ag LSV polarization study on the Cu surface (22 °C), the Pd deposition occurred at potential of -600 to -650 mV cathodic than the Ag deposition. Nikolova et al. [147] also reported large difference between the Pd and Ag deposition potentials (~600 mV) during the Pd-Ag co-deposition from the aminonitrite bath.

B.2. EDTA influence on the Pd and Ag deposition

B.2.1. Individual Pd and Ag polarization from EDTA bath

In the case of EDTA, the Pd deposition started at more anodic potential than that observed for NH_3 . Both LSV (Fig. B.4a) and CV (Fig. B.4b) indicated the position of Pd deposition peak at approximate potential of -450 to -500 mV which was 200 mV more anodic potential than that observed for NH_3 . Both LSV and CV (Fig. B.4c and Fig. B.4d) polarization scan on the Ag surface showed the Pd deposition peak position at potential similar to that observed on the Pd surface i.e. -450 to -500 mV. Based on the Nernst equation and stability constant of Pd with EDTA [117], the equilibrium potential for the concentration of 10 mM Pd and 0.18 M EDTA in the bath, was calculated to be 0.40 V (SHE) or 0.21 V (Ag/AgCl, 3 M NaCl, 25 °C). The actual deposition occurred at approximate potential of -450 to -500 mV, therefore again, the large overpotential (~660 mV), very similar to that for NH_3 , was observed for the Pd deposition in the case of EDTA also.

The Ag deposition on the Ag surface occurred at approximate potential of 75 to 100 mV (Fig. B.5a and Fig. B.5b). The Ag deposition characteristics on the Pd surface were very similar to that on the Ag surface (Fig. B.5c and Fig. B.5d) and the Ag deposition on the Pd surface occurred at approximate potential of 50 mV. The calculated equilibrium potential for 3 mM Ag and 0.18 m EDTA in the bath was 0.26 V (SHE) or 0.07 V (Ag/AgCl, 3 M NaCl, 25 °C). The actual deposition was observed at potential of 0.075 V and very little overpotential was associated with the Ag deposition in the case of EDTA, very similar to the NH_3 case.

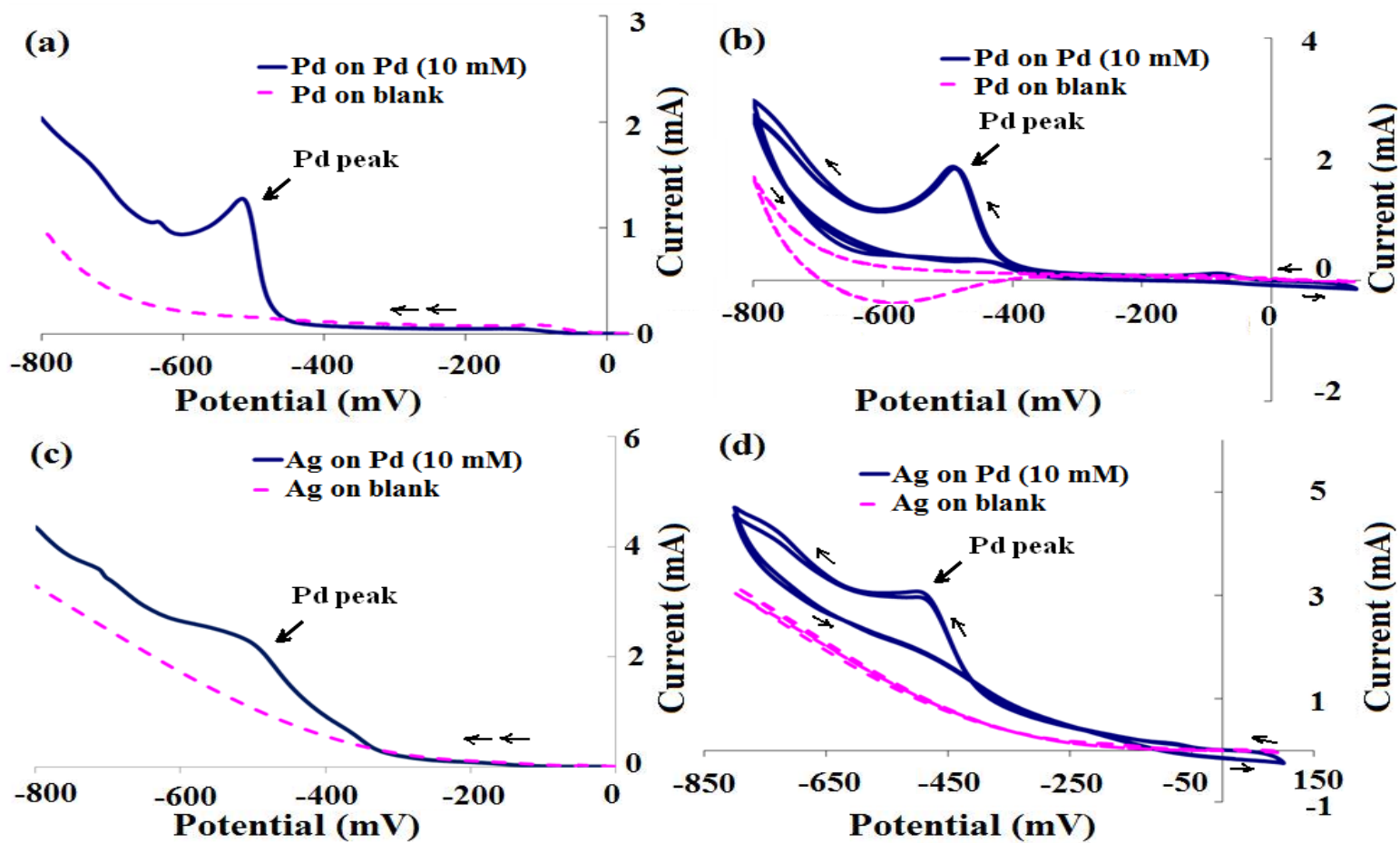


Fig. B.4. Pd polarization characteristics in the presence of EDTA (see Chapter 6, Section 6.2 for bath composition) (a). LSV scan on the Pd surface (b). CV scan on the Pd surface (c). LSV scan on the Ag surface (d). CV scan on the Ag surface

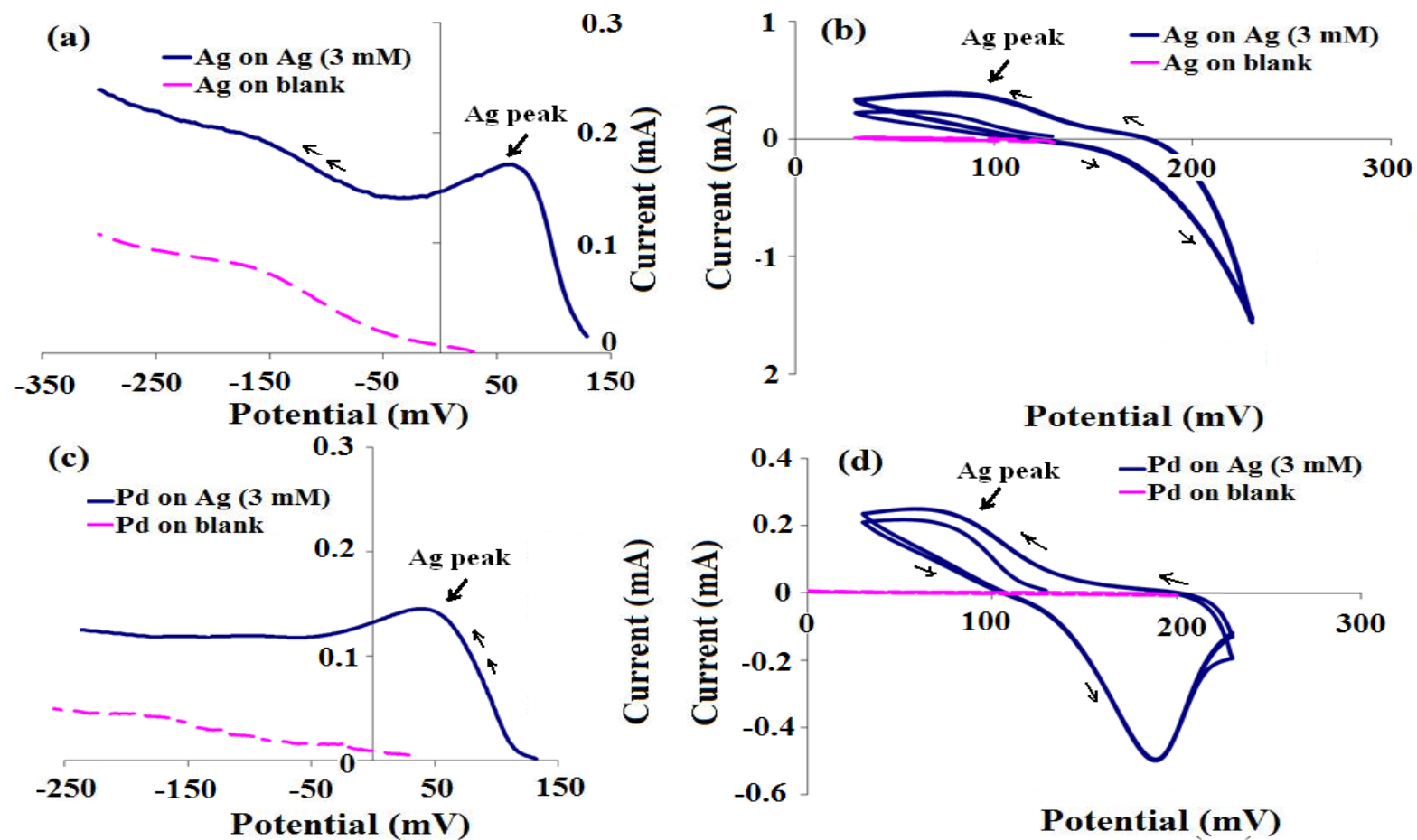


Fig. B.5. Ag polarization characteristics in the presence of EDTA (see Chapter 6, Section 6.2 for bath composition) (a). LSV scan on the Ag surface (b). CV scan on the Ag surface (c). LSV scan on the Pd surface (d). CV scan on the Pd surface

B.2.2. Simultaneous Pd and Ag polarization characteristics from EDTA bath

Fig. B.6 shows the polarization characteristics for the EDTA bath in the presence of Pd and Ag in bath. The polarization characteristics were very similar to that noticed for the single Pd and Ag EDTA baths (Fig. B.4 and Fig. B.5). The simultaneous presence of Pd and Ag in the bath did not alter their deposition characteristics. The Pd peak was observed at potential of -450 to -500 mV and the Ag peak was observed at potential of 100 mV. The potential difference of 550 to 600 mV was observed between the Pd and Ag deposition peaks similar to that observed in the presence of NH_3 (550 to 600 mV).

B.3. Glycine influence on the Pd and Ag deposition

B.3.1. Individual Pd and Ag polarization from glycine bath

Individual polarization characteristics of Pd and Ag are shown in Fig. B.7 and Fig. B.8 respectively. Both LSV and CV scan (Fig. B.7a and Fig. B.7b) in the case of Pd polarization showed similar deposition characteristics. The Pd deposition occurred in the potential range of -550 to -575 mV. The surface change in the case of Pd deposition did not alter the Pd deposition characteristics. The Pd deposition on the Ag surface (Fig. B.7c and Fig. B.7d) occurred approximately in the same potential range, -550 to -575 mV, as that observed on the Pd surface.

Glycine at pH value of 11 exists in the form of gly^- ($\text{NH}_2\text{CH}_2\text{COO}^-$) and gly^- is the form taking part in the complexing reactions with metal ions in the solution [129]. The value stability constant for the complexing reaction of glycine with Pd is reported as $10^{17.5}$ [117]. The equilibrium potential for 10 mM Pd concentration and 0.8 M glycine

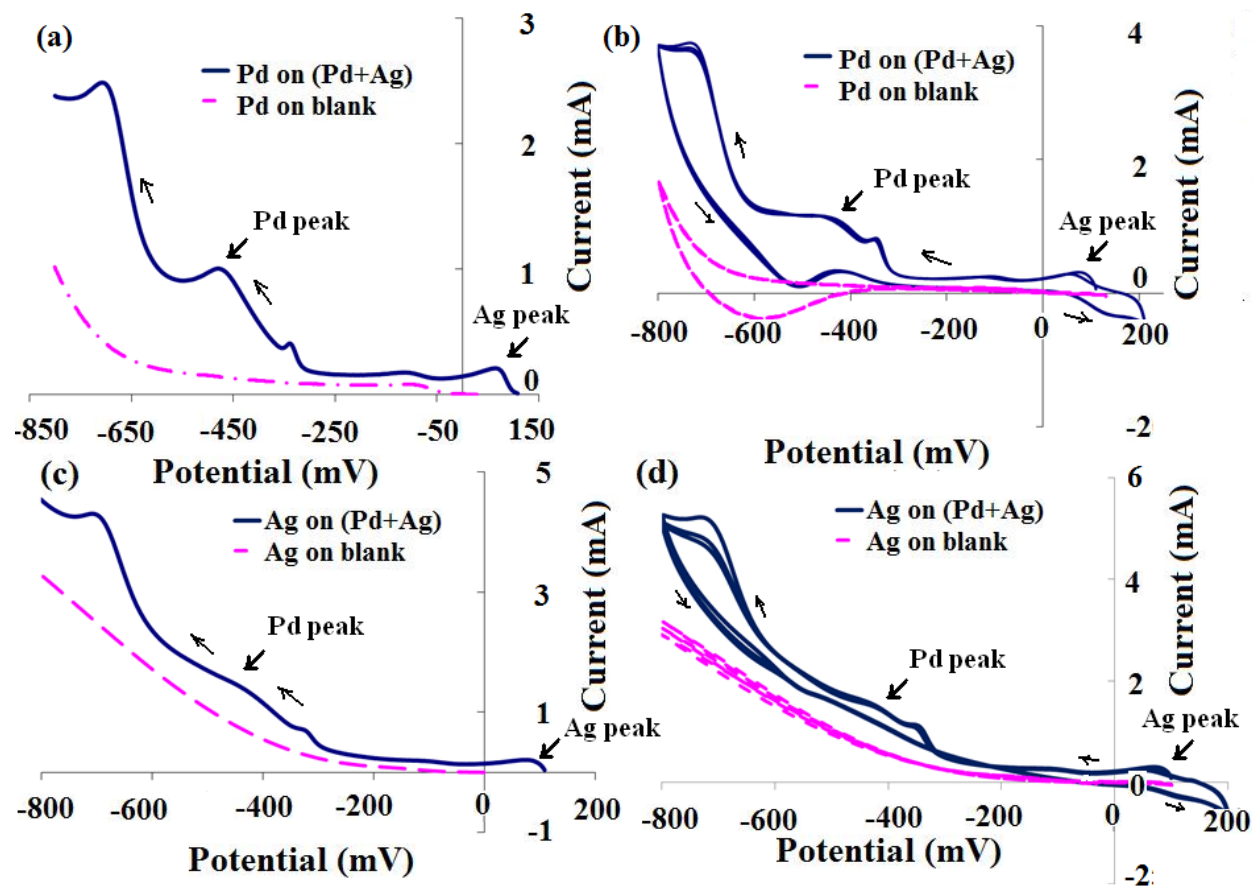


Fig. B.6. Pd and Ag polarization characteristics in the presence of EDTA (see Chapter 6, Section 6.2 for bath composition) (a). LSV scan on the Pd surface (b). CV scan on the Pd surface (c). LSV scan on the Ag surface (d). CV scan on the Ag surface

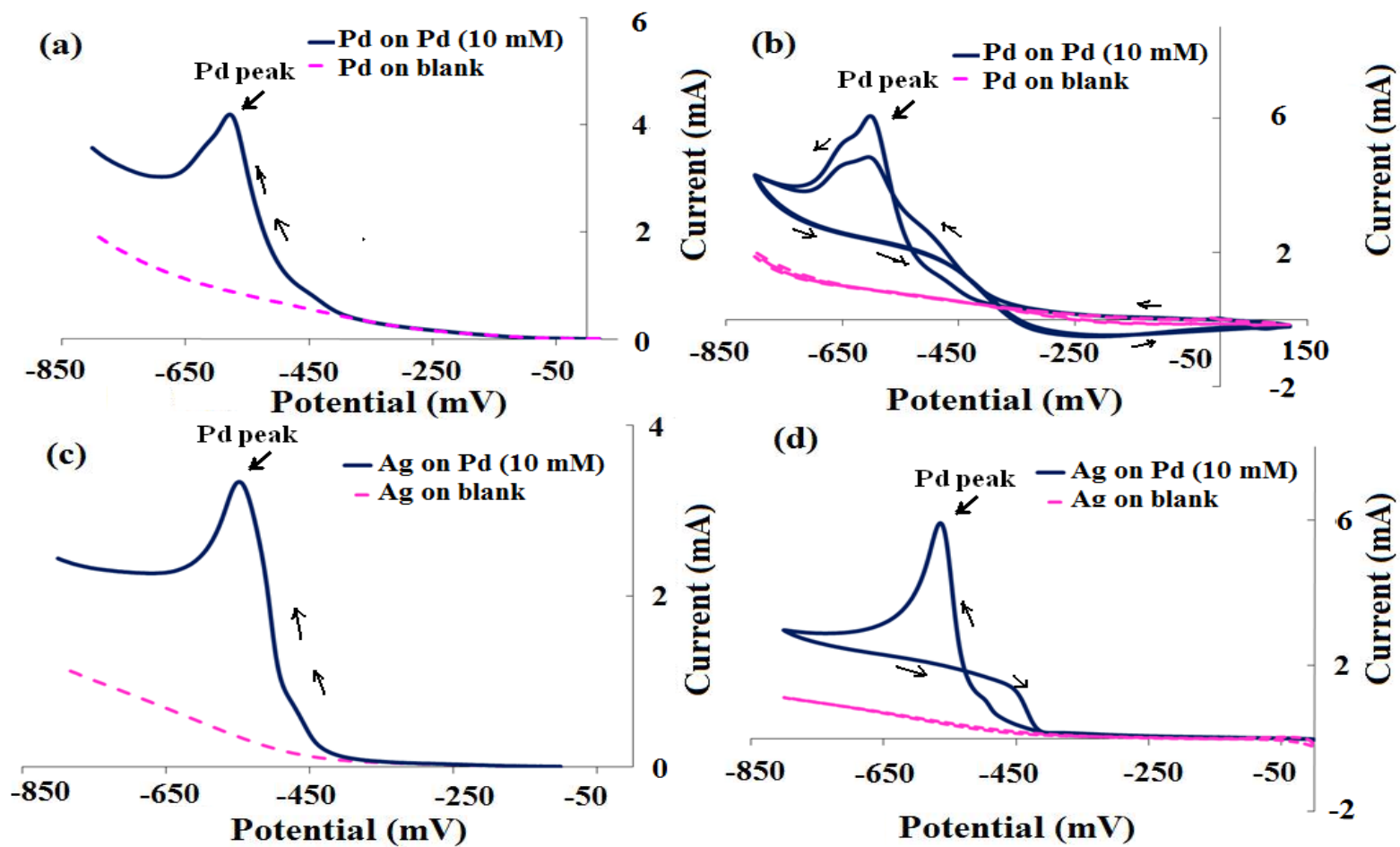


Fig. B.7. Pd polarization characteristics in the presence of glycine (see Chapter 6 for bath composition) [a]. LSV scan on the Pd surface [b]. CV scan on the Pd surface [c]. LSV scan on the Ag surface [d]. CV scan on the Ag surface

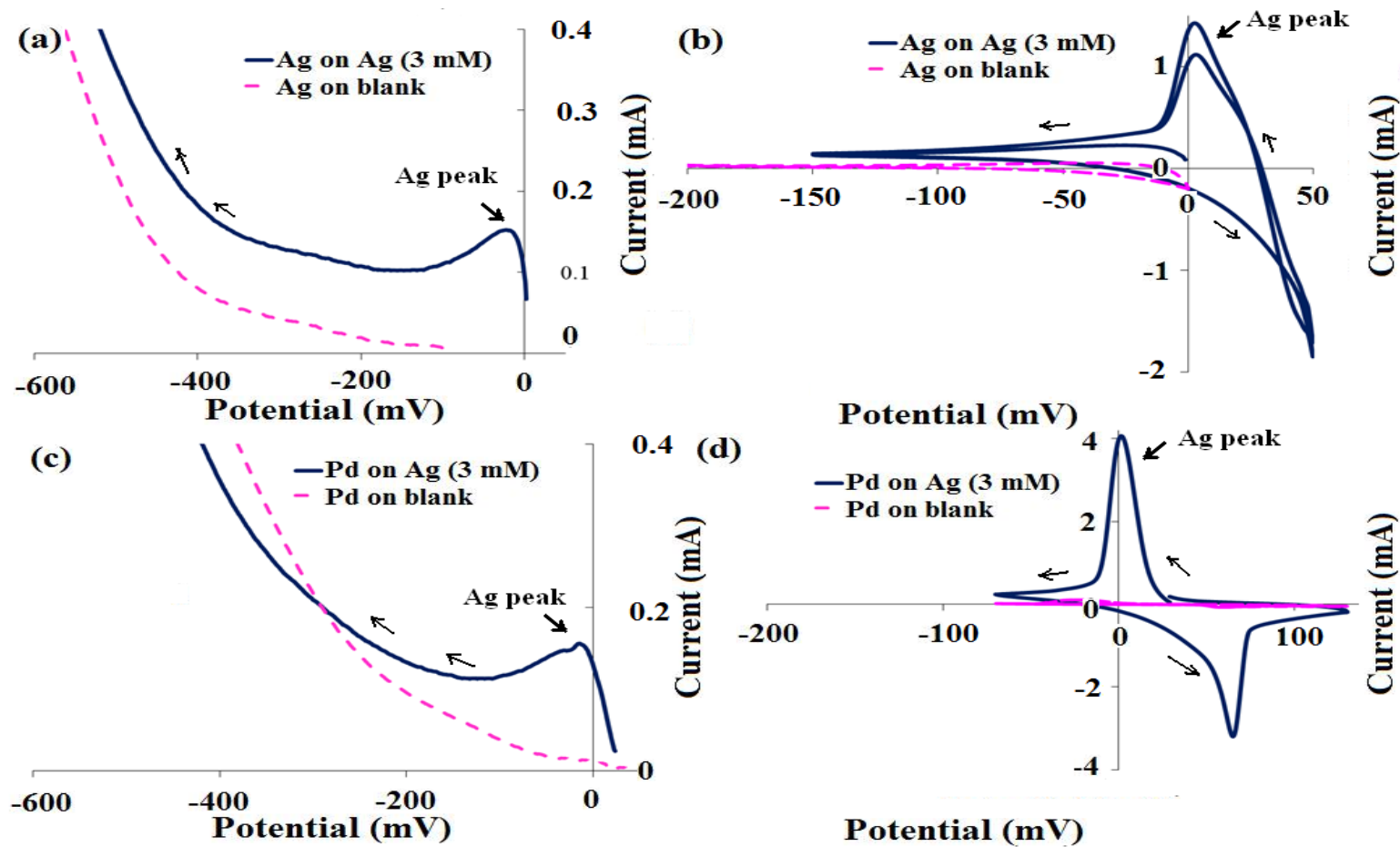


Fig. B.8. Ag polarization characteristics in the presence of glycine (see Chapter 6, Section 6.2 for bath composition) (a). LSV scan on the Ag surface (b). CV scan on the Ag surface (c). LSV scan on the Pd surface (d). CV scan on the Pd surface

concentration in the bath was calculated to be 0.41 V (SHE) or 0.22 V (Ag/AgCl, 3 M NaCl, 25 °C). The actual Pd deposition in the presence of glycine started in the potential range of -550 to -575 mV, therefore the overpotential associated with the Pd deposition in the presence of glycine was approximately in the range of 770 to 795 mV. The actual value of overpotential associated with the Pd deposition at 60 °C might be significantly different from the calculated value because the value of stability constant of Pd at 60 °C with glycine might be significantly different from the value at 25 °C used in the calculation.

Fig. B.8 shows the Ag polarization scans obtained in the presence of glycine. Fig. B.8a and Fig. B.8b show the LSV and CV scans respectively obtained on the Ag surface. As can be seen in the figures, the Ag deposition started in the potential range of 10 to -15 mV. The Ag polarization characteristics on the Pd surface were very similar to the Ag surface (Fig. B.8c and Fig. B.8d). The Ag deposition on the Pd surface started in the same potential range i.e. 10 to -15 mV as on the Ag surface. The difference in the current value observed between the LSV and CV scans on both Ag (Fig. B.8a and Fig. B.8b) and Pd (Fig. B.8c and Fig. B.8d) surface was due to the CV scans were taken relatively in the more anodic direction which led to the dissolution of Ag in the case of CV scans. The dissolved Ag was then deposited back during the cathodic direction of the scans, giving rise to relatively higher Ag peaks in the CV scan as compared to the LSV scan. Also there was difference in the shape of CV scans obtained between the Ag surface (Fig. B.8b) and the Pd surface (Fig. B.8d). The CV scan obtained on the Pd surface shows increase in the anodic current value up to 70 mV potential and then the current started to decrease on further increasing the anodic potential. The decrease was due to the depletion of Ag on the Pd surface and there was almost no Ag left on the Pd

surface when the potential reached to value of 100 mV in the anodic direction. Had the CV scan on the Pd surface been limited to maximum anodic potential less than 70 mV, the shape of the CV scan would have been similar to that obtained on the Ag surface (Fig. B.8b).

The value of stability constant for the complexing reaction of glycine with Ag has been reported to be $10^{7.20}$ [117]. Using the Nernst equation and the stability constant value, the equilibrium potential for Ag (3 mM) and glycine (0.8 M) was calculated to be 0.25 V (SHE) or 0.06 V (Ag/AgCl, 3 M NaCl, 25 °C). The potential for the actual deposition of the Ag was observed to be approximately 10 mV. As compared to the Pd deposition, very little overpotential (~ 50 mV) was observed for the Ag deposition.

B.3.2. Simultaneous Pd and Ag polarization characteristics from glycine bath

Fig. B.9 shows the polarization characteristics for Pd and Ag in their simultaneous presence in the glycine bath. The Ag deposition peak occurred at potential of -15 to -25 mV on the Pd surface (Fig. B.9a and Fig. B.9b). The Pd deposition on the Pd surface occurred in the potential range of -550 to -600 mV. The Pd and Ag deposition on the Ag surface occurred approximately in the same range as on the Pd surface (Fig. B.9c and Fig. B.9d). The Ag peak relative to the Pd peak was very small and is not very clear from the Fig. B.9a Fig. B.9b and Fig. B.9c. However the Pd surface color turned white in the potential range -15 to -25 mV, indicating the Ag deposition. The Ag peak can be very clearly seen on the CV scan obtained on the Ag surface because the maximum anodic potential for the scan exceeded the dissolution potential of Ag and the large

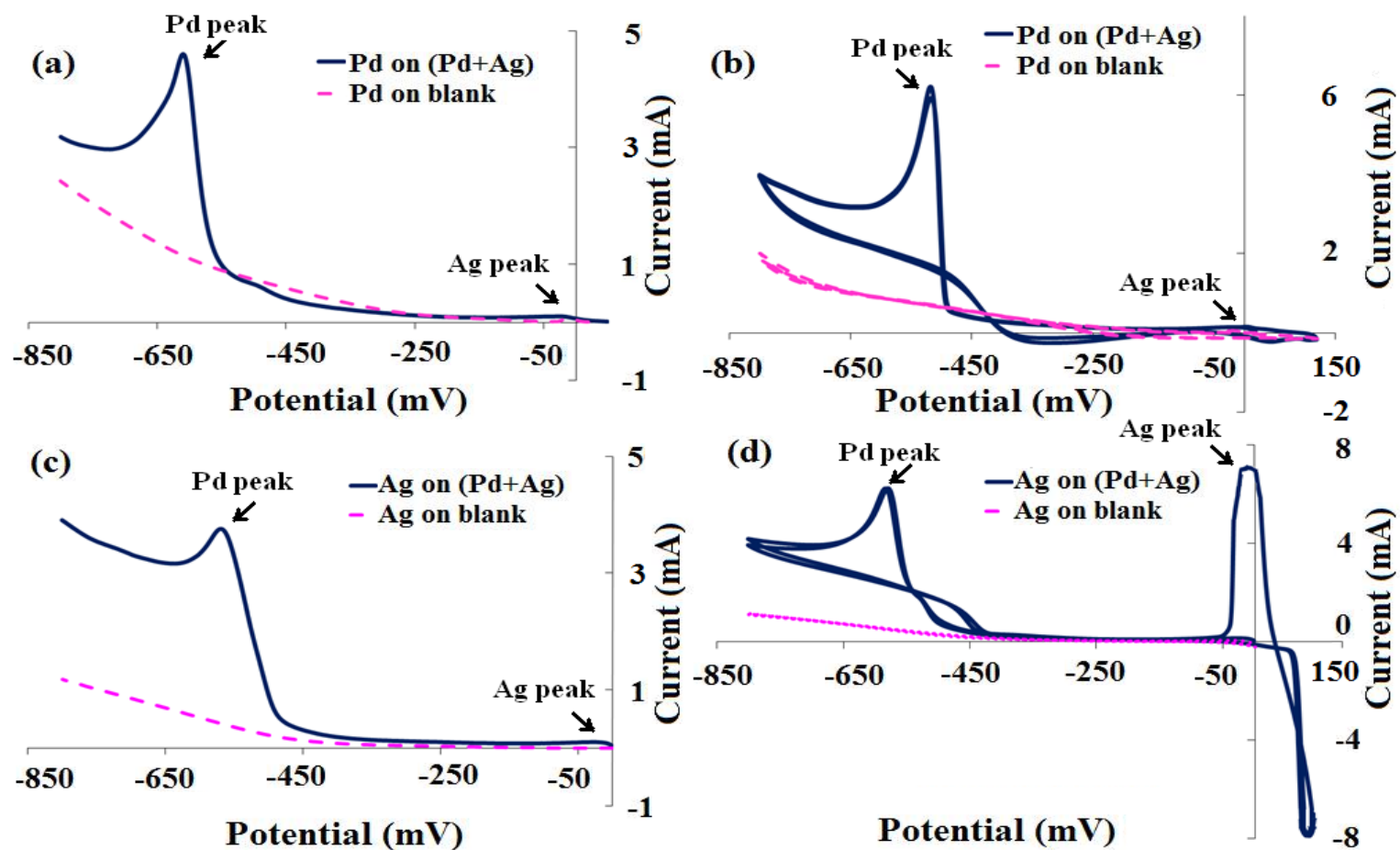


Fig. B.9. Pd and Ag polarization characteristics in the presence of glycine (see Chapter 6, Section 6.2 for bath composition) (a). LSV scan on the Pd surface (b). CV scan on the Pd surface (c). LSV scan on the Ag surface (d). CV scan on the Ag surface

amount of Ag dissolved during the anodic potential (0 to 100 mV). When the direction of the scan was reversed the dissolved Ag gave rise to large Ag deposition peak. The Ag peak on the Pd surface was very small than that on the Ag surface. The difference could be due to the incomplete coverage of the Pd and Ag surface. In both cases, the CV scan started from 0 mV to -800 mV in the cathodic direction and then was reversed to the anodic direction (-800 to 100 mV in the case of Ag surface and -800 to 125 mV in the case of Pd surface). During the cathodic scan both Pd and Ag deposited but the beneath layer was not covered totally during the cathodic scan. Therefore during the anodic scan (between 0 to 100 mV), the uncovered Ag surface showed large amount of Ag dissolution current but in the case Pd surface, the only Ag present was due to the deposition along with Pd obtained in the cathodic direction, therefore no such large Ag anodic peak was obtained in the case of Pd surface. The difference in the Pd and Ag deposition potential observed was approximately in the range of 530 to 580 mV.

The large difference (~ 700 mV) between the Pd and Ag deposition potential in the presence of glycine was also reported by Hasler et al. [119]. The potential-current curve reported by authors [119] were obtained at 25 °C on the brass surface.

B.4. KCl influence on the Pd and Ag deposition

B.4.1. Individual Pd and Ag polarization from KCl bath

The Pd deposition in the case of KCl started at relatively very high noble potential than that for the other complexing agents investigated in this study. Fig. B.10 shows the Pd polarization characteristics obtained on the Pd (Fig. B.10a and Fig. B.10b) and Ag (Fig. B.10c and Fig. B.10d) surface. The Pd deposition showed clear difference for the

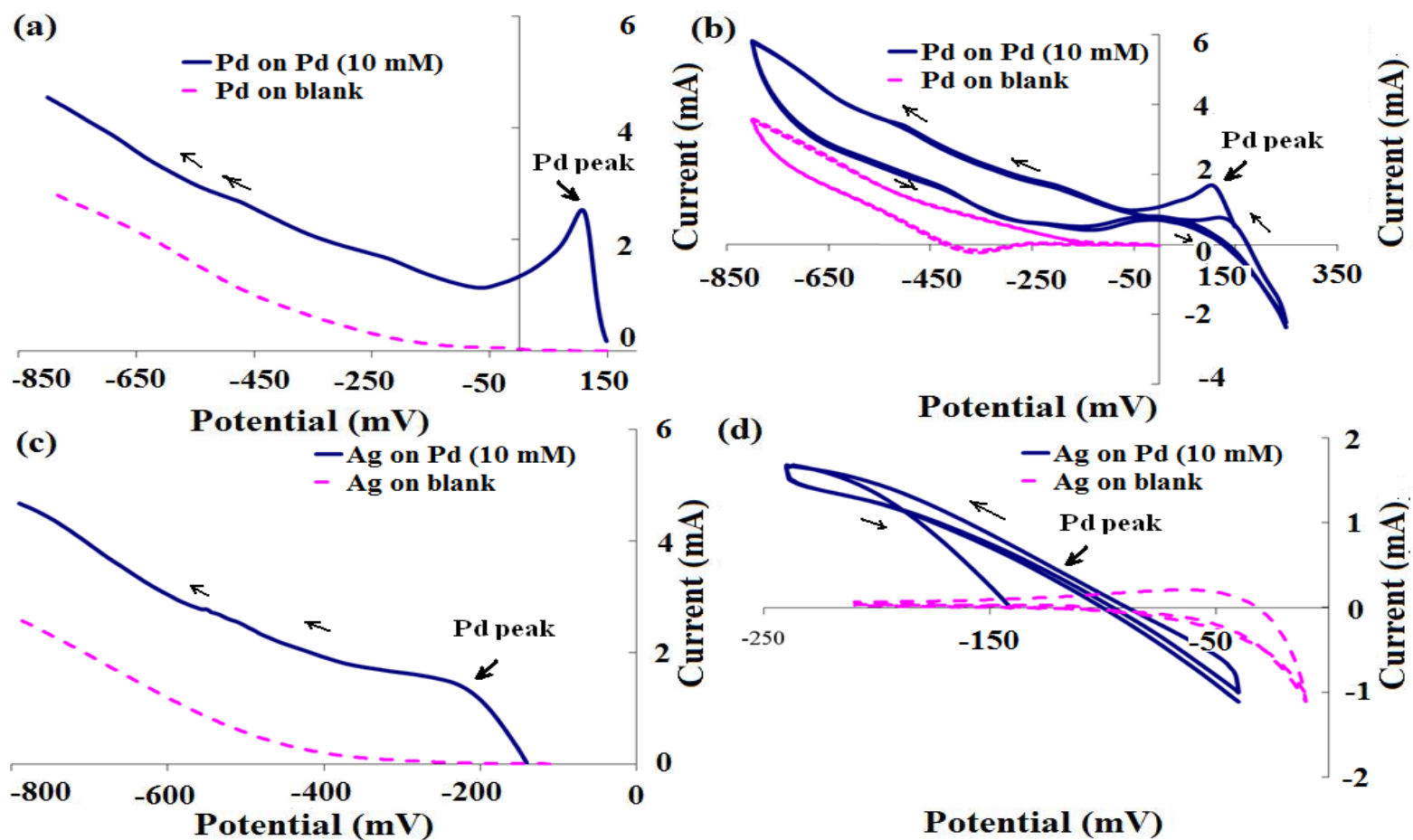


Fig. B.10. Pd polarization characteristics in the presence of KCl (see Chapter 6, Section 6.2 for bath composition) (a). LSV scan on the Pd surface (b). CV scan on the Pd surface (c). LSV scan on the Ag surface (d). CV scan on the Ag surface

surface on which the deposition was initiated i.e., Ag or Pd surface. The Pd deposition on Pd surface occurred in the potential range of 130 to 150 mV as indicated by both LSV and CV scans (Fig. B.10a and Fig. B.10b). In the case of Ag surface, Pd started depositing in the potential range of -100 to -150 mV i.e. approximately at potential -265 mV more cathodic than on the Pd surface. The equilibrium potential for Pd (10 mM) in the presence KCl (4 M) was calculated to be 0.38 V (SHE) or 0.19 V (Ag/AgCl, 3 M NaCl, 25 °C). The actual deposition for Pd on the Pd surface started at approximate potential of 0.15 V (150 mV), therefore very little overpotential was associated with the Pd deposition in the presence of KCl contrary to other complexing agents investigated in this study. The difference observed between the equilibrium potential and the actual deposition could be due to the difference in the temperature for the equilibrium potential calculation (25 °C) and the actual deposition temperature (60 °C).

The Ag deposition characteristics were nearly very similar on both Ag and Pd surface (Fig. B.11). The Ag deposition started around -125 mV potential on both the surfaces. The equilibrium potential for Ag (3 mM) in the presence KCl (4 M) was calculated to be 0.18 V (SHE) or -0.01 V (Ag/AgCl, 3 M NaCl, 25 °C). The actual deposition for Ag on the Ag surface started at approximate potential of -0.125 V (-100 mV). The actual deposition occurred approximately at 115 mV potential more cathodic than the calculated equilibrium potential and the part of the discrepancy could be due to the difference between the equilibrium potential calculation temperature (25 °C) and the actual deposition temperature (60 °C) and the difference in the concentration range of Cl⁻ used in this study

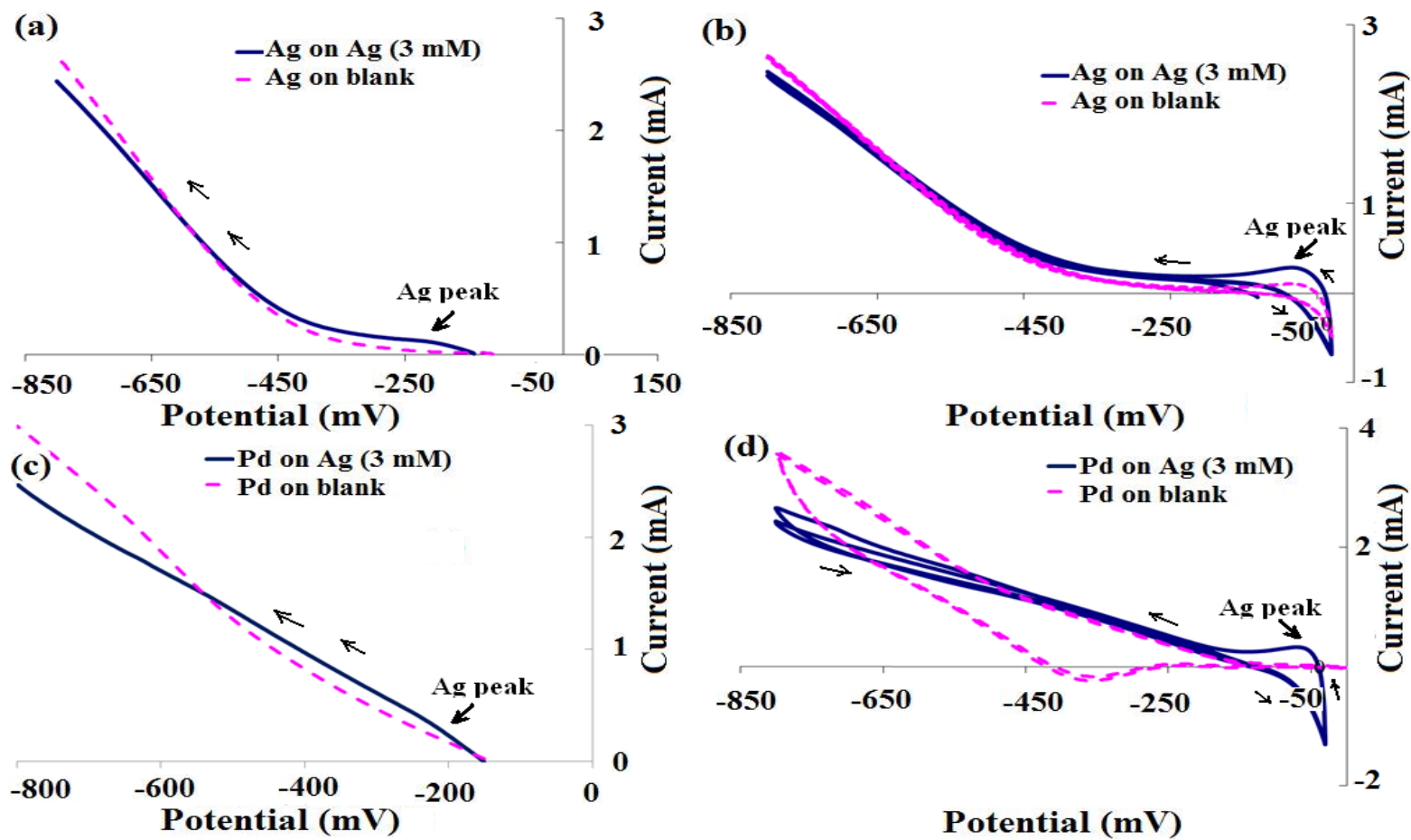


Fig. B.11. Ag polarization characteristics in the presence of KCl (see Chapter 6, Section 6.2 for bath composition) (a). LSV scan on the Ag surface (b). CV scan on the Ag surface (c). LSV scan on the Pd surface (d). CV scan on the Pd surface

B.4.2. Simultaneous Pd and Ag polarization characteristics from KCl bath

Fig. B.12 shows the Pd and Ag polarization characteristics in their simultaneous presence in the bath. The LSV scan on the Pd surface (Fig. B.12a) shows a peak at approximate potential of 150 mV due to the Pd deposition. The Ag peak is not very Pd surface. The Ag peak in the case of simultaneous deposition could be anywhere between 150 mV and -100 mV. The potential range for the CV scan (Fig. B.12b) on the Pd surface was between -25 mV and -800 mV. Only cathodic current was obtained in this range on the Pd surface, indicating that the actual Pd deposition started at higher potential than -25 mV which was 150 mV as shown by the LSV scan (Fig. B.12a). The Ag peak in the case of CV scan on the Pd surface is not very clear and could be anywhere between 150 and -100 mV. The LSV scan on the Ag surface (Fig. B.12c) showed a peak at potential of -150 mV which could be due to both Pd and Ag deposition. The CV scan on the Ag surface was obtained between 100 mV and -800 mV (Fig. B.12d). The anodic peak obtained at approximate potential of 50 mV could be due to the dissolution of both Pd and Ag. From the single metal deposition experiments (Fig. B.10c and Fig. B.11a), the Pd and Ag deposition started at -100 to -150 mV potential on the Ag surface, therefore 50 mV potential was anodic potential for both Pd and Ag. The cathodic peak obtained at -50 mV potential was just deposition of the dissolved Pd and Ag during the anodic direction scan at 50 mV. Therefore the potential difference between the Pd and Ag deposition on both Pd and Ag surface did not exceed 275 mV which was relatively lower than that observed for other complexing agents in this study.

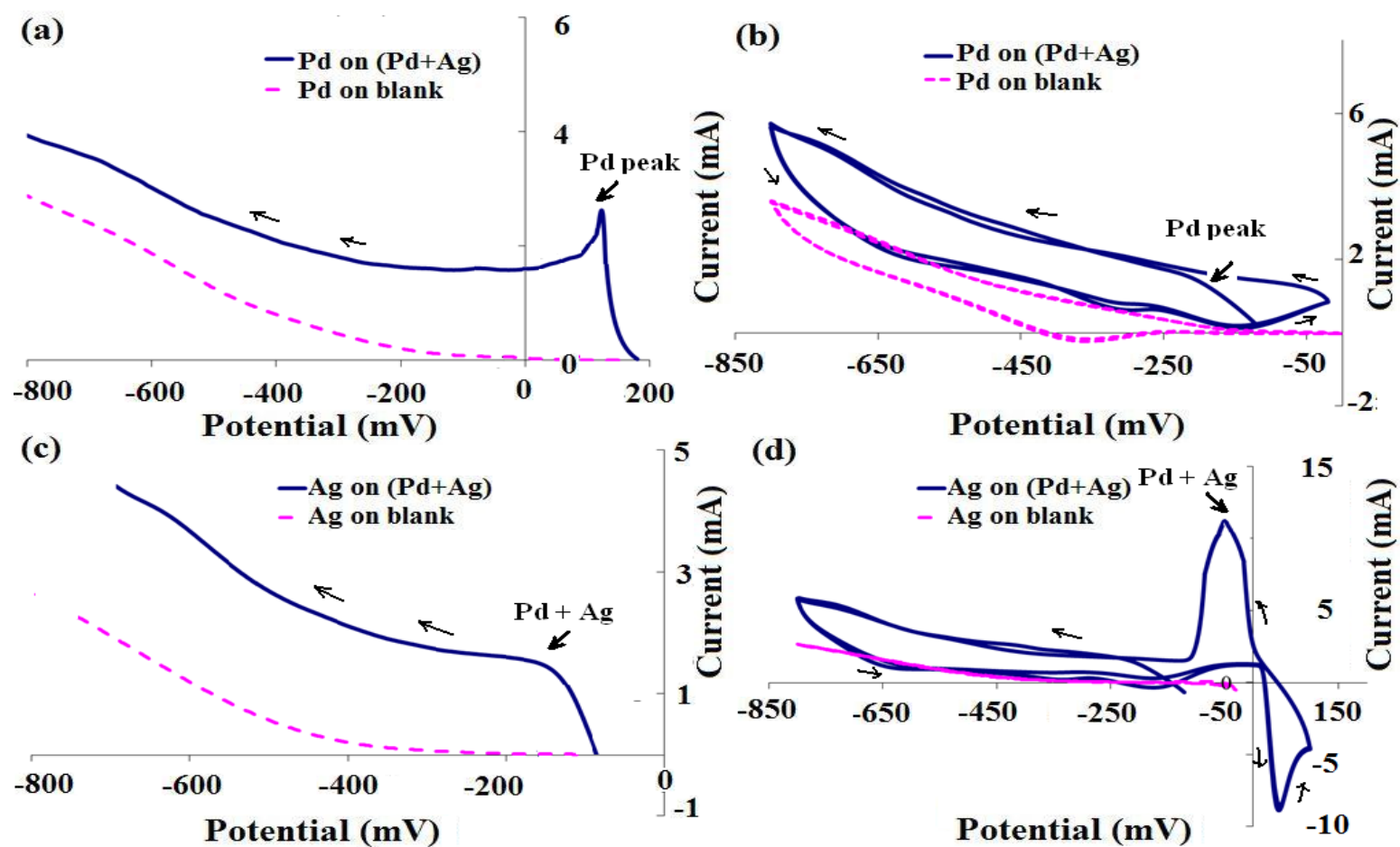


Fig. B.12. Pd and Ag simultaneous polarization characteristics in the presence KCl (see Chapter 6, Section 6.2 for bath composition) (a). LSV scan on the Pd surface (b). CV scan on the Pd surface (c). LSV scan on the Ag surface (d). CV scan on the Ag surface

C. Appendix-Electroless potential calculations for the Pd and Ag deposition using conventional NH_3 +EDTA based bath

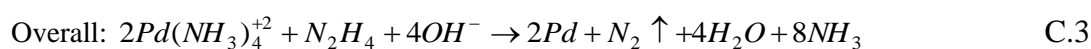
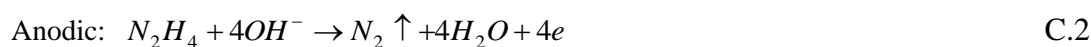
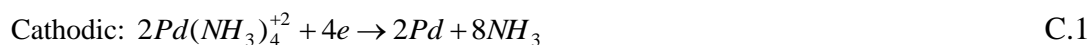
C.1. Pd, Ag and N_2H_4 bath LSV polarization characteristics

The electroless deposition occurs with the mechanism similar to the electro deposition with the difference that both oxidation and reduction reactions occur on the same electrode surface and the net external current is zero for the electroless plating. Therefore, the effect of the plating conditions on the electroless plating deposits properties (morphology, composition etc., see Chapter-5 and Chapter-6)) could better be understood by the polarization characteristics of the individual redox reactions involved in the electroless plating using electrochemical techniques such as linear sweep voltammetry (LSV). According to the mixed potential theory [116], the rate of a redox reaction depends on the electrode potential and is independent of other redox reactions taking place on the same electrode. Therefore, the polarization curve of the individual redox reactions associated with the electroless plating can be added to predict the overall polarization characteristics of the electrode and its influence on the obtained electroless deposits properties.

Fig. 5.6 shows (see Chapter-5, Section 5.3.3.1) the LSV scans associated with the Ag (Fig. 5.6 a) and Pd (Fig. 5.6 b) deposition on the Ag and Pd surface respectively. For all the polarization scans, Ag/AgCl (3 M NaCl) was used as the reference electrode. EDTA and NH_3 were used as the complexing agents in the conventional plating bath, however due to the relatively higher stability constant value of NH_3 towards Pd and the large NH_3 concentration in the bath as compared to EDTA, NH_3 acted as the

main complexing agent for both Pd and Ag. The overall reactions of the electroless Pd and Ag deposition based on N_2H_4 as the reducing agent used in this study is widely accepted with the following redox reactions [68].

Pd:



Ag:

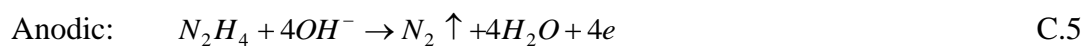
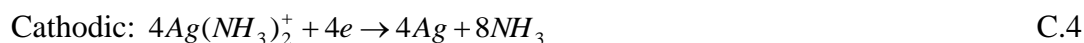


Fig. 5.6a shows (Chapter-5, Section 5.3.31) the polarization curve of the Ag solution (3 mM Ag concentration, pH = 11, solution volume = 50 ml and cathode surface area = 0.63 cm^2) on the Ag surface. As discussed in Chapter-5, Section 5.3.3.1, the cathodic polarization curve for the Ag bath showed fast reduction kinetics for the metal. The solid line curve shows the scan obtained in the presence of Ag while the dotted line curve shows the scan obtained in the blank solution with no Ag present in the solution. The Ag deposition started approximately at the electrode potential of 17.5 mV (very close to the equilibrium potential (-30 mV) of the Ag ions, based on the stability constant ($10^{7.3}$) for the complexing reaction of Ag with NH_3 and the Nernst equation) and within the overpotential of 15 to 25 mV, the Ag deposition reached a point where the overall deposition process was limited by the mass transfer step of the Ag ions to the sample surface as indicated by no increase in the current on further

increasing the overpotential for the Ag deposition (Fig. 5.6a). In the case of the Pd bath (Pd concentration = 3 mM, solution volume = 50 ml, pH=11 and cathode surface area = 0.63 cm^2), the polarization curve on the Pd surface as shown in Fig. 5.6b indicated large overpotential associated with the reduction of Pd. The solid line curve and dotted line curve show the LSV scans obtained on the solution with and without Pd ions respectively. It can be seen in Fig. 5.6b (see Chapter-5, Section 5.3.3.1) that the Pd deposition occurred at the electrode potential between -650 and -700 mV (Note: the calculated equilibrium electrode potential for the Pd ions (3 mM) in the solution was -230 mV with respect to Ag/AgCl, 3 M NaCl). The overpotential associated with the Pd deposition lied in the range 420-470 mV, an order of magnitude higher than that associated with the Ag deposition process. The reduction characteristics of the two metals did not alter significantly with the change in the nature of electrode surface. Fig. 5.7 (see Chapter-5, Section 5.3.3.1) shows the LSV scans of Pd and Ag solutions on the Ag and Pd surface respectively. As can be seen from Fig. 5.7, the electrode potentials at which the Pd and Ag deposition started were more or less same, irrespective of the nature of the electrode surface.

The anodic polarization curves obtained for the N_2H_4 (note: N_2H_4 was used as the reducing agent in the bath) bath (N_2H_4 concentration = 3 mM, solution volume = 50 ml, pH =11 and anode surface area = 0.63 cm^2) solution on the Pd and Ag surface are shown in Fig. 5.8 (see Chapter-5, Section 5.3.3.2). Both metals, Ag in particular, showed large overpotential (based on the Nernst equation, the equilibrium potential for the redox reaction associated with N_2H_4 with 3 mM concentration of N_2H_4 and pH =11 in the bath was -1.09 V) for the N_2H_4 oxidation. Fig. 5.8a and Fig. 5.8b show the polarization curves for the N_2H_4 oxidation obtained on the Ag and Pd surface

respectively. The solid line and dotted line curves show the polarization characteristics of the solution with and without N_2H_4 presence respectively. The Pd surface showed more catalytic activity than the Ag surface for the N_2H_4 oxidation. At the electrode potential of 0 V, the anodic current associated with the oxidation of N_2H_4 was an order of magnitude higher for the Pd surface than that for the Ag surface.

The polarization characteristics of Pd and Ag in the solution did not change in the case of co-deposition bath also i.e., in the case of simultaneous presence of two metals in single bath. The polarization curve (see Fig. 6.1, Chapter-6, Section 6.3.1) showed two separate peaks associated with the Pd and Ag deposition and the deposition peaks were observed at approximately similar potentials at which the Pd and Ag deposition was observed for the individual metal bath (see Fig. 5.6, Chapter-5, Section 5.3.3.1).

C.2. Kinetics parameters estimation for the Pd, Ag and N_2H_4 polarization

According to the mixed potential theory [116], the rate of a redox reaction depends on the electrode potential and is independent of other redox reactions taking place on the same electrode. The polarization curve of individual redox reactions can be added to predict the overall polarization characteristics of the electrode (see Chapter 2, Section 2.3.2. for more details). In the case of electroless plating, the actual electrode potential at which the electroless plating occurs corresponds to the potential with net zero current and lies between the electrode potential of the metal ions and the reducing agent in the bath [116]. The use of the mixed potential theory could be better understood if all the cathodic and anodic reactions involved in the electroless plating are controlled by the charge transfer reaction and the effect of the mass transfer step of the reacting species in

the plating solution is eliminated. The LSV scans (see Fig. 5.6, Fig. 5.7, Fig. 5.8 (Chapter-5, Section 5.3.3) and Fig. 6.1 (Chapter 6, Section 6.3.1)) for Pd, Ag and N₂H₄ in this study were obtained without stirring the electrodes to eliminate the mass transfer effect of the reacting in the solution. Therefore, the LSV scans ((see Fig. 5.6, Fig. 5.7, Fig. 5.8 (Chapter-5, Section 5.3.3)) indicated the combined effect of the mass transfer step in the solution and the charge transfer steps at the electrode surface on the overall polarization characteristics of Pd, Ag and N₂H₄. The parameters for the kinetics of the charge transfer steps associated with the reduction of Pd and Ag ions and the oxidation of N₂H₄ could be deduced from the LSV scans shown in Fig. 5.6, Fig. 5.7 and Fig. 5.8 (Chapter-5, Section 5.3.3)) if only that portions of the scans are considered where the reduction or oxidation just started and the concentration of the reacting species is not significantly different at the electrode surface than the bulk of the plating solution. Fig. C.1a and Fig. C.1c show the portion of the Ag and Pd LSV polarization curves, where the reduction was just started, with the net current associated with the Ag and Pd reduction (i.e., the current for 3 mM metal concentration – the current for the 0 mM metal concentration solution). Fig. C.1b and Fig. C.1d show the fitting of the polarization curves shown in Fig. C.1a and Fig. C.1c respectively to the Butler-Volmer equation to get the kinetics parameter for the charge transfer reactions associated with the Ag and Pd reduction respectively. As shown in Fig. 5.6 (see Chapter-5, Section 5.3.3.1), Ag showed fast reduction kinetics and the deposition started very close to the calculated equilibrium potential in the solution. The Ag polarization curve data shown in Fig. C.1a was fitted to the low overpotential approximation of the Butler-Volmer equation [120] (Eqn. C.7) as shown in Fig. C.1b.

$$i = \frac{Ai_o\eta F}{RT} \tag{C.7}$$

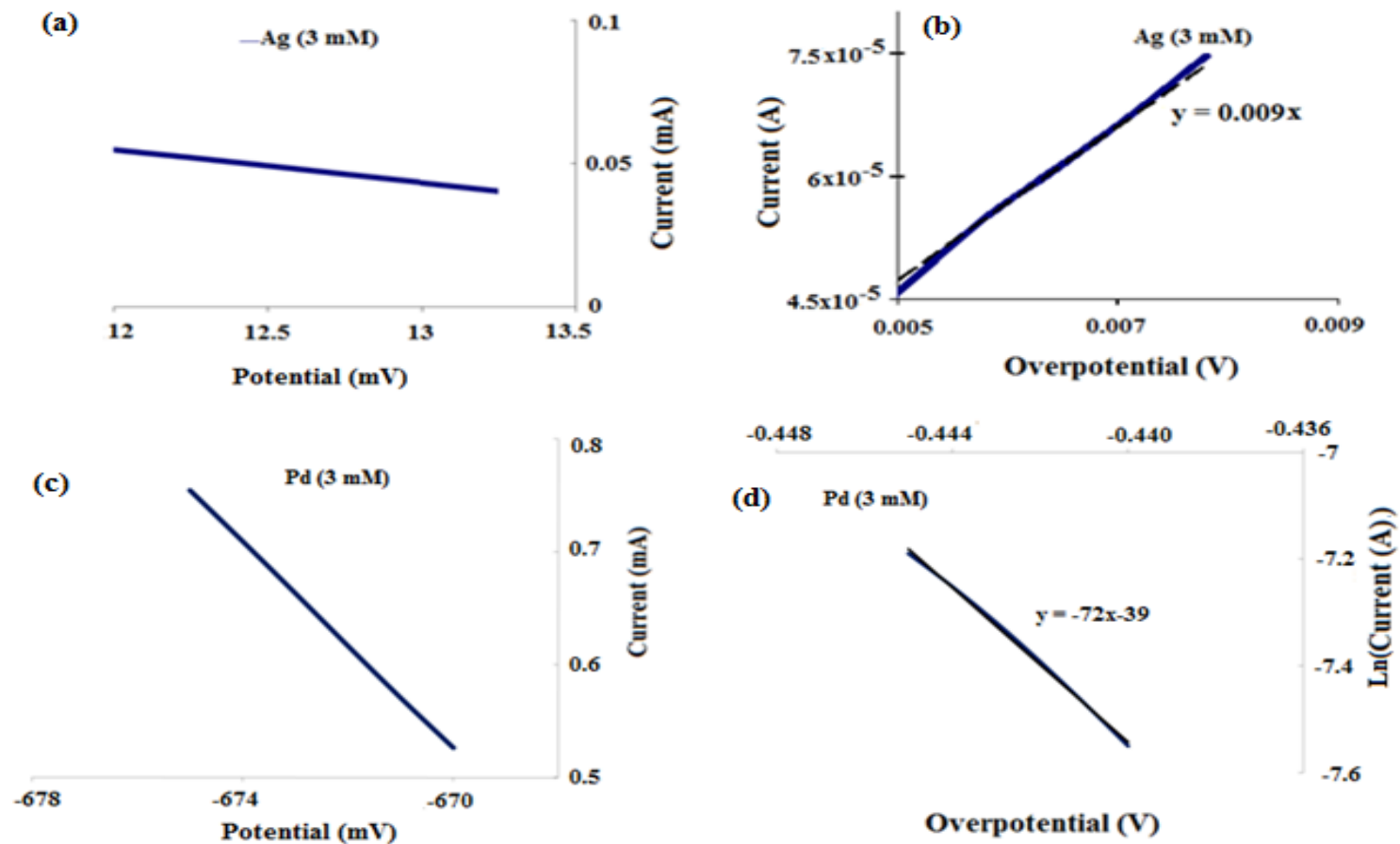


Fig. C.1. Fitting the LSV scan data obtained on Ag and Pd solution to the Butler-Volmer equation in order to determine the kinetic parameters for the charge transfer reaction associated with Ag and Pd reduction. (a) the LSV polarization curve with the net current for Ag (b) fitting the Ag LSV polarization curve to the Butler-Volmer equation (c) the LSV polarization curve with the net current for Pd (d) fitting the Pd LSV polarization curve to the Butler-Volmer equation

Where

i = Current measured at the Ag (cathode) surface (i.e. at the Ag surface due to the reduction of the Ag ions in the solution), A

i_o = Equilibrium exchange current density at the Ag (cathode) surface, (i.e. the exchange current density for the redox reaction associated with Ag ions in the solution and the Ag surface), A/cm²

η = Ag (cathode) electrode surface overpotential, V

A = Ag electrode (cathode) surface area, cm²

F = Faradays constant, C/mole

R = Gas constant, J/mole-K

T = Temperature, K

In the case of Pd, the large overpotential was associated with its reduction, therefore the data shown in Fig. C.1c was fitted to the high overpotential field approximation of the Butler-Volmer equation [120] (see Eqn. C.8) as shown in Fig. C.1d.

$$i = Ai_o \exp\left[-\frac{\alpha\eta F}{RT}\right] \quad \text{C.8}$$

Eqn. C.8 could be written in linear form as shown in Eqn. C.9

$$\ln i = \ln Ai_o + \frac{\alpha F}{RT}\eta \quad \text{C.9}$$

Where

i = Current measured at the Pd (cathode) surface (i.e. at the Ag surface due to the reduction of the Ag ions in the solution), A

i_o = Equilibrium exchange current density at the Pd (cathode) surface, (i.e. for the redox reaction associated with Pd ions in the solution and the Pd surface), A/cm²

η = Pd (cathode) electrode surface overpotential, V

α = Transfer co-efficient

A = Pd electrode (cathode) surface area, cm^2

F = Faradays constant, C/mole

R = Gas constant, J/mole-K

T = Temperature, K

Similar to the Pd reduction reaction, the large overpotential was associated with the N_2H_4 oxidation both on the Ag and Pd surface. The equilibrium potential (based on the Nernst equation for N_2H_4 bath with 3 mM N_2H_4 concentration and pH = 11) for the solution with 3 mM N_2H_4 concentration was calculated -1.09 V. The actual oxidation current were noticed approximately at -0.65 V and -0.13 V on the Pd and Ag surface respectively. Fig. C.2a and Fig. C.2c show the polarization curves with the net current (the current for the polarization curve with 3 mM N_2H_4 concentration in the solution – the current for the polarization curve with 0 mM N_2H_4 concentration in the solution, see Fig. 5.8, Chapter-5, Section 5.3.3.2) associated with the N_2H_4 oxidation on the Ag and Pd surface respectively. The polarization curves in Fig. C.2a and Fig. C.2c included only that portion of the polarization curves shown in Fig. 5.8a and Fig. 5.8b where the oxidation was just started so that the N_2H_4 concentration at the electrode surface was not significantly different than that in the bulk solution. The data shown in Fig. C.2a and Fig. C.2c were fitted to the high overpotential approximation of the Butler-Volmer equation as shown in Fig. C.2b and Fig. C.2d similar to the data for the Pd reduction (see Fig. C.1d).

Table C.1 shows the list of the estimated kinetics parameter associated with the Ag and Pd reduction and the N_2H_4 oxidation. The Ag reduction involved one electron transfer step. The low overpotential approximation could not provide the symmetry (β)

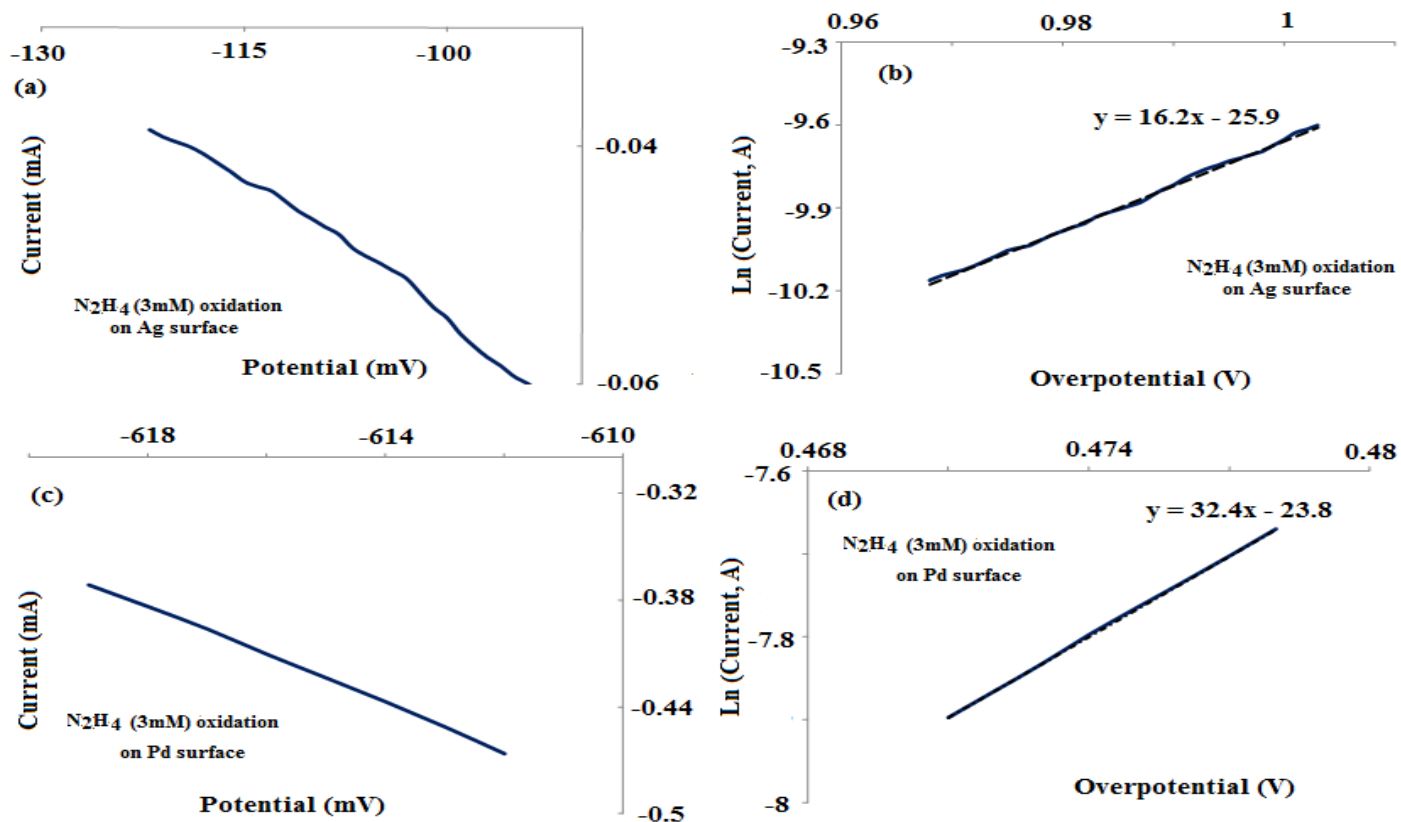


Fig. C.2. Fitting the N_2H_4 LSV polarization data to the high overpotential approximation Butler-Volmer equation. (a) LSV polarization curve with the net current associated with the oxidation of N_2H_4 [3 mM] on the Ag surface (b) Fitting the N_2H_4 oxidation polarization data on the Ag surface to the high field approximation of Butler-Volmer equation (c) LSV polarization curve with the net current associated with the oxidation of N_2H_4 [3 mM] on the Pd surface (d) Fitting the N_2H_4 oxidation LSV polarization data on the Pd surface to the high field approximation of Butler-Volmer equation.

Table C.1. Kinetics parameter obtained after fitting the LSV curves for the Ag reduction, Pd reduction and the N_2H_4 oxidation

Reaction Kinetics parameter ↓	Ag reduction	Pd reduction	N_2H_4 oxidation on Ag surface	N_2H_4 oxidation on Pd surface
Exchange current density, i_0 (A/cm ²)	4.1×10^{-4}	1.8×10^{-17}	8.9×10^{-9}	1.6×10^{-7}
Transfer co-efficient	0.5*	2.0	0.46	0.94

*Ag reduction involved transfer of one electron. The symmetry factor (β) for the Ag reduction reaction was assumed 0.5. The low overpotential approximation form of the Butler-Volmer was not suitable to find the symmetry factor (β) for the Ag reduction. Symmetry factor (β) was used to calculate the Ag reduction current at high overpotential range.

factor associated with the Ag reduction. The symmetry factor (β) for the Ag reduction reaction was assumed 0.5. Symmetry factor (β) of 0.5 was used to calculate the current associated with the Ag reduction especially in the high overpotential range.

C.3. Overall electroless deposition potentials

The kinetics parameter shown in Table C.1 were used to simulate the polarization characteristics of the overall Pd and Ag electroless deposition when the charge transfer reaction step was the rate controlling step for each individual reaction (i.e. for the Ag or Pd reduction and the N_2H_4 oxidation reaction) involved in the electroless deposition. The following equations with kinetics parameters listed in Table C.1 were used for obtaining the polarization curves for the Ag and Pd reduction and the N_2H_4 oxidation.

Ag reduction:

$$i = Ai_o \left[\exp\left(-\frac{\beta\eta F}{RT}\right) - \exp\left(\frac{(1-\beta)\eta F}{RT}\right) \right] \quad C.10$$

Pd reduction:

$$i = Ai_o \exp\left[-\frac{\alpha\eta F}{RT}\right] \quad C.11$$

N_2H_4 oxidation:

$$i = Ai_o \exp\left[\frac{\alpha\eta F}{RT}\right] \quad C.12$$

Fig. C.3 shows the polarization characteristics of the overall Ag and Pd electroless bath. Fig. C.3a shows the polarization characteristics for the overall Ag deposition on the Ag surface. The Ag reduction started at approximate 17.5 mV and the N₂H₄ oxidation started at potential of -150 mV, however the overall Ag electroless deposition on the Ag surface (Fig. C.3a) occurred at potential of - 3 mV (note: the electroless deposition occurs at potential where reduction current associated with metal ions = oxidation current associated with the reducing agent). Due to the high N₂H₄ oxidation catalytic activity of the Pd surface, the overall Ag deposition on the Pd surface occurred at more negative electrode potential (-423 mV) ((Fig. C.3b). The Pd deposition started ((Fig. C.3c) at -630 mV and the N₂H₄ oxidation at -750 mV and the overall Pd plating on the Pd surface occurred at -663 mV. The Pd deposition on the Ag surface was not possible (see (Fig. C.3d) due to the N₂H₄ oxidation starting at higher electrode potential than the potential for the Pd reduction.

The polarization characteristics of the overall Pd-Ag co-deposition bath ([Pd] = 3mM, [Ag] = 3 mM and [N₂H₄] = 3 mM are shown in Fig. C.4. It can be observed from Fig. C.4a that the simultaneous deposition of Pd and Ag was not possible on the Pd surface under the conditions where the charge transfer reaction was the rate controlling step (i.e. the diffusion step was relatively very fast which could be achieved by vigorously rotating the electrode or agitating the plating solution and the charge transfer reaction was the rate controlling step for the Pd and Ag reduction and the N₂H₄ oxidation reactions). The Ag reduction reaction polarizes the N₂H₄ oxidation reaction towards the anodic potential (-423 mV) at which the Pd reduction was not feasible (Note: Pd required electrode potential of -630 mV for its reduction) (Fig. C.4a). The

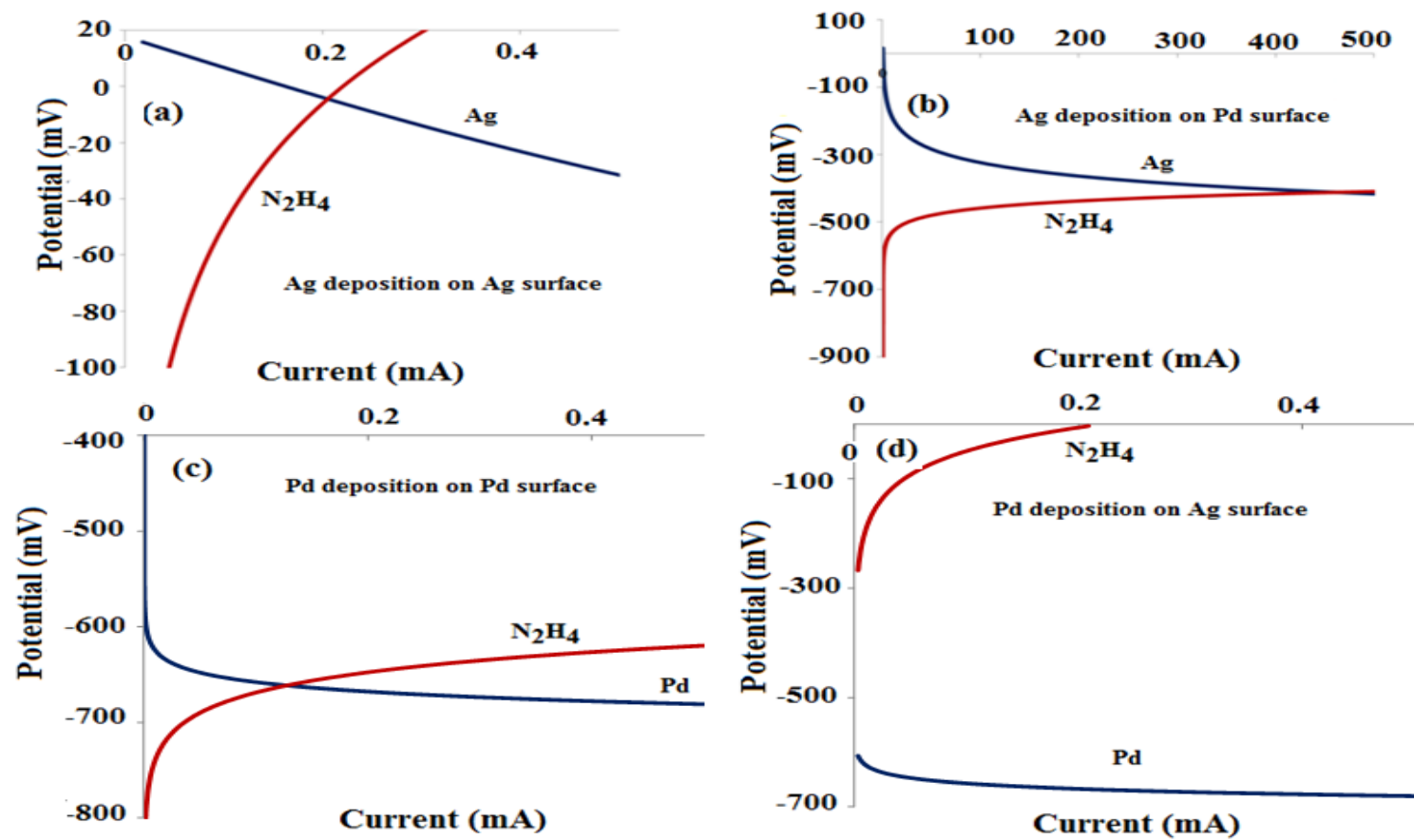


Fig. C.3. Overall Pd and Ag electroless plating polarization characteristics. (a) Ag deposition on the Ag surface (b) Ag deposition on the Pd surface (c) Pd deposition on the Pd surface (d) Pd deposition on the Ag surface [Ag] = 3mM, [Pd] = 3 mM and [N₂H₄] = 3 mM and electrode area = 0.63 cm²

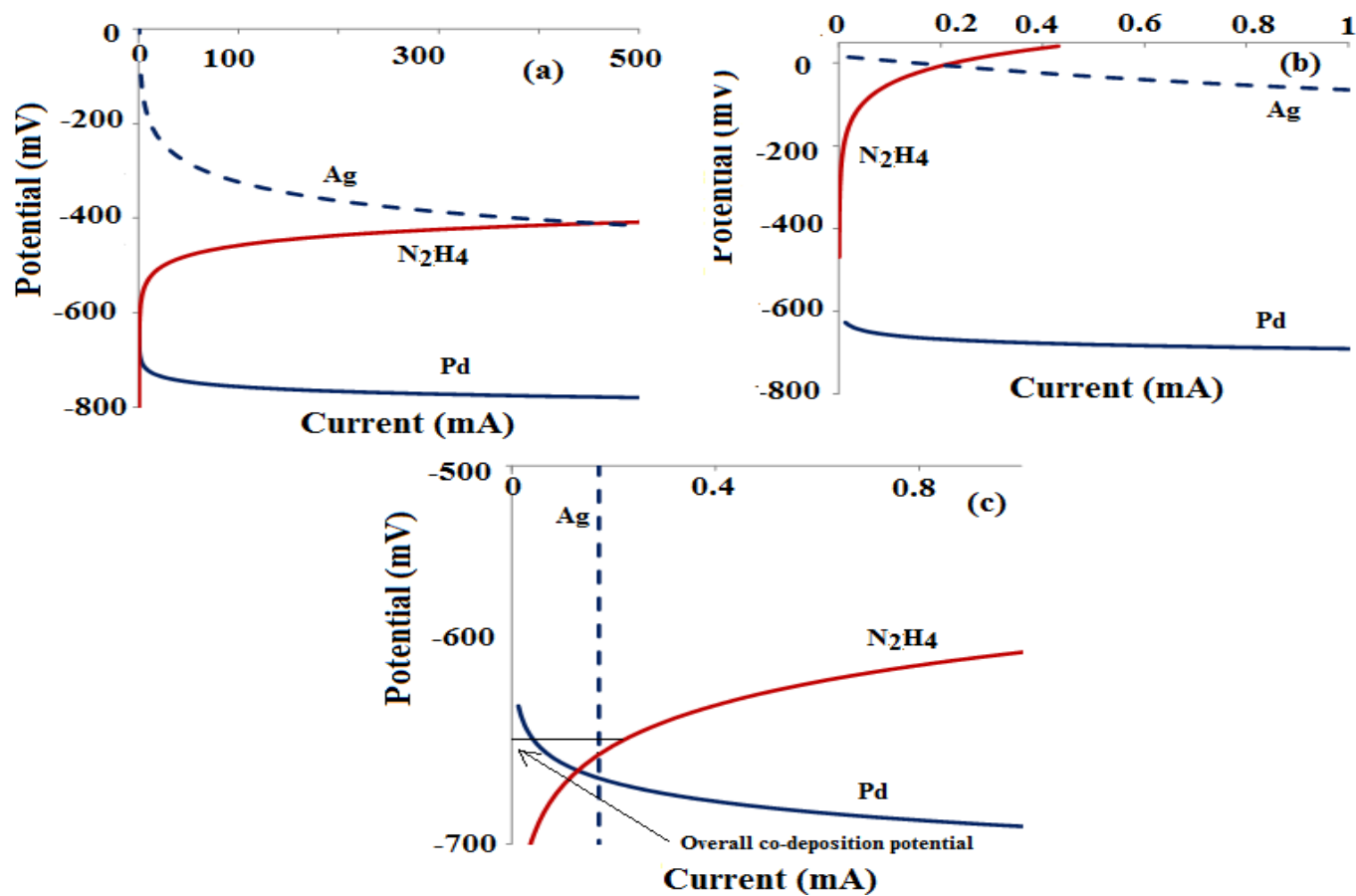


Fig. C.4. Overall Pd-Ag electroless co-plating polarization characteristics. (a) Pd-Ag co-deposition on the Pd surface (b) Pd-Ag deposition on the Ag surface (c) Pd-Ag co-deposition on the Pd surface when Ag is depositing under the mass transfer controlled conditions (d) Pd deposition on the Ag surface $[Ag] = 3\text{mM}$, $[Pd] = 3\text{mM}$ and $[N_2H_4] = 3\text{mM}$ and electrode area = 0.63 cm^2

coupon study for Pd-Ag co-deposition shown in Chapter-6, Section 6.3.8 also showed only Ag deposition when the coupons were rotated at 300 and 500 rpm during the Pd-Ag co-deposition. Fig. C.4b shows the Pd-Ag co-deposition on the Ag surface. Due to the low catalytic activity of the Ag surface toward the N_2H_4 oxidation, the overall electroless deposition occurred at electrode potential of -3mV at which Pd deposition was not possible.

Fig. C.4c shows the scenario for the Pd-Ag co-deposition on the Pd surface when the solution is not agitated or electrode is not rotated. Under the scenario shown in Fig. C.4c, the overall electroless plating would occur at potential where the current due to the reduction of Ag and Pd is equal to the N_2H_4 oxidation current. Since the N_2H_4 concentration (3 mM) was 4 times the stoichiometric requirement for 3 mM Ag concentration (see Eqn. C.6) in the solution and the large potential difference existed between the Ag reduction (17.5 mV, see Fig. C.3a) and the N_2H_4 oxidation potential (-750 mV), the overall plating potential would be shifted more towards the N_2H_4 oxidation potential. In addition, the Pd reduction potential (-630 mV) was closer to the N_2H_4 oxidation potential (-750 mV) than the Ag deposition potential (17.5 mV), therefore the overall electroless co-deposition potential on the Pd surface will be closer to the Pd reduction potential (-630 mV) and N_2H_4 oxidation potentials (-750 mV). As shown in the LSV polarization scan for Ag (Fig. 5.6, Chapter-5, Section 5.3.3.1.), the Ag deposition started being controlled by its diffusion in the solution within 20-25 mV electrode overpotential, therefore, in the case of no electrode rotation or solution agitation, the Ag deposition in the case of co-plating would occur at large overpotential and under the mass transfer controlled conditions. The Ag polarization curve in Fig. C.4c is represented by the flat line indicating diffusion controlled deposition. Since the

overall co-plating potential was closer to the potential where the Pd reduction started (-630 mV) or the potential where the N_2H_4 oxidation started (-750 mV), the polarization curves for the scenario in Fig. C.4c associated with Pd reduction and N_2H_4 oxidation were considered to be determined by the charge transfer step than the diffusion step. Fig. C.4c shows that for the Pd and N_2H_4 presence in the bath (as also shown in Fig. C.3c), the electroless potential was -663 mV and then on addition Ag into the bath (i.e. co-plating bath), the overall potential for the co-deposition shifted to the value of -647 mV.

As shown in the calculation in the previous paragraphs, the polarization curves of the individual redox reactions could be very useful tool to develop the electroless plating bath. The difference in the deposition potentials of the two metals plays an important role in the co-deposition of the metals and should be closer to each other in order to achieve the co-deposition. For example, the large difference existed in the deposition potentials of Pd and Ag in the case of conventional bath (NH_3 +EDTA based) with overall electroless plating occurring at potential of -647 mV (see Fig. C.4c) far negative than the Ag deposition potential (17.5 mV). Therefore, the Ag deposition occurred under severe mass transfer controlled conditions in the case of Pd-Ag co-deposition (as discussed in Chapter-6, Section 6.3.1). The polarization curves associated with the reducing agent aids in determining the suitability of the reducing agent and the nature of the surface required for initiating the electroless deposition. For example, in the case of N_2H_4 and conventional bath (NH_3 +EDTA), Ag surface was not suitable for Pd and Pd-Ag co-deposition because of N_2H_4 oxidation on the Ag surface occurring at higher potential than the Pd deposition potential on the Ag surface.

D. Appendix: List of membranes synthesized

Table D.1. Substrates used for the membrane preparation and their pre-treatment before the plating step

Membrane	Substrate Media grade/alloy	Intermetallic diffusion barrier step	Support grading
R-01	0.1 μm /PSS	Oxidation/500 $^{\circ}\text{C}$ /air/10 h	None
R-05	0.1 μm /PSS	Oxidation/500 $^{\circ}\text{C}$ /air/10 h	None
R-06	0.1 μm /inconel	γ -alumina layer by sol gel (550 $^{\circ}\text{C}$ calcination/air/10 h)	alumina powder (0.3 μm)
R-09	0.1 μm /inconel	Oxidation/500 $^{\circ}\text{C}$ /air/10 h	alumina powder (0.3 μm)
R-10	0.1 μm /inconel	γ -alumina layer by sol gel (550 $^{\circ}\text{C}$ calcination/air/10 h)	alumina powder (0.3 μm)
R-11	0.1 μm /inconel	γ -alumina layer by sol gel (550 $^{\circ}\text{C}$ calcination/air/10 h)	alumina powder (0.3 μm)
R-12	0.1 μm /inconel	Oxidation/500 $^{\circ}\text{C}$ /air/10 h	alumina powder (0.3 μm)
R-13a	0.1 μm /inconel	γ -alumina layer by sol gel (550 $^{\circ}\text{C}$ calcination/air/10 h)	alumina powder (0.3 μm)
R-13b**	0.1 μm /inconel	γ -alumina layer by sol gel (550 $^{\circ}\text{C}$ calcination/air/10 h)	alumina powder (0.3 μm)
R-14	0.1 μm /inconel	γ -alumina layer by sol gel (550 $^{\circ}\text{C}$ calcination/air/10 h)	alumina powder (0.3 μm)

**Substrate for R-13b is same as for R-13a.

Table D.2. Membrane plating steps and their descriptions

Membrane	Plating type and details	Total thickness, μm
R-01	Pure Pd plating	21.5
R-05	Pd-Ag co- plating (NH_3 +EDTA bath) (deposits gently polished during plating)	33.5
R-06	Sequential Pd (electroless) and Ag (electro) plating Pd-Ag-Pd-Ag-Pd (2.2-1.0-3.0-1.0-1.4 μm)	8.6
R-09	Pd-Ag co-plating (glycine bath)	7.1-8.1
R-10	Sequential Pd (electroless) and Ag (electroless) plating Pd-Ag-Pd-Ag-Pd (2.6-1.3-3.2-1.0-1.3 μm)	9.4
R-11	Sequential Pd (electroless) and Ag (electroless) plating Pd-Ag-Pd-Ag-Pd (1.8-1.0-2.1-1.8-2.0 μm)	8.7
R-12	Pd-Ag co-plating (glycine bath) (deposits gently polished during plating)	8.3-9.5
R-13a	Sequential Pd (electroless) and Ag (electroless) plating Pd-Ag-Pd-Ag-Pd (0.8-0.3-0.8-0.3-5.0 μm)	7.0
R-13b*	Pd-Ag sequential plating (7.2 μm)-annealing-polishing + (Pd plating-annealing-polishing) repeated three times + Pd plating	17.1
R-14*	(Pd = 1.5-2.5 μm and Ag = 0.7-1.0 μm electroless sequential plating-annealing-polishing) repeated two times + Pd plating (2 μm)	14.7

*Annealing was performed at 550 °C for 10 h in H_2

E. Appendix: He flow through the substrate

The typical data for the He flow through the substrate (inconel porous tube with diameter = 1.27 cm, length = 5.8 cm and media grade = 0.1 μm) used for the membrane preparation in this study is shown in Fig. E.1. The He flow data in Fig. E.1 is represented in the form of He permeance versus average pressure (average of the pressures on the two side of the substrate) across the substrate and was fitted to the following equation (Eqn E.1)

$$\frac{He(flux)}{\Delta P} = \alpha + \beta \times P_{avg} \quad \text{E.1}$$

The intercept (α , $\text{m}^3/\text{m}^2\text{-atm-h}$) of the line indicated the contribution of the Knudsen flow and the slope of the line (β , $\text{m}^3/\text{m}^2\text{-atm}^2\text{-h}$) signified the contribution of viscous flow to the overall He flow through the substrate [134]. At the pressure difference of 1 atm, the Knudson and viscous flow contribution to the He flux (for the substrate represented in Fig. E.1) was 245 and 201 $\text{m}^3/\text{m}^2\text{-h}$ respectively. The average pore size of the substrate shown in Fig. E.1 could be estimated using the following equation (Eqn. E.1) [148, 149].

$$D_{pore} = 8.4 \times 10^{-5} \mu \left(\frac{RT}{M} \right)^{0.5} \frac{\beta}{\alpha} \quad \text{E.2}$$

Where D_{pore} , μ , R , T , M , β and α in Eqn. E.2 stand for the average pore size of the substrate (m), viscosity of He gas (kg/m-s), gas constant (J/mol-K), temperature (K), molecular weight of He gas (kg/mole), contribution of the viscous flow to the He flux ($\text{m}^3/\text{m}^2\text{-h-atm}^2$) and contribution of the Knudson flow ($\text{m}^3/\text{m}^2\text{-h-atm}$) to the He flux

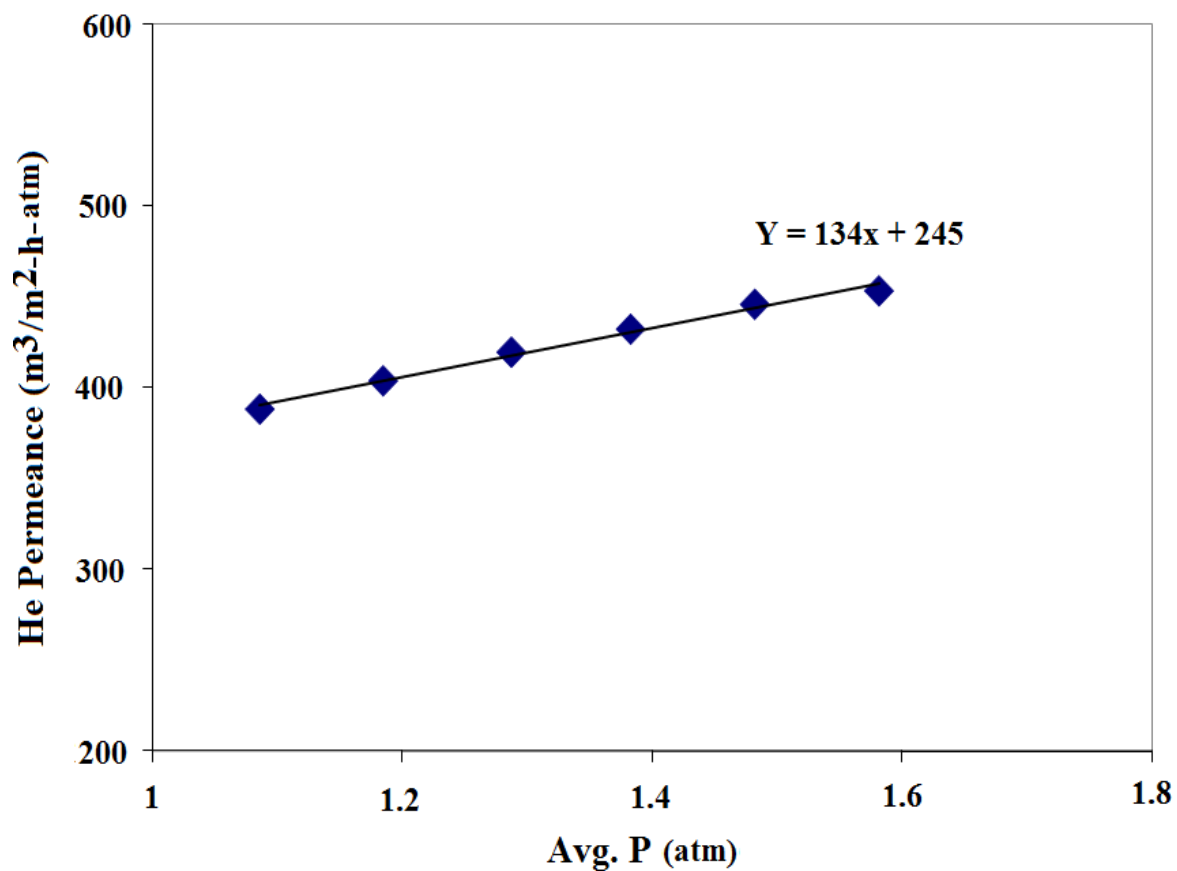


Fig. E.1. The typical He permeance vs. average pressure (average of the pressures on the higher pressure end and lower pressure end) data of the substrate (measured at room temperature) used in this study for the Pd and Pd-Ag membrane preparation.

respectively. Based on the calculation using Eqn. E.2 and the He flow data (Fig. E.1), the average pore size of the substrate (represented in Fig. E.1) was estimated 0.6 μm . Table E.1 shows the average pore size of some of the substrates used in this study for the Pd and Pd-Ag membrane preparation using Eqn. E.2 and the He flow data similar to Fig. E.1.

Table E.1. Average pore size of some of the substrates used in this study for the Pd and Pd-Ag membrane preparation

Substrate for membrane	β $\text{m}^3/\text{m}^2\text{-h-atm}^2$	α, $\text{m}^3/\text{m}^2\text{-h-atm}$	Avg. pore size μm
R-06	44	276	0.2
R-10	134	207	0.8
R-11	134	245	0.6
R-13	73	348	0.3
R-14	51	230	0.3

F. Appendix: A case study of He leak in Pd membrane

The membranes prepared in this study (see Chapter 7) without involving any annealing and polishing sequence showed decline in the H₂/He selectivity on heating. The decline in the selectivity (H₂/He) could be attributed to the formation of through-through pinholes due to the presence of defects present in as deposited Pd [80]. Based on the presence of the defects in Pd deposits [80], the possible mechanism for the decline in membrane selectivity (H₂/He) could be agglomeration of these defects on heating and forming the through-through pinholes in the Pd film allowing He gas to pass through the Pd film and causing the decline in the membrane selectivity. The formation of pinholes can be better understood by a case study using a pure Pd membrane (Pd layer thickness = 8 μm) supported on a porous inconel tube (0.1 μm media grade) used in this study. The following assumptions and parameters values were used in this case study.

1. For substrate (typical values for the substrate used in this study):

Substrate He flow (see Appendix E for typical substrate He flux value)
 $= \alpha + \beta \times P_{avg} = 350 + 73 \times P_{avg}$, therefore, substrate He flux (for $\Delta P = 1 \text{ atm}$, room temperature) was equal to $460 \text{ m}^3/\text{m}^2\text{-h}$ which was equivalent to 17633 ml/min for substrate with $23 \times 10^{-4} \text{ m}^2$ (23 cm^2) area

Contribution of Knudson flow: viscous flow through substrate pores ($\Delta P = 1 \text{ atm}$)
 $= 350 \text{ m}^3/\text{m}^2\text{-h}$: $110 \text{ m}^3/\text{m}^2\text{-h}$ which was equivalent to 13417 ml/min : 4216 ml/min for substrate with $23 \times 10^{-4} \text{ m}^2$ (23 cm^2) area

Substrate area and porosity = 23 cm^2 and 0.3

Substrate thickness = 0.15 cm

Substrate average pore diameter (see Appendix D) = 0.3 μm

2. For Pd film:

Pd film thickness = 8 μm

Pinholes geometry = cylindrical

Void volume in the film = 0.005

Table F.1 and Table F.2 show the calculations for the case study. Table F.2 shows the detailed calculation for the different pore sizes of pinholes in the Pd film and corresponding He leak values considered in Table F.1. In Table F.1, the row 1 shows the number of substrate pores based on the substrate area of 23 cm², substrate porosity of 0.3 and average pore size of 0.3 μm . The value of Knudson and viscous flow per substrate pore ($\Delta P = 1 \text{ atm}$) in row 2 and 3 (Table F.1) was calculated by dividing the respective values of Knudson and viscous flow for the substrate by the number of substrate pores. Total void volume in the Pd film (row 4, Table F.1) was calculated based on 0.005 fractional volume porosity (as reported by Rhoda [80] for the Pd deposits) in the Pd film. The He flow data for the substrate was used to calculate the He flow through the pinholes in the Pd film (see Table F.2 for detailed calculation). The values of α (Knudson flow contribution) and β (viscous flow contribution) for the He flow through the substrate (row 2 and 3, Table F.1) was used to calculate the values of α (Knudson flow contribution) and β (viscous flow contribution) for the He flow through the Pd film for the different pinholes sizes assumed (0.3, 0.1 and 0.05 μm) in this case study (see Table F.2 for more details). The α (Knudson contribution) and β (viscous flow contribution) value calculation for the He flow through the Pd film pinholes based

Table F.1. He flow through the Pd film in the case when all the defects contribute to the through-through pinholes formation

Step	Step description	Step value
1	Number of substrate pores	9.8×10^9
2	Knudson flow/ substrate pore, ml/min	4.3×10^{-7}
3	Viscous flow/ substrate pore, ml/min	3.8×10^{-6}
4	Total Void volume in Pd film, μm^3	9.2×10^7
5	Pore size (0.3 μm), Pore numbers,	1.63×10^8
	He flow or leak (ml/min)	1.34×10^4
6	Pore size (0.1 μm), Pore numbers,	1.46×10^9
	He flow or leak (ml/min)	1.57×10^4
7	Pore size (0.05 μm), Pore numbers,	5.86×10^9
	He flow or leak (ml/min)	1.61×10^4

Table F.2. He leak formation in composite Pd membrane (Substrate + Pd film) due to the voids present in the electroless deposited Pd film

Substrate calculation						
Area (cm^2), porosity	Average pore size (μm)	Number of pore ¹	Knudson flow ² (ΔP =1atm) (m^3/m^2-h), (ml/min)	viscous flow ³ (ΔP =1atm) (m^3/m^2-h), (ml/min)	Knudson flow/pore (ml/min)	viscous flow/pore (ml/min)
23, 0.3	0.3	9.76×10^9	350, 13416	110, 4216	1.37×10^{-6}	4.31×10^{-7}
Pd film calculation						
Total void volume in Pd film ⁴ (μm^3)	Number of pores (for avg. pore size of 0.3, 0.1 and 0.05) (μm^5)	Knudson flow/pore ⁶ (at $\Delta P = 1 atm$) (for avg. pore size of 0.3, 0.1 and 0.05 μm) (ml/min)	viscous flow/pore ⁶ (at ΔP = 1 atm) (for avg. pore size of 0.3, 0.1 and 0.05 μm) (ml/min)	Total Knudson flow ⁷ (for avg. pore size of 0.3, 0.1 and 0.05 μm) (ml/min)	Total viscous flow ⁷ (for avg. pore size of 0.3, 0.1 and 0.05 μm) (ml/min)	
9.2×10^7	1.63×10^8 , $1.46 \times$	2.58×10^{-4} , 8.59×10^{-5} ,	8.10×10^{-5} , 8.99×10^{-6} ,	4.19×10^4 , $1.26 \times$	1.32×10^4 , 1.32×10^4 , $1.32 \times$	

$10^9, 5.86 \times 10^9$	4.29×10^{-5}	2.25×10^{-6}	$105, 2.51 \times 10^5$	10^4
He leak calculation for the substrate + Pd film combination for different pore sizes in Pd film				
For pore size $0.3 \mu\text{m}^8$ (ml/min)	For pore size $0.1 \mu\text{m}^8$ (ml/min)	For pore size $0.05 \mu\text{m}^8$ (ml/min)		
13451	15715	16132		

1: Number of pores = (substrate area x substrate porosity)/single pore area

2: Knudson flow (ml/min) = Knudson flux x substrate area

3: Viscous flow (ml/min) = viscous flux x substrate area

4: Total volume of Pd film x void fraction

5: Number of pores in film = total void volume/volume per pore

6: Flow through film pore (the film pore was exposed to $\Delta P = 1$ atm similar to the substrate pore) was calculated from the flow through the substrate pore such that Knudson flow α (pore size/length of pore) and viscous flow β (pore size²/pore length)

7: Total viscous or Knudson flow through Pd film = flow through Pd film for one pore x total number of pores

8: The He leak for the substrate and Pd film combination (subjected to $\Delta P = 1$ atm) was calculated using the values of α (Knudson contribution) and β (viscous contribution) for the substrate and Pd film (row 3 and row 6 in the table). The He leak calculation involved randomly picking the value of pressure at the interface between the substrate and Pd film until the condition of He flow through the substrate equal to He flow through the Pd film (because Pd film and substrate were in series) was satisfied.

on the fact that the flow (both viscous, β and Knudsen contribution, α) was inversely proportional to the length of the pinholes, directly proportional to the pore size for the Knudsen flow and directly proportional to the square of the size of the pinholes for the viscous flow. The values of α (Knudson flow contribution) and β (viscous flow contribution) for the substrate and Pd film pores were then used next to calculate the He flow (at $\Delta P = 1$ atm) through the Pd membrane (substrate + Pd film combination) (see Table F.2 for more details). The He flow through the Pd membrane (substrate + Pd film) was obtained by randomly selecting the value of pressure at the interface between the substrate and Pd film until the condition of He flow through the substrate was equal to the He flow through the Pd film (the substrate and Pd film were in series, therefore the condition of He flow through substrate equal to the He flow through the film was required to be satisfied) was satisfied. The row 5, 6 and 7 (Table F.1) show the He flow or leak through the Pd membrane (substrate + Pd film) with pinholes of different sizes (0.3, 0.1 and 0.05 μm). Fig. F.1 shows the SEM images of the surface of the membranes studied in Chapter 7 after the annealing and H_2 permeation study step. The membranes were annealed at 550 $^\circ\text{C}$ and then characterized for H_2 permeation study between 250 and 500 $^\circ\text{C}$ (see Chapter 7, Section 7.3.3 and 7.3.4). No clear presence of the pinholes was observed (Fig. F.1) on the membranes surface. The absence of pinholes formed at temperatures ≤ 550 $^\circ\text{C}$ shown in the SEM images (Fig. F.1) indicated the pinholes of being size below the SEM resolution. Therefore, the pinholes sizes, 0.3, 0.1 and 0.05 μm considered in this study were in the approximate SEM resolution range or below. Guazzone [11] also reported that pinholes formed became visible in SEM images when the Pd deposits were heated to temperature as high as 650 $^\circ\text{C}$.

The maximum possible He flow or leak ($\Delta P = 1$ atm) through the Pd membrane with

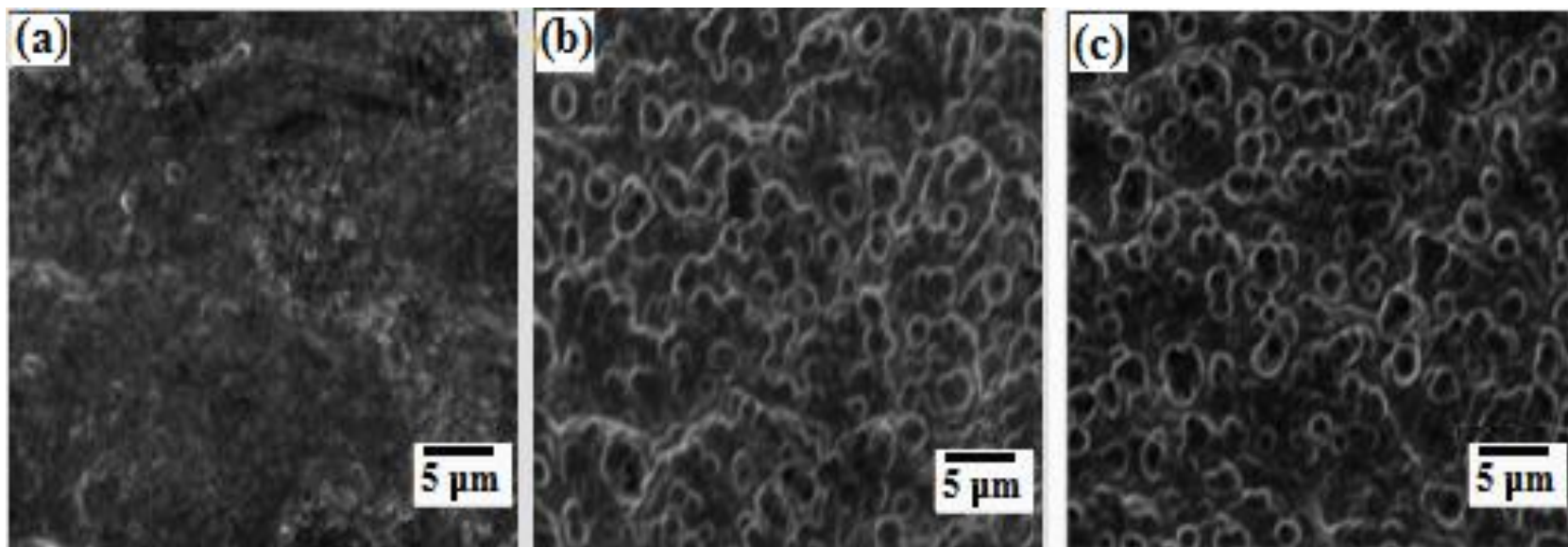


Fig. F.1. Typical SEM images of the membranes surface after annealing and H_2 permeation characteristics study in the temperature range of 250-550 °C (see Chapter 7, Section 7.3.3 and 7.3.4) (a) R-06 (b) R-10 (c) R-11.

pinholes was in the range of 10^4 ml/min (see row 5, 6 and 8 in Table F.1) which was much higher than the typical He leak measured for the membranes annealed and characterized in Chapter-7 (~ 3 ml/min). The difference could be described on the basis of alignment of the formed pinholes. The voids in the as plated deposits formed pinholes on agglomeration on heating. The possibility that all the pinholes formed contributed to through-through pinholes formation is very low and only very small fraction of the pinholes formed aligned themselves on heating to make through-through pinholes in the Pd film and causing the He leak and decline in the membrane selectivity.